Sponsor TBD Report No.:_____

AISI/DOE Technology Roadmap Program

Final Report

Development of Appropriate Resistance Spot Welding Practice for Transformation-Hardened Steels

by

Wayne Chuko
and
Jerry Gould

July 2002

Work Performed under Cooperative Agreement
No. DE-FC07-97ID13554

Prepared for
U.S. Department of Energy

Prepared by
American Iron and Steel Institute
Technology Roadmap Program Office
Pittsburgh, PA 15220

DISCLAIMER

Number of pages in report: 179

DOE and DOE contractors can obtain copies of this report
from:
Office of Scientific and Technical Information,
P.O. Box 62, Oak Ridge, TN 37831.
(865) 576-8401

This report is publicly available from the department of Commerce,

National Technical Information Service,
5285 Port Royal Road,
Springfield, VA 22161.
(703) 605-6000 (1-800-553-6847).

CONTENTS

Page

TABLES

TABLES
(Continued)

FIGURES

FIGURES
(Continued)

Page

EXECUTIVE SUMMARY

This report describes work accomplished in the project titled "Development of Appropriate Resistance Spot Welding Practice for Transformation-Hardened Steels." The first year of the program (Phase 1: Development of Temper Diagrams) involved development of in-situ temper diagrams for two gauges [nominally 0.8- and 1.55-mm (0.030- and 0.61-in.)] of representative dual-phase and martensitic grades of steels (Appendix I). The diagrams are based on the fact that spot welds made in C-Mn sheet steels typically transform to martensite upon cooling during resistance spot welding. Tempering can then be performed by adding a cool and post-weld current pulse (tempering step) to the welding sequence. The results showed that tempering is an effective way of reducing hold-time sensitivity (HTS) in hardenable high-strength sheet steels. Temper diagrams could be broken up in two regimes. These included a steady-state temperature region (so-called C-curve region), which was typical of temper times longer than about 30 cycles. The second was a transient regime, extending to shorter times and significantly higher tempering currents. This allowed tempering to be done in as short as 2-3 cycles. Performance in the C-curve region was examined in detail, including metallographic and mechanical properties studies. Some preliminary metallurgical and thermal modeling was also done to interpret the general in-situ tempering behavior in these steels.

In Phase 2 ('Evaluation of Post-Weld Cooling Rate Techniques') of the study, the same four steels were examined. These included two thin gauges of dual-phase and martensitic steels. Work was conducted in two parts. The first was to examine, in a preliminary way, three alternative methods for HTS reduction not studied in the Phase 1 work. These included post-heating, downsloping, and spike tempering. The latter was included as some promise was shown in the Phase 1 work. Based on these preliminary results, downsloping was selected for detailed additional study. Downslope was selected as tempering effects were covered in the Phase 1 work, and downsloping appeared to be the most promising of the cooling rate control methods.

Downsloping maps then were developed for each of the candidate steels paralleling the previously developed temper-map methodology. The basic method for developing the tempering maps included making resistance spot welds at standard conditions, then downsloping for a range of times and final currents. A full matrix of downslope times and currents were used for developing these maps. Welds made at each downslope condition were subjected to Rockwell surface hardness testing and standard peel testing.

Results from these tests were plotted, using a two-dimensional contour plot, with respect to downslope time and current. The resulting plots made up the downsloping maps for each material. The data showed the areas of peak response with respect to surface hardness of the weld, and resulting nugget morphology after peel testing.

The downsloping maps for each of the candidate steels were used to locate the conditions necessary for the peak response. Three specific downslope conditions were chosen for further metallurgical and mechanical testing. These conditions were done at a fixed final current (for each material), timed for a zero-, medium-, and full-softening response. Representative samples were inspected metallographically, examining both local hardness variations and microstructures. Mechanical testing of each of the three selected temper conditions was also done, and included lap-shear testing, tensile-fatigue testing, cross-tension tensile testing, and cross-tension drop impact testing. Results from the mechanical testing were used to quantify the effectiveness of downsloping on mechanical performance of the representative welds.

The resulting downslope diagrams were found to consist largely of a C-curve. The softening observed in these curves, however, was not supported by subsequent metallography. This metallography showed that all welds made, regardless of material and downslope condition, were essentially martensitic. These micrographs also showed adjacent areas surrounding the martensitic weld as an apparently partial transformed zone (ferrite + martensite) and outside this, an untransformed ferrite zone. These zones were well defined on the heavier-gauge steels, and intermittently observed on the thin-gauge steels.

Simplified thermal modeling showed that regions adjacent to the electrode-sheet interface were, for the thin-gauge steels, in the two-phase regime, and for the heavier-gauge steels, well below this two-phase regime. In addition, the thermal models showed that "natural cooling rates" (those without downslope) were at least an order of magnitude greater than that required for the formation of martensite in these grades of steels.

CCT/TTT diagrams for the dual-phase and martensitic grades of steels were generated based on microstructural modeling done at Oak Ridge National Laboratories. Resulting diagrams showed that minimum downslope times of 2 and 10 s for the martensitic and dual-phase grades of steels, respectively, were required to avoid martensite formation. These times, however, were beyond those examined in this study.

Downslope response was then related to changes that occur in the ferrite + martensite layer on cooling. This layer, at peak temperature, is ferrite + austenite. Slower cooling rates will allow some austenite to back-transform to ferrite before the interceding martensitic reaction occurs. As a result, different downsloping conditions will result in different fractions of ferrite and martensite in this surface layer, affecting the measured surface hardness. Clearly then, the developed downslope diagrams relate to microstructural variations in this surface layer, and not the bulk of the weld. As such, these diagrams do not represent either softening affects in the weld, or variations in HTS. Not surprisingly, mechanical properties also did not vary significantly over the conditions covered in these maps.

Clearly, these results show that downsloping is not an effective means of reducing HTS for production resistance spot welding (RSW). The necessary downslope times (2-10 s) are prohibited by the welding rates currently used today (up to 60 welds/s). Based on the observations made in this and the Phase 1 work, spike tempering appears to be the best compromise of microstructural improvement and short cycle time. It is recommended that future work be focused on exploring the robustness of this approach, and its applicability for a wider range of steels.

Appendix I

Development of Appropriate Resistance Spot Welding Practice for Transformation-Hardened Steels
Phase 1: Development of Temper Diagrams

Contents

Contents
(Continued)

Page

Tables

Tables
(Continued)

Tables
(Continued)

Figures

Figures
(Continued)

Page

Figures
(Continued)

Page

Summary

This report describes work accomplished in the first year efforts of the American Iron and Steel Institute (AISI) project "Development of Appropriate Resistance Spot Welding Practice for Transformation-Hardened Steels". Previous studies performed by EWI defined a methodology for developing temper diagrams for C-Mn grades of high-strength sheet steel based on post-weld in-situ tempering behavior of resistance spot welds.[1] The diagrams are based on the fact that spot welds made in C-Mn sheet steels typically transform to martensite upon cooling during resistance spot welding. Tempering can then be performed by adding a post-weld current pulse (tempering step) to the welding sequence. This tempering step is a relatively simple way of reducing weld hardness and, therefore, susceptibility to hold-time sensitivity (HTS) behavior. The original methodology was defined and applied to 0.87-mm (0.034-in.) C-Mn steels. In the AISI project additional C-Mn grades of high-strength sheet steels were examined using a similar methodology.

Four steels were included in the study. These included two thin gauges of dual-phase and martensitic steels. In-process tempering maps were developed for each of the candidate steels using the previously developed methodology. The basic method for developing the tempering maps included making resistance spot welds at standard conditions, in-process quenching for a sufficient amount of time to produce a fully martensitic weld microstructure, then in-process tempering of the welds. A full matrix of tempering times and currents were used for developing the maps. Welds made at each temper condition were subjected to Rockwell surface hardness testing and standard peel testing. Results from these tests were plotted, using a 2D contour plot, with respect to temper time and current. The resulting plots made up the tempering maps for each material. The data showed the areas of peak tempering response with respect to surface hardness of the weld, and resulting nugget morphology after peel testing.

The tempering maps for each candidate steel were used to locate the conditions necessary for the peak tempering response. Three specific temper conditions were chosen for further metallurgical and mechanical testing. These conditions included a zero-, medium-, and full-temper condition. Representative samples, were inspected metallographically, examining both local hardness variations and microstructures. Mechanical testing of each of the three selected temper conditions was also done, and included lap-shear testing, tensile fatigue testing, cross-tension tensile testing, and cross-tension drop impact testing. Results from the mechanical testing were

used to quantify the effectiveness of tempering on mechanical performance of the representative welds.

The resulting temper diagrams were found to consist of two distinct regions, a C-curve characteristic of isothermal tempering, and a transient region for very short tempering times. The lower limit of these diagrams was defined by the currents and times required to achieve initial softening. The upper limit of these diagrams was defined by the currents and times required to re-austenitize the material (with subsequent quenching to martensite). Relatively simple modeling was found to be able to predict the shape of these curves. This modeling utilized relatively simple equations for the peak temperature of spot welds, and the "tempering parameter" defined by Holloman-Jaffee.[2] This modeling showed that the transient region of the diagram was both the result of the relationship between temper current and temperature at short temper times, and the necessity (based on Holloman-Jaffee) for higher tempering temperatures at these shorter times.

Metallographic analyses of temper welds showed that the microstructure consisted of a series of "shells", defining different states of temper. These states of temper based on increasing initiating temperature, include un-tempered martensite, tempered martensite, and re-austenization (which results in a martensite once the current is terminated). In the most developed state (full temper), this structure consisted of a martensite core (the remnant of re-austenitized material), surrounded by a region of tempered martensite, with perhaps un-tempered martensite adjacent to the electrodes. This distribution of microstructures does raise some question to the validity of the surface hardness tests used to define the temper diagrams. These measurements most closely correlated with the outermost shells of the developed microstructure. However, the surface measurements are still indicative of the progression of tempering, and effective for predicting performance changes in these welds.

The dual phase steels show good correlation between softening during tempering and button failure modes during peel testing. The relationship between softening and peel mode for the martensitic steels, however, was much more complex. These effects were related to the relatively high strength of the base material, and the roles played by the various softened regions on the failure path. General mechanical properties of tempered welds were affected by a range of factors, including specimen geometry, base material properties, weld geometry, and distributions of microstructure. Generally, tensile shear tests favored the no-temper condition, cross tension tests favored the intermediate temper condition, cross tension impact tests favored the full temper condition, and the fatigue results were unaffected by tempering. It was noted,

however, that the presence of interfacial type failures did reduce the mechanical performance of the weld.

Finally, a review of the results suggests that spike tempering, that is using high currents and very short temper times, offer potential for effective tempering with minimal increases in cycle time. Spike tempering was not fully investigated in this phase of the work, will be re-visited during the second year of the program.

1.0 Introduction

Current design trends in automotive manufacture have shifted emphasis to alternative lightweight materials in order to aid in producing vehicles with higher fuel efficiency. In response to this, a range of high-strength steels is now commercially available which offer advantages over typical low-carbon steels. In particular, high-strength steels facilitate gauge reduction in the assembled component. These steels achieve their strength through a combination of chemistry and processing, yielding tensile strengths ranging from 340 MPa (40 ksi) up to 1500 MPa (220 ksi).

A range of these newer high-strength steels is so-called transformation-hardened steels. These steels use varying fractions of degenerate austenite as a strengthening mechanism. Through complex thermal processing, strength levels up to 1500 MPa (220 ksi) can be achieved. A specific welding-related concern with these steels is a phenomenon known as hold-time sensitivity (HTS). HTS is demonstrated during destructive (peel) testing. Specifically, for typical spot welding hold times of 30 to 60 cycles, the spot weld fractures interfacially when peeled. However, for shorter hold times (5 cycles or less), the weld peels with a full-button morphology. The presence of even partial interfacial failure exhibited during a peel test makes the weld unacceptable by current automotive welding standards.

One of the proven methods of alleviating the problem of HTS is through in-process quench and tempering of the weld. After the weld has been made, it is held between the electrodes long enough to sufficiently quench to martensite. A subsequent temper pulse is then applied to soften the microstructure of the weld. Steels of varying composition and processing react differently to tempering and it is unknown how some of the newer transformation-hardened steels will react during such tempering.

In this project, dual-phase and martensitic, transformation-hardened steels were examined. Two different gauges of roughly 0.8 and 1.5 mm (0.31 and 059 in.) were examined for each steel. The steels were welded and in-process quenched and tempered using a matrix of temper times and currents to define the range of effective tempering. Effectiveness of tempering was then related to hardness on the surface of the weld nugget, and corresponding temper diagrams were produced for each sample. After developing the temper diagrams, the most robust area of the plot was further developed.

Representative samples were then welded and tempered using a tempering current that was located in the area of peak tempering response. Three different temper times at the selected tempering current were examined. These included zero-, medium-, and full-temper conditions. Metallurgical and mechanical test samples were made at these three different states of tempering, and the data was then used to interpret the temper diagram.

2.0 Background

2.1 High-Strength Steels

High-strength steels generally fall into three basic categories, classified by the strengthening mechanism employed. These include solid-solution-strengthened steels, grain-refined steels, and transformation-hardened steels. Manufacturing and material properties of the types of high-strength steels are well documented in papers by Bleck[3] and Davies and Magee.[4] Solid-solution-strengthened steels are basically low-carbon steels with small amounts solid-solution-strengthening elements added. Phosphorous is the most common addition; these steels are commonly referred to as "rephos" steels. Rephos steels have a tensile strength level ranging from 250-340 MPa. These have high strength and good formability. Past studies have shown, however, that additions of P are detrimental to resistance spot welding, in that they are more likely to coarse solidification with increased porosity levels.[5,6] This increases the possibility of cracking and interfacial weld failure in a peel test.

Grain-refined steels use small amounts of carbo/nitride-forming elements to achieve their strength. These are also referred to as micro-alloyed steels. The carbide-forming elements are typically additions of Nb, V, or Ti. The formed carbo/nitrides from these elements stabilize the grain structure during hot rolling. Upon subsequent cold rolling they result in a fine grain size. Grain-refined steels generally have a tensile strength ranging from 350-550 MPa.

Transformation-hardened steels are the third type of high-strength steels. These steels use predominately higher levels of C and Mn along with heat treatment to increase strength. The finished product will have a duplex microstructure of ferrite with varying levels of degenerate martensite. This allows for varying levels of strength. There are three basic types of transformation-hardened steels. These are dual-phase, transformation-induced plasticity (TRIP), and martensitic steels.

The annealing process for dual-phase steels consists of first holding the steel in the $\alpha + \gamma$ temperature region for a set period of time. During that time C and Mn diffuse into the austenite leaving a ferrite of greater purity. The steel is then quenched so that the austenite is transformed into martensite, and the ferrite remains on cooling.[3] The steel is then subjected to a temper cycle to allow some level of martensite decomposition. By controlling the amount of martensite in the steel, as well as the degree of temper, the strength level can be controlled. Depending on processing and chemistry, the strength level can range from 350 to 960 MPa.

TRIP steels also use C and Mn, along with heat treatment, in order to retain small amounts of austenite and bainite in a ferrite matrix. Thermal processing for TRIP steels again involves annealing the steel in the $\alpha + \gamma$ region for a period of time sufficient to allow C and Mn to diffuse into austenite. The steel is then quenched to a point above the martensite start temperature and held there. This allows the formation of bainite, an austenite decomposition product. While at this temperature, more C is allowed to enrich the retained austenite. This, in turn, lowers the martensite start temperature to below room temperature. Upon final quenching a metastable austenite is retained in the predominately ferrite matrix along with small amounts of bainite (and other forms of decomposed austenite). This combination of microstructures has the added benefits of higher strengths and resistance to necking during forming. This offers great improvements in formability over other high-strength steels.[4] Essentially, as the TRIP steel is being formed, it becomes much stronger. Tensile strengths of TRIP steels are in the range of 600-960 MPa.[4]

Martensitic steels are also high in C and Mn. These are fully quenched to martensite during processing. The martensite structure is then tempered back to the appropriate strength level, thus adding toughness to the steel. Tensile strengths for these steels range as high as 1500 MPa.

2.2 Hold-Time Sensitivity

A steel is considered hold-time sensitive when, using conventional hold-times of 30 to 60 cycles, the resulting weld fails interfacially upon peel testing. When using reduced hold times (around 5 cycles or less) a full-button morphology is observed upon peel testing. Indications of partial button cracking (so-called “irregular buttons”) are also indicative of hold-time sensitivity.

2.2.1 Causes for Hold-Time Sensitivity Failure

The occurrence of hold-time sensitivity has been well documented.[5,7-13] However, the underlying causes have only recently been defined. In a paper by Gould, Lehman, and Holmes,[6] it was suggested that susceptibility to interfacial failure was due to three factors. These are a disadvantageous stress state of the weld, the presence of preferential crack paths within the nugget, and a susceptible microstructure. Small nugget diameters combined with thicker sections result in a greater degree of triaxiality during peel testing. This disadvantageous stress state has been known to promote interfacial failure. The presence of preferential crack paths such as porosity or solidification cracks can allow a crack to initiate at the faying surface notch and to propagate from one porosity or crack location to another along the faying surface of the weld. Finally, a hardened microstructure with a large amount of martensite could allow for brittle cleavage fracture.

The possibility of forming martensite in resistance spot welds even at low carbon levels is supported by models by Gould, Li, Dong, and Kimchi[12] and Feng, Gould, Babu, Santella, and Reimer.[14] These have shown that cooling rates associated with spot welding are extremely rapid (on the order of 10^3 to 10^5°C/sec). These harder martensites will provide a path for a crack to propagate through. In addition, rapid cooling rates can lead to porosity entrapment toward the outer edges of the weld where the stress concentration is greatest in a peel test.[5] Rapid cooling rates have also been associated with tendency for solidification cracking which can add to the chances of interfacial failure of a spot weld. Using shorter hold times will allow the weld to cool at a slower rate and thus minimize cracking. However, shorter hold times cannot be guaranteed by many industrial welding guns, and are not always practical in automotive-assembly operations.

Chemistry of the particular steel is a major a contributing factor to hold-time sensitivity. Additions of P, common in solid-solution-strengthened steels, have been associated with additional porosity in the solidified weld nugget.[5] As mentioned, the location and amount of porosity in a spot weld can effect its mode of failure in a peel test. Additions of C and Mn, the main elements that are added to transformation-hardened steels, are well known to aid in the formation of martensite on cooling. These steels, of course, also have an increased risk of hold-time sensitivity.

Material thickness has multiple effects on the mode of failure during a peel test. First, the thickness of the material can alter the solidification mode. Thicker materials will allow for a slower, more three-dimensional mode of solidification. Slower cooling rates can reduce the tendency for solidification cracking. In addition, these slower cooling rates reduce the risk of martensite formation. It has also been shown that slower cooling rates tend to relocate porosity away from the nugget periphery. As mentioned previously, however, thicker materials result in a greater degree of triaxiality on cooling.

Clearly, there are several factors contributing to hold-time sensitivity. Reasons for actual unacceptable weld failure are due a combination of some or all of the factors involved.

2.3 Fracture Modes

Interfacial failure during a standard peel test in a high-strength steel resistance spot weld is not uncommon. Research by Gould and Workman,[5] as well as Ferrasse, Verrier, and Messemaecker et al.[12] has shown that the cracking that occurs can be combination of ductile and brittle fracture modes. Typically, the crack initiates at the faying surface notch between the sheets being joined. From there, it propagates through the weld nugget by following paths of hard brittle phases of martensite, or by following a path of porosity. Through either path, a combination of ductile and brittle cleavage-type fracture is seen. Work by Gould and Workman[5] documented this on both solid-solution-strengthened and transformation-hardened steels.

3.0 Approach

3.1 Materials and Equipment

In this first year of the project, temper diagrams were developed for four transformation-hardened steels using in-process quench and temper schedules. A 1ϕ, AC, Taylor Winfield, 100-kVA, pedestal-type resistance spot welder was used for all welding performed in the project. An ATEK TruAmp V constant-current controller was used for regulating welding and tempering schedules. The current was monitored by the ATEK controller and verified using a Miyachi Weld Checker MM 121A current meter. Welding force was verified using an oil-filled Waka force gauge. Electrodes used for welding were Class II, flat-faced, truncated-cone electrodes. Actual electrode geometries were selected based on steel gauge, as taken from the Ford

specification for high-strength steels (BA13-04).[15] Electrode diameters chosen for each material are listed in Table 1.

3.2 Selection of Candidate Materials

Four high-strength steels were selected for study. These included two gauges each of a 960-MPa (140-ksi) dual-phase steels, and a 1380-MPa (200-ksi) martensitic steel. Thicknesses of the dual-phase steel were 0.83 and 1.55 mm (0.033 and 0.061 in.). The nominal chemical content for the dual-phase steel was 0.15C, 1.41Mn, and 0.3Si. Thicknesses of the martensitic steel were 0.94 and 1.58 mm (0.037 and 0.062 in.). Nominal chemical content for the martensitic steel was 0.19C and 0.46Mn. An exact matrix including thickness and chemical composition of the candidate steels is found in Table 2.

3.3 Development of Temper Diagrams

All welding was performed on 38- ×100-mm (1.5- × 4-in.) coupons. Temper diagrams were developed using a methodology previously developed by EWI. The methodology is outlined in the following steps:

(1) **Current-range evaluations.** Steels were first subjected to current-range testing as per Ford Motor Company Specification BA 13-4.[15] This was done to establish the base (expulsion) current and 4v t welding current for the temper diagram development. This relatively small weld size was selected, as small welds are typically more susceptible to HTS.

(2) **Quench-time selection.** Quench time was then selected. The function of the quench time was to allow the weld to fully transform to martensite before the temper current was applied. Quench times were selected for each gauge of steel using available thermal modeling and previous experience.[1,7]

(3) **Welding trials.** Welds were then made over a range of tempering currents and times. Welds were configured as standard peel test coupons, including both a shunt weld and a test weld. All subsequent evaluations were done on the test weld of the coupon.

(4) **Initial temper diagram matrix.** A coarse approximation of the temper characteristics of each material was made using a linear variation of the temper

current, and a geometric progression of tempering times. Temper currents started at 15% of the expulsion current for the steel, and increased by 15% steps to 120% of the expulsion current (15, 30, 45, 60, 75, 90, 105, and 120% of the expulsion current). Tempering times began at 2 cycles, and progressively doubled to a maximum of 64 cycles (2, 4, 8, 16, 32, and 64 cycles). One test coupon was made at each of these combinations of temper current and temper time.

(5) **Hardness testing.** Hardness testing of the welds was done on the exterior weld surface, at the center of the electrode contact area. If electrode indentation into the test coupon was observed, one surface of each sample was ground flat before hardness testing. On each sample, a single Rockwell C (Rc) hardness indent was made. The resulting hardness readings were used for the subsequent contour plots.

(6) **Preliminary contour plotting.** Rc hardness values were then presented as a two-dimensional contour plot with temper current as the vertical axis, and temper time as the horizontal axis. This preliminary contour plot allowed critical areas of the diagram (where hardness changed most radically as a function of temper currents and times) to be identified.

(7) **Diagram refinement trials.** Based on the results of the preliminary contour plot, additional temper trials were made. These trials were used largely to refine the "nose" of the temper curve, and were made at much finer increments of current and time. Resulting welds were prepared and hardness tested in the fashion described in Step 5 above. They were then applied to the contour plot described in Step 6. In this case, three samples were made at each combination of temper current and temper time. Surface hardness measurements from each sample were then averaged for inclusion in the final diagram.

(8) **Preparation of final temper diagrams.** Temper diagrams were then prepared using a SigmaPlot 2000® contour-plotting package. This package allowed some averaging of the data, as scatter is inherent with most hardness testing. As mentioned, final temper diagrams took advantage of the results from both the preliminary and refinement tempering trials.

3.4 Metallographic Examinations

Metallographic sections were taken from welds that represented tempering currents and times for a zero-, medium-, and full-temper condition of each specific steel. Samples made using these tempering conditions were first verified using the surface hardness testing method from Step 5 above. Once verified, these samples were sectioned and examined using standard metallographic procedures. Hardness traverses using Vickers hardness testing were also made across the section of the weld. The diagonal hardness traverse was performed in order to clarify hardness variations in the joint, as well as to interpret the surface hardness measurements.

3.5 Destructive Testing

Destructive peel tests were performed on samples that were made at each set of conditions to define the temper diagram. Standard peel testing techniques were used, and the failure mode was recorded. The resulting button morphologies were then superimposed on the refined contour plot.

3.6 Representative Mechanical Properties

Representative welds made at each of the three temper conditions (for the four steel variations studied) were subjected to mechanical testing. Mechanical tests included lap-shear, tensile-fatigue, cross-tension tensile, and cross-tension drop-impact testing. For each temper condition, 20 samples were made and tested.

3.6.1 Lap-Shear Testing

Test coupons were prepared using the 38- $\times$ 100-mm (1.5- $\times$ 4-in.) coupon size. The coupons were then overlapped by 38 mm (1.5 in.) and joined by a single spot weld. Spacers were used in the grips of the testing machine to avoid bending in the samples during testing. Testing was performed on a Southwark-Emery tensile testing machine using a constant head speed of 50.8 mm/min (2 ipm). Five samples for each temper condition were tested and averaged.

3.6.2 Tensile-Fatigue Testing

Test coupons were prepared using the 38- $\times$ 100-mm (1.5- $\times$ 4-in) coupon size. The coupons were then overlapped 38 mm (1.5 in.) and joined by a single spot weld. The samples were then secured in the clamping fixture using spacers of equal (sheet) thickness to the material being

tested in order to assure vertical positioning. Testing was performed on a Satec Systems model SF1UA fatigue machine using a 30-Hz cycle frequency. Loading of the samples was varied from the maximum total load capability of the machine [8.0 kN (1800 lb)], to a minimum load allowing a fatigue life of 10^6 cycles for each sample. The loading of the machine was set up using an R-ratio of 0.1. S-N curves were developed for each temper condition of each material. At least five samples of each tempering condition were used to create the curves and a fatigue life of 10^6 cycles was used as an end of test condition.

3.6.3 Cross-Tension Tensile Testing

Cross-tension coupons for all samples were prepared using a coupon size of 50.8×152.4 mm (2×6 in.). Both ends of each coupon were pre-drilled with a 19-mm (3/4-in.) hole to be used for mounting the sample in the cross tension fixture. Coupons were symmetrically overlapped and joined using a single weld and tempering condition. The welded coupon was then mounted in the cross tension fixture using 19-mm (3/4-in.) bolts. The entire fixture was then placed in the tensile testing grips for testing. A Southwark-Emery tensile testing machine was used and samples were strained at a head speed of 50.8 mm/min (2 ipm). Five samples for each temper condition were tested and averaged.

3.6.4 Cross-Tension Drop-Impact Testing

Samples were prepared in the same manner as those used for cross-tension tensile testing. Cross weld impact coupons for all samples were prepared using a coupon size of 50.8×152.4 mm (2×6 in.). Both ends of each coupon were pre-drilled with a 19-mm (3/4-in.) hole to be used for mounting the sample in the cross tension fixture. Coupons were symmetrically overlapped and joined using a single weld and tempering condition. Testing was performed using a Dynatup-Drop Tower. The procedure followed AWS C1.1 accepted practice for drop impact testing. A 25-lb (11.34-kg) mass was dropped from a height of 4-ft (1.219-m) and reached a velocity of approximately 16 ft/sec (4.876 m/sec). Impact energy absorbed was measured in accordance with ASTM designation E604.

4.0 Results

4.1 Current-Range Evaluations

A current range test for each material and gauge was performed using a short (5-cycle) hold time. This was performed for the purpose of establishing an expulsion level for the material as well as the current required to produce a 4v t minimum nugget size. The expulsion level was

used as a reference point for selecting the tempering current (i.e., tempering currents were expressed as a percentage of the expulsion level for the sample material). The 0.83-mm (0.033-in.) dual-phase steel (Material A) had an 8.8-kA expulsion level and a 6.9-kA welding current. The 1.55-mm (0.061-in.) dual-phase steel (Material B) had a 12.3-kA expulsion level and a 9.2-kA welding current. The 0.94-mm (0.037-in.) martensitic steel (Material C) had an 8.5-KA expulsion level and a 6.6-kA welding current. The 1.58-mm (0.062-in.) martensitic steel (Material D) had a 12.3-kA expulsion level and a 9.3-kA welding current. These results are presented in Table 2. Clearly, both the expulsion level and welding current necessary to produce a $4\sqrt{t}$ nugget size were similar for similar thickness materials.

4.2 Quench-Time Selection

Quench times were selected using thermal modeling and previous experience.[1,7] Quench times necessary to cool the materials to approximately 200°C (392°F) were chosen. This temperature is well below the M_f for any of the steels studied (~500°C).[16,17] The quench time used for the thin steel samples (0.83 and 0.94 mm) was 20-cycles, and the quench time used for the thick steel samples (1.55 and1.58 mm) was 46 cycles.

4.3 Coarse Temper Matrix

After establishing appropriate welding parameters to achieve a $4\sqrt{t}$ weld in each material combination, coarse temper matrices were designed. Samples were welded and hardness tested in accordance with the temper diagram development methodology. The resulting rough plot allowed the critical areas of the diagram to be distinguished. In all cases, the area of peak tempering response was located between 45 and 75% of the expulsion current for the material. This mapped out a general C-curve where lower temper currents required longer temper times. In addition, each material also showed a tendency toward softening at higher currents and shorter tempering times. The data taken from the coarse matrix was used to build a refined tempering matrix with smaller current steps.

4.4 Refined Matrix

The refinement trials were focused around the area of critical softening that was observed in the results of the coarse matrix. For each refinement trial, three welds were made. Tempering current was incremented in 5% steps (of the expulsion level) around the critical tempering response area. Tempering time in the refinement trials was also carried out to 200 cycles, as

compared with the 64 cycles of maximum temper time used in the coarse matrix. This allowed for a more complete plot of the temper diagram. In region of tempering that tended to higher currents and shorter times, 10% current intervals were used.

Within each refinement matrix, there appeared to be a critical temper current at each temper time (lower bound) where no effective tempering response was observed. There was also an upper bound of temper currents, where the surface hardness measurements were similar to the untempered condition. The upper and lower bounds defined the window of tempering response. As mentioned above, high temper currents and very short weld times were also seen to soften the weld. In this transient region, temper trials were carried up to the highest currents possible for the temper times used. For short temper times (2 cycles) a current level was reached were expulsion occurred during tempering. At this point, temper trials were halted. At longer temper times, excessive indentation of the weld eventually was observed. Once excessive indentation occurred, temper trials were also halted. For all materials, welding was halted and no additional tempering trials were conducted once the upper and lower bounds of the tempering curve were clearly established. For the sake of producing a clear temper diagram plot, surface hardness measurements outside of the upper and lower bounds of the plot were estimated from the averaged hardness measurements taken from the zero-temper condition of each material. These are highlighted in the tables by darker (red) shading. Actual hardness measurements for each tested combination of temper time and current are highlighted in lighter (blue) shading. Results from surface hardness testing of the refinement trials were averaged together and are presented in Tables 3-6.

4.5 Peel Testing

Welded samples from both the coarse initial matrix and the refinement matrix were peel tested after performing surface hardness measurements. The modes of failure, ranging from full-button peels to interfacial failures were then recorded and related to the matrix of temper currents and times. Results are presented in Tables 7-10 and also plotted on the temper diagrams presented in Figures 1-4. Button peels in the tables are represented by the letter "B" and highlighted in a darker shade (red). Partial or full-interfacial failures are represented by the letter "P" and highlighted in a lighter shade (blue).

4.5.1 0.83-mm (0.033-in.) Dual-Phase Steel

For the 0.83-mm (0.033-in.) dual-phase steel, peel tests outside the upper and lower bounds defined by surface hardness testing resulted in a mixture of button peels (B) and partial interfacial failures (P). Inside the bounds of the region of effective tempering, the peel tests resulted in a much more consistent button peel mode of failure. The critical hardnesses that separated the button peels from the interfacial failures were around 37 Rc. Peel testing results are presented both on the temper diagram of Figure 1, as well as Table 7.

4.5.2 1.55-mm (0.061-in.) Dual-Phase Steel

The 1.55-mm (0.061-in.) dual-phase steel had peel test results similar to those of the 0.83-mm (0.033-in.) dual-phase steel. Outside the upper and lower bounds of the region of effective tempering (defined by the surface hardness measurements) there was a scattering of button peel and interfacial failures. Inside the window the failure mode was a full-button peel. The apparent critical hardness that separated button peel from interfacial failure was around 33 Rc. It is worth noting that the scattering of button peel and interfacial failures outside the upper and lower bounds for weld hardness were much lower in the thicker dual-phase steel than in the thinner dual-phase steel. Peel testing results are presented in Table 8 and Figure 2.

4.5.3 0.94-mm (0.037-in.) Martensitic Steel

The peel tests for the 0.94-mm (0.037-in.) martensitic steel resulted in mostly interfacial failures up to a temper current of approximately 40% of the expulsion level. Between temper currents of 40 and 45% (of the expulsion level) and 32 to 128 cycles of temper time there was a grouping of button peel failures. At 128 cycles of temper time this group of button peels rose to slightly higher currents. For the same window of temper time, an additional increase in current resulted in interfacial failures. At much higher currents (75% of the expulsion level and higher) for temper times longer than 8 cycles there is a large grouping of button peels. Those were related to the excessive indentation, which occurred during these tempering currents and times. Results from the peel tests are presented in Table 9 and Figure 3.

4.5.4 1.58-mm (0.062-in.) Martensitic Steel

The 1.58-mm (0.062-in.) martensitic steel had a mixture of both button peels and interfacial failures below a temper current of 45% of the expulsion level for the material. Within the window of effective tempering indicated by surface hardness testing of the welds, most of the peel tests yielded buttons. There was a small grouping of interfacial failures within the upper and lower bounds of the window of effective tempering. This occurred between temper currents of 55 to 65% of the expulsion level for the material and between the temper times of 64 to 80 cycles. Hardness measurements of the welds in this area were considerably softer (around 28 Rc) than those in the zero-temper condition. Results from the peel tests are presented in Table 10 and Figure 4.

4.6 Temper Diagrams

Data obtained from Rockwell hardness testing of the tempered welds was subsequently plotted with respect to time and current (expressed as a percentage of the expulsion level for the material) used to temper the weld. Temper times were plotted on the X-axis and temper currents were plotted on the Y-axis. The individual contour lines represent distinctions between different levels of hardness. The actual data points used for the plot were both the averaged data from the three refinement trials, and the data from the initial coarse matrix. Contour lines represent differences in weld hardness of two Rockwell hardness points.

In each contour plot, a similar softening of the weld due to tempering trend was observed. The curves were largely defined by a C-curve located around 50-65% of the expulsion level for the material and beginning after 32-64 cycles of temper time. Each plot also contained a second component that sloped toward higher currents and shorter times in an asymptotic fashion. This is defined as the initial transient of the curve. In addition to the contour plot of the tempered welds, peel test results were also plotted and superimposed onto the contour plot. Peel test results were expressed as button peel failures (white circles) and partial interfacial failures (black squares). The combination of the two plots allowed a correlation to be made between the failure mode of the tempered weld during peel testing, with the softening of the weld due to tempering. Detailed results for each steel studied are described in detail in the following paragraphs. Temper diagrams for each material studied are presented in Figures 1-4.

4.6.1 0.83-mm (0.033-in.) Dual-Phase Steel

The resulting temper diagram for the 0.83-mm (0.033-in.) dual-phase steel is presented in Figure 1. Hardnesses on this diagram range from about 42 Rc in the zero-temper condition down to about 29 Rc in the maximum tempering condition. As mentioned, the tempering curve is largely defined by a C-curve, with the peak tempering response occurring around 65% of the expulsion level. For this region of the curve, effective softening of the martensite begins around 8 cycles of temper time and peak softening occurs after about 32 cycles of temper time. The range of effective temper currents in this region of the diagram occurs between roughly 55 and 75% of the expulsion level.

In initial transient of the curve, effective tempering is seen at currents as high as 120% of the expulsion level. The time window of the curve in this region is relatively small, suggesting that slight changes in temper time or current would effectively eliminate the tempering effect.

When superimposing the plot of peel test results over the temper diagram, a clearer picture of the relationship between failure morphology and tempering effect is observed. Below the lower bound of the C-curve, peel tests result in a scattering of button peels and interfacial failures. Within the C-curve, peel tests result in full buttons. Along the upper bound of the curve and outside the C-curve, interfacial failures are observed. The initial transient region of the curve also shows a pattern of button peel failures within the curve, and interfacial failures outside of the curve, although it is not as clear as around the C-curve. At high currents (above 90%) and somewhat longer temper times (8-32 cycles) peel tests result in button morphology and no interfacial failures are observed.

4.6.2 1.55-mm (0.061-in.) Dual-Phase Steel

The temper diagram for the 1.55-mm (0.061-in.) dual-phase steel is presented in Figure 2. Hardnesses for this steel range from about 38 Rc in the zero-temper condition to 23 Rc in the maximum temper condition. The larger C-curve for the steel falls between roughly 45 and 65% of the expulsion level with peak tempering response occurring around 55% of the expulsion level. Effective softening of the martensite begins after about 32 cycles of temper time and maximum softening occurs after about 50 cycles. In the initial transient region of the diagram, effective tempering of the weld is seen up to 120% of the expulsion level. Small changes in either current or time effectively eliminate the tempering effect; however, the transient region of the curve is somewhat larger than that of the thinner dual-phase steel.

When superimposing the plot of peel test results over the temper diagram, a clear correlation between the results is again observed. Results here generally parallel those described for the thinner dual-phase steel above.

4.6.3 0.94-mm (0.037-in.) Martensitic Steel

The temper diagram for the 0.94-mm (0.037-in.) martensitic steel is presented in Figure 3. Hardness measurements on the diagram range form about 46 Rc in the zero-temper condition to 24 Rc with maximum tempering. Peak tempering response within the C-curve occurs around 53% of the expulsion level. The nose of the C-curve, where effective softening of the martensite first begins, is located around 8 cycles of weld time, with peak softening occurring after about 32 cycles. The range of tempering currents in the C-curve occurs roughly between 45 and 60% of the expulsion level. The inter-transient region of the diagram is again relatively narrow, where slight shifts in temper time or current effectively eliminate the tempering effect.

Peel test results (shown on the diagram) show that for the lowest temper currents (below 40% of the expulsion level), a scattering of button peels and interfacial failures, with a bias toward interfacial failures is seen. At the nose of the C-curve (around 16 cycles of temper time) there is a grouping of full-button peels. At the same current levels but longer temper times a region of interfacial failures are again seen. When tempering for still longer times (128 cycles) button peel failures are again observed. Toward the upper bound of the C-curve (at higher currents) a mixture of button peel and interfacial failures is seen with the bias toward interfacial failures again. The transient region of the diagram shows a fairly strong correlation between interfacial failures and softening of the weld due to tempering. This is contrary to the results observed for the dual-phase steels. At high temper currents and longer times, failure modes were for the button peel type. It is worth noting that there was an extreme amount of indentation on these welds.

4.6.4 1.58-mm (0.062-in.) Martensitic Steel

The temper diagram for the 1.58-mm (0.062-in.) martensitic steel is presented in Figure 4. Hardness measurements for this steel range from about 41 Rc in the zero-temper condition to about 22 Rc in the maximum tempering condition. Within the C-curve, maximum tempering response occurs around 55% of the expulsion level. At this level (55% of the expulsion level) softening begins around 32 cycles, with peak softening occurring at roughly 80 cycles. In this

temper diagram the large C-curve itself trends toward higher currents at shorter temper times. For this reason, it is less obvious where the nose of the curve begins and where the transient region begins. The transient itself extends up to 140% of the expulsion level where effective tempering still identifiable.

Regarding the peel test results, below the lower bound of the C-curve a scattering of button peel and interfacial failures are observed. Button peel failures are also seen at the nose of the C-curve. At 64 cycles of tempering and within the C-curve, a group of interfacial failures are clearly present. At still longer times within the C-curve full-button peels are once again observed. In the transient region, interfacial failures from the peel tests are seen, similar to the result for the 0.94-mm (0.037-in.) martensitic steel. Outside of the transient region, button peel failures are observed.

4.7 Metallurgical Evaluations

After developing temper diagrams for the steels, additional welds were made at selected temper schedules. Using the diagram, tempering times were chosen at the current that correlated with the peak tempering response current of the C-curve. Temper conditions included corresponded to zero-, medium-, and full-temper responses. The zero-temper samples were welded, quenched, and held with no additional temper time applied. The medium-temper samples were welded, quenched, tempered for a time that corresponded with the nose of the C-curve, then held for 60 additional cycles with no current applied. The full-temper samples were welded, quenched, tempered for a time that corresponded with a point well within the C-curve, then held for an additional 60 cycles with no current. These welds were then sectioned and mounted using standard metallographic procedures. Hardness traverses, using the Vickers hardness testing machine, were subsequently performed on the metallographic sections in order to assess how the microstructure of the weld corresponded to the temper diagram. The specific tempering conditions used for these samples are designated on the respective temper diagrams by black triangles. Actual parameters used for the three temper conditions, along with the Rockwell surface hardness measurement for each condition (on each material), are presented in Table 11. Results from Vickers hardness testing are described in detail in the following paragraphs.

4.7.1 0.83-mm (0.033-in.) Dual-Phase Steel

The metallographic and hardness results for the spot weld on the 0.83-mm dual-phase steel are shown in Figure 5. The micrograph (Figure 5b) shows the formation of a relatively small, $4\sqrt{t}$

weld nugget. Also, apparent is a larger zone, roughly 5 mm in diameter, with full through-thickness penetration, presumably representing the extent of austenization and subsequent martensitic decompression. The hardness traverse in the diagonal direction (Figure 5a) shows a "top-hat" profile. This profile is typical for spot welds undergoing martensitic decomposition from the austenite. The extent of this top-hat region roughly corresponds to the 5-mm (0.2-in.)-diameter transformation zone seen in the micrograph. In this plot the base metal hardness is approximately 286 HV, while a hardness of approximately 450 HV is observed through the transformation zone and weld nugget. There is also a slight dip in hardness on one side of the transformation zone, suggesting some degree of HAZ softening. A transverse hardness profile (in the through-thickness direction) is shown in Figure 5c. This was done in order to verify the relationship between a Rockwell hardness measurement taken at the surface of the weld with the actual hardness in the center of the nugget. Hardness measurements completely through the weld remain constant at around 450 HV. This is consistent with (although slightly higher than) the Rockwell surface hardness measurements from the refinement trials [42 Rc (412 HV)].

The metallographic and hardness results for the medium-temper sample on the 0.83-mm (0.033-in.) dual-phase steel are presented in Figure 6. The micrograph (Figure 6b) shows here again the relatively small ($4\sqrt{t}$) nugget, but an apparently much more diffuse transformation zone. The diagonal hardness profile is shown in Figure 6a. In this plot, the base metal hardness is similar to that from the no-temper condition, and there is again evidence of HAZ softening. However, the hardness variation through the transformation zone differs substantially from the no-temper condition. In this case, hardness peaks at the edge of the transformation zone at a level of 420-460 HV. Into the transformation zone the weld hardness drops to a low of approximately 325 HV in the center of the nugget. There is also indications of a hardness rise in the base metal on one side of the transformation zone. Reasons for this are not clear, and a measurement error may be at fault. The hardness traverse taken in the vertical direction through the cross section of the weld is presented in Figure 6c. This shows a hardness of about 400 HV at the front surface of the weld, and a low point in the center around 320 HV. The Rockwell hardness measurement of similarly tempered welds made during the refinement trials was around 33.4 Rc (330 HV), apparently higher than the center of the nugget.

The metallographic and hardness tests for the full-temper condition samples on the 0.83-mm (0.033-in.) dual-phase steel are presented in Figure 7. The microstructure here (Figure 7b) shows a relatively large martensitic zone [roughly 5 mm (0.2 in.) in diameter] with an elliptical shape. This zone appears to be banded by a diameter etching region. This region appears to extend to the face surfaces of the attached sheets. The diagonal hardness traverse shows a base

metal hardness of 295 HV followed by a softened region around 246 HV in the HAZ. Through the center of the weld nugget, hardness increased again to around 460 HV. This hardness was fairly constant through the nugget. Continuing along the traverse, the hardness drops off again in the HAZ and increases slightly into the base metal. The traverse taken in the through-thickness direction shows that the hardness near the surface of the weld is around 300 HV, then immediately increases to around 460 HV through the transformed region. Similar welds, made during the refinement trials, had Rockwell hardness measurements of about 32 Rc (318 HV), similar to that observed near the electrode sheet interfaces.

4.7.2 1.5-mm (0.061-in.) Dual-Phase Steel

A cross section of a weld made in the zero-temper condition, along with the transverse and through-thickness hardness profiles for the 1.55-mm (0.061-in.) dual-phase steel is presented in Figure 8. The micrograph of the weld is presented in Figure 8b. Again, indications of roughly a $4\sqrt{t}$ weld [5-mm (0.2-in.) diameter]. A slightly larger zone [6- to 7-mm (0.004- to 0.008-in.) diameter] is also observed, presumably defining the extent of martensite in the weld. This martensitic zone, however, does not reach the free surface, as was the case with for the 0.8-mm dual-phase steel. Here, a thin band of untransformed material is observed over a distance of 0.1-0.2 mm from the electrode sheet interface. The transverse hardness profile is shown in Figure 8a. The hardness profile is quite similar to that seen for the untempered 0.8-mm dual-phase steel, with a base metal hardness of roughly 300 HV, and a transformed zone hardness of roughly 450 HV. The transverse hardness profile again shows the "top-hat" profile, suggesting the transformed zone largely consists of martensite. There is also again some indication of HAZ softening directly adjacent to the martensitic area. The through-thickness hardness profile for this weld is shown in Figure 8c. These results show that the transformed zone is of consistent hardness (roughly 450 HV). This distribution is demonstrative of martensite in this region. The relatively low hardness regions near each electrode-sheet surface (roughly 340 HV) are co-incident with the thin band of untransformed material described above.

Similar results for a weld made in the "medium-temper" condition are provided in Figure 9. In this case, only the micrograph of the weld and the transverse hardness profile are shown. The micrograph (Figure 9b) reveals a relatively complex distribution of microstructures for this material and temper condition of spot weld. At the center is a relatively small zone [roughly 3 mm (0.12 in.) in diameter] of apparently martensitic material. Outside of this region, the remains of the resistance spot weld nugget [roughly 5 mm (0.2 in.) in diameter] are still visible. Here, however, the microstructure shows some evidence of tempering. Outside the nugget, the

transformed zone appears to extend over a range roughly similar to that observed in the zero-temper condition. The narrow band of material of apparently untransformed material adjacent to the electrode-sheet interfaces described for the zero-temper weld is also observed in this micrograph. The transverse hardness profile is shown in Figure 9a. The hardness profile in this case is relatively complex. The outside edges of the profile show the characteristic hardness of the base material (roughly 300 HV). Moving toward the center of the weld, there is first a slight dip in hardness (roughly 280 HV). Microstructurally, this appears to correspond to a region just outside the observable transformation zone. Further toward the center, the hardness appears to increase to nearly 400 HV. This corresponds to the farthest edges of the observed transformation region. In toward the weld nugget itself the hardness level again drops to nearly 300 HV (matching the dark band observed around the center of the weld nugget), with the nugget center increasing in hardness to nearly 480 HV.

Results for the "full-temper" condition are presented in Figure 10. The micrograph (Figure 10b) now shows a relatively large elliptical transformed region, over 6 mm (0.24 in.) in diameter, which appears to completely mask the weld nugget. This region is surrounded by a thin band of darker etching material, roughly 0.1-0.2 mm (0.034-0.059 in.) in thickness. Outside this band, the remnants of the prior transformed zone (identified for the zero- and medium-temper conditions above) are still faintly observable. The transverse hardness profile for this weld is shown in Figure 10a. The outside limits of the profile show the characteristic base metal hardness of around 300 HV. A relatively wide softened region is noted [roughly 1- to 1.5-mm (0.039- to 0.059-in.) wide] over which the hardness falls to about 250 HV. This softened region appears to extend from outside the remnant transformed zone to the dark band surrounding the weld center. The center of the weld region, however, appears to be fully martensitic, with a hardness level of roughly 450 HV. The profile in this region also shows the characteristic "top-hat" shape, again indicating the presence of martensite. The through-thickness hardness profile is shown in Figure 10c. The center of the weld region is again of uniform hardness (roughly 450-460 HV) demonstrating martensite formation in that region. However, the plot also shows a relatively wide band [0.5 mm (0.01 in.)] of softened material extends along the top and bottom surfaces of the weld region. Hardnesses here drop to less than 300 HV.

4.7.3 0.94-mm (0.037-in.) Martensitic Steel

The metallographic and hardness results for the 0.94-mm (0.037-in.) martensitic steel in the zero-temper condition are presented in Figure 11. A micrograph of the weld region is shown in Figure 11b. In this case, the weld region is dominated by an apparently martensitic

transformation zone, of roughly 4-5 mm (0.12-0.2 in.) in diameter, extending across the entire thickness of the two sheets. Within this zone, some residual columnar grain structure is observable, indicative of the 4√ t weld nugget. Outside of this zone, there is an extended darkly etched region, apparently representing an area where some decomposition of the base metal has occurred. For this sample, only the transverse hardness data were collected. The resulting hardness trace is shown in Figure 11a. The trace shows a relatively hard base metal hardness of roughly 450-470 HV. The apparent martensitic region shows a consistent hardness of nearly 500 HV. The darkly etching region described above appears to represent a region of softening. In this region, the hardness drops to a low level of near 300 HV.

Similar results for the medium-temper weld are presented in Figure 12. The metallographic results here (Figure 12b) are quite similar to those for the zero-temper condition described above, with the exception that the apparent nugget region is slightly more heavily etched. Again, only the transverse hardness profile was taken from this sample. This profile is presented in Figure 12a. This profile is quite similar to that seen for the zero-temper weld, showing similar base metal hardnesses (450 HV), roughly equivalent softening behavior in the far HAZ (300 HV minimum), and peak hardnesses in the transformed region (>500 HV). Of note, however, is that there seems a softening event happening across the width of the transformation zone. Peak hardnesses occur to appear at or near the transition between the transformed zone and the far HAZ. Hardnesses appear to then decrease toward the center of the nugget, reaching a minimum of roughly 440 HV. The majority of this apparent softening appears to be related to the slightly more heavily etched region (detailing the weld nugget) described above. This observation suggests that the heavier etching effect at the nugget is co-coincident with local thermal decomposition of the originally formed martensite.

Results for the full-temper weld are presented in Figure 13. The metallographic cross section of a representative weld is presented in Figure 13b. Here, the weld appears to be heavily tempered, with all regions responding strongly to the applied etchant. The basic weld shows the similar zones discussed for the medium-temper weld above. These include a base metal, somewhat darkly etched far HAZ, a now much more heavily etched transformation zone, and a differentially etched weld nugget. The transverse hardness profile for this weld is presented in Figure 13a. Again, no through-thickness hardness profile was taken for this sample. The hardness results here now show the extent of the tempering effect. Base metal hardnesses are still represented at both ends of the trace (450 HV). The previously described HAZ softening is also observable, again reaching a minimum of around 300 HV. As with the medium-temper weld described above, the hardness then again rises to a peak value at the edge of the

transformed zone. However in this case, that hardness is only on the order of 400-430 HV. Now there is substantial softening across the breadth of the transformed zone, reaching a minimum at the weld center, at a level of roughly 340 HV.

4.7.4 1.58-mm (0.062-in.) Martensitic Steel

The metallographic and hardness results for the 1.58-mm (0.062-in.) martensitic steel in the zero-temper condition are presented in Figure 14. A metallographic cross section of a representative weld is presented in Figure 14. A large transformed zone, extending over a diameter of roughly 6-7 mm (0.24-0.27 in.), as well as the through thickness of the two sheets dominates the microstructure of the weld area. Within this transformed zone, the remnant microstructure of a weld nugget can be observed. This apparent nugget diameter is about 5 mm (0.2 in.), consistent with the $4\sqrt{t}$ set-up conditions used to generate these welds. Outside of the transformed zone is an apparent far HAZ, roughly 1 mm (0.04 in.) in thickness, extending across the entire two sheet cross section. The transverse hardness profile for this section is shown in Figure 14a. This hardness profile is quite similar to that seen for the thinner section martensitic material under zero-temper conditions. Base metal hardness levels can be observed at the edges of the trace (440-450 HV). HAZ softening, roughly correlating with the far HAZ described above, is also apparent. In this region, the hardness gradually decreases from the base metal value to a low of roughly 280 HV at the edge of the transformed zone. The hardness across the transformed zone peaks at the edges, at a value of roughly 500 HV. This suggests a largely martensitic transformed zone. There is some indication of softening toward the center of the nugget (to roughly 450 HV) indicating some auto-tempering may be occurring. The through thickness hardness profile is presented in Figure 14c. The trace is relatively flat, with hardness values ranging from 450-475 HV.

The corresponding metallographic and hardness results for the medium-temper weld are presented in Figure 15. The metallographic cross section of a representative weld is presented in Figure 15b. The distribution of microstructures observed here is morphologically similar to that seen in the zero-temper condition above. This includes base material, an apparent far HAZ, and a relatively large transformed zone. The transformed zone is again roughly 6 mm (0.24 in.) in diameter, extending across the two-sheet cross section. Again, a faint outline of the weld nugget can be seen within this transformed zone. The corresponding transverse hardness results are plotted in Figure 15a. Again, though thickness hardness data were not collected. Base metal hardnesses in this trace are again measured at roughly 450 HV, and softening in the outer heat affected zone (to a level of about 300 HV) can be seen. These results, however, show that

extensive tempering of the transformed zone compared to the zero-temper condition described above. Within the transformed zone, highest hardnesses are measured at the periphery (410-420 HV). These hardnesses are substantially below those seen for the zero-temper transformed zone. In addition, there is continued softening toward the center of the transformed zone/weld nugget. Minimum hardness, at the center of this zone, is roughly 320-330 HV.

Metallographic and hardness results for a weld made at full-temper conditions are presented in Figure 16. The metallographic cross section of this weld is presented in Figure 16b. This weld is morphologically quite similar to the full-temper weld made on the thick-section dual-phase steel described in Section 3.7.2 above. A new transformation zone is defined which shows an elliptical shape, a diameter of roughly 7 mm (0.276 in.), and about 80% penetration of the two-sheet stackup. Remnants of the weld nugget are still visible within this zone. The original transformed zone, as observed for the zero- and medium-temper conditions, is still faintly visible at the upper and lower surfaces of this new elliptical-shaped zone. Outside these transformed zones, a wide far HAZ is observed. This zone appears to extend perhaps an additional 2-3 mm (0.079-0.12 in.) outside the transformed zone(s). Transverse hardness results are presented in Figure 16a. In this case, the hardness trace clearly did not extend to into the base metal; hardness levels on each end of the trace were only in the 350-375 HV range, well below the 450 HV level seen for the other two temper conditions. This is consistent with the wide far HAZ described above. Softest regions in this zone are again adjacent to the (new) transformed zone, achieving levels less than 300 HV. The transformed zone itself is of relatively uniform hardness, ranging from 470-500 HV. There, again, is some indication of a slight reduction in hardness at the weld center, which might be related to some slight auto-tempering. The through-thickness hardness profile for this weld is presented in Figure 16c. Again, the bulk of the transformation zone is relatively hard (450-500 HV) indicating the predominance of martensite. There is again, however, a slight dip in the hardness at the center of the weld, suggesting an auto-tempering effect. The hardness profile also shows a distinct drop in the region between the edge of the newly developed transformation zone and the electrode sheet interfaces. This plot suggests that the hardness at the electrode-sheet interfaces can drop as low as 225 HV.

4.8 Mechanical Testing

Mechanical testing was done to quantify the performance of welds made on each material, under some representative temper conditions. Three temper conditions were examined for each material, and corresponded to those described for the metallurgical evaluation samples. These included a zero-, medium-, and full-temper conditions. Five duplicate lap-shear, cross-tension,

cross-tension drop-impact, and lap-fatigue tests were conducted for each material/temper condition combination.

4.8.1 Lap-Shear Testing

4.8.1.1 0.83-mm (0.033-in.) Dual-Phase Steel

Lap shear test results for the 0.83-mm (0.033-in.) dual-phase steel are presented in Table 12. Data are for the peak load to failure on these tests. The zero-tempered samples had the highest average peak load to failure of 9.81 kN (2204 lb). The samples from the medium-temper condition had the lowest peak load to failure strength of 8.24 kN (1852 lb) and samples from full-temper condition had an average peak load to failure strength between the zero- and medium-temper conditions of 8.82 kN (1983 lb).

4.8.1.2 1.55-mm (0.061-in.) Dual-Phase Steel

Results from lap-shear testing of the 1.55-mm (0.061-in.) dual-phase steel are presented in Table 13. Zero-tempered samples had an average peak load to failure strength of 19.08 kN (4289 lb). Medium-temper samples had the highest peak load to failure strength of 20.48 kN (4602 lb). Samples for the full-temper condition had the lowest strength of 17.72 kN (3982 lb).

4.8.1.3 0.94-mm (0.037-in.) Martensitic Steel

Results from lap-shear testing of the 0.94-mm (0.037-in.) martensitic steel are presented in Table 14. The zero-tempered samples had the highest average peak load to failure value of 11.42 kN (2566 lb). The samples from the medium-temper condition had a slightly lower value of 10.17 kN (2286 lb). Samples from the full-temper condition had the lowest values in lap-shear testing of 8.29 kN (1863 lb).

4.8.1.4 1.58-mm (0.062-in.) Martensitic Steel

Results from lap-shear testing of the 1.58-mm (0.062-in.) martensitic steel are presented in Table 15. The zero-tempered welds had the highest peak load to failure strength of 20.19 kN (4536 lb). The welds made in the medium-temper condition had the lowest strength of 15.98 kN (3590 lb). The welds made in the full-temper condition had an average strength between the zero- and medium-temper conditions of 17.03 kN (4011 lb).

4.8.2 Tension Shear Fatigue Testing

Tension shear fatigue tests were conducted on all combinations of material and temper condition. For each combination, full S-N curves were developed. These S-N curves were nominally run from fatigue lives of 10^3-10^4 cycles to 10^7 cycles. Sets of curves for the individual steels were grouped together in separate plots. These fatigue results are presented in Sections 4.8.2.1 to 4.8.2.2 below.

4.8.2.1 0.83-mm (0.033-in.) Dual-Phase Steel

The S-N curves for spot welds made on the 0.83-mm (0.033-in.) dual-phase steel using zero-, medium-, and full-temper conditions are presented in tabular form in Table 16 and graphically in Figure 17. These plots all showed a maximum load for nominally 10^3-10^4 cycles to failure of roughly 4.6 kN (1000 lb). The fatigue limit (10^7 cycles) occurred at roughly 1.4 kN (300 lb). There is some indication that the medium-temper conditions out-performed both the full- and zero-temper conditions at higher load levels, but these results are all within the scatter of normal high-cycle fatigue data.

4.8.2.2 1.55-mm (0.061-in.) Dual-Phase Steel

The S-N curves for the resistance spot welds made on the 1.55-mm (0.061-in.) dual-phase steel using zero-, medium-, and full-temper conditions are again presented in tabular form in Table 17 and in graphical form in Figure 18. In this case, maximum forces on the fatigue-testing machine [8.3 kN (1800 lb)] corresponded with roughly 10^4 cycles fatigue life for the spot welds of all three temper conditions. The fatigue limits (10^7 cycles) were all in the range of 1.8-2.3 kN (400-500 lb). Again, results for the three temper conditions were quite similar. There is some indication that the medium-temper conditions again out-performed welds with the other two temper conditions, but these results are all well within the typical scatter for high-cycle fatigue data.

4.8.2.3 0.94-mm (0.037-in.) Martensitic Steel

S-N curves for the resistance spot welds made on the 0.94-mm (0.037-in.) martensitic steel for the three temper conditions are presented in tabular form in Table 18 and graphically in Figure 19. The results here are quite similar to those for the 0.83-mm (0.033-in.) dual-phase steel

described above. Nominal loads for roughly 10^4 cycles to failure were about 4.6 kN (1000 lb). The fatigue limit (10^7 cycles) occurs at roughly 0.9-1.4 kN (200-300 lb). The fatigue curves were again nearly identical for all three temper conditions, although consistently longer lives were seen for the full-temper condition.

4.8.2.4 1.58-mm (0.062 -in.) Martensitic Steel

The S-N curves for the resistance spot welds made on the 1.58-mm (0.062-in.) martensitic steel using the three different temper conditions are presented in tabular form in Table 19 and graphically in Figure 20. The results presented here are nearly identical to those shown for the 1.55-mm (0.061-in.) dual-phase steel described above. Again, maximum loads on the fatigue machine [8.5 kN (1800 lb)] corresponded to fatigue lives on the order of 10^4 cycles to failure. The fatigue limits (10^7 cycles) occurred at roughly 1.8 kN (400 lb), and no discernable difference was noted between the curves made for the various temper conditions.

4.8.3 Cross-Tension Tension Testing

Samples for cross-tension tensile testing were prepared as described in Section 3.6.3. Five samples each were tested, representing all combinations of base steel and temper condition (zero, mid, and full). The results for each steel are presented in the subsequent sections below.

4.8.3.1 0.83-mm (0.033-in.) Dual-Phase Steel

All cross-tension test data for the 0.83-mm (0.033-in.) dual-phase steel are presented in Table 20. Average cross tension strengths for the zero-, medium-, and full-temper conditions are presented graphically in Figure 21. These cross-tension strengths averaged 3.03, 3.18, and 2.99 kN (682, 715, and 673 lb) for the zero-, medium-, and full-temper conditions, respectively. There was also some scatter in the data, with standard deviations ranging from 0.08 to 0.44 kN (18 to 95 lb). There is some indication that the medium-temper condition offered a slight improvement in cross-tension strength. However, with this level of scatter, such a conclusion is tenuous.

4.8.3.2 1.55-mm (0.061-in.) Dual-Phase Steel

Cross-tension results for welds using the three different tempering conditions on the 1.55-mm (0.061-in.) dual-phase steel are presented in Table 21. Average cross-tension strengths for the three temper conditions are presented in Figure 22. These cross-tension strengths averaged 10.7, 12.3, and 11.2 kN (2400, 2750, and 2520 lb) for the zero-, medium-, and full-temper conditions, respectively. Again, there is some indication that the medium-temper condition offers best performance; however, the observed standard deviations for these datasets [1.2-3.7 kN (260-840 lb)] casts some doubt on that conclusion.

4.8.3.3 0.94-mm (0.037-in.) Martensitic Steel

Cross-tension results for the spot welds on the 0.94-mm (0.037-in.) martensitic steel with the three temper conditions are presented in Table 22. The average cross-tension strengths for each of the three temper conditions are presented graphically in Figure 23. These cross-tension strengths averaged 4.8, 4.3, and 3.8 kN (1080, 970, and 840 lb) for the zero-, medium-, and full-temper conditions, respectively. The actual cross-tension strength values are similar to those seen for the 0.83-mm (0.033-in.) dual-phase steel above. However, Figure 23 clearly shows a decrease in cross-tension strengths with increasing degree of temper. Even given the standard deviations on these datasets [0.35-0.5 kN (78-113 lb)] the effect is still significant.

4.8.3.4 1.58-mm (0.062-in.) Martensitic Steel

Cross-tension results for resistance spot welds on the 1.58-mm (0.062-in.) martensitic steel using the three temper conditions are presented in Table 23. Averaged cross-tension results for these three temper conditions are shown graphically in Figure 24. For this steel, average cross-tension strengths range from 5.4 kN (1220 lb) for the zero-temper condition, 8.4 kN (1900 lb) for the medium-temper condition, and 4.7 kN (1060 lb) for the full-temper condition. These variations are far outside the measured standard deviations for these datasets [0.47-1.46 kN (110-330 lb)]. It is also of interest that the zero- and full-conditions offer cross-tension strengths typical of the thinner gauge steels examined in this study; only the medium-temper condition offers strengths comparable with the 1.55-mm (0.061-in.) dual-phase steel described above.

4.8.4 Cross-Tension Impact Testing

4.8.4.1 0.83-mm (0.033-in.) Dual-Phase Steel

Results for cross-tension impact tests for the 0.83-mm (0.033-in.) dual-phase samples, using the range of temper conditions employed, are presented in tabular form in Table 24. Averaged cross-tension impact results for each of temper conditions are presented in Figure 25. Absorbed energy in the zero- and medium-temper condition samples averaged 30.03 and 29.30 J (40.75 and 39.75 ft-lb), respectively. The energy absorbed for the full-temper samples averaged a higher amount of absorbed energy of 34.08 J (46.25 ft-lb). Peel test results for the individual welds are also presented in Table 24. All tested welds failed with a full-button mode of failure.

4.8.4.2 1.55-mm (0.061-in.) Dual-Phase Steel

Results for cross-tension impact tests for the 1.55-mm (0.061-in.) dual-phase samples, employing the range of tempering conditions are presented in Table 25. Averaged impact test results for the three temper conditions are presented graphically in Figure 26. In this case, the absorbed energy for the zero-temper samples averaged 50.48 J (68.5 ft-lb) The medium-tempered samples showed a considerably higher average impact energy of 67.43 J (91.5 ft-lb). Finally, the energy absorbed for the full-temper samples showed the highest values at 72.22 J (98.00 ft-lb). Peel test results for the individual welds are presented in Table 25. The failure mode for the zero-temper samples was a mix between partial- and full-interfacial failures, where the medium- and full-temper samples failed with full buttons.

4.8.4.3 0.94-mm (0.037-in.) Martensitic Steel

Results for cross-tension impact tests on the 0.94-mm (0.037-in.) martensitic steel samples, employing the range of temper conditions, are presented in Table 26. Averaged cross-tension impact energies for the three temper conditions are shown graphically in Figure 27. Absorbed energy for the zero-temper samples averaged 36.66 J (49.75 ft-lb). The medium-tempered samples showed a slightly lower average impact energy of 32.98 J (44.75 ft-lb). The energy absorbed for the full-temper samples averaged the lowest for the set, at 31.51 J (42.75 ft-lb). Absorbed energy levels here are slightly higher than those for similar conditions presented in Section 3.8.4.1 above. Peel test results for the individual welds are presented in Table 26. All of the tested welds failed with a full-button mode of failure.

4.8.4.4 1.58-mm (0.062-in.) Martensitic Steel

Results for cross-tension impact tests on the spot welded 1.58-mm (0.062-in.) martensitic steel samples, using the three different temper conditions, are presented in Table 27. Averaged impact energies for the three temper conditions are presented graphically in Figure 28. Here, the absorbed energy for the zero-temper samples averaged 33.17 J (45 ft-lb). Absorbed energies for the medium-temper samples were higher, averaging 34.14 J (46.33 ft-lb). The energy absorbed for the full-temper samples showed the highest levels of absorbed energy at 36.85 J (50.00 ft-lb). It is of note, however, that these impact energies are more consistent with those observed for the two thin-gauge steels above, and substantially less than for the thick-gauge dual-phase steel (Section 3.8.4.2). Peel test results for the individual welds are presented in Table 27. The failure mode for all tested samples was a mix between partial- and full-interfacial failure with a greater number of full interfacial failures occurring in welds with lesser amounts of tempering.

5.0 Discussion

5.1 Basic Characteristics of the Temper Diagram

As suggested previously in this report, the temper diagrams developed in this program actually consist of two parts. These include a so-called C-curve region and a transient region. The C-curve region can be directly related to conventional time/temperature-based C-curves.[2] It is implied here that heat generation in the weld due to the temper current is balanced with heat extraction through the electrodes, resulting in a steady-state temper temperature distribution in the workpiece. Under these conditions, the temper current is analogous to temperature for time/temperature-based C-curves. The upper boundary is then defined by the current necessary to re-austenitize the steel, with subsequent quenching to martensite. The lower boundary of this curve is defined by the diffusional kinetics necessary to achieve initial softening, again over a region extending to the electrode-sheet surface. Generally, this is defined by exponentially longer times for lower temperatures.

The overall shape of the temper diagram, as well as the two regimes (transient region and C-curve region) can be relatively easily implied from simple modeling relating both temperature variations in spot welds, as well as tempering kinetics of steel. Temperature excursions in resistance spot welds on steel have been approximated by the following equation:[18]

$$\Delta T = \frac{I^2 R}{2K\left(\frac{A}{\Delta x}\right)\left(\frac{\Delta x^2}{a\Delta t}+1\right)} \quad (1)$$

In this equation, ΔT refers to the peak temperature in the spot weld, I is the welding current, R is the resistance of the spot weld, K and α are the thermal conductivity and diffusivity, respectively, of the steel sheet, A is the area of the welding electrodes, Δx is the thickness of a single sheet, and Δt is the weld time. This equation can further be modified by substituting the equation relating the resistance of the spot weld to the contact area and sheet thickness:

$$R = r\frac{2\Delta x}{A} \quad (2)$$

(ρ = the electrical resistivity) into the overall temperature equation, yielding:

$$\Delta T = \frac{I^2 r}{K\left(\frac{A}{\Delta x}\right)^2\left(\frac{\Delta x^2}{a\Delta t}+1\right)} \quad (3)$$

This equation is quite useful in understanding the relationships between several of the process variables in resistance heating during spot welding. Most notably, this equation shows the strong relationship between peak temperature and current (a squared term), as well as the more complex relationship with weld time. Here, an essentially linear relationship with temperature is inferred for short weld times, while the peak temperature is relatively independent of weld time for longer values.

Defining the lower boundary of the temper diagram can now be done using a combination of this equation to define temperature, with existing theory defining combinations of times and temperatures to achieve specific reductions in hardness. This is defined through the "tempering parameter" defined by Holloman and Jaffee,[2] and is related through the following rate equation:

$$\frac{1}{\Delta t} = A^* \exp\left(-\frac{Q}{R^*\Delta T}\right) \quad (4)$$

where A^* and Q are an empirically defined scaling factor and activation energy, respectively, and R^* is the Boltzman constant. This equation was defined for tempering times and temperatures under isothermal conditions. The tempering effect for spot welds can be estimated by combining Eqs. (3) and (4) above, to now relate current and time for specific hardnesses. After simplification, the resulting equation is as follows:

$$I = \sqrt{\frac{QK\left(\frac{A}{\Delta x}\right)^2\left(\frac{\Delta x^2}{a\Delta t}+1\right)}{R^* r \ln\left(A^*\Delta t\right)}} \tag{5}$$

For a specific steel, where only the temper current and time are varying, this can be reduced to a general equation with three empirical constants as follows:

$$I = \sqrt{B^*\left(\frac{\frac{C^*}{\Delta t}+1}{\ln\left(A^*\Delta t\right)}\right)} \tag{6}$$

where A^*, B^*, and C^* can all be defined empirically for a specific steel spot weld application and hardness value.

The austenization temperature defines the upper bound of the curve. The locus of temper currents and times resulting in re-austinization of the spot weld can be estimated by re-arranging Eq. (3) above as follows:

$$I = \sqrt{\left(\frac{K\Delta T_{aust}}{r}\right)\left(\frac{A}{\Delta x}\right)^2\left(\frac{\Delta x^2}{a\Delta t}+1\right)} \tag{7}$$

where ΔT_{aust} is the austenization temperature of the steel. For a specific steel spot-weld application, this can reduced to a general equation with two empirical constants as follows:

$$I = \sqrt{D^*\left(\frac{C^*}{\Delta t}+1\right)} \tag{8}$$

where D^* is an empirical constant (related to the austenization temperature) and C^* is the same as that for Eq. (6) above.

Eqs. (6) and (8), then, can be scaled to define a temper diagram for a specific spot welding application using only four constants. For the 0.83-mm (0.033-in.) dual-phase steel, some iterations with these constants shows that the temper diagram can be described with the following values:

$A^* = 5000$ 1/cycle
$B^* = 4$ (% expulsion)^2
$C^* = 2$ cycles
$D^* = 0.6$ (% expulsion)^2

In this case, constants B^* and D^* are scaled to reflect the percent of the expulsion current for the application, rather than the absolute temper current used. The resulting predicted temper diagram is shown in Figure 29. Similarities between the predicted diagram and the actual diagram (Figure 1) are unmistakable. The models presented above predict both the initial transient and C-curve regions of the diagram. These models verify two basic observations of this diagram. The first is that the C-curve region corresponds to nominally isothermal (with respect to time) conditions in the weld, bounded by the austenization temperature (current) on the top, and the Holloman-Jaffee relationship on the bottom. This initial transient, however, is bounded by the current required to achieve the austenization temperature (for a given time) on the top, and the complex relationship between current, time, temperature, and the Holloman-Jaffee relationship on the bottom. In fact, as the model suggests, these two regions are part of the same continuum, bounded on one extreme by Holloman-Jaffee effects, and on the other by the transient nature of short thermal cycles.

5.2 In-Situ Tempering Characteristics of Spot Welds

Recent developments in microstructural modeling of low-alloy steels has shown that for even the leanest mild steels (0.02% C, 0.3% Mn) cooling rates on the order of roughly 5×10^3 ^{o}C/sec are sufficient to form martensite.[7,19] Considerable thermal modeling of resistance spot welds[7,18] also shows that these cooling rates are achieved in steels up to 1.5-mm thick. Therefore, for the steels examined here, it is not surprising that all show a martensitic character in the as-welded (un-tempered) state. The previous thermal modeling work has also shown that cooling rates are remarkably insensitive to position in the weld.[18] This is consistent with the observations made

in this work that untempered spot welds in the materials studied are essentially martensite across the entire through thickness. This also accounts for the relatively good correlation between the measured (macro) surface hardnesses and the cross section hardnesses of the untempered welds.

The tempering response of these welds, as described above, is strongly a function of both the time and temperature the material receives on application of the temper current. It is of note that the temperature profiles in resistance spot welds during tempering are essentially a function of the applied temper current and the time the current is applied. As compared to resistance spot welding, where contact resistances play a major role in the specific details of the temperature distribution developed,[18] during tempering, these contact resistances have essentially been eliminated. This is because formation of the weld itself eliminates the sheet-to-sheet contact surface, and allows intimate matchup of the electrodes to the sheet, eliminating these contact resistances. The result is that during tempering essentially parabolic temperature distributions arise, with the peak temperature presumably at the center of the weld. With sufficient tempering time, resistance heating of the weld reaches a balance with the cooling capabilities of the electrodes, resulting in a steady-state parabolic temperature profile. Tempering response for the steady-state condition then becomes a function of the current applied, the relative position in the through thickness of the weld, and the temper time.

The microstructural observations presented in this work suggest that the metallurgical response of tempering goes through a number of stages depending on the current, time, and location in the weld. These can be characterized in four stages:

1. Occurrence of base martensite (under-tempering)
2. Tempered martensite
3. Re-austenization
4. Re-formation of martensite

Obviously, for regions of the weld where the original martensite is retained, under-tempering has occurred. This occurs alternately because of low temper currents, insufficient temper time, or that the electrodes exerted an un-due cooling influence. The presence of tempered martensite suggests that sufficient temperatures and times have been experienced to decompose the martensite. Re-austenization suggests that temper temperatures have exceeded the A_3 temperature, resulting in the re-formation of austenite. This occurs with too high a temper current, or in regions toward the center of the weld where tempering temperatures reach their peak. Re-formation of martensite occurs when the re-formed austenite is quenched under the

cooling influence of the electrodes once the temper current has been terminated. For the gauges and compositions of steels included in this study, such quenching is unavoidable once the current has been terminated.

The non-uniform temperature distribution inherent during in-situ tempering, as well as the stages of tempering response described above are basically responsible for the microstructures observed in the representative welds of this study. In the untempered state, of course, welds are martensitic. Initial temper response is to soften this martensite at the center of the weld (highest temperature) while maintaining hardness closer to the electrodes (lower temperatures). As tempering progresses, the softening effects continually expand towards the electrodes. However, at the same time the inherent higher temperatures at the weld center promote re-austenization of the steel. On cooling, of course, this material re-transforms to martensite, resulting in the martensitic cores noted in the "full" tempered welds detailed in this study. All this results in an observable series of microstructural "shells" as tempering proceeds. These shells initiate at the center of the weld, and as tempering proceeds grow toward the electrode surfaces, with new microstructural shells initiating at the weld center. In the most developed state, such tempering shows the martensitic weld core, surrounded by layers of material characteristic of the lesser stages of tempering.

A secondary effect here is the role of HAZ hardening. The materials examined in this study are all transformation-hardened steels and, as such, are either partially or fully made up of mildly tempered martensite. To some degree then, the welding pulse has the same effect on the base material as the temper pulse has on the martensitic base material. To some degree the presence of this tempered base material (or HAZ softened region) simply acts to add another layer of microstructure onto those described for the weld tempering response described above.

Most of the microstructrual development discussed above deals with the changes that occur under nominally "steady-state" temperature profiles. This corresponds to the C-curve portion of the temper diagram. Although not investigated in detail, it is believed that slightly different microstructural changes occur in the transient region of the diagram. Here, as detailed above, substantially more current is required to achieve the temperatures necessary to accomplish tempering in the relatively short times. Also, when short tempering times are used, the cooling role of the electrodes is greatly reduced. As a result, heating is more adiabatic, offering potential for more uniform degrees of tempering across the through thickness of the joint. This, however, was not verified experimentally in this work.

It should be noted that the temper diagrams, as presented in this report, are based on relatively macroscopic surface hardness measurements. As suggested in the discussion above, the microstructures in the through thickness of the majority of these welds is decidedly heterogeneous, and the measurements made tend to be representative of the outer shells of developed microstructure rather than a sampling of the microstructure as a whole. Still, such surface hardness measurements offer a window into the changes in weld microstructure, and can effectively be used as a gauge to define the progress of the tempering process.

5.3 Relationships between Failure Mode and Microstructure for Different Regions of the Temper Diagram

Each of the temper diagrams presented in this work is superimposed with the failure mode of the resulting spot welds. Failures range from interfacial to partial interfacial to full button peel. To interpret these results, and relate them to the temper diagrams themselves, it is first important to understand the basic factors that lead to interfacial fracture in spot welds. These factors have been discussed at length elsewhere,[5,6,11] but can be simply summarized as:

- The degree of constraint
- The susceptibility of the local microstructure
- Presence of a preferential fracture path

The degree of constraint largely refers to the resultant stress state during peel testing. The more the stress state Mode 1-type loading (tri-axial stress conditions) the more likely interfacial fracture will occur. Factors contributing to a more severe stress state include smaller weld sizes (this is, in fact, why $4\sqrt{t}$ welds were examined in this study), thicker attached sheets, and harder base materials. Susceptibility of the local microstructure refers to the underlying metallurgical fracture toughness of the weld metal, and is a direct function of the local hardness. The presence of a preferential fracture path refers largely to the pre-existence of welding-related defects (offering a preferential fracture path) and is generally not a concern for the types of materials used in this study.

These basic factors can be used to explain the relationships between the softening effects defined by the temper diagram, and the resulting peel mode behavior. For the dual-phase steels, it was found that peel mode generally tracked the softening effects defined by the temper diagram; that is, softening effects largely correlated with a transition from interfacial failure to peel-type failure. Clearly, untempered welds tended to fail interfacially, both due to constraint and

hardness effects. For this material, the thicker gauge dual-phase steel showed particularly good correlation, largely due to the higher levels of constraint implied. For these steels, the tempered martensite (of the weld area) appeared to retain higher strengths than the base material, while improving toughness. This had the effect of deflecting the propagating crack during peel testing, resulting in a peel mode of failure. It was of note that for extended temper times, the peel mode was retained, even though the core of the weld had re-formed martensite. For these welds, however, the martensite core was (as described above) surrounded by a tempered shell, providing the necessary fracture resistance to accomplish a button peel mode.

The martensitic steels, however, did not show the same relationship between softening (as defined by the temper diagram) and peel failure mode. In this case, as-welded samples (as previously described) showed button-type peel modes, partially tempered samples showed an interfacial-type peel mode, and fully tempered welds showed again a button-type peel mode. For welds on this grade of steel, two factors play a dominant role. First is the relative hardness of the base metal. This suggests a higher level of constraint compared to the dual-phase steel described above. Second is the role of localized softening of the microstructure during both welding and tempering. For this grade of steels, tempering can result in a local microstructure of substantially lower strength than the base material. This softened material then can act as a preferential fracture path. For the as-welded samples, softening in the HAZ results in a circumferential low-strength fracture path, allowing a peel mode of button failure. With modest in-situ tempering, however, this softened region appears to extend completely throughout the weld zone. In this case, the high-strength base material, as well as un-tempered martensite adjacent to the welding electrodes, drives any cracking event though the softened weld zone, resulting in interfacial failure on peel testing. As described above, further tempering results in a martensitic core surrounded by a tempered shell. In this case, the martensitic core acts as a "crack arrester", driving the subsequent failure event through the tempered shell, again resulting in a button peel mode.

5.4 Relationships between Microstructure and Mechanical Properties on Tempered Welds

Mechanical performance of the spot welds made from the different materials under the different temper conditions was a function of many factors. These factors included:

- Loading condition
- Parent material thickness

- Parent material strength
- Weld size
- Microstructual variations
- Weld failure mode

Loading condition refers to the type of test conducted, and has a strong influence on the implied stress state in the test conducted. Parent material thickness, strength, and weld size all relate to the implied stress state and degree of tri-axiality, as described in the previous section. Microstructural variations also play a role in terms of preferential deformation and failure paths, again as defined in the previous section. Finally, variations in failure mode (ductile/brittle) also affect mechanical performance.

In examining the lap-shear test results, is of note that no-temper condition generally showed best performance. This, to some degree, was related to the test configuration, which tended to load the welds themselves in shear. Under shear (Mode 3) loading, any tendency for brittle fracture was minimized, and strengths were largely defined by an area average of the strengths of the weld microstructures themselves. In this case, fully martensitic microstructures provide the best tensile strengths, and overall best joint strengths. Tempering, to a more or less degree, resulted in lower strength microstructures, which in an additive way appeared to reduce the strength of the joint.

The cross-tension results, on the other hand, appeared to show best performance with an intermediate temper. To some degree, the benefit of the temper is related to the implied stress state of the cross-tension specimen. For this specimen, loading around the spot weld is at worst Mode 1, promoting interfacial fracture of the weld nugget. This case was clearly seen for the thick-section martensitic steel. For that steel, the zero-temper condition showed mostly interfacial failures on testing. Tempering, of course, reduced the susceptibility of the microstructure to interfacial failure, and improved results. The results for the other steels differed somewhat, in that some sheet deformation effectively changed the loading mode from Mode 1 (at the nugget) to local tension (bending) in the HAZ. In this mode, failure is defined by both local HAZ softening, as well as the width of this zone. Both aspects of softening tend to reduce cross-tension performance.

The cross-tension impact tests tended to show the opposite trend compared to their static counterparts. For these tests, increased tempering appeared to inevitably lead to improved

impact energies. Clearly, the more ductile tempered microstructures, combined with a wider extent of these microstructures, improved impact performance. Of particular note are the results for the thick-section martensitic steel. Weld failures here were all either full or partial interfacial failures, and measured impact energies were on the order of half that for the thick-section dual-phase steel (which consistently showed button pull failure modes). These results indicate the influence of failure mode on subsequent impact performance.

Fatigue results were largely independent of temper condition. This was not surprising, in that the fatigue tests conducted here were all in the high-cycle fatigue regime, resulting in nominally elastic loading conditions. Under these conditions, the specific strength of the weld is not a factor, and performance is largely geometry dominated.

5.5 Potential for "Spike Tempering"

Much consideration is given above to the mechanical performance of welds tempered nominally in the C-curve regime of the temper diagram. This appears to be an effective mode of both tempering the microstructure and improving certainly impact performance; however, relatively long cycle times are implied (~100 cycles). The analysis of the diagram, as well as the developed diagrams themselves suggest, however, that short-duration, high-current tempers may be at least equally effective in improving the performance of resistance spot welds on high-strength steels. The use of spike tempering certainly offers potential for achieving effective tempering at shorter cycle times, but in addition, as described above, also may provide more-uniform (through-thickness) tempering. Such spike tempering was not considered in detail in this study, but should be pursued in the second phase of this program.

6.0 Conclusions

In this program, in-situ resistance spot welding temper diagrams have been developed for two gauges of two high-strength steel types. The steels have included a dual-phase grade and a martensitic grade. In-situ tempering is a method to both reduce "hold-time sensitivity" effects in the steel, and modify mechanical performance of the resulting joints. The in-situ temper diagrams are essentially maps of necessary temper currents and times to achieve specific levels of softening of the martensite formed following formation of the actual spot weld. In this work, the temper diagrams have been generated, and augmented with the peel behavior over the space defined by these diagrams. In addition, representative samples, characteristic of zero, medium, and peak tempering, were metallographically examined in detail. Also, a range of mechanical

properties tests were conducted on samples representing these three temper conditions. Specific conclusions from this work are provided below:

1. **General shape of the temper diagram:** Developed temper diagrams were defined by two distinct regions, a C-curve region analogous to isothermal tempering response, and a transient region at very short welding times.

2. **Limits of the temper diagram:** The lower limit of the temper diagram was defined by the currents and times required to achieve initial softening. The upper limit of the diagram was defined by the currents and times required to re-austenitize the material.

3. **Required quench times:** Roughly 20 and 46 cycles of quench time (between the main weld pulse and the temper pulse) for the thin- and thick-section steels, respectively, were required to form the initial martensite in the weld, and facilitate proper tempering.

4. **Modeling of the temper diagrams:** The shape of the temper diagram could be readily modeled using a closed-form thermal model for spot welding, and the equation for the "tempering parameter" from Holloman-Jaffee.[2]

5. **Definition of the transient region of the temper curve:** Temper diagram modeling shows that the transient region of the curve results from both the relationship between temperature and time for short temper cycles, and the necessity for higher tempering temperatures at such short times.

6. **Temperature distribution during tempering:** The temperature distribution in the spot weld during tempering is roughly parabolic in shape, with peak temperatures always at the weld centerline.

7. **Microstructural changes during tempering:** Actual tempered microstructures appeared as a series of shells, progressing from untempered martensite, tempered martensite, to re-austenization with subsequent martensite formation. Increasing tempering times resulted in the initial transformation behavior (for each stage) at the center of the weld, corresponding to the highest temperatures. This developed microstructure then progressed out toward the electrodes for longer temper times.

8. **Microstructure of "fully tempered" welds:** Welds well into the C-curve region of the temper diagram were typically characterized by an internal martensitic nugget, surrounded by a shell of tempered material.

9. **Relationship between surface hardness and weld hardness:** The temper diagrams presented here were largely based on surface hardness measurements. With such heterogeneous microstructures, these surface hardness measurements are reflective of the outermost shell in the weld. Such surface hardness measurements, however, are still reflective of the degree of tempering in the weld.

10. **Relationships between temper response and susceptibility to interfacial failure:** The dual-phase steels showed good correlation between softening effects and improvements in peel failure mode. The martensitic steels, however, demonstrated a much more complex relationship between softening and failure mode. This was related to the relatively high strength of the base material, and the role softened regions play on peel response.

11. **Factors affecting the mechanical performance of tempered high-strength steel spot welds:** Mechanical performance behavior of the tempered spot welds was affected by several factors, including the test geometry, strength and thickness of the base material, weld size, and distribution of microstructures in the weld itself.

12. **Tempering effects on high-strength steel spot welds:** Tensile shear tests favored the no-temper condition, cross-tension tests favored the intermediate condition, cross-tension impact tests favored the full-temper condition, and fatigue tests were largely independent of temper condition. These effects were largely related to the loading condition on the specimen, the level of stresses involved, and the distribution of the tempered microstructure.

13. **Effect of interfacial failure mode:** The presence of an interfacial failure mode in the cross tension tests typically resulted in a reduction of mechanical properties.

14. **Potential for spike tempering:** Spike tempering, that is using very short high-current tempering pulses, offers potential for improvements in properties with minimum cycle time increase. However, spike tempering was not extensively investigated in this study.

7.0 References

1. Chuko, W. L. and Gould, J. E., "Development of Appropriate Resistance Spot Welding Practice for Transformation-Hardened Steels," *Proceedings of Sheet Metal Welding Conference IX,* AWS Detroit Section, Detroit, MI (Oct. 2000).

2. Holloman, J. H. and Jaffee, L. D. 1945. *Trans. AIME*, pp. 162-223.

3. Bleck, W., "Cold-Rolled, High-Strength Sheet Steels for Auto Applications", *J. of Metals*, pp. 26-30 (July 1996).

4. Davies, R. G. and Magee, C. L., "Physical Metallurgy of Automotive High Strength Steels, Structure and Properties of Dual-Phase Steels," AIME Annual Meeting, New Orleans, LA (Feb. 19-21, 1979).

5. Gould, J. E. and Workman, D., "Fracture Morphologies of Resistance Spot Welds Exhibiting Hold Time Sensitivity," *Proceedings of Sheet Metal Welding Conference VIII,* AWS Detroit Section, Detroit, MI (1998).

6. Gould, J. E., Lehman, L. R., Holmes, S., "A Design-of-Experiments Evaluation of Factors Affecting the Resistance Spot Weldability of High-Strength Steels," *Proceedings of Sheet Metal Welding Conference VII,* AWS Detroit Section, Detroit, MI (1996).

7. Li, M. V., Dong, P., and Kimchi, M., "Modeling and Analysis of Microstructure Development in Resistance Spot Welds of High Strength Steels," 98IBECC-8 (1997).

8. Dickinson, D. W., "Welding in the Automotive Industry," Republic Steel Research Report SG 81-5 (1981).

9. Gould, J. E., "Modeling Primary Dendrite Arm Spacings in Resistance Spot Welds, Part 1 - Modeling Studies," *Welding Journal Research Supplement*, 73(4):67s-74s (1994).

10. Gould, J. E., "Modeling Primary Dendrite Arm Spacings in Resistance Spot Welds, Part 2 - Experimental Studies," *Welding Journal Research Supplement,* 73(5):91s-100s (1994).

11. Peterson, W., "Dilution of Weld Metal to Eliminate Interfacial Fractures of Spot Welds in High and Ultra High Strength Steels," ICAWT, Columbus, OH (Sept. 17-19, 1997).

12. Ferrasse, S., Verrier, P., and Meesemaecker, F., "Resistance Spot Weldability of High Strength Steels for Use in Car Industry," *Welding in the World* (June 1998).

13. Han, Z., Indacochea, J. E., Chen, C. H., and Bhat, S., "Weld Nugget Development and Integrity in Resistance Spot Welding of High-Strength Cold-Rolled Sheet Steels," *Welding Journal Research Supplement*, pp. 209-s to 216-s (May 1993).

14. Feng, Z., Gould, J. E., Babu, S. S., Santella, M. L., and Reimer, B. W., "Model for Resistance Spot Welding," Department of Energy.

15. Ford Motor Company, "Resistance Spot Weldability Tests for High Strength Steels," *Ford Laboratory Test Methods*, BA 13-4 (1980).

16. Oak Ridge National Laboratory Website, http://engmol.ms.ornl.gov/IGORgraph1acg.

17. Koistien, D. P. and Marburgh, R. E., "A General Equation Prescribing the Extent of the Austenite-Martensite Transformation in Pure Iron-Carbon Alloys and Plain Carbon Steels", *Acta Metallurgica* 7:59-60 (1959).

18. Gould, J. E., "An Examination of Nugget Development during Spot Welding using Both Experimental and Analytical Techniques"., *Welding Journal Research Supplement*, pp. 1s to 10s (Jan. 1987).

19. Babu, S. S., Riemer, B, W., Santella, M. L., and Feng, Z. "Integrated Thermal-Microstructure Model to Predict the Property Gradients in Resistance Spot Steel Welds", *Sheet Metal Welding Conference VIII*, AWS Detroit Section, Detroit, MI (1998).

Table 1. Electrodes Used for Phase 1 – Quench and Temper Processing Maps
(Electrodes were selected following the Ford specification BA 13-04.)

Project 43280GTH Year 1 **Quench and Temper Electrodes**								
Sample ID	**A**		**B**		**C**		**D**	
Sample Material	**DF140T**		**DF140T**		**M190**		**M190**	
	SI units	English units	SI units	English units	SI units	English units	SI units	English units
Sample Thickness –mm (in)	0.83	0.033	1.55	0.061	0.94	0.037	1.58	0.062
Electrode Material	Class II	Class II	Class II		Class II		Class II	
Electrode Type	Truncated Cone		Truncated Cone		Truncated Cone		Truncated Cone	
Electrode Cap Diameter (mm / in)	16	0.63	19.05	0.75	16	0.63	19.05	0.75
Electrode Cap Cone Angle (degrees)	45		45		45		45	
Electrode Cap Taper	RWMA #5		RWMA #6		RWMA #5		RWMA #6	
Face Diameter (mm / in)	6.35	0.25	7.9	0.31	6.35	0.25	7.9	0.31

Table 2. Nominal Chemistry and Selected Welding Parameters for Candidate Steels
(Chemistry for the steels was supplied by the steel manufacturer. Welding parameters nominally followed the Ford specification BA 13-04. Welding currents were selected based upon a 4vt minimum weld nugget size. Quench times were selected to sufficiently quench the weld to a martensitic microstructure.)

Material Chemistry and Welding Parameters								
ID	**A**		**B**		**C**		**D**	
Material	**DF140T**		**DF140T**		**M190**		**M190**	
	Dual Phase		**Dual Phase**		**Martensitic**		**Martensitic**	
	SI units	English units	SI units	English units	SI units	English units	SI units	English units
Thickness –mm (in)	0.83	0.033	1.55	0.061	0.94	0.037	1.58	0.062
TS -MPa(ksi)	1000	145	1060	154	1460	212	1410	205
YS -Mpa (ksi)	680	98.9	720	105	1250	182	1230	179
Carbon	0.1452		0.1537		0.1931		0.1946	
Manganese	1.41		1.41		0.46		0.47	
Silicon	0.319		0.321		0.055		0.021	
Electrode Size - face dia. –mm (in)	6.4	0.25	7.9	0.31	6.4	0.25	7.9	0.31
Weld Force -kN (lbf)	3.1	700	5.1	1140	3.2	725	5.2	1160
Squeeze Time (cycles)	70		130		130		130	
Weld Current (kA)	6.9		9.2		6.6		9.3	
Weld Time(cycles)	10		17		10		17	
Expulsion Limit (kA)	8.8		12.3		8.5		12.3	
4 sq.rt.(t) button size (mm/in)	3.64	0.14	5	0.2	3.88	0.15	5.02	0.2
Actual average button size from 10 welds made at the welding current with zero temper and 5cycles hold time. (mm/in)	3.8	0.149	5.035	0.198	3.871	0.152	5.289	0.208
Quench Time (cycles)	20		46		20		46	
Hold Time used during tempering trials (cycles)	60		60		60		60	
Cooling water temp °C(°F)	21	70	21	70	21	70	21	70
Cooling Flow Rt. Top electrode/bottom electrode l/min (gpm)	2.84/2.84	0.75/0.75	5.68/2.84	1.50/.75	3.79/2.84	1.0/0.75	5.68/2.84	1.5/0.75

Table 3. **Averaged Rockwell C Surface Hardness Values for 0.83-mm (0.033-in.), Dual-Phase Steel** [Tempering was performed using a matrix of time from 2 to 200 cycles and current from 45 to 130% of the established expulsion limit (%Exp). Rc hardness values highlighted in blue (light) were the average of three actual measurements from testing. Rc values highlighted in red (dark) were averaged from those taken from the zero-temper condition welds.]

A	Avg. of Refinement Trials	DF140T, 0.83mm							
		Temper Cycles	Hardness (Rc)						
Temper Current (kA)	%Exp	2	4	8	16	32	64	128	200
11.4	130	42.1	42.1	42.1	42.1	42.1	42.1	42.1	42.1
10.6	120	30.2	44.2	42.1	42.1	42.1	42.1	42.1	42.1
9.7	110	39.0	44.0	42.1	42.1	42.1	42.1	42.1	42.1
8.8	100	42.3	32.7	44.8	42.1	42.1	42.1	42.1	42.1
7.9	90	42.4	37.1	38.9	44.0	42.1	42.1	42.1	42.1
7.0	80	42.3	40.4	30.9	40.6	42.0	42.1	42.1	42.1
6.6	75	42.1	41.6	34.5	33.6	40.2	37.6	37.7	39.1
6.2	70	42.1	42.6	37.6	33.0	38.1	35.9	34.2	33.2
5.7	65	42.1	42.7	41.7	33.4	32.1	32.3	32.4	32.6
5.3	60	42.1	42.9	43.1	41.3	38.0	33.9	29.8	29.2
4.8	55	42.1	42.1	42.1	43.1	42.1	41.8	40.0	39.2
4.4	50	42.1	42.1	42.1	42.1	42.1	42.6	41.9	41.1
4.0	45	42.1	42.1	42.1	42.1	42.1	42.1	42.8	41.8

Austenitized and Quenched Rockwell C hardness values (zero tempering effect)
Measured Rockwell C surface hardness values

Table 4. **Averaged Rockwell C Surface Hardness Values for 1.55-mm (0.061-in.), Dual-Phase Steel** [Tempering was performed using a matrix of time from 2 to 200 cycles and current from 40 to 120% of the established expulsion limit (%Exp). Rc hardness values highlighted in blue (light) were the average of three actual measurements from testing. Rc values highlighted in red (dark) were averaged from those taken from the zero-temper condition welds.]

B	Avg. of Refinement Trials	DF140T, 1.55mm								
		Temper Cycles	Hardness (Rc)							
Temper Current (kA)	%Exp	2	4	8	16	32	64	80	128	200
14.8	120	34.5	33.0	38.0	38.0	38.0	38.0	38.0	38.0	38.0
13.5	110	36.6	25.4	39.9	38.0	38.0	38.0	38.0	38.0	38.0
12.3	100	38.9	33.2	36.1	38.0	38.0	38.0	38.0	38.0	38.0
11.1	90	38.2	33.4	29.4	40.1	38.0	38.0	38.0	38.0	38.0
9.8	80	38.4	37.1	30.8	33.1	39.6	38.0	38.0	38.0	38.0
9.2	75	37.6	36.0	28.5	30.1	39.0	38.0	38.0	38.0	38.0
8.6	70	41.4	37.9	35.5	29.7	37.3	38.0	38.0	38.0	38.0
8.0	65	38.0	37.0	36.7	30.5	29.0	32.7	34.3	33.4	38.0
7.4	60	39.3	40.5	37.7	34.4	27.5	29.2	28.5	25.4	27.3
6.8	55	38.0	38.0	38.2	38.2	32.0	26.3	25.5	24.2	23.0
6.2	50	38.0	38.0	38.2	37.6	37.5	30.7	27.5	25.4	23.8
5.5	45	38.0	38.0	37.9	37.3	38.5	39.5	36.4	37.9	37.3
4.9	40	38.0	38.0	38.0	38.0	38.5	38.9	36.7	38.0	38.0

Austenitized and Quenched Rockwell C hardness values (zero tempering effect)
Measured Rockwell C surface hardness values

Table 5. **Averaged Rockwell C Surface Hardness Values for 0.94-mm (0.037-in.), Martensitic Steel** [Tempering was performed using a matrix of time from 2 to 200 cycles and current from 30 to 130% of the established expulsion limit (%Exp). Rc hardness values highlighted in blue (light) were the average of three actual measurements from testing. Rc values highlighted in red (dark) were averaged from those taken from the zero-temper condition welds.]

C	Avg. of Refinement Trials	M190 0.94mm							
		Temper Cycles						Hardness (Rc)	
Temper Current (kA)	%Exp	2	4	8	16	32	64	128	200
11.1	130	28.1	46.3	46.3	46.3	46.3	46.3	46.3	46.3
10.2	120	26.5	46.3	46.3	46.3	46.3	46.3	46.3	46.3
9.4	110	31.7	46.1	46.3	46.3	46.3	46.3	46.3	46.3
8.5	100	40.4	32.0	46.3	46.3	46.3	46.3	46.3	46.3
7.7	90	43.2	25.8	45.9	46.3	46.3	46.3	46.3	46.3
6.8	80	45.2	32.3	43.4	45.7	46.3	46.3	46.3	46.3
6.4	75	44.7	35.8	33.9	46.9	46.3	46.3	46.3	46.3
6.0	70	45.5	40.5	30.2	45.9	46.0	46.3	46.3	46.3
5.5	65	46.5	46.7	29.0	39.5	44.7	44.2	42.2	36.9
5.1	60	46.3	43.4	28.3	24.9	36.0	35.2	36.6	38.3
4.7	55	46.3	45.9	38.7	29.9	31.8	28.6	25.3	26.2
4.3	50	46.3	45.9	46.3	39.4	28.0	23.5	32.2	25.5
3.8	45	46.3	45.7	45.8	45.6	43.9	44.2	42.7	42.4
3.4	40	46.3	45.1	46.0	45.5	45.6	44.6	46.5	44.5
3.0	35	46.3	46.3	46.3	46.3	46.3	45.5	47.3	46.7
2.6	30	46.3	46.3	46.3	46.3	46.3	45.9	46.9	46.8

Austenitized and Quenched Rockwell C hardness values (zero tempering effect)
Measured Rockwell C surface hardness values

Table 6. **Averaged Rockwell C Surface Hardness Values for 1.58-mm (0.062-in.), Martensitic Steel** [Tempering was performed using a matrix of time from 2 to 200 cycles and current from 45 to 140% of the established expulsion limit (%Exp). Rc hardness values highlighted in blue (light) were the average of three actual measurements from testing. Rc values highlighted in red (dark) were averaged from those taken from the zero-temper condition welds.]

D	Avg. of Refinement Trials	M190, 1.58mm								
		Temper Cycles							Hardness (Rc)	
Temper Current (kA)	%Exp	2	4	8	16	32	64	80	128	200
17.2	140	35.9	32.9	41.3	41.3	41.3	41.3	41.3	41.3	41.3
16.0	130	37.2	31.6	41.3	41.3	41.3	41.3	41.3	41.3	41.3
14.8	120	36.5	24.0	41.6	41.3	41.3	41.3	41.3	41.3	41.3
13.5	110	40.5	26.2	40.4	41.3	41.3	41.3	41.3	41.3	41.3
12.3	100	40.0	33.9	30.8	42.5	41.3	41.3	41.3	41.3	41.3
11.1	90	41.3	37.2	24.1	38.8	41.3	41.3	41.3	41.3	41.3
9.8	80	41.3	40.3	30.9	38.3	38.3	41.3	41.3	41.3	41.3
9.2	75	41.3	41.2	34.6	25.4	39.2	41.3	41.3	41.3	41.3
8.6	70	41.3	38.5	39.8	27.0	32.6	41.2	41.3	39.3	41.3
8.0	65	41.3	39.8	41.9	29.7	28.5	31.7	37.0	39.2	41.3
7.4	60	41.3	42.0	40.7	39.3	27.7	28.3	27.3	31.2	27.3
6.8	55	41.3	39.0	40.5	41.9	38.1	29.8	26.8	23.7	21.7
6.2	50	41.3	41.3	41.3	39.8	39.3	39.9	38.7	33.1	25.6
5.5	45	41.3	41.3	41.3	41.3	41.3	41.3	41.3	40.8	39.5

Average Austneitized and Qeuenched Hardness (no softening due to tempering)
Actual averaged Rc hardness measurements made and averaged

Table 7. Resulting Button Morphology From Peel Testing 0.83-mm (0.033-in.) Dual-Phase Steel (Material A) [Peel tests resulting in a pulled button are represented by the letter B and shaded in red (dark). Peel tests resulting in interfacial failure are represented by the letter P and shaded in blue (light). No data was taken for the blank areas of the table.]

A	Avg. of Peel Tests			DF140T, 0.83mm				
Failure Mode (Button (B), Partial Interfacial Failure (P)								
	Temper Cycles							
%Exp	2	4	8	16	32	64	128	200
130								
125								
120	B	B	B					
115								
110	B	B						
105	B	B	B	B				
100	B	B	B					
95								
90	P	P	P	B	B			
85								
80	P	B	B	P	P	P		
75		P	B	B	P	P	P	P
70		B	B	B	B	B	P	P
65		B	B	B	B	B	B	B
60	B	P	B	B	B	B	B	B
55				B	B	B	B	B
50						B	B	B
45	B	B	P	P	B	B	B	B
40								
35								
30	B	B	B	B	B	B		
25								
20								
15	P	B	B	P	B	B		
10								
5								
0	P	P	P	B	B	B		

P = partial or full interfacial failure
B = Full button morphology
Blank = no peel test data

Table 8. Resulting Button Morphology From Peel Testing 1.55-mm (0.061-in) Dual-Phase Steel (Material B) [Peel tests resulting in a pulled button are represented by the letter B and shaded in red (dark). Peel tests resulting in interfacial failure are represented by the letter P and shaded in blue (light). No data was taken for the blank areas of the table.]

B	Avg. of Peel Tests			DF140T 1.58mm				
Failure Mode (Button (B), Partial Interfacial Failure (P)								
%Exp	2	4	8	16	32	64	80	128	200
140									
135									
130									
125									
120	B	B							
115									
110	B	B	B						
105	B	B	P						
100	B	B	P						
95									
90	P	B	B	B					
85									
80	P	B	B	P	B				
75	P	B	B	B	B	B			
70	P	P	B	B	B				
65	P	B	B	B	B	B	B	B	
60	P	P	B	B	B	B	B	B	B
55			B	B	B	B	B	B	B
50			B	B	B	B	B	B	B
45	P	P	P	P	P	B	P	B	P
40				P	P	B	B		
35									
30	P	P	P	P	P	P			
25									
20									
15	P	P		P	P	P			
10									
5									
0	P	P	P	P	P				

P = partial or full interfacial failure
B = Full button morphology
Blank = no peel test data

Table 9. **Resulting Button Morphology from Peel Testing 0.94-mm (0.037-in.) Martensitic Steel (Material C)** [Peel tests resulting in a pulled button are represented by the letter B and shaded in red (dark). Peel tests resulting in interfacial failure are represented by the letter P and shaded in blue (light). No data was taken for the blank areas of the table.]

C	Avg. of Refinement Trials				M190 0.94mm			
Failure Mode (Button (B), Partial Interfacial Failure (P)								
		Temper Cycles						
%Exp	2	4	8	16	32	64	128	200
130	P							
125								
120	P	P	B	B	B	B		
115								
110	B	P						
105	B	P	B	B	B	B		
100	P	P						
95								
90	P	P	P	B	B	B		
85								
80	B	P	P	B				
75	B	P	P	P	B	B		
70	B	B	P	P	B			
65	P	B	B	P	P	P	P	P
60	B	P	P	B	B	P	P	B
55		P	P	B	P	P	B	P
50		B	B	P	P	P	B	B
45	B	P	P	P	B	B	B	B
40		P	P	P	B	B	B	P
35						P	P	B
30	B	B	B	P	P	P	P	B
25								
20								
15	P	P	P	P	P	P		
10								
5								
0								

P = partial or full interfacial failure
B = Full button morphology
Blank = no peel test data

Table 10. Resulting Button Morphology From Peel Testing 1.58-mm (0.062-in.) Martensitic Steel (Material D) [Peel tests resulting in a pulled button are represented by the letter B and shaded in red (dark). Peel tests resulting in interfacial failure are represented by the letter P and shaded in blue (light). No data was taken for the blank areas of the table.]

D	Avg. of Peel Tests				M190 1.58mm				
Failure Mode (Button (B), Partial Interfacial Failure (P)									
% Exp	2	4	8	16	32	64	80	128	200
140	P	P							
135									
130	P	B							
125									
120	B	P	B						
115									
110	P	P	P						
105	P	B	B						
100	B	B	B	B					
95									
90		B	P	P					
85									
80		B	B	B	B				
75	P	P	B	P	P				
70		B	B	B	B	B			
65		B	B	B	B	P	B	B	
60	B	B	B	B	B	P	P	B	B
55		B	B	B	B	P	B	B	B
50				P	B	B	B	B	B
45	P	P	B	P	P	P	B	B	B
40									
35									
30	B	P	B	P	P	P			
25									
20									
15	P	P	P	B	B	B			
10									
5									
0	P	B	P	P	P	P			

P = partial or full interfacial failure
B = Full button morphology
Blank = no peel test data

Table 11. Weld, Quench and Temper Parameters used for the Representative Metallurgical Sections and Mechanical Test Samples (Zero-, medium-, and full-temper conditions are shown for each material examined.)

Tempering Parameters for Metallurgical Section Samples											
Sample ID	Temper Condition	Squeeze Time (cycles)	Weld Force kN (lbs)	Weld Time (cycles)	Weld Current (kA)	Quench Time (cycles)	Temper Time (cycles)	Temper Current (kA)	Temper Current (%expulsion)	Hold Time (cycles)	Surface Hardness Measurment (Rockwell C)
A - DF140T 0.83mm											
AM0	Zero	130	3.1 (700)	10	6.9	20	0	5.7	65	60	43
AMM	Medium	130		10	6.9	20	16	5.7	65	60	36
AMF	Full	130		10	6.9	20	32	5.7	65	60	30
B - DF140T 1.55mm											
BM0	Zero	130	5.1 (1140)	17	9.2	46	0	6.8	55	60	38
BMM	Medium	130		17	9.2	46	32	6.8	55	60	26
BMF	Full	130		17	9.2	46	80	6.8	55	60	24
C - M190 0.94mm											
CM0	Zero	130	3.2 (725)	10	6.7	20	0	4.5	53	60	47
CMM	Medium	130		10	6.7	20	16	4.5	53	60	46
CMF	Full	130		10	6.7	20	128	4.5	53	60	37
D - M190 1.58mm											
DM0	Zero	130	5.2 (1160)	17	9.3	46	0	6.8	55	60	39
DMM	Medium	131	5.2 (1160)	17	9.3	46	57	6.8	55	60	29
DMF	Full	132	5.2 (1160)	17	9.3	46	90	6.8	55	60	25

Table 12. Lap-Shear Test Results for 0.83-mm (0.033-in.) Dual-Phase Steel (Material A) [Representative samples for each of three tempering conditions (zero-, medium-, and full-temper) were tested.]

Static Tensile Test Results - **A** **DF140T, 0.83mm**

Speed = 15 on dial (2ipm)

Peak Load

Sample #	Zero Temper (AT0)			Medium Temper (ATM)			Full Temper (ATF)		
	(kN)	(lbs)	Failure Mode	(kN)	(lbs)	Failure Mode	(kN)	(lbs)	Failure Mode
1	9.81	2205	IF (S)	7.97	1790	IF (S)	9.26	2080	B
2	10.46	2350	B	8.39	1885	IF (S)	8.59	1930	B
3	9.23	2075	IF (S)	8.61	1935	IF (S)	8.88	1995	B
4	9.79	2200	IF (S)	8.19	1840	IF (S)	8.37	1880	B
5	9.75	2190	IF (S)	8.05	1810	IF (S)	9.03	2030	B
Average:	**9.81**	**2204**		**8.24**	**1852**		**8.82**	**1983**	
STD:	0.43	98		0.26	59		0.35	79	

IF (S) = Interfacial failure in shear mode
B = Pulled a full button

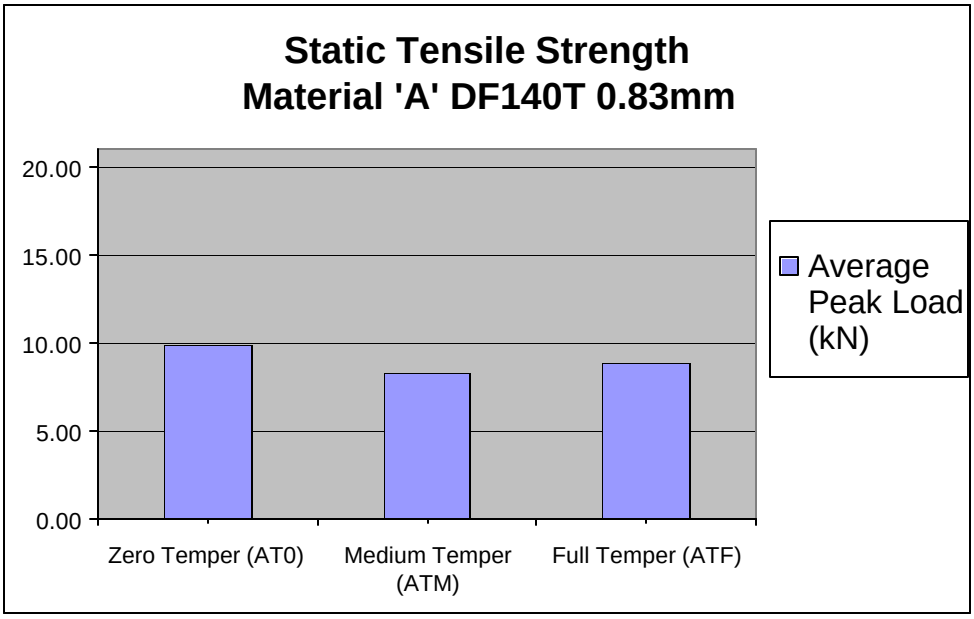

Table 13. Lap-Shear Test Results for 1.55-mm (0.061-in.) Dual-Phase Steel (Material B) [Representative samples for each of three tempering conditions (zero-, medium-, and full-temper) were tested.]

Static Tensile Test Results - B **DF140T, 1.55mm**

Speed = 15 on dial (2ipm)

Peak Load

Sample #	Zero Temper (BTQ)			Medium Temper (BTM)			Full Temper (BTF)		
	(kN)	(lbs)	Failure Mode	(kN)	(lbs)	Failure Mode	(kN)	(lbs)	Failure Mode
1	18.78	4220	IF (S)	20.83	4680	IF (S)	na	na	IF (S)
2	18.65	4190	IF (S)	19.09	4290	IF (S)	20.56	4620	IF (S)
3	17.44	3920	IF (S)	21.05	4730	IF (S)	14.91	3350	IF (S)
4	18.69	4200	IF (S)	21.00	4720	IF (S)	18.47	4150	IF (S)
5	19.85	4460	IF (S)	21.36	4800	IF (S)	18.82	4230	IF (S)
6	17.22	3870	IF (S)	19.54	4390	IF (S)	15.84	3560	IF (S)
7	21.67	4870	IF (S)						
8	20.38	4580	IF (S)						
Average:	**19.08**	**4289**		**20.48**	**4602**		**17.72**	**3982**	
STD:	1.49	335		0.93	209		2.31	518	

IF (S) = Interfacial failure in shear mode

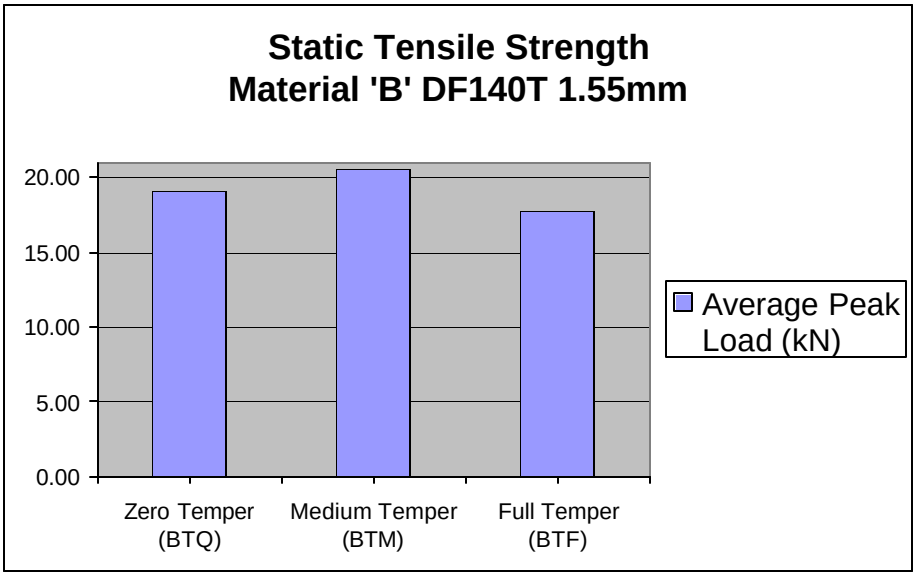

Table 14. Lap-Shear Test Results for 0.94-mm (0.037-in.) Martensitic Steel (Material C)
[Representative samples for each of three tempering conditions (zero-, medium-, and full-temper) were tested.]

Static Tensile Test Results -		C	M190 0.94mm					
Speed = 15 on dial (2ipm)			Peak Load					
Sample #	Zero Temper (CT0)			Medium Temper (CTM)			Full Temper (CTF)		
	(kN)	(lbs)	Failure Mode	(kN)	(lbs)		(kN)	(lbs)	
1	11.86	2665	IF (S)	9.97	2240	IF (S)	8.25	1855	IF (S)
2	11.81	2655	IF (S)	9.43	2120	IF (S)	8.43	1895	IF (S)
3	9.70	2180	IF (S)	10.97	2465	IF (S)	9.21	2070	IF (S)
4	11.39	2560	IF (S)	10.50	2360	IF (S)	8.14	1830	IF (S)
5	12.33	2770	IF (S)	9.99	2245	IF (S)	7.41	1665	IF (S)
Average:	**11.42**	**2566**		**10.17**	**2286**		**8.29**	**1863**	
STD:	1.02	228		0.58	131		0.65	145	

IF (S) = Interfacial failure in shear mode

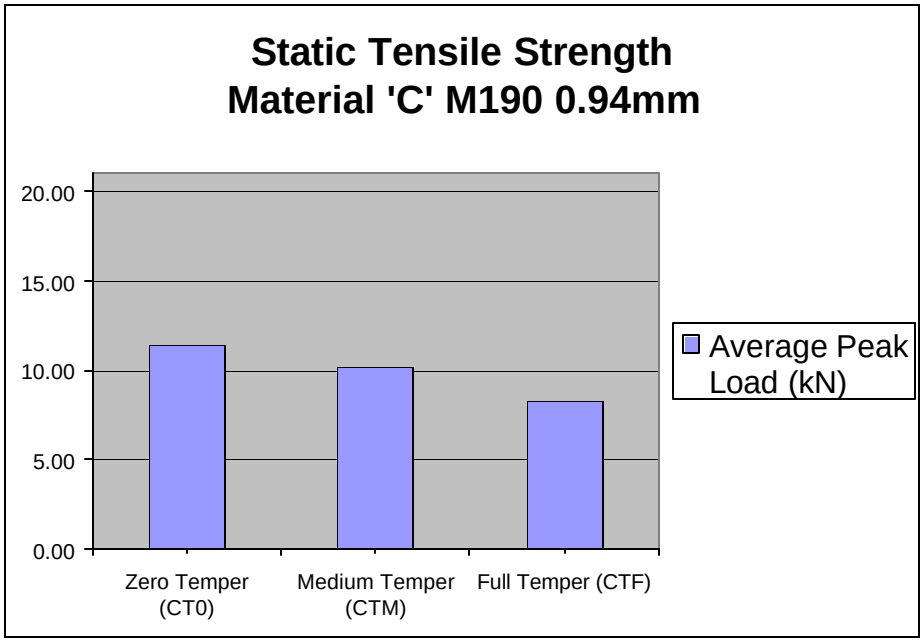

Table 15. Lap-Shear Test Results for 1.58-mm (0.062-in.) Martensitic Steel (Material D)
[Representative samples for each of three tempering conditions (zero-, medium-, and full-temper) were tested.]

Static Tensile Test Results - **D** **M190, 1.58mm**

Speed = 15 on dial (2ipm)

Peak Load

Sample #	Zero Temper (DFQ)			Medium Temper (DFM)			Full Temper (DFF)		
	(kN)	(lbs)	Failure Mode	(kN)	(lbs)	Failure Mode	(kN)	(lbs)	Failure Mode
1	15.40	3460	IF (S)	15.31	3440	IF (S)	20.65	4640	IF (S)
2	20.51	4610	IF (S)	19.85	4460	IF (S)	18.65	4190	IF (S)
3	22.96	5160	IF (S)	16.47	3700	IF (S)	20.16	4530	IF (S)
4	21.45	4820	IF (S)	12.64	2840	IF (S)	18.69	4200	IF (S)
5	20.60	4630	IF (S)	15.62	3510	IF (S)	7.03	1580	IF (S)
Average:	**20.19**	**4536**		**15.98**	**3590**		**17.03**	**3828**	
STD:	2.85	641		2.60	583		5.66	1272	

IF (S) = Interfacial failure in shear mode

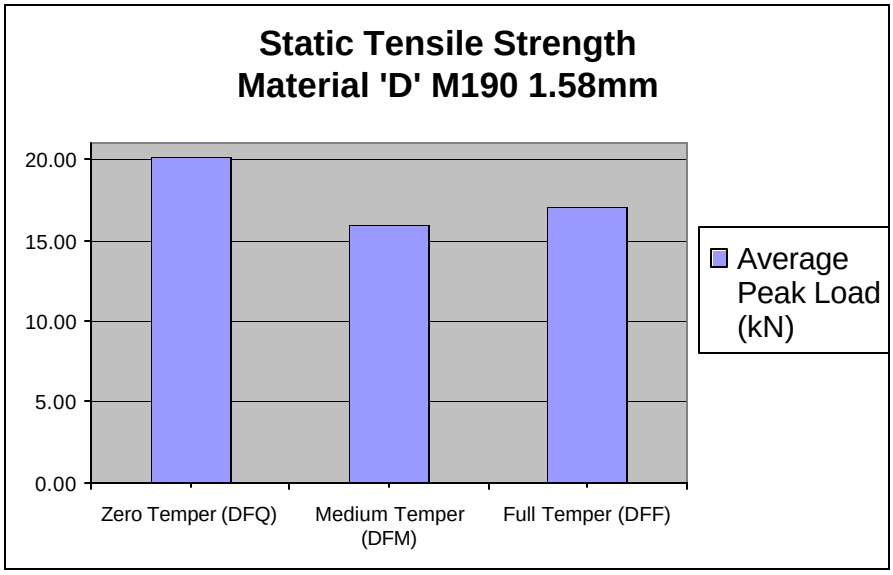

Table 16. S-N Curve Data for Tensile Fatigue Testing of Material A, 0.83-mm (0.033-in.) Dual-Phase Steel (Loading conditions and number of cycles to failure are presented for zero-, medium-, and full-temper conditions.)

Tensile Fatigue Data **A** **DF140T 0.83mm**

Zero Temper

	Max Load		Static Load		Dynamic Load			
Sample	**kN**	**lbs**	**kN**	**lbs**	**kN**	**lbs**	****Cycles to Failure**	
AF0-1	8.01	1800.00	4.40	990.00	3.60	810.00	489	
2	4.45	1000.00	2.45	550.00	2.00	450.00	2,542	
3	2.67	600.00	1.47	330.00	1.20	270.00	27,464	
4	1.78	400.00	0.98	220.00	0.80	180.00	283,362	
9	1.69	380.00	0.93	209.00	0.76	171.00	436,282	
10	1.56	350.00	0.86	192.50	0.70	157.50	853,708	
8	1.33	300.00	0.73	165.00	0.60	135.00	9,990,472	
5	0.89	200.00	0.49	110.00	0.40	90.00	10,703,828	**

***Terminate test after 10,000,000 cycles*

Tensile Fatigue Data **A** **DF140T 0.83mm**

Mid Temper

	Max Load		Static Load		Dynamic Load			
Sample	**kN**	**lbs**	**kN**	**lbs**	**kN**	**lbs**	****Cycles to Failure**	
AFM-4	4.45	1000.00	2.45	550.00	2.00	450.00	8,182	
3	2.67	600.00	1.47	330.00	1.20	270.00	75,875	
2	1.78	400.00	0.98	220.00	0.80	180.00	768,765	
5	1.60	360.00	0.88	198.00	0.72	162.00	1,353,385	
AFM-1	0.89	200.00	0.49	110.00	0.40	90.00	10,369,132	**

***Terminate test after 10,000,000 cycles*

Tensile Fatigue Data **A** **DF140T 0.83mm**

Full Temper

	Max Load		Static Load		Dynamic Load			
Sample	**kN**	**lbs**	**kN**	**lbs**	**kN**	**lbs**	****Cycles to Failure**	
AFF-1	4.45	1000.00	2.45	550.00	2.00	450.00	6,656	
2	2.67	600.00	1.47	330.00	1.20	270.00	35,897	
5	1.51	340.00	0.83	187.00	0.68	153.00	657,384	
3	1.78	400.00	0.98	220.00	0.80	180.00	847,048	
4	0.89	200.00	0.49	110.00	0.40	90.00	10,369,141	**

***Terminate test after 10,000,000 cycles*

Table 17. S-N Curve Data for Tensile Fatigue Testing of Material B, 1.55-mm (0.061-in.) Dual-Phase Steel (Loading conditions and number of cycles to failure are presented for zero-, medium-, and full-temper conditions.)

Tensile Fatigue Data			B DF140T 1.55mm					
Zero Temper								
	Max Load		Static Load		Dynamic Load			
Sample	kN	lbs	kN	lbs	kN	lbs	**Cycles to Failure	
BFO-1	8.01	1800.00	4.40	990.00	3.60	810.00	4,984	
2	6.67	1500.00	3.67	825.00	3.00	675.00	16,731	
3	4.45	1000.00	2.45	550.00	2.00	450.00	108,192	
4	2.67	600.00	1.47	330.00	1.20	270.00	1,193,776	
5	1.78	400.00	0.98	220.00	0.80	180.00	8,984,240	
6	1.33	300.00	0.73	165.00	0.60	135.00	12,653,165	**

***Terminate test after 10,000,000 cycles*

Tensile Fatigue Data			B DF140T 1.55mm					
Mid Temper								
	Max Load		Static Load		Dynamic Load			
Sample	kN	lbs	kN	lbs	kN	lbs	**Cycles to Failure	
BFM-1	8.01	1800.00	4.40	990.00	3.60	810.00	22,603	
2	6.67	1500.00	3.67	825.00	3.00	675.00	57,492	
4	4.45	1000.00	2.45	550.00	2.00	450.00	100,849	
5	3.56	800.00	1.96	440.00	1.60	360.00	348,946	
3	2.67	600.00	1.47	330.00	1.20	270.00	5,282,267	
6	1.78	400.00	0.98	220.00	0.80	180.00	12,580,922	**

***Terminate test after 10,000,000 cycles*

Tensile Fatigue Data			B DF140T 1.55mm					
Full Temper								
	Max Load		Static Load		Dynamic Load			
Sample	kN	lbs	kN	lbs	kN	lbs	**Cycles to Failure	
Bff-1	8.01	1800.00	4.40	990.00	3.60	810.00	600	
2	6.67	1500.00	3.67	825.00	3.00	675.00	12,949	
4	4.45	1000.00	2.45	550.00	2.00	450.00	86,957	
3	2.67	600.00	1.47	330.00	1.20	270.00	708,649	
5	1.78	400.00	0.98	220.00	0.80	180.00	7,875,131	
6	1.33	300.00	0.73	165.00	0.60	135.00	10,622,357	**

***Terminate test after 10,000,000 cycles*

Table 18. S-N Curve Data for Tensile Fatigue Testing of Material C, 0.94-mm (0.037-in.) Martensitic Steel (Loading conditions and number of cycles to failure are presented for zero-, medium-, and full-temper conditions.)

Tensile Fatigue Data **C** **M190 0.94mm**

Zero Temper

	Max Load		Static Load		Dynamic Load			
Sample	**kN**	**lbs**	**kN**	**lbs**	**kN**	**lbs**	****Cycles to Failure**	
CF0-1	4.45	1000.00	2.45	550.00	2.00	450.00	5,467	
2	2.67	600.00	1.47	330.00	1.20	270.00	77,837	
3	1.78	400.00	0.98	220.00	0.80	180.00	560,596	
4	1.33	300.00	0.73	165.00	0.60	135.00	3,117,299	
5	0.89	200.00	0.49	110.00	0.40	90.00	10,322,071	**

***Terminate test after 10,000,000 cycles*

Tensile Fatigue Data **C** **M190 0.94mm**

Mid Temper

	Max Load		Static Load		Dynamic Load			
Sample	**kN**	**lbs**	**kN**	**lbs**	**kN**	**lbs**	****Cycles to Failure**	
CFM-1	4.45	1000.00	2.45	550.00	2.00	450.00	7,024	
3	3.56	800.00	1.96	440.00	1.60	360.00	22,757	
2	2.67	600.00	1.47	330.00	1.20	270.00	125,296	
4	1.33	300.00	0.73	165.00	0.60	135.00	2,573,802	
5	0.89	200.00	0.49	110.00	0.40	90.00	15,560,382	**

***Terminate test after 10,000,000 cycles*

Tensile Fatigue Data **C** **M190 0.94mm**

Full Temper

	Max Load		Static Load		Dynamic Load			
Sample	**kN**	**lbs**	**kN**	**lbs**	**kN**	**lbs**	****Cycles to Failure**	
CFF-2	6.67	1500.00	3.67	825.00	3.00	675.00	7,024	
CFF-1	4.45	1000.00	2.45	550.00	2.00	450.00	22,757	
3	2.67	600.00	1.47	330.00	1.20	270.00	125,296	
4	1.78	400.00	0.98	220.00	0.80	180.00	2,573,802	
5	1.33	300.00	0.73	165.00	0.60	135.00	15,560,382	**

***Terminate test after 10,000,000 cycles*

Table 19. S-N Curve Data for Tensile Fatigue Testing of Material D, 1.58-mm (0.062-in.) Martensitic Steel (Loading conditions and number of cycles to failure are presented for zero-, medium-, and full-temper conditions.)

Tensile Fatigue Data **D** **M190 1.58mm**

Zero Temper

	Max Load		Static Load		Dynamic Load			
Sample	**kN**	**lbs**	**kN**	**lbs**	**kN**	**lbs**	****Cycles to Failure**	
DTQ-1	8.01	1800.00	4.40	990.00	3.60	810.00	10,790	
DTQ-2	6.67	1500.00	3.67	825.00	3.00	675.00	26,719	
DTQ-3	4.45	1000.00	2.45	550.00	2.00	450.00	110,649	
DTQ-4	2.67	600.00	1.47	330.00	1.20	270.00	1,010,676	
DTQ-5	1.78	400.00	0.98	220.00	0.80	180.00	16,000,000	**

***Terminate test after 10,000,000 cycles*

Tensile Fatigue Data **D** **M190 1.58mm**

Mid Temper

	Max Load		Static Load		Dynamic Load			
Sample	**kN**	**lbs**	**kN**	**lbs**	**kN**	**lbs**	****Cycles to Failure**	
DTM-2	8.01	1800.00	4.40	990.00	3.60	810.00	3,081	
3	6.67	1500.00	3.67	825.00	3.00	675.00	3,925	
4	4.45	1000.00	2.45	550.00	2.00	450.00	191,023	
DTM-1	2.67	600.00	1.47	330.00	1.20	270.00	1,922,822	
5	1.78	400.00	0.98	220.00	0.80	180.00	10,325,756	**

***Terminate test after 10,000,000 cycles*

Tensile Fatigue Data **D** **M190 1.58mm**

Full Temper

	Max Load		Static Load		Dynamic Load			
Sample	**kN**	**lbs**	**kN**	**lbs**	**kN**	**lbs**	****Cycles to Failure**	
DTF-1	8.01	1800.00	4.40	990.00	3.60	810.00	35,235	
2	6.67	1500.00	3.67	825.00	3.00	675.00	61,356	
3	4.45	1000.00	2.45	550.00	2.00	450.00	114,308	
4	2.67	600.00	1.47	330.00	1.20	270.00	1,861,742	
5	1.78	400.00	0.98	220.00	0.80	180.00	12,935,982	**

***Terminate test after 10,000,000 cycles*

Table 20. Cross-Tension Tensile Test Results from Material A, 0.83-mm (0.033-in.) Dual-Phase Steel (Results for zero-, medium-, and full-temper conditions are presented. Maximum load to failure for each sample was measured and the failure mode was noted.)

Cross Tension Tensile Results	A	DF140T 0.83mm							
Speed = 15 on dial (2ipm)				Peak Load					
Sample #	Zero Temper (AC0)			Medium Temper (ACM)			Full Temper (ACF)		
	(kN)	(lbs)	Failure Mode	(kN)	(lbs)	Failure Mode	(kN)	(lbs)	Failure Mode
1	3.00	675	B	3.14	705	B	3.47	780	B
2	2.98	670	B	3.52	790	B	2.40	540	B
3	3.07	690	B	3.29	740	B	2.98	670	B
4	3.16	710	B	3.07	690	B	3.12	700	B
5	2.96	665	B	2.89	650	B	na	na	B
Average:	**3.03**	**682**	B	**3.18**	**715**	B	**2.99**	**673**	B
STD:	0.08	18	B	0.24	53	B	0.44	100	B

B = Full button mode of failure

Table 21. Cross-Tension Tensile Test Results from Material B, 1.55-mm (0.061-in.) Dual-Phase Steel (Results for zero-, medium-, and full-temper conditions are presented. Maximum load to failure for each sample was measured and the failure mode was noted.)

Cross Tension Tensile Results	B	DF140T1.55mm							
Speed = 15 on dial (2ipm)				Peak Load (lbs)					
Sample #	Zero Temper (BC0)			Medium Temper (BCM)			Full Temper (BCF)		
	(kN)	(lbs)	Failure Mode	(kN)	(lbs)	Failure Mode	(kN)	(lbs)	Failure Mode
1	7.97	1790	B /LT	8.90	2000	B	10.99	2470	B
2	10.97	2465	B	12.91	2900	B	12.91	2900	B
3	12.86	2890	B	17.11	3845	B	10.48	2355	B
4	10.70	2405	B	8.19	1840	B	10.41	2340	B
5	10.95	2460	B	14.17	3185	B			B
Average:	**10.69**	**2402**		**12.26**	**2754**		**11.20**	**2516**	
STD:	1.75	394		3.72	837		1.17	262	

B = Full button mode of failure
LT = Lamelar Tear

Table 22. Cross-Tension Tensile Test Results from Material C, 0.94-mm (0.037-i.) Martensitic Steel (Results for zero-, medium-, and full-temper conditions are presented. Maximum load to failure for each sample was measured and the failure mode was noted.)

Cross Tension Tensile Results	C	M190 0.94mm							
Speed = 15 on dial (2ipm)									
			Peak Load						
Sample #	Zero Temper (CC0)			Medium Temper (CCM)			Full Temper (CCF)		
	(kN)	(lbs)	Failure Mode	(kN)	(lbs)	Failure Mode	(kN)	(lbs)	Failure Mode
1	5.43	1220	B	5.05	1135	B	3.56	800	B
2	4.09	920	B	4.03	905	B	3.56	800	B
3	4.72	1060	B	3.83	860	B	3.40	765	B
4	5.07	1140	B	4.63	1040	B	4.07	915	B
5	4.74	1065	B	4.07	915	B	4.18	940	B
Average:	**4.81**	**1081**		**4.32**	**971**		**3.76**	**844**	
STD:	0.49	111		0.50	113		0.35	78	

B = Button

Table 23. Cross-Tension Tensile Test Results from Material D, 1.58-mm (0.062-in.) Martensitic Steel (Results for zero-, medium-, and full-temper conditions are presented. Maximum load to failure for each sample was measured and the failure mode was noted.)

Cross Tension Tensile Results	D	M190 1.58mm							
Speed = 15 on dial (2ipm)									
			Peak Load						
Sample #	Zero Temper (DCO)			Medium Temper (DCM)			Full Temper (DCF)		
	(kN)	(lbs)	Failure Mode	(kN)	(lbs)	Failure Mode	(kN)	(lbs)	Failure Mode
1	4.61	1035	PIF	7.08	1590	B	4.63	1040	B
2	5.45	1225	PIF	10.19	2290	B	5.16	1160	LT
3	5.79	1300	PIF	8.28	1860	B	5.38	1210	B
4	5.52	1240	PIF	9.08	2040	B	6.10	1370	LT
5	5.72	1285	B	7.59	1705	B	2.27	510	B
Average:	**5.42**	**1217**		**8.44**	**1897**		**4.71**	**1058**	
STD:	0.47	106		1.23	277		1.46	328	

PIF = Partial Interfacial Failure
B = Full button mode of failure
LT = Lamelar tear

Table 24. Cross-Tension Impact Results for Material A, 0.83-mm (0.033-in.) Dual-Phase Steel (Absorbed energy was measured and failure mode was recorded for samples from each temper condition. Full-button failure is denoted by the letter B.)

Cross Tension Impact Results Material 'A' 0.83-mm (0.033-in) Dual Phase 140T									
	Zero Temper			Medium Temper			Full Temper		
	AIQ-1			AIM-1			AIF-1		
Sample	(J)	(ft-lbs.)	Failure Mode	(J)	(ft-lbs.)	Failure Mode	(J)	(ft-lbs.)	Failure Mode
-1	35.38	48	B	29.48	40	B	35.38	48	B
-2	31.69	43	B	28.74	39	B	36.85	50	B
-3	28.01	38	B	28.74	39	B	32.43	44	B
-4	25.06	34	B	30.22	41	NA	31.69	43	B
Average:	**30.03**	**40.75**		**29.30**	**39.75**		**34.09**	**46.25**	
STD:	**4.48**	**6.08**		**0.71**	**0.96**		**2.44**	**3.30**	

Table 25. Cross-Tension Impact Results for Material B, 1.55-mm (0.061-in.) Dual-Phase Steel (Absorbed energy was measured and failure mode was recorded for samples from each temper condition. Full-button failure is denoted by the letter B. Partial interfacial failure is denoted by the letters "PIF".)

Cross Tension Impact Results Material 'B' 1.55-mm (0.061-in) Dual Phase 140T									
	Zero Temper			Medium Temper			Full Temper		
	BIQ-1			BIM-1			BIF-1		
Sample	(J)	(ft-lbs.)	Failure Mode	(J)	(ft-lbs.)	Failure Mode	(J)	(ft-lbs.)	Failure Mode
-1	57.49	78	PIF	64.12	87	B	75.17	102	B
-2	43.48	59	FIF	70.75	96	B	na	na	NA
-3	44.22	60	PIF	na	na	B	70.75	96	B
-4	56.75	77	PIF	na	na	B	70.75	96	B
Average:	**50.48**	**68.50**		**67.44**	**91.50**		**72.23**	**98.00**	
STD:	**7.67**	**10.41**		**4.69**	**6.36**		**2.55**	**3.46**	

Table 26. Cross-Tension Impact Results for Material C, 0.94-mm (0.037-in.) Martensitic Steel (Absorbed energy was measured and failure mode was recorded for samples from each temper condition. Full-button failure is denoted by the letter B.)

Cross Tension Impact Results Material 'C' 0.94-mm (0.037-in) Martensitic									
	Zero Temper			Medium Temper			Full Temper		
	CIO-1			CIM-1			CIF-1		
Sample	(J)	(ft-lbs.)	Failure Mode	(J)	(ft-lbs.)	Failure Mode	(J)	(ft-lbs.)	Failure Mode
-1	33.90	46	B	29.48	40	B	30.22	41	B
-2	31.69	43	B	34.64	47	B	30.22	41	B
-3	42.75	58	B	28.01	38	B	31.69	43	B
-4	38.32	52	B	39.80	54	B	33.90	46	B
Average:	**36.67**	**49.75**		**32.98**	**44.75**		**31.51**	**42.75**	
STD:	**4.90**	**6.65**		**5.36**	**7.27**		**1.74**	**2.36**	

Table 27. Cross-Tension Impact Results for Material D, 1.58-mm (0.062-in.) Martensitic Steel (Absorbed energy was measured and failure mode was recorded for samples from each temper condition. Full-button failure is denoted by the letter B. Partial interfacial failure is denoted by the letters PIF. Full interfacially failed welds are denoted by the letters "FIF".)

Cross Tension Impact Results Material 'D' 1.58-mm (0.062-in) Martensitic									
	Zero Temper			Medium Temper			Full Temper		
	DIO-1			DIM-1			DIF-1		
Sample	(J)	(ft-lbs.)	Failure Mode	(J)	(ft-lbs.)	Failure Mode	(J)	(ft-lbs.)	Failure Mode
-1	36.85	50	FIF	na	na	NA	35.38	48	FIF
-2	32.43	44	FIF	33.17	45	PIF	39.80	54	PIF
-3	32.43	44	PIF	30.22	41	FIF	36.11	49	PIF
-4	30.95	42	PIF	39.06	53	PIF	36.11	49	PIF
Average:	**33.17**	**45.00**		**34.15**	**46.33**		**36.85**	**50.00**	
STD:	**2.55**	**3.46**		**4.50**	**6.11**		**2.00**	**2.71**	

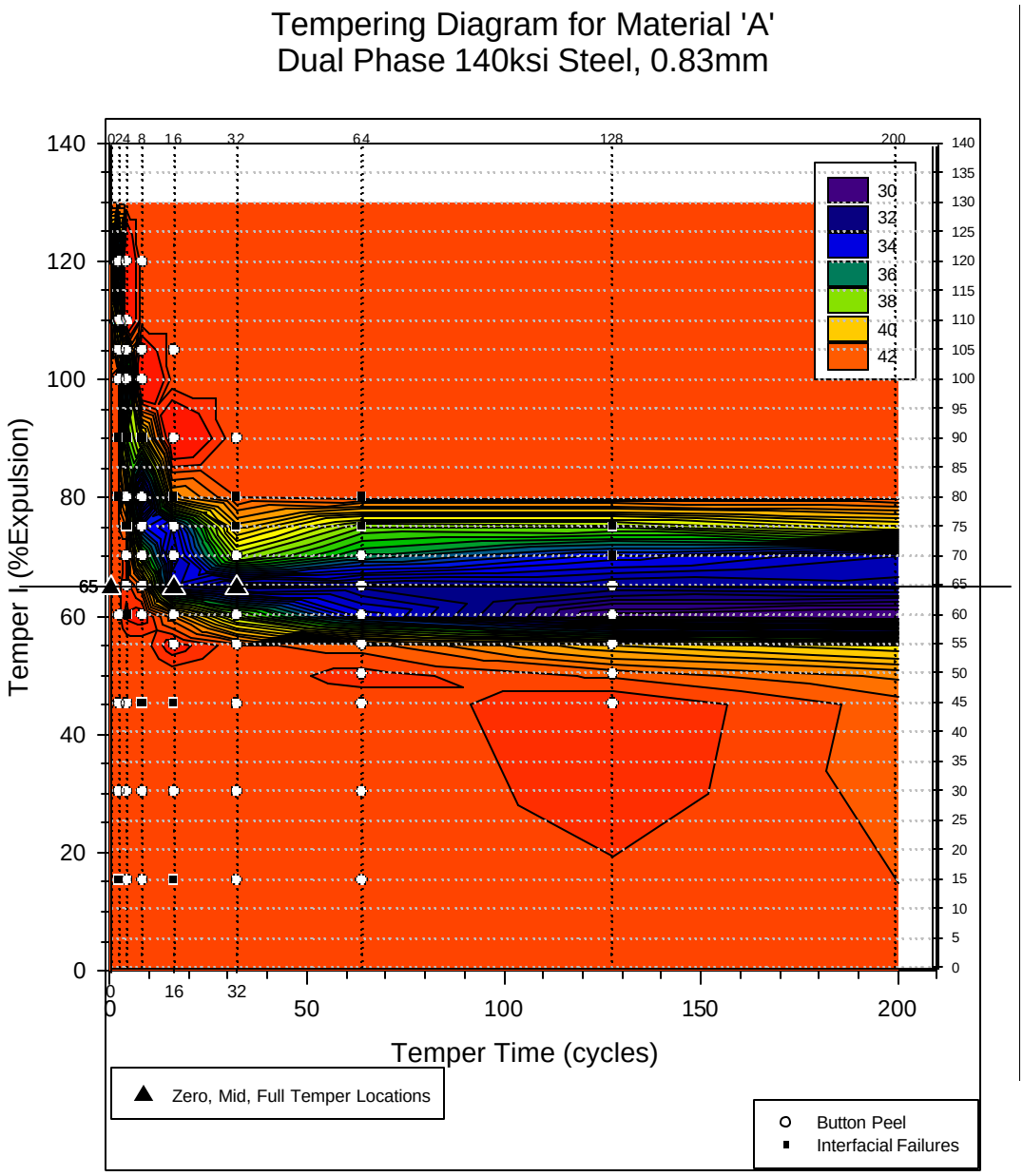

Figure 1. **Quench and Temper Processing Map for 0.83-mm (0.033-in.) Dual-Phase Steel (Material A)** (The matrix of tempering times and currents was applied to welded samples immediately following an established, in-process, quench time. Surface measurements of hardness of the weld were performed using the Rc scale. Hardness results were then plotted as a function of temper time and percentage of the expulsion limit for the steel using a contour plot. Resulting peel test results showing the button morphology were overlaid onto the contour plot. Reference points showing the tempering conditions for the metallurgical sections and mechanical test samples are also shown.)

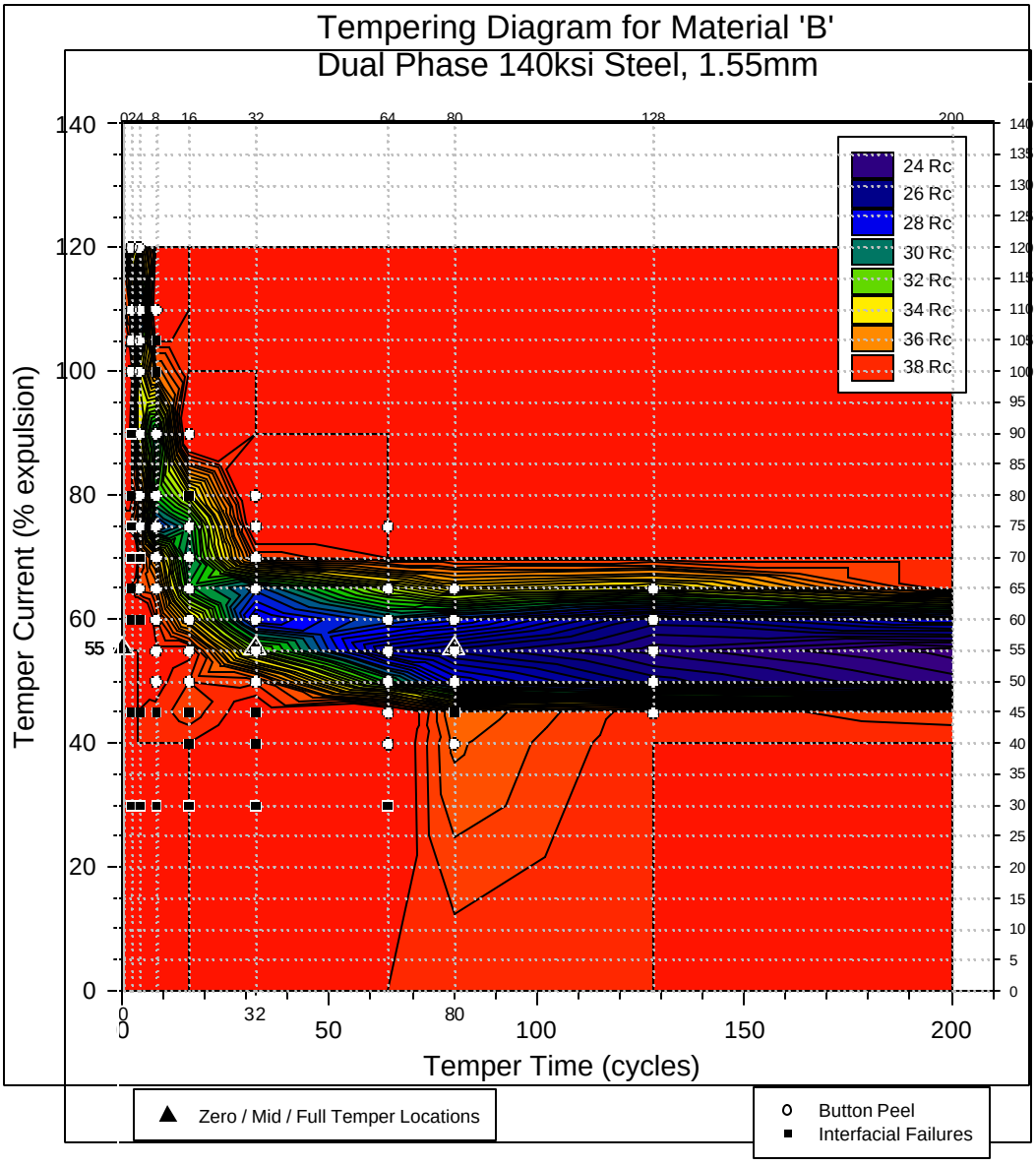

Figure 2. **Quench and Temper Processing Map for 1.55-mm (0.061-in.) Dual-Phase Steel (Material B)** (The matrix of tempering times and currents was applied to welded samples immediately following an established, in-process, quench time. Surface measurements of hardness of the weld were performed using the Rc scale. Hardness results were then plotted as a function of temper time and percentage of the expulsion limit for the steel using a contour plot. Resulting peel test results showing the button morphology were overlaid onto the contour plot. Reference points showing the tempering conditions for the metallurgical sections and mechanical test samples are also shown.)

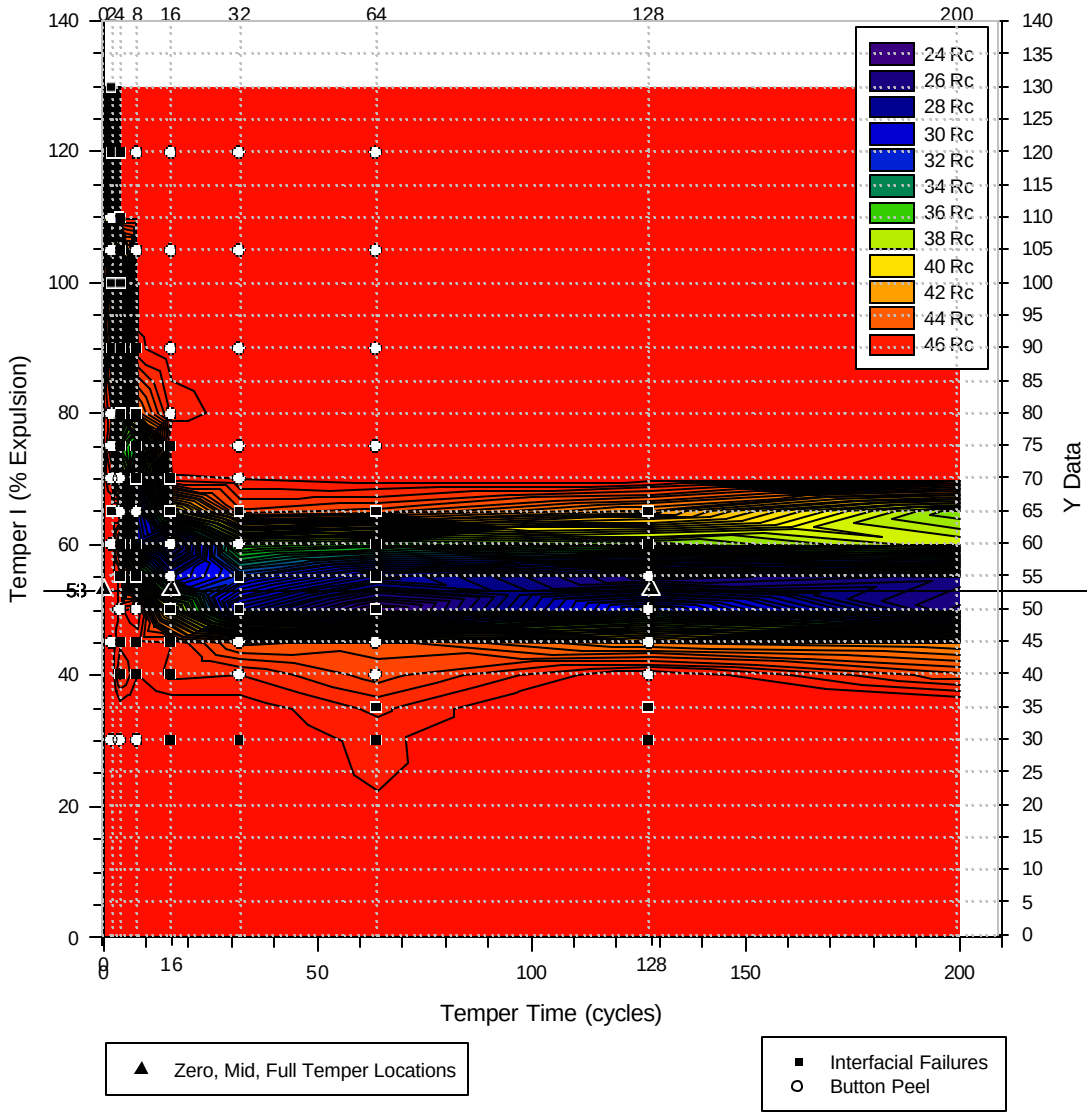

Figure 3. **Quench and Temper Processing Map for 0.94-mm (0.037-in.) Martensitic Steel (Material C)** (The matrix of tempering times and currents was applied to welded samples immediately following an established, in-process, quench time. Surface measurements of hardness of the weld were performed using the Rc scale. Hardness results were then plotted as a function of temper time and percentage of the expulsion limit for the steel using a contour plot. Resulting peel test results showing the button morphology were overlaid onto the contour plot. Reference points showing the tempering conditions for the metallurgical sections and mechanical test samples are also shown.)

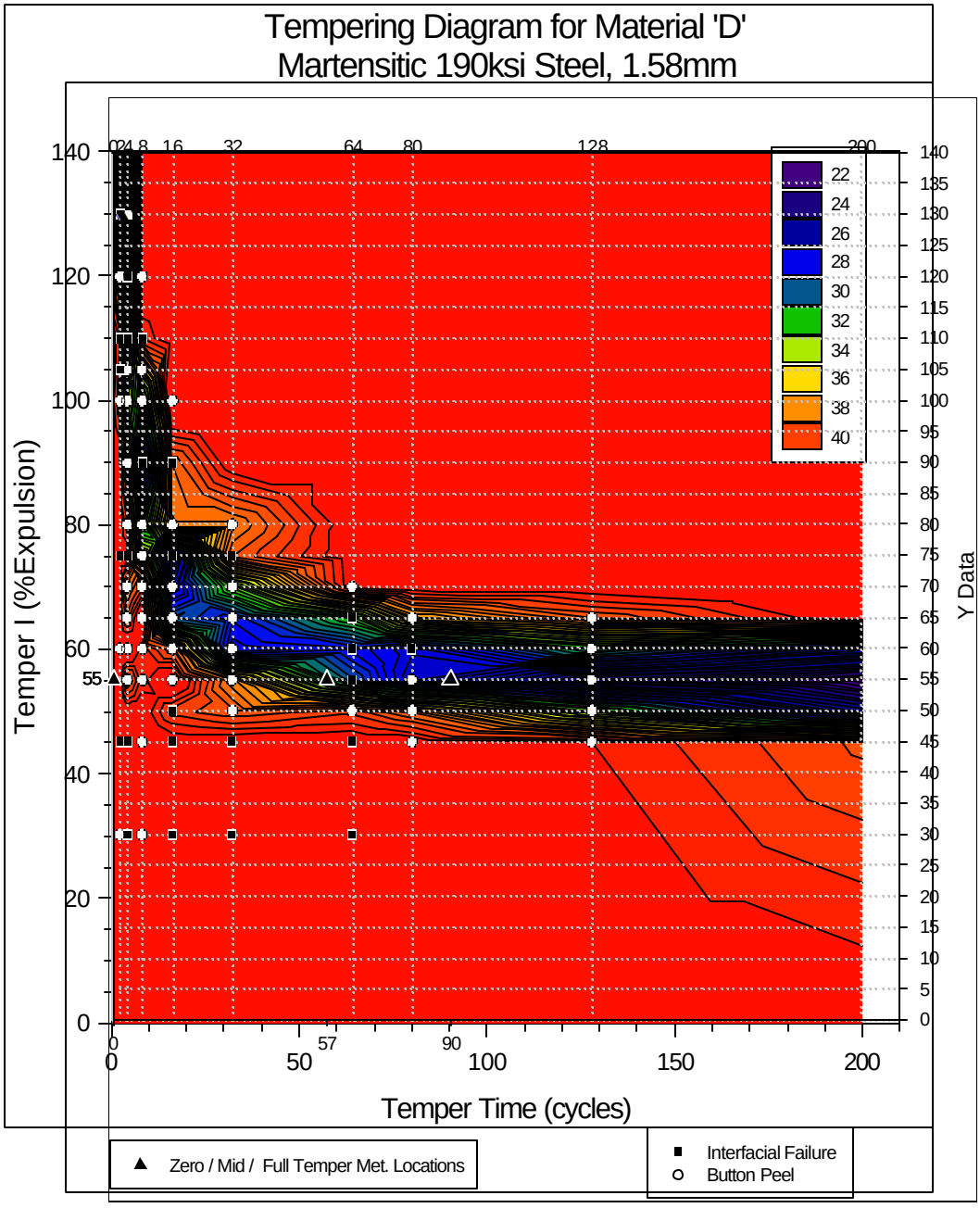

Figure 4. **Quench and Temper Processing Map for 1.58-mm (0.062-in.) Martensitic Steel (Material D)** (The matrix of tempering times and currents was applied to welded samples immediately following an established, in-process, quench time. Surface measurements of hardness of the weld were performed using the Rc scale. Hardness results were then plotted as a function of temper time and percentage of the expulsion limit for the steel using a contour plot. Resulting peel test results showing the button morphology were overlaid onto the contour plot. Reference points showing the tempering conditions for the metallurgical sections and mechanical test samples are also shown.)

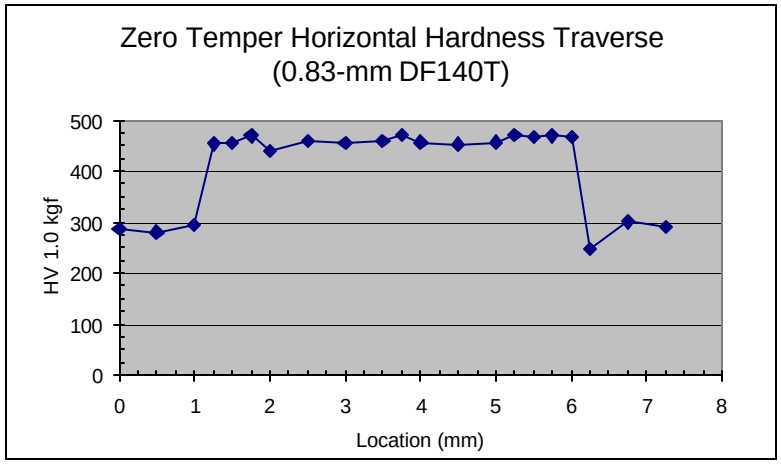

(a) Diagontal hardness traverse of 0.83-mm DF140T in the zero-temper condition

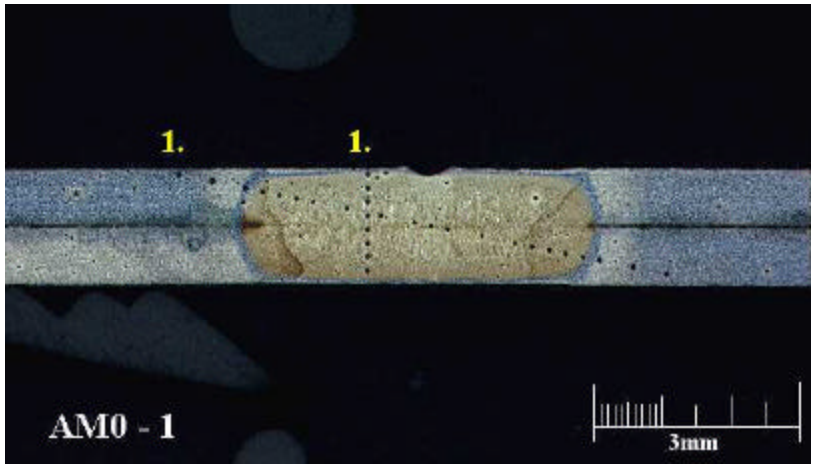

(b) Micrograph of 0.83-mm DF140T in the zero-temper condition

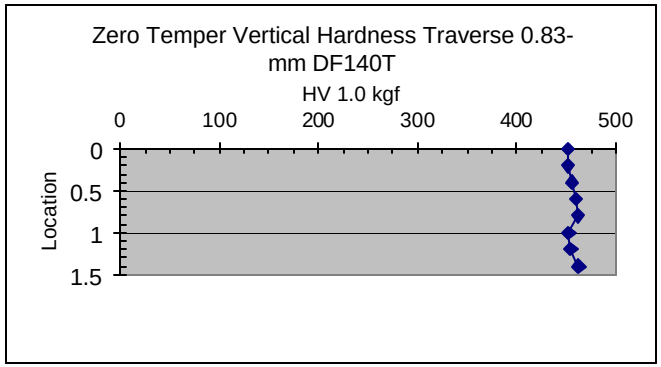

(c) Through-thickness hardness traverse of 0.83-mm DF140T in the zero-temper condition

Figure 5. **Hardness Traverse Plots for Material A, 0.83-mm (0.033-in.) Dual-Phase Steel in the Zero-Temper Condition** [The sample was welded and quenched using established parameters for Material A. No tempering time was applied and the sample was held for an additional 60 cycles without current. Results from the hardness traverse in the through-thickness direction and the diagonal hardness traverse are presented using the VHN scale.]

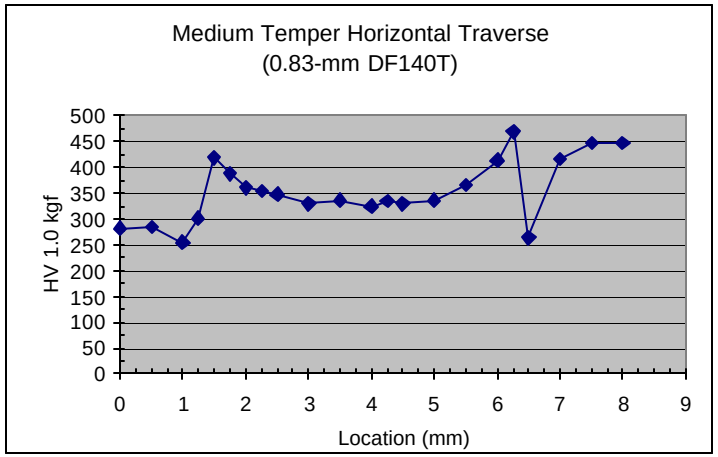

(a) Diagonal hardness traverse of 0.83-mm DF140T in the medium-temper condition

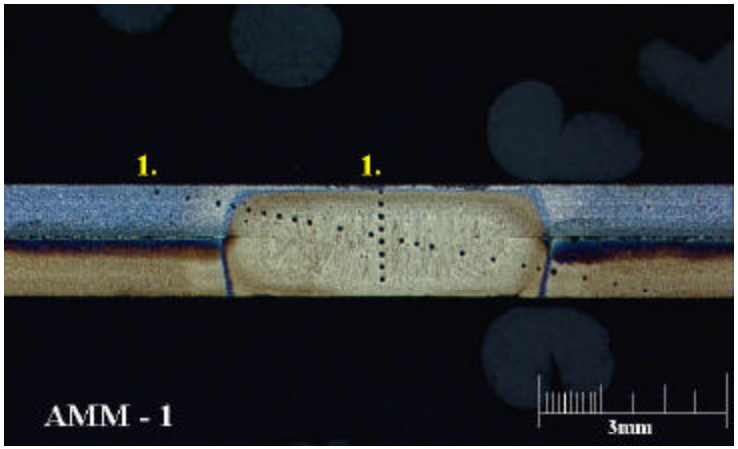

(b) Micrograph of 0.83-mm DF140T in the medium-temper condition

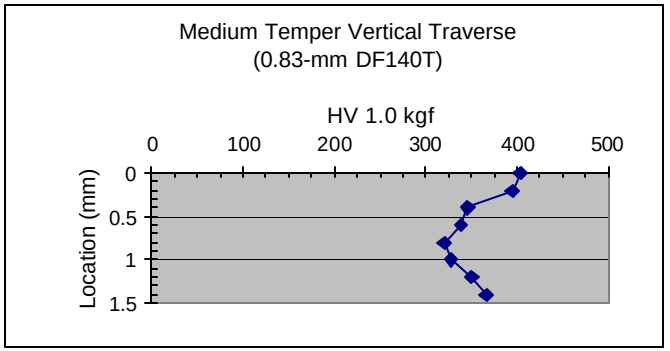

(c) Through-thickness hardness traverse of 0.83-mm DF140T in the medium-temper condition

Figure 6. Hardness Traverse Plots for Material A, 0.83-mm (0.033-in.) Dual-Phase Steel in the Medium-Temper Condition [The sample was welded and quenched using established parameters for Material A then tempered for 16 cycles at 5.7 kA (65% of the expulsion limit). This was followed by a 60-cycle hold time. Results from the hardness traverse in the through-thickness direction and the diagonal hardness traverse are presented using the VHN scale.]

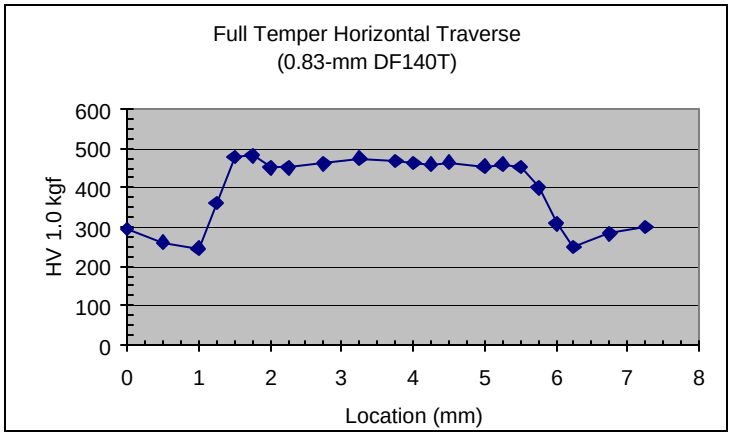

(a) Diagonal hardness traverse of 0.83-mm DF140T in the full-temper condition

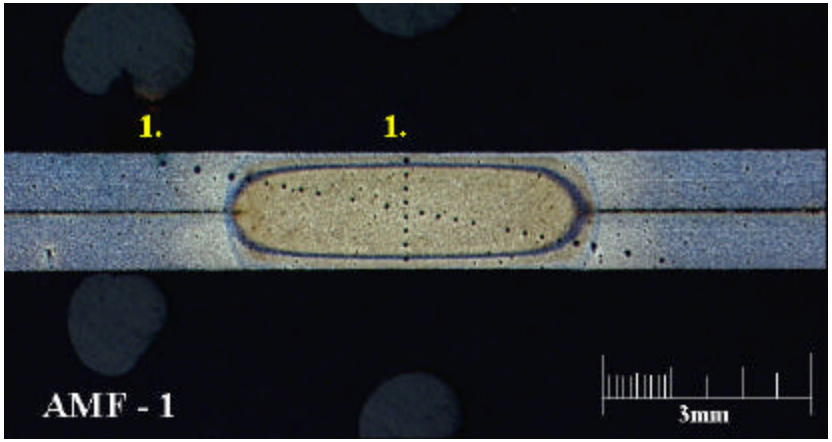

(b) Micrograph of 0.83-mm DF140T in the full-temper condition

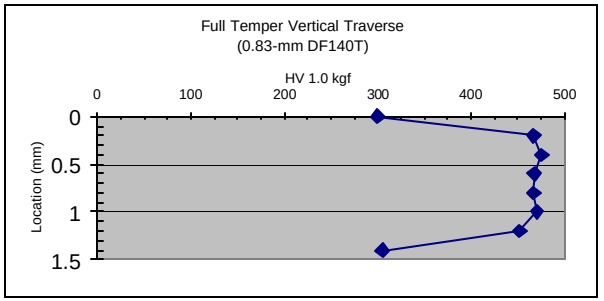

(c) Through-thickness hardness traverse of 0.83-mm DF140T in the full-temper condition

Figure 7. Hardness Traverse Plots for Material A, 0.83-mm (0.033-in.) Dual-Phase Steel in the Full-Temper Condition [The sample was welded and quenched using established parameters for Material A then tempered for 32 cycles at 5.7 kA (65% of the expulsion limit). This was followed by a 60-cycle hold time. Results from the hardness traverse in the diagonal direction and the hardness traverse in the through-thickness direction are presented using the VHN scale.]

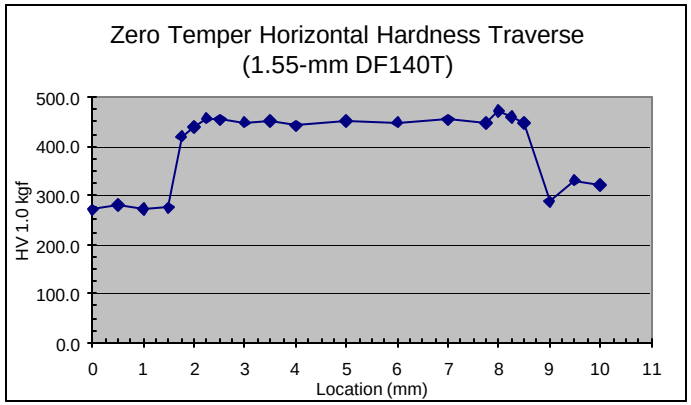

(a) Diagonal hardness traverse of 1.55-mm DF140T in the zero-temper condition

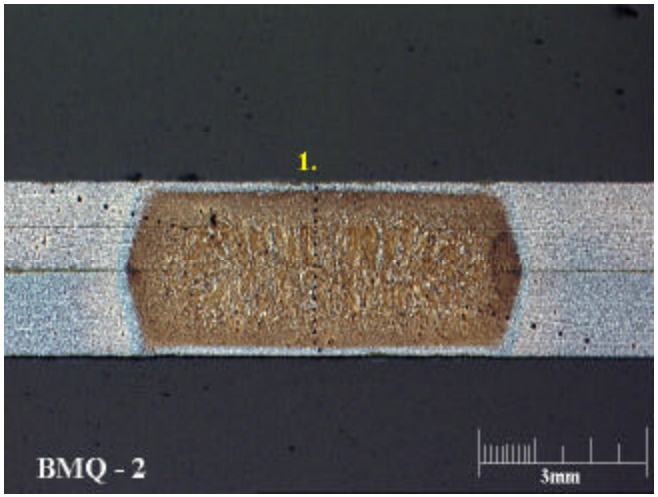

(b) Micrograph of 1.55-mm DF140T in the zero-temper condition

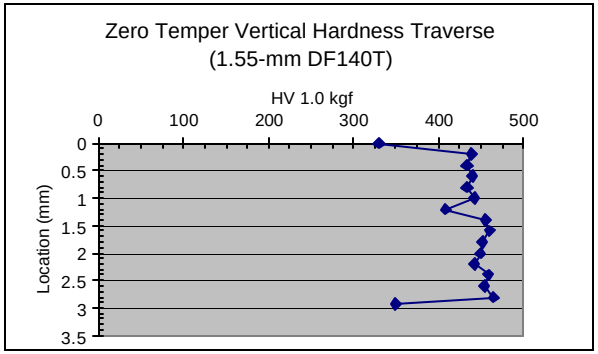

(c) Through-thickness hardness traverse of 1.55-mm DF140T in the zero-temper condition

Figure 8. Hardness Traverse Plot for Material B, 1.55-mm (0.061-in.) Dual-Phase Steel in the Zero-Temper Condition (The sample was welded and quenched using established parameters for Material B. No tempering time was applied and the sample was held for an additional 60 cycles after welding. Results from the diagonal and through-thickness hardness traverses are presented using the VHN scale.)

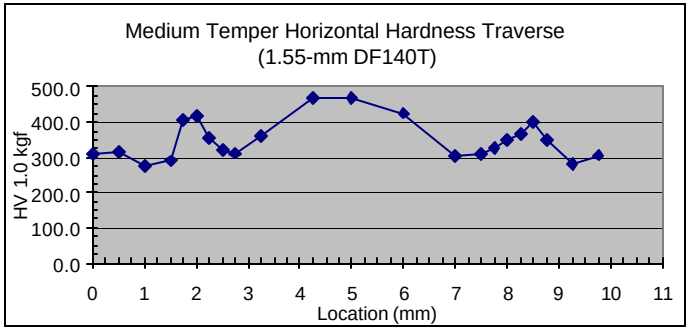

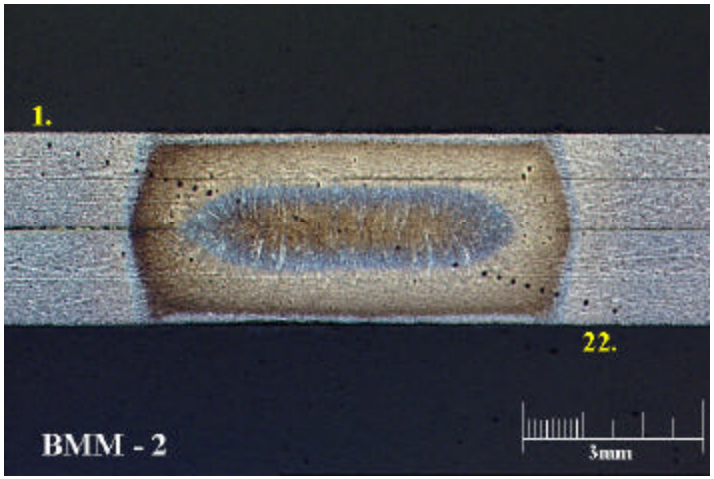

(a) Diagonal hardness traverse of 1.55-mm DF140T in the medium-temper condition
(b) Micrograph of 1.55-mm DF140T in the medium-temper condition

Figure 9. Hardness Traverse Plot for Material B, 1.55-mm (0.061-in.) Dual-Phase Steel in the Medium-Temper Condition [The sample was welded and quenched using established parameters for Material B then tempered for 32 cycles at 6.8 kA (55% of the expulsion limit). This was followed by a 60-cycle hold time. Results from the hardness traverse are presented using the VHN scale.]

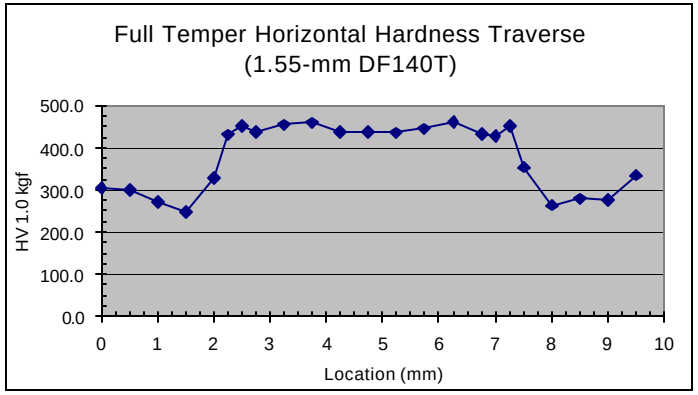

(a) Diagonal hardness traverse of 1.55-mm DF140T in the full-temper condition

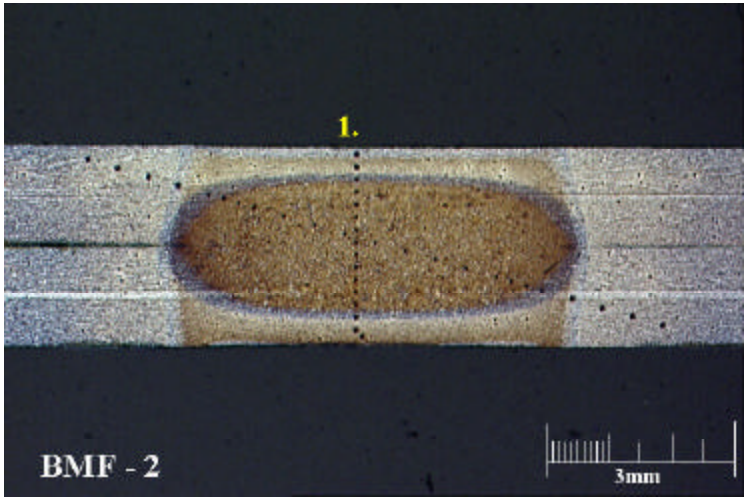

(b) Micrograph of 1.55-mm DF140T in the full-temper condition

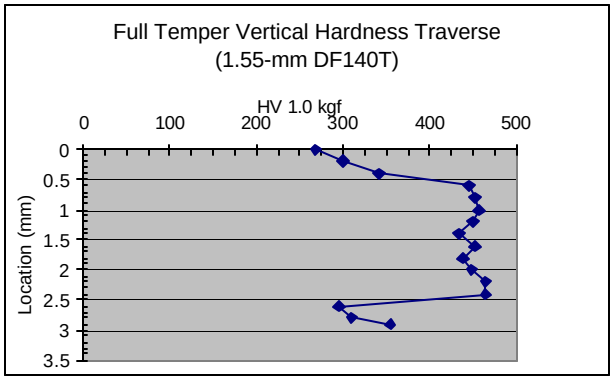

(c) Through-thickness hardness traverse of 1.55-mm DF140T in the full-temper condition

Figure 10. Hardness Traverse Plots for Material B, 1.55-mm (0.061-in.) Dual-Phase Steel in the Full-Temper Condition [The sample was welded and quenched using established parameters for Material B then tempered for 80 cycles at 6.8 kA (55% of the expulsion limit). This was followed by a 60-cycle hold time. Results from the hardness traverse in the diagonal and through-thickness directions are presented using the VHN scale.]

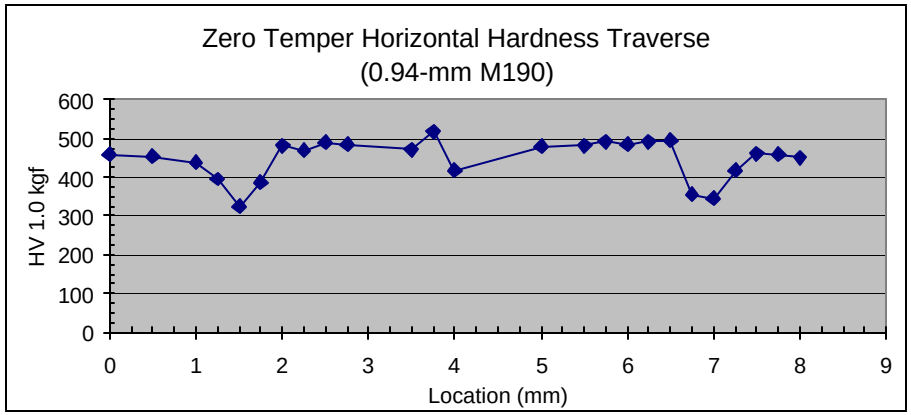

(a) Diagonal hardness traverse of 0.94-mm M190 in the zero-temper condition

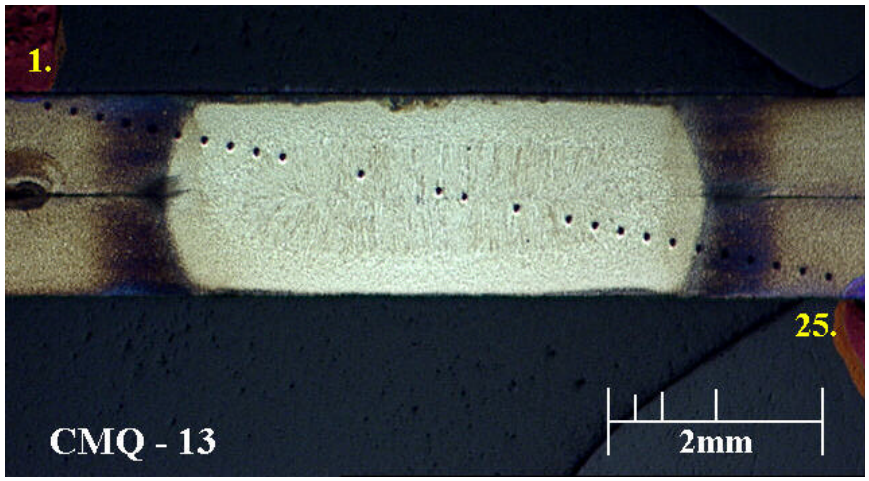

(b) Micrograph of 0.04-mm M190 in the zero-temper condition

Figure 11. Hardness Traverse Plot for Material C, 0.94-mm (0.037-in.) Martensitic Steel in the Zero-Temper Condition (The sample was welded and quenched using established parameters for Material C. No tempering time was applied and the sample was held for an additional 60 cycles. Results from the hardness traverse are presented using the VHN scale.)

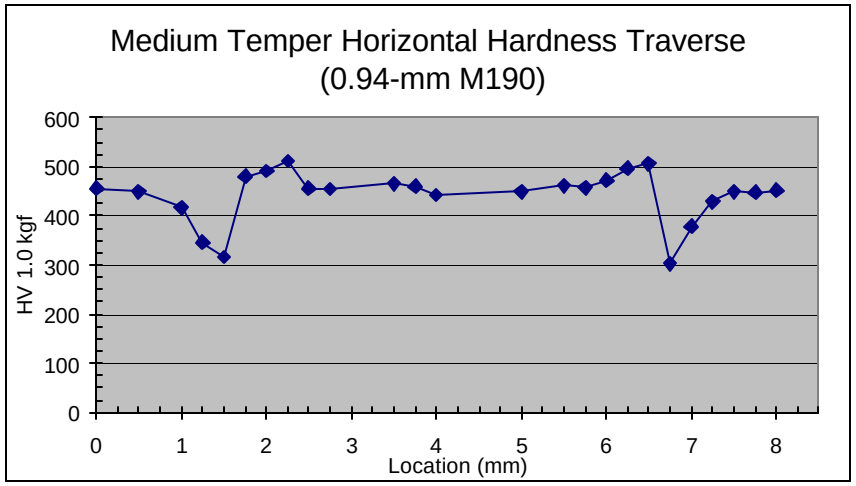

(a) Diagonal hardness traverse of 0.94-mm M190 in the medium-temper condition

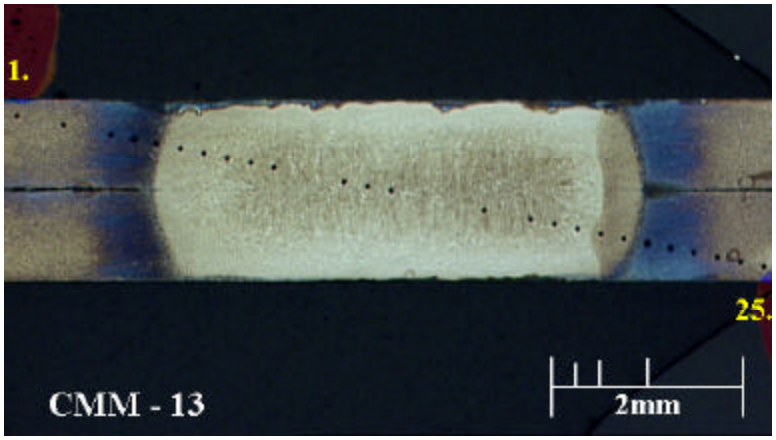

(b) Micrograph of 0.94-mm M190 in the medium-temper condition

Figure 12. Hardness Traverse Plot for Material C, 0.94-mm (0.037-in.) Martensitic Steel in the Medium-Tempered Condition [The sample was welded and quenched using established parameters for Material C then tempered for 16 cycles at 4.5 kA (53% of the expulsion limit). This was followed by a 60-cycle hold time. Results from the hardness traverse are presented using the VHN scale.]

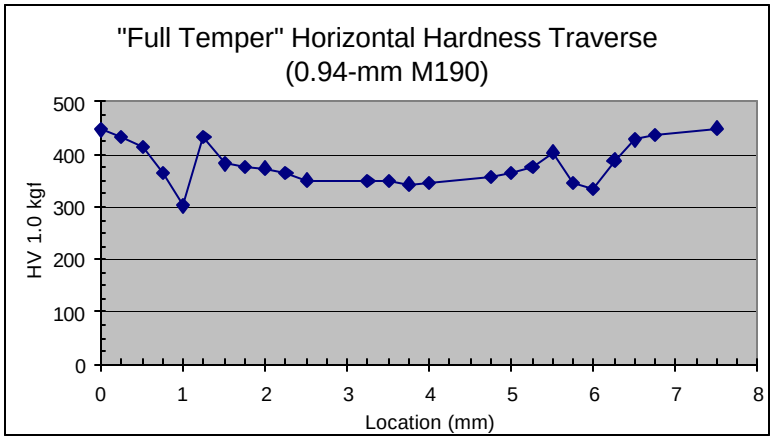

(a) Diagonal hardness traverse of 0.94-mm M190 in the full-temper condition

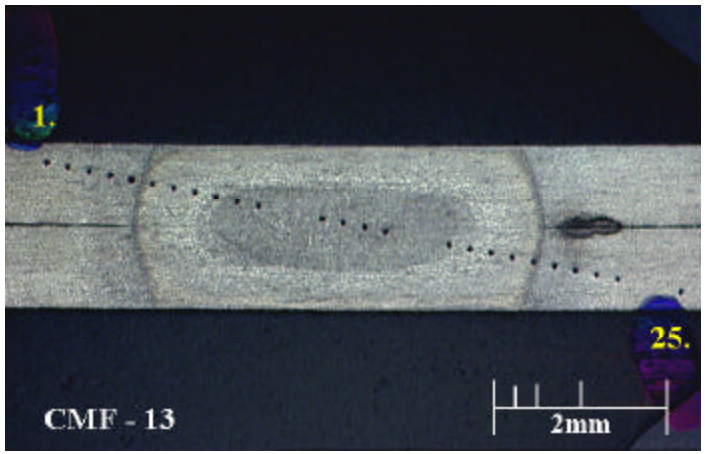

(b) Micrograph of 0.94-mm M190 in the full-temper condition

Figure 13. Hardness Traverse Plot for Material C, 0.94-mm (0.037-in.) Martensitic Steel in the Full-Temper Condition [The sample was welded and quenched using established parameters for Material C then tempered for 128 cycles at 4.5 kA (53% of the expulsion limit). This was followed by a 60-cycle hold time. Results from the hardness traverse are presented using the VHN scale.]

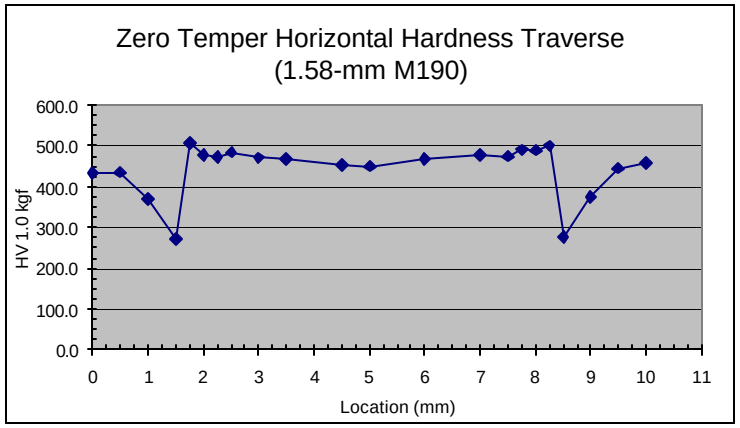

(a) Diagonal hardness traverse of 1.58-mm M190 in the zero-temper condition

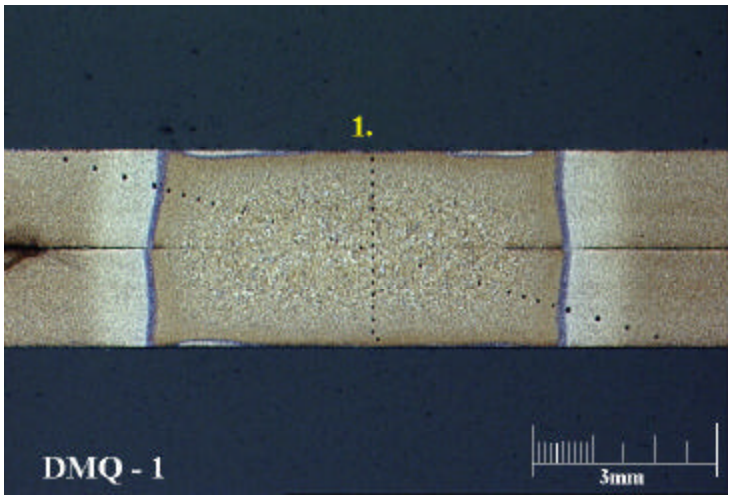

(b) Micrograph of 1.58-mm M190 in the zero-temper condition

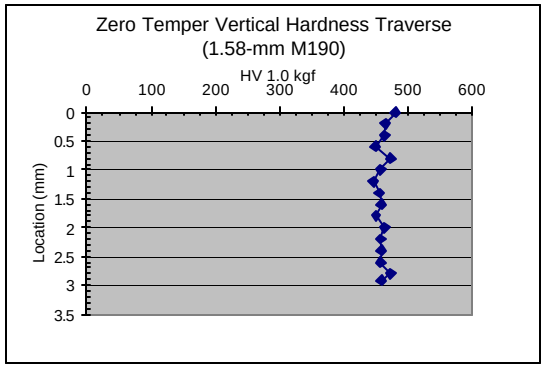

(c) Through-thickness hardness traverse of 1.58-mm M190 in the zero-temper condition

Figure 14. Hardness Traverse Plots for Material D, 1.58-mm (0.062-in.) Martensitic Steel in the Zero-Tempered Condition (The sample was welded and quenched using established parameters for Material D. No tempering time was applied and the sample was held for an additional 60 cycles after welding. Results from the hardness traverses in the diagonal and through-thickness direction are presented using the VHN scale.)

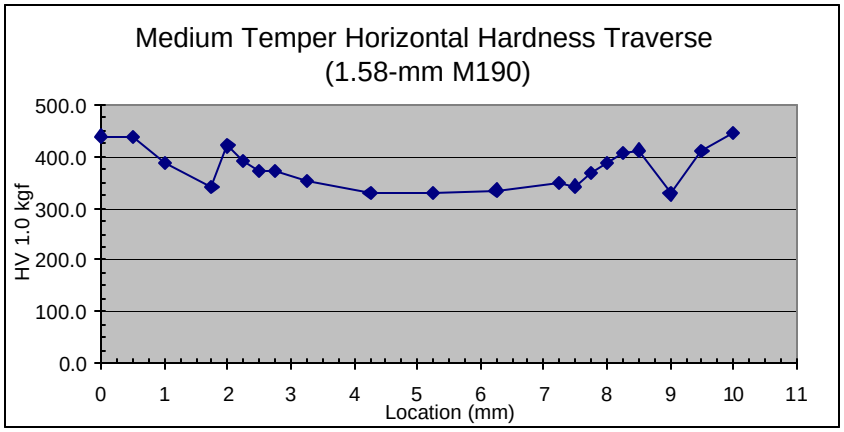

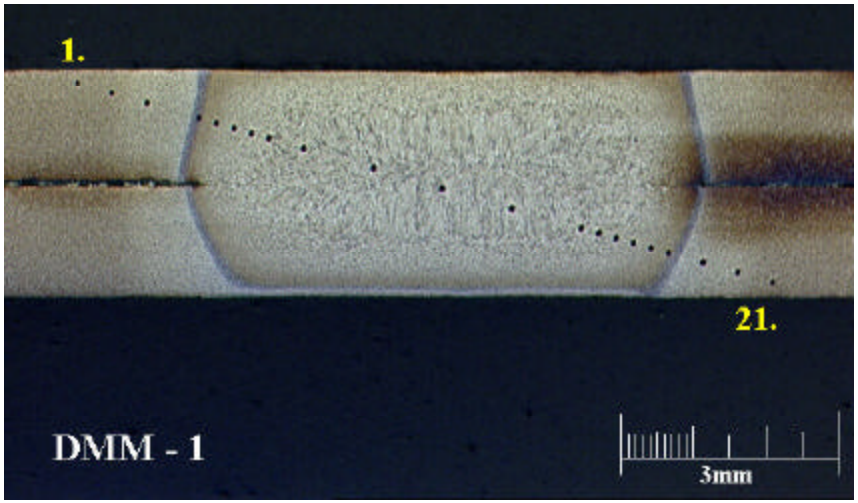

(a) Diagonal hardness traverse of 1.58-mm M190 in the medium-temper condition
(b) Micrograph of 1.58-mm M190 in the medium-temper condition

Figure 15. Hardness Traverse Plot for Material D, 1.58-mm (0.062-in.) Martensitic Steel in the Medium-Tempered Condition [The sample was welded and quenched using established parameters for Material D then tempered for 57 cycles at 6.8 kA (55% of the expulsion limit). This was followed by a 60-cycle hold time. Results from the hardness traverse are presented using the VHN scale.]

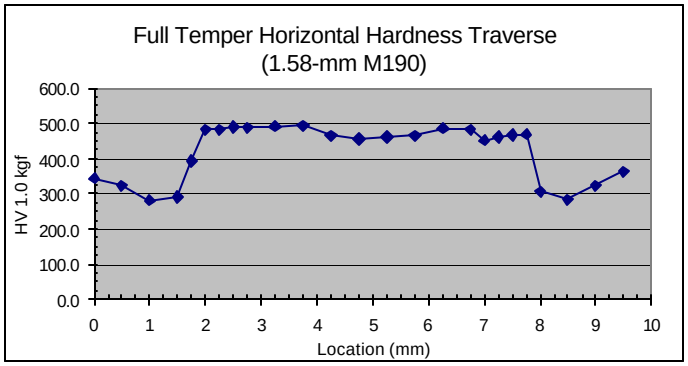

(a) Diagonal hardness traverse of 1.58-mm M190 in the full-temper condition

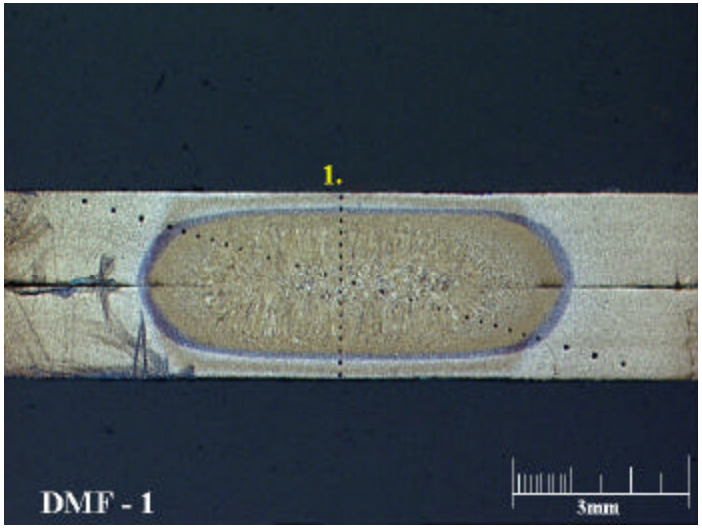

(b) Micrograph of 1.58-mm M190 in the full-temper condition

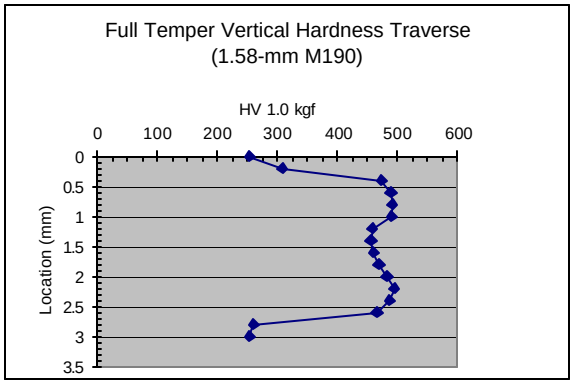

(c) Through-thickness hardness traverse of 1.58-mm M190 in the full-temper condition

Figure 16. Hardness Traverse Plot for Material D, 1.58-mm (0.062-in.) Martensitic Steel in the Full-Temper Condition [The sample was welded and quenched using established parameters for Material D then tempered for 90 cycles at 6.8 kA (55% of the expulsion limit). This was followed by a 60-cycle hold time. Results from the hardness traverse in the diagonal and through-thickness direction are presented using the VHN scale.]

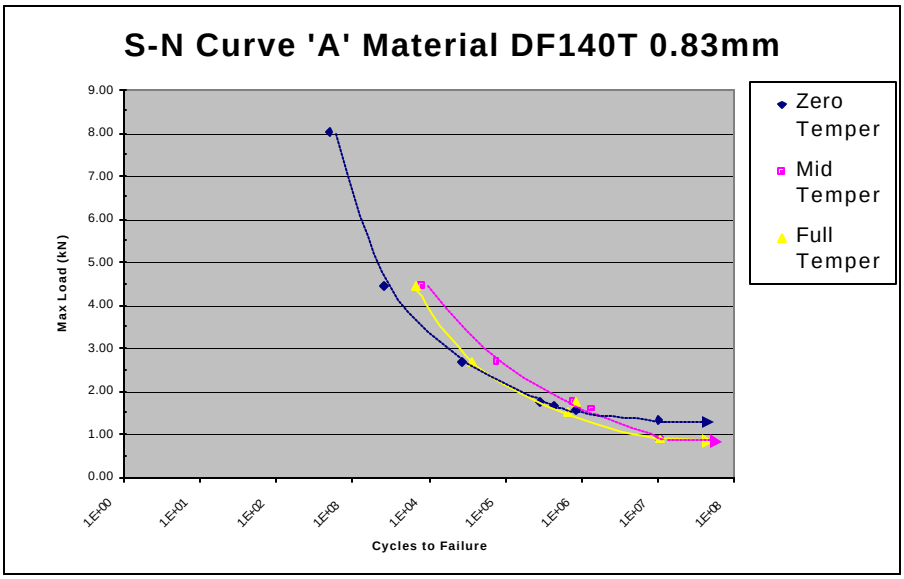

Figure 17. **S-N Curves for Material A, 0.83-mm (0.033-in.) Dual-Phase Steel** (Zero-, medium-, and full-temper conditions are plotted. Fatigue life was halted after 10,000,000 cycles and represented by the dotted arrows.)

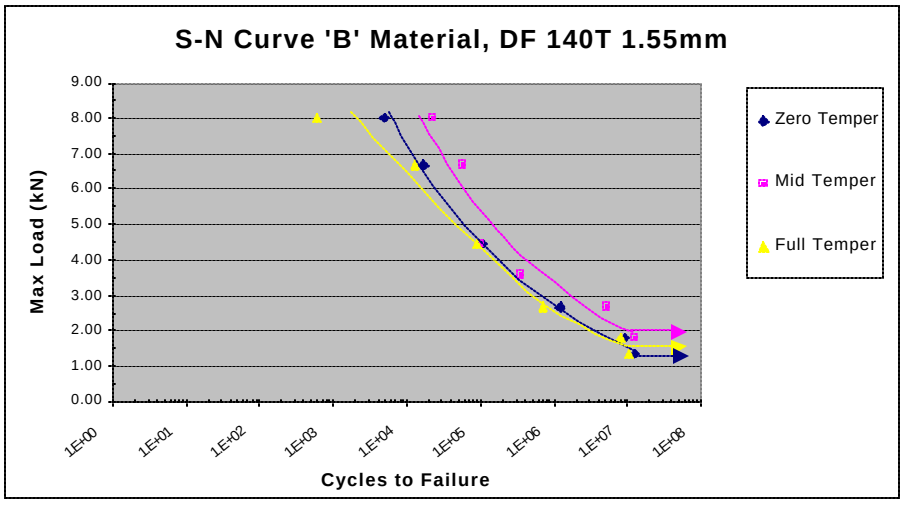

Figure 18. **S-N Curves for Material B, 1.55-mm (0.061-in.) Dual-Phase Steel (**Zero-, medium-, and full-temper conditions are plotted. Fatigue life was halted after 10,000,000 cycles and represented by the dotted arrows.)

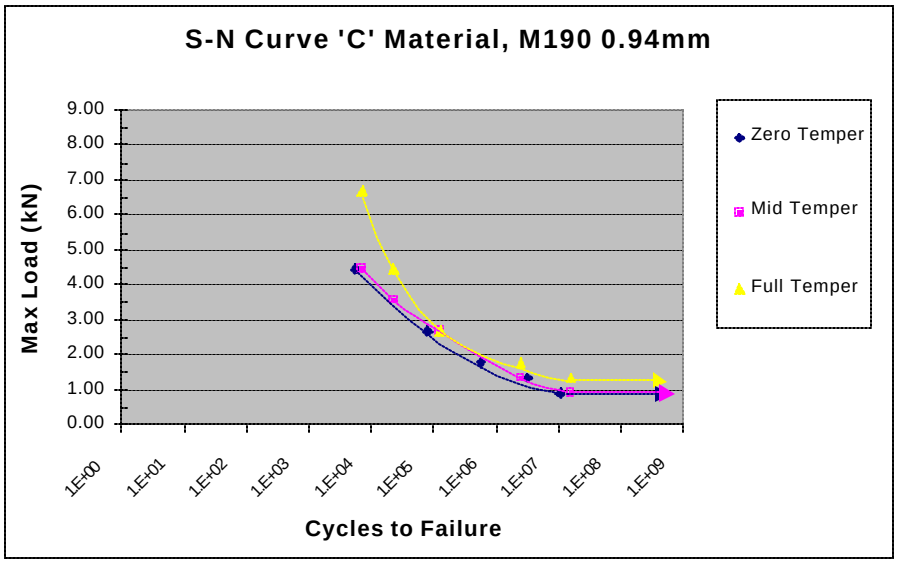

Figure 19. **S-N Curves for Material C, 0.94-mm (0.037-in.) Martensitic Steel** (Zero-, medium-, and full-temper conditions are plotted. Fatigue life was halted after 10,000,000 cycles and represented by the dotted arrows.)

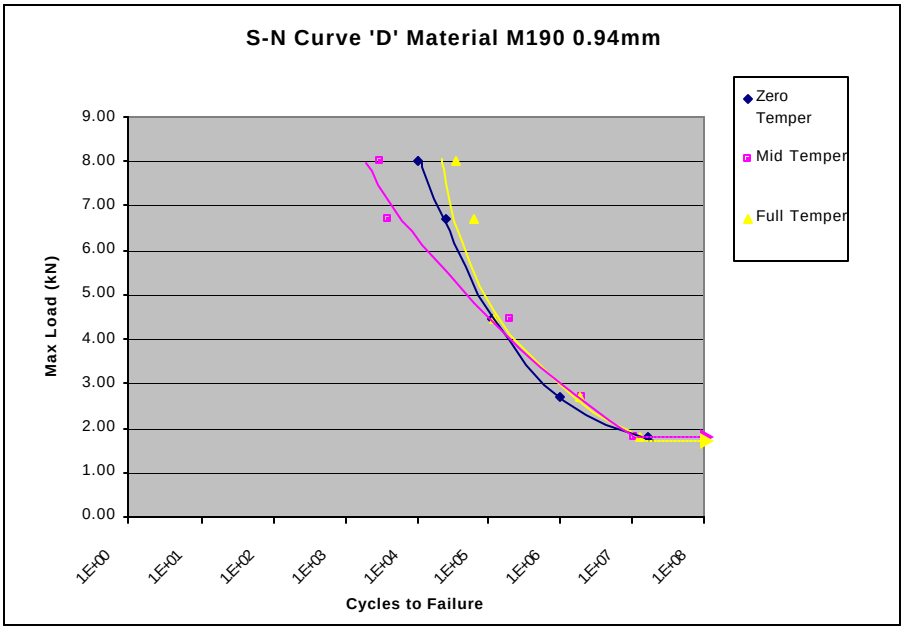

Figure 20. **S-N Curves for Material D, 1.58-mm (0.062-in.) Martensitic Steel** (Zero-, medium-, and full-temper conditions are plotted. Fatigue life was halted after 10,000,000 cycles and represented by the dotted arrows.)

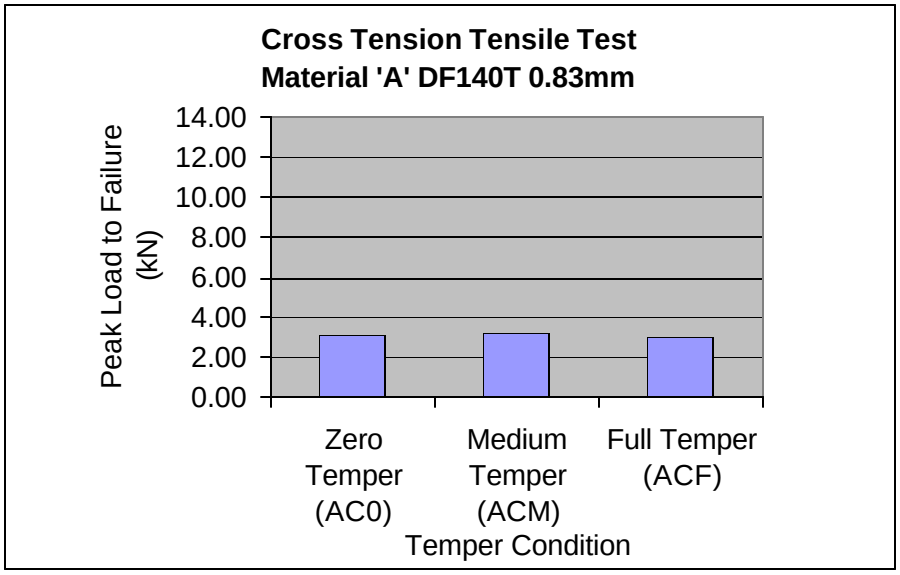

Figure 21. Cross-Tension Testing Results for Material A, 0.83-mm (0.033-in.) Dual-Phase Steel (Zero-, medium-, and full-temper conditions are plotted.)

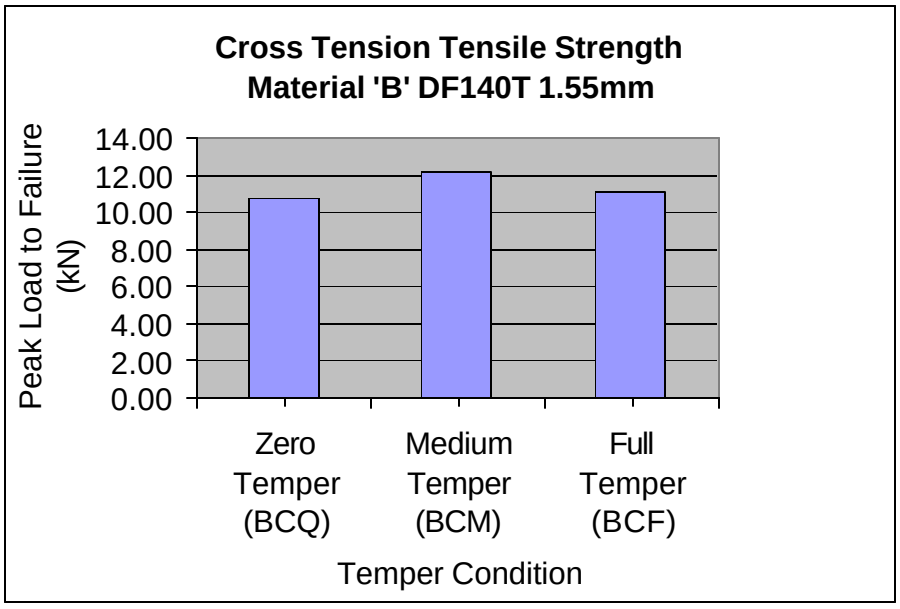

Figure 22. Cross-Tension Testing Results for Material B, 1.55-mm (0.061-in.) Dual-Phase Steel (Zero-, medium-, and full-temper conditions are plotted.)

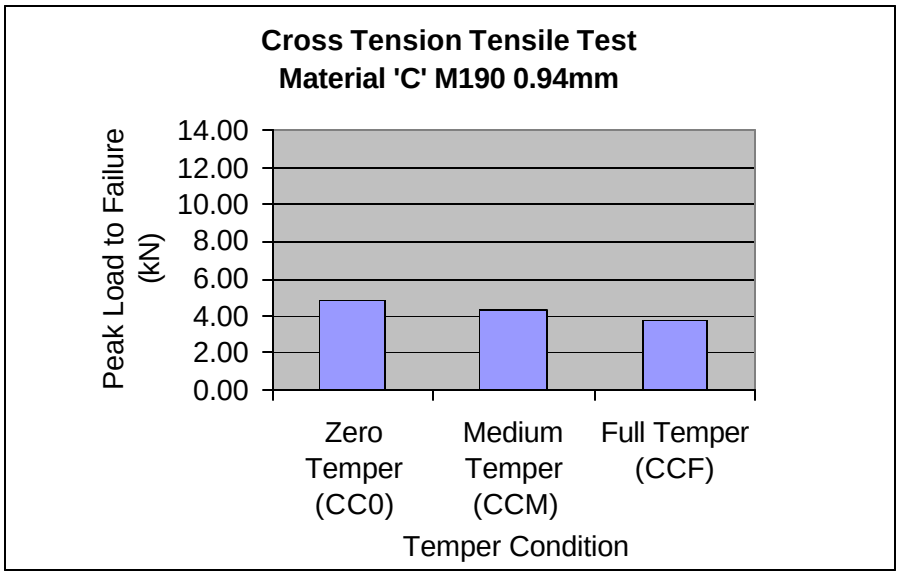

Figure 23. **Cross-Tension Testing Results for Material C, 0.94-mm (0.037-in.) Martensitic Steel** (Zero-, medium-, and full-temper conditions are plotted.)

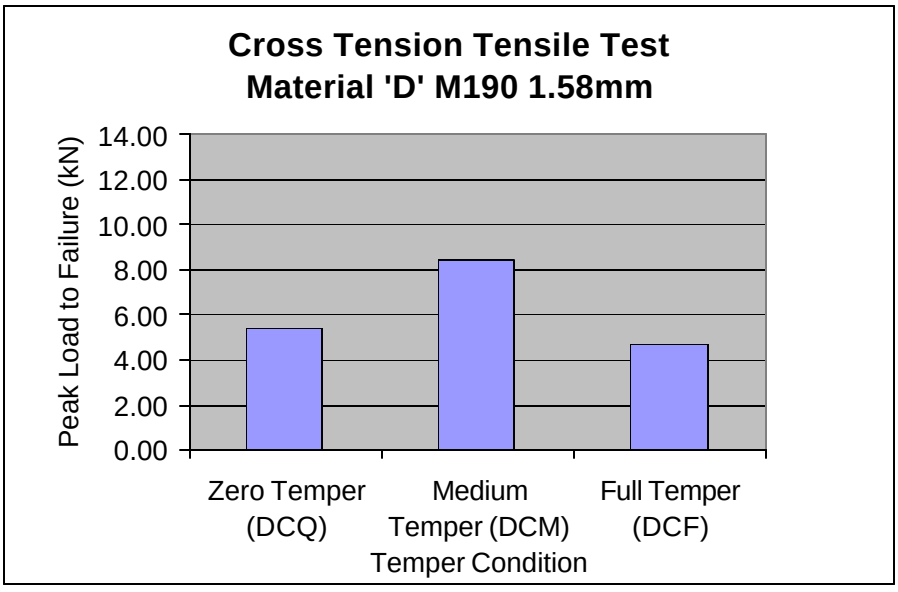

Figure 24. **Cross-Tension Testing Results for Material D, 1.58-mm (0.062-in.) Martensitic Steel** (Zero-, medium-, and full-temper conditions are plotted.)

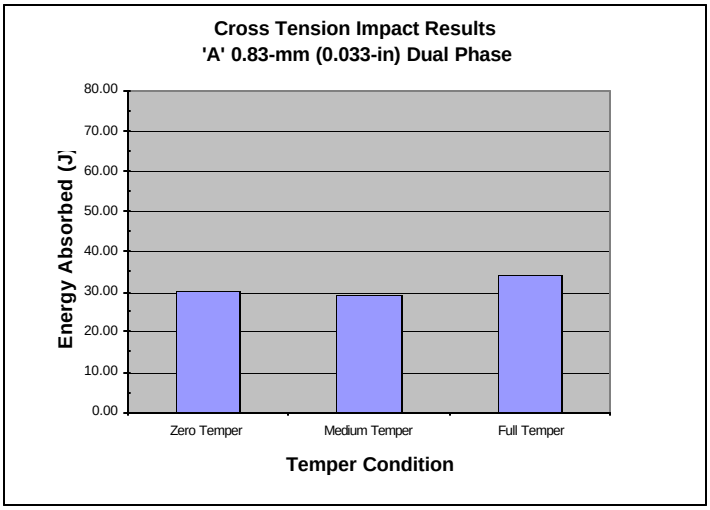

Figure 25. Cross-Tension Impact Results for Material A, 0.83-mm (0.033-in.) Dual-Phase Steel [All samples were welded with the established welding parameters for Material A. Zero-temper welds (AIQ) were tested as welded with no additional tempering step. Medium-temper welds (AIM) were quenched for 20 cycles and tempered for 16 cycles at 65% of the expulsion level for the material. Full-tempered welds (AIF) were quenched for 20 cycles and tempered for 32 cycles at 65% of the expulsion level for the material.]

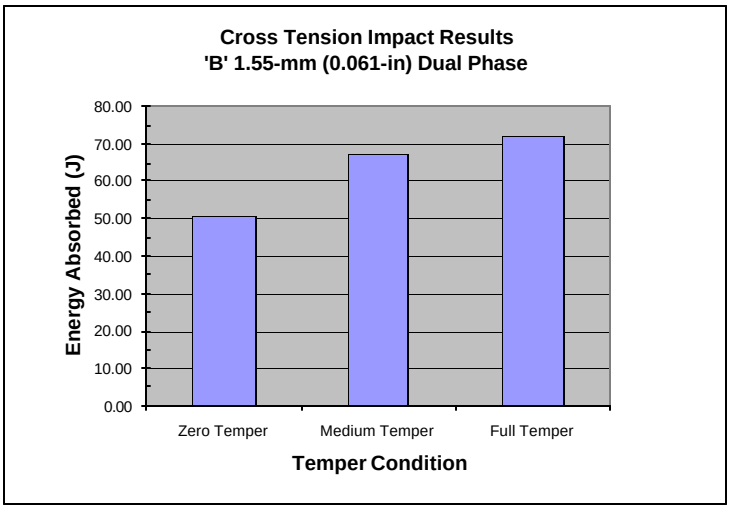

Figure 26. Cross-Tension Impact Results for Material B, 1.55-mm (0.061-in.) Dual-Phase Steel [All samples were welded with the established welding parameters for Material B. Zero-temper welds (BIQ) were tested as welded with no additional tempering step. Medium-temper welds (BIM) were quenched for 46 cycles and tempered for 32 cycles at 55% of the expulsion level for the material. Full-tempered (BIF) welds were quenched for 46 cycles and tempered for 80 cycles at 55% of the expulsion level for the material.]

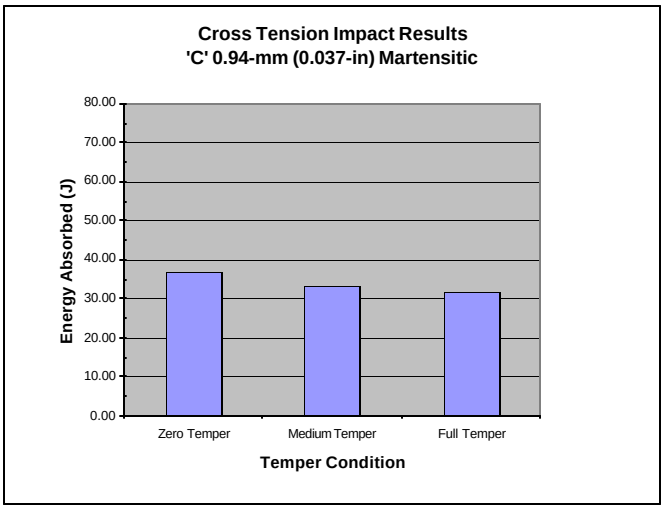

Figure 27. Cross-Tension Impact Results for Material C, 0.94-mm (0.037-in.) Martensitic Steel [All samples were welded with the established welding parameters for Material C. Zero-temper welds (CIQ) were tested as welded with no additional tempering step. Medium-temper welds (CIM) were quenched for 20 cycles and tempered for 16 cycles at 53% of the expulsion level for the material. Full-tempered (CIF) welds were quenched for 20 cycles and tempered for 128 cycles at 53% of the expulsion level for the material.]

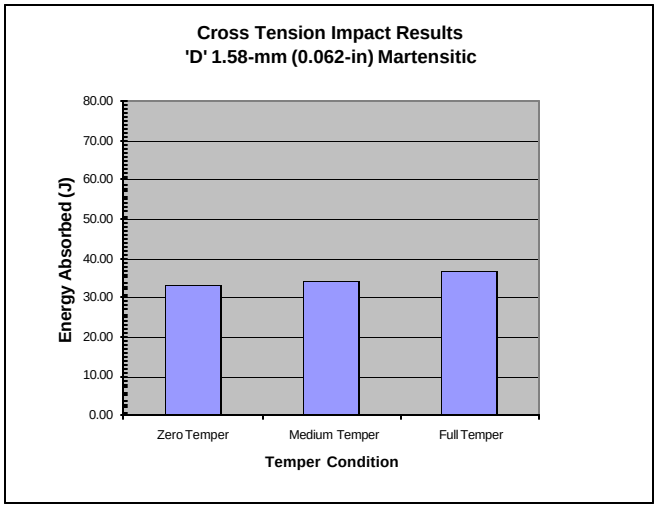

Figure 28. Cross-Tension Impact Results for Material D, 1.58-mm (0.062-in.) Martensitic Steel [All samples were welded with the established welding parameters for Material D. Zero-temper welds (DIQ) were tested as welded with no additional tempering step. Medium-temper welds (DIM) were quenched for 46 cycles and tempered for 57 cycles at 55% of the expulsion level for the material. Full-tempered (DIF) welds were quenched for 46 cycles and tempered for 90 cycles at 55% of the expulsion level for the material.]

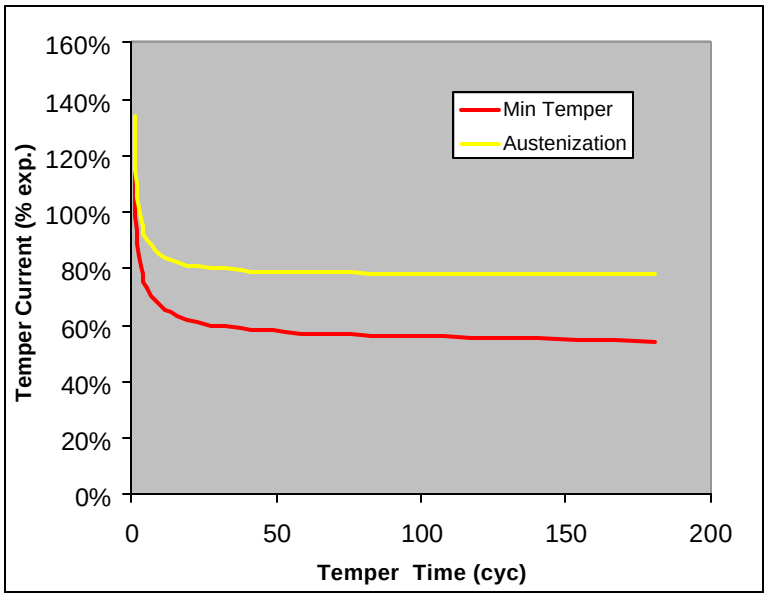

Figure 29. Predicted Temper Diagram of the 0.83-mm (0.033-in.) Dual-Phase Steel [Upper and lower bounds are predicted from equations defining, alternately, minimum temper requirements (lower bound) and the austenization temperature (upper bound) as described in the report. Equations have been scaled to match the experimentally defined temper diagram.]

Development of Appropriate Resistance Spot Welding Practice for Transformation-Hardened Steels

Wayne Chuko and Jerry Gould
EDISON WELDING INSTITUTE
1250 Arthur E. Adams Drive
Columbus, OH 43221

1.0 Introduction

In 1998 the first version of the Steel Technology Roadmap mapped out a vision for the U.S. steel industry of the future. From this, it was clear that the steel industry of the future would need to be responsive to the ever-changing demands of its customers. Constant innovation, such as advances in steel-making technology that allow for faster response and newer grades of steel would be necessary to allow continued dominance in the industry.

Governmental pressure on the U.S. automotive industry to produce vehicles with higher fuel efficiency and lower emissions has led to large-scale efforts to reduce the weight of the vehicles. To date, steel has maintained the position as the material of choice in the automotive industry. Qualities such as strength, recyclability, and affordability help to keep it there. However, increasing competition from non-ferrous alternative materials continues to threaten that position. In addition, current overcapacity in the automotive industry combined with increasing foreign competition will ultimately drive down auto prices. This, in turn, will cause the automakers to reduce their costs. Cost-cutting measures will include designing on more global platforms and reducing development time for lower production vehicles. As a response to this, the steel industry is attempting to promote R&D that will help reduce manufacturing costs and keep capital expense at a minimum. This will allow the U.S. auto companies to remain profitable at lower prices and lower unit sales.

The UltraLight Steel Auto body (ULSAB) consortium was formed for the purpose of creating a stronger and lighter steel auto body that will help to allow the U.S. automakers achieve their necessary goals while still maintaining the dominance of steel in the industry. Results from the project allow for a 25% weight reduction of the body-in-white structure. This initial design relies heavily on newer alloys of high-strength steels (HSS) and more recently, advanced high-strength steels (AHSS). These steels offer greater strength in lighter gauges. This combination allows for better steel performance while reducing weight of the structure. However, these steels do come with their own fabrication concerns. In order to successfully put the new design into production, several fabrication issues must be resolved.

As part of the 1999 AISI/DOE research solicitation, EWI was selected to address a specific concern with resistance spot welding (RSW) of transformation-hardened high strength steels (HSS) known as hold-time sensitivity (HTS).[1] This report presents the results of investigations on in-process heat-treating as a method of reducing HTS in AHSSs.

2.0 Background

RSW has been and will continue to be the preferred joining method when considering HSS and AHSS in the automotive industry. Reliability, economy, and versatility of the process, regarding performance in automotive fabrication make it the most widely used welding process. Although RSW has proven successful with mild steels, and much is known about the process, the widespread implementation of HSS and particularly AHSS depends on further RSW research.

The AHSSs, also known as transformation-hardened steels, include three basic types. These are dual-phase, TRIP, and martensitic steels. Increased levels of C and Mn along with complex thermal processing, allow for complex, multi-phase microstructures that achieve much higher strength levels while still maintaining a level of formability.

HTS, as mentioned earlier, is a specific concern when spot welding steels containing higher levels of C and Mn. Typically, HTS shows up during peel testing (the accepted method for production testing spot welds). Hold time is typically used to allow the weld to solidify under full electrode force. For hold time-sensitive steels, welds made with a short hold time (<5 cycles) fail with a full-button morphology, while those made with a more typical hold time (30 to 60 cycles) fail interfacially. Reasons for this phenomenon include, stress state of the weld, formation of a susceptible microstructure, and preferential crack paths.[1] HTS and the causes for it, as well different types of HSS, are discussed in greater detail in Appendix 1 ("Development of Appropriate Resistance Spot Welding Practice for Transformation-Hardened Steels – Phase 1: Development of Temper Diagrams").

2.1 Development of Temper Diagrams

The 2-year project, "Development of Appropriate Resistance Welding Practice for Transformation-Hardened Steels," was proposed to investigate the benefits of in-process RSW heat treating on HTS in transformation-hardened steels. Two gauges of both dual-phase and martensitic steels were investigated. The first year of the project was focused on in-process quench and tempering of the spot welds. The basis for the direction of the project came from previous studies by Edison Welding Institute (EWI) regarding HTS and quench and tempering effects.[2] In Phase 1, individual quench and temper diagrams were developed for each steel

involved in the project using a methodology previously developed during EWI cooperative research (Appendix 1).

In brief, sets of welds were in-process tempered using a matrix of times and currents. Hardness testing on the surface of the welds was then used to obtain quantitative data relating to the degree of tempering achieved. The hardness data were then plotted as a function of temper time and temper current using a two-dimensional contour plot. This plot illustrated the effectiveness of tempering on weld hardness. In addition, results from destructive peel testing were overlaid onto the plot for the purpose of correlating weld failure mode with weld hardness and temper schedule. After completing the temper processing maps, additional representative welds were made using temper conditions from selected areas of the plot. These welds were then subjected to mechanical testing and metallurgical examination. Results were then related back to the processing maps and conclusions were drawn as to the effects of in-process quench and tempering on HTS and weld performance.

From this analysis, two distinct regions of these curves were defined. The bulk of these diagrams constituted a C-curve, analogous to isothermal tempering response. In addition, a transient region was identified, that tended toward shorter temper times at higher currents. Effective tempering was observed in the C-region of the curve after 16 to 32 cycles of temper time. The maps also showed that there was potential for much shorter effective temper times by “spike tempering” using very high currents. Effective tempering, using the spike-tempering method, could theoretically be achieved after only 1-5 cycles of tempering. Further detail on this study is presented in Appendix 1.

2.2 Phase 2: Evaluation of Post-Weld Cooling Rate Techniques

The workscope for the second year of the project was to include evaluation of alternative methods for reducing HTS. In the original workscope, downslope, and post-heat were to be investigated and compared for potential effectiveness in reducing HTS, as well as applicability in industry. After initial comparisons between the two, one method was to be chosen for further investigation, including development of processing maps in a similar manner to that used in Phase 1 for quench and tempering.

As a result of the Phase 1 quench and tempering work, spike tempering was defined as a third potentially effective and practical means of reducing HTS. Original tasks of Phase 2 were, therefore, modified to include spike tempering. The initial evaluation of post-heat, downslope, and spike tempering concluded that the most useful information could be gained by further investigating downslope during subsequent tasks of the project. A methodology, similar to that used in Phase 1, was then followed in Phase 2 for developing downslope processing maps for

each steel. As in Phase 1, mechanical testing and metallurgical examination were also used to evaluate the characteristics of welds subjected to downslope. The following report presents the methods used for developing the downslope processing maps and the results obtained from evaluation of welds made using the maps.

3.0 Approach

3.1 Materials and Equipment

All welding trials for the Phase 2 post-weld cooling diagram development effort were performed using the same equipment used for the Phase 1 quench and temper diagram development (Appendix 1). This included a 1ϕ, AC, Taylor Winfield 100-kVA, pedestal-type resistance spot welder equipped with an ATEK TruAmp V constant-current controller. As in Phase 1 current was monitored using the ATEK controller and verified using a Miyachi MM 121A Weldchecker current meter. Welding force was verified using an oil-filled Waka force gauge. Electrodes used for welding were of the same composition and geometry as those used in Phase 1. Electrode specifications used for each steel can be found in Table 1.

The steels selected for this study of post-weld cooling techniques included two gauges of 960-MPa (140-ksi) dual-phase steels and two gauges of 1380-MPa (200-ksi) martensitic steels. The gauge thicknesses were 0.83- and 1.55-mm (0.033- and 0.061-in.) for the dual-phase, and 0.94- and 1.58-mm (0.037- and 0.062-in.) for the martensitic steels, respectively. Nominal chemical composition of the dual-phase steels was 0.15C, 1.4Mn, 0.32Si. Nominal chemical composition of the martensitic steels was 0.19C and 0.46Mn. The compositions and thickness of each steel are presented in Table 2.

3.2 Comparison of Downslope, Post-Heat and Spike Tempering

As mentioned, Phase 1 of this project examined in-process quench and tempering, and its effect on HTS. From that research, spike tempering was defined as a potential method of quench and tempering that could reduce HTS of a spot weld in transformation-hardened steels. Controlled cooling methods such as downslope and post-heat are other known methods of alleviating HTS. Initially, the three methods were examined on a macro level for each material using series of iterative welding trials.

For each steel, the current necessary to achieve a 4$\sqrt{t}$ nugget size was first verified against that found in Phase 1 (Appendix 1). This was achieved by running current ranges using a 5-cycle hold time and no additional post-weld heating. The minor diameter of the resulting nugget was then measured using knife-edge calipers. Ten welds at the 4$\sqrt{t}$ current were made and averaged together for determining the nugget size. All welds for the current ranges, as well as

those used in subsequent tasks, were made on 38- × 100-mm (1.5- × 4-in.) coupons. A shunt weld was made first followed by a second (test) weld. After establishing the weld current, additional welds were made with included in-process downslopes, post-heats, or quench and spike tempers. Each post-weld heating application was followed by a 200-cycle hold time under full welding force.

Downslope times for the weld trials were varied from very short (2 to 5 cycles) to long (60 to 90 cycles). Downsloping was done in a linear fashion starting at the respective 4√t welding current (Iweld) for each steel, and ending at varying currents expressed as a percentage of Iweld. For the range of downslope currents and times, weld schedules were recorded, and each weld was subjected to destructive peel testing. The goal of the iterative trials was to establish some level of effectiveness of downslope. This was done based on nugget failure morphology, examining the degree of interfacial failure.

Post-heat iterative trials were run in a similar manner. Immediately following the welding pulse, a constant additional current was applied for varying lengths of time (no quench time). As with downslope, varying levels of post-heat current were applied for times ranging form short (2 to 5 cycle heating times) to much longer (60 to 90 cycles). The resulting welds were again subjected to destructive peel testing. The goal of the post-heat iterative trials was again to attempt to find a combination of current and time allowing avoidance of interfacial failures.

Spike tempering, as defined in the earlier research, is the immediate in-process quenching of a weld to martensite followed by a short-duration, high-current pulse for the purpose of tempering the martensitic microstructure. Effectiveness of spike tempering was evaluated by first verifying the short time regions of the general quench and temper plots previously defined in Phase 1 (Appendix 1). Each spike-temper weld trial was again subjected to destructive peel testing.

Peel test results from the downslope, post-heat, and spike-temper samples were individually plotted for each steel as a function of time and current. The presence of interfacial weld nugget failure or full-button failure served to define the range of effectiveness for each method of post-weld processing. Results from Phase 1 (Appendix 1) showed that peel test results were much more discernable when studied in conjunction with hardness testing results. Therefore, in addition to peel testing, surface hardness testing was also utilized. A significant reduction in surface hardness (as compared with that of a quenched weld) was then used for determining the range of effectiveness of the post-heat process. Prior knowledge gained in Phase 1 (Appendix 1), along with the comparison of the nugget morphologies, were used to determine the method of post-weld processing that would be most suitable for further examination.

3.3 Development of Downslope Diagrams

The comparison of post-weld heating methods concluded that the downslope method of post-weld heating would be most readily applicable in manufacturing. A description of this comparison is presented in the "Results" section found later in this report. After determining that downslope should be the post-weld processing method for further examination, development of detailed downslope processing diagrams began. The methodology used for developing the downslope diagrams was similar to that used in the previous development of quench and temper diagrams, and included the following steps:

(1) **Current-Range Evaluations.** Steels were first subjected to current-range testing as per Ford Motor Company Specification BA 13-4.[3] This was done to establish the base (expulsion) current and 4v t welding current for the downslope diagram development. This relatively small weld size was selected, as small welds are typically more susceptible to HTS.

(2) **Welding Trials.** Welds were then made over a range of downslope currents and times. Weld samples were configured as standard peel test coupons, including both a shunt weld and a test (second) weld. All subsequent evaluations were done on the test weld of the coupon.

(3) **Initial Downslope Diagram Matrix.** A broad approximation of the downslope characteristics of each material was made using variations of downslope time from 0 to 90 cycles. Downsloping was done in a linear fashion, starting from the welding current and ending at a current expressed as a percentage of the welding current. The downslope end currents were varied from 100% down to 30% of the welding current. Following the predetermined downslope time, the weld was held under full electrode force for 300 additional cycles without additional current. One test coupon was made at each of these combinations of downslope end current and time.

(4) **Hardness Testing.** Hardness testing was done on the exterior weld surface, at the center of the electrode contact area. If electrode indentation into the test coupon was observed, one surface of each sample was ground flat before hardness testing. On each sample, a single Rockwell C (Rc) hardness indent was made. The resulting hardness readings were used for the subsequent contour plots.

(5) **Preliminary Contour Plotting.** Rc hardness values were then presented as a two-dimensional contour plot with downslope end current as the vertical axis, and downslope time as the horizontal axis. This preliminary contour plot allowed critical areas of the diagram (where hardnesses changed most radically as a function of terminal temper currents and times) to be identified.

(6) **Diagram Refinement Trials.** Based on these initial results, additional trials were performed using downslope times and end currents that fell within the critical areas of the preliminary plot. These trials served largely to refine the most effective areas of downslope softening. Resulting welds were prepared and hardness tested in the fashion described in Step 4 above. They were then added to, and used to refine the resulting downslope diagram. For these trials, three samples were made at each combination of downslope end current and downslope time. Surface hardness measurements from each sample were then averaged for inclusion in the final diagram.

(7) **Preparation of Final Downslope Diagrams.** Downslope diagrams were then prepared using a SigmaPlot 2000® contour-plotting package. This package allowed some averaging of the data. This was used, as scatter is inherent with most hardness testing. As mentioned, final downslope diagrams took advantage of the results from both the preliminary and refinement tempering trials.

3.4 Weld Property Evaluation

Using the processing maps, specific downslope current levels resulting in the greatest change in surface hardness were selected. Using this final current, three downslope times representative of no downslope effect, medium effect, and maximum effect were used. Series of additional welds were then made for further evaluation. Destructive peel testing, metallography, and mechanical property testing were all performed on these welds in a similar manner as that described in the Phase 1 effort (Appendix 1). These results were then related to the downslope diagrams in order to further define the effectiveness of downsloping for reducing HTS.

4.0 Results

4.1 Comparison of Downslope, Post-Heat, and Spike Tempering

Currents necessary to achieve a 4vt button size were verified by performing current range evaluations for each material. Both the current necessary to achieve the 4vt button size and the maximum current attainable before expulsion (expulsion level) were found to be similar to those used in Phase 1 (Appendix 1). The 4vt welding currents and expulsion level currents used during the post-weld heat comparisons are presented in Table 2, along with other critical operating parameters. Of note here are the long (200-cycle) hold times. In initial trials, it was determined that longer downslope times with higher end currents caused considerable heating of the base metal, to the point where a 60-cycle hold time might be insufficient to cool the weld and the heat-affected zone (HAZ) past the critical transformation temperature. For this reason, hold time was increased to 200 cycles for all subsequent post-weld heating trials.

4.1.1 Preliminary Downslope Results

Preliminary downslope results for the 0.83-mm (0.033-in.) dual-phase steel showed that short downslope times regardless of downslope end current resulted in interfacially failed welds. Using a downslope end current of 50% Iweld, the welds failed with a full-button morphology after 30 cycles of downslope time. Using long times and lower end currents again resulted in interfacial failures. These downslope trial results are presented graphically in Figure 1(a).

Preliminary downslope trial results on the 1.55-mm (0.061-in.) -thick dual-phase steel suggested similar trends to the 0.83-mm (0.033-in.) –thick dual-phase steel. Results from these initial downslope weld trials are presented graphically in Figure 2(a). The plot suggests that welds made with lower end currents, and shorter downslope times tended to show partial interfacial failures. Alternatively, those at higher end currents and longer times tended to show button-type failures. A line of separation, extending from 100% end current and 10 cycles of downslope time, to 0% end current and 60 cycles of downslope time, appeared to differentiate these two regions.

Downslope trials for the martensitic steels were carried out in a similar manner. In addition to peel testing, surface hardness testing was also used for assessing the effectiveness of downslope current. Results from the thin 0.94-mm (0.037-in.) martensitic steel trials are presented in Figure 3(a). These results showed that when using a downslope end current of 50% Iweld, softening first started to occur after 30 cycles, and significant softening was present at 99 cycles of downslope time. Peel testing of these samples resulted in predominantly full

buttons, although a few partial interfacial failures were recorded for slow cooling rates (associated with long downslope times).

Contrary to the 1.55-mm (0.061-in.) dual-phase steel, the 1.58-mm (0.062-in.) martensitic steel tended to show partial interface failures at higher end currents and longer downslope times. The changeover from button to partial interfacial failure occurred across a locus of end currents and temper times extending from roughly 80% Iweld, 10 cycles of downslope time, to 0% Iweld, 50 cycles of weld time. This change in failure mode appeared essentially co-committant with a drop in the weld hardness. Relationships between reduced weld hardness and interfacial failure on martensitic steels were discussed thoroughly in the Phase 1 report (Appendix 1). The results here are consistent with those observations. Results from the trials on the 1.58-mm (0.062-in.) martensitic steel are presented in Figure 4(a).

4.1.2 Preliminary Post-Heat Trials

As mentioned above, post-heat was also studied as a method for effectively slowing the weld cooling rate, and reducing HTS. Post-heating refers to a second, contiguous current pulse, immediately following the weld pulse. Both post-heat time and current level were varied until a noticeable change in button morphology or surface hardness was noted.

The post-heat weld trial data for the 0.83-mm (0.033-in.) dual-phase steel are presented in Figure 1(b). Peel tests with a 100% post-heat of the welding current resulted in a change from partial interfacial failure to full-button failure around 5 cycles of post-heat time. Using a post-heat of 83% Iweld resulted in a change in failure mode after 15 cycles of post-heat time.

Results from the post-heat weld trials for the 1.55-mm (0.061-in.) dual-phase steel are presented in Figure 2(b). Post pulses at or above the baseline welding current resulted in full buttons on peel testing. This high current also resulted in excessive heating and weld indentation. When dropping the post-heat pulse to 90% Iweld, interfacial failures were observed out to 80 cycles of post-heat time.

Results for the post-heat trials using the 0.94-mm (0.061-in.) martensitic steel are presented in Figure 3(b). Again, hardness measurements, along with peel testing, were used to evaluate welds on the martensitic grades of steels. Here, weld samples failed almost exclusively by button peel. It is also of note that some hardness reduction occurred after 40 cycles of post-heat (at 60% Iweld).

Results from the 1.58-mm (0.062-in.) martensitic steel are shown in Figure 4(b). In these trials nearly all the welds failed either partially or fully interfacially. Changes in surface hardness

measurements were first noted using a post-heat of 86% Iweld after about 40 cycles of post-heat time. At this point the surface hardness measurement was around 33 vs. 35 to 37 Rc for an as-quenched weld.

4.1.3 Spike Tempering

Iterative trials using the spike-tempering method were performed while taking into account the quench and temper maps produced in Phase 1 of the project. The maps from Phase 1 showed that effective tempering occurred toward high currents and at short temper times (after quenching). This part of the curve was verified for each material using specific currents expressed as a percentage of the expulsion current. The full quench and temper processing maps for each material are presented in Figures 1-4 of the Phase 1 report (Appendix 1).

Results for the spike-tempering evaluation are presented in Figures 1(c)-4(c). In the case of the dual-phase steels the peel test nugget morphologies matched up well with the spike-temper region defined in Phase 1 (Appendix 1). Selected currents and times yielded buttons and interfacial failures in the areas predicted using the original quench and temper diagrams. Again, as with the other post-weld processing evaluations, surface hardness measurements were made on the martensitic steels before peel testing. The change in surface hardness for both the thin and thick martensitic steels also corresponded well with the original quench and temper diagrams. As with the other methods described above, weld nugget failure morphology for both the martensitic steels was more difficult to discern.

4.1.4 Consideration of the Downslope Method

As mentioned, the objective of the preliminary trials was to gain a general understanding of the effectiveness of some candidate methods on reducing HTS, in order to determine which one offered the most potential for further development. Both downslope and post-heat showed promise in controlling the cooling rate of the weld, to the point where weld failure mode changes were observed. While weld failure modes were inconsistent on the martensitic steels, they corresponded with observed reductions in surface hardness.

Alternatively, weld trials using the quench and spike-temper method verified the region of the quench and temper diagrams (developed in Phase 1 – Appendix 1) that tended toward high currents and short times. Again, a clear transition from partial or full interfacial failure to full-button morphology can be seen across that region of the diagram in dual-phase steels, while a corresponding change in surface hardness can be seen in the martensitic steels.

It is of note, however, that during the post-heat trials significant material deformation (due to electrode indentation) occurred for the longer post-heat times and high currents necessary to affect weld failure morphology. Excessive indentation of the material is generally considered undesirable. In contrast, downslope achieved the desired weld softening and weld failure mode with better consistency and without adverse effects on the surface of the steel. Spike tempering was effective as defined by the Phase 1 quench and temper diagrams (Appendix 1). However, toward higher current levels, expulsion and some surface indentation were again observed. (This, however, was not observed using lower, but still effective, spike-tempering currents.)

From the iterative trials, results showed that either downsloping or spike tempering showed the most promising effects on nugget failure mode and surface hardness without excessive surface deformation. Since spike tempering had been documented, although not completely refined, in Phase 1, downsloping as a method of controlling HTS was further pursued in this study. Downslope, controlling cooling rate of the weld, takes a contrasting approach toward HTS versus quench and tempering. By further investigating downslope, additional information on the spot welding response of these steels could be obtained. This would also serve to allow for a comparison and discussion of the effect of controlled cooling versus quench and tempering on HTS.

4.2 Downslope Diagrams

Downslope diagrams for the four steels included in the program were developed following the methodology outlined in the “Approach” section of the report. As previously described, two-dimensional contour plotting was used to present surface hardness values of the welds as a function of downslope time and downslope end current. Weld failure modes during peel testing were then superimposed upon the contour plot. The individual downslope diagrams are presented in Figures 5-8.

In these plots, Rc hardness measurements for welds made at specific sets of downslope conditions were averaged together. These average hardness values were then used to construct the contour plot. These average values are indicated above the weld locations on the diagram. The average hardness values at each downslope condition are also presented in Tables 3-6. Differentiating lines on the contour plots were incremented in steps of one Rc point. These steps are indicated by a color scale ranging from red (highest values) to dark blue (lowest values), and are also outlined by dotted lines.

For each steel studied, surface hardness values showed a gradual decrease with longer downslope times and lower downslope end currents. Significant softening (defined by a drop in

hardness of approximately five Rc points) occurred after approximately 60 cycles of downslope time for the thin steels, as compared with 40 to 50 cycles for the thick steels.

Typically, the thin steels showed softening effects at higher percentages of the welding current compared to the heavier-gauge steels. Significant softening for the thin, dual-phase steel occurred at approximately 80% Iweld and occurred for the thin martensitic steel at approximately 60% Iweld. Significant softening for both of the thick steels occurred around 40 to 50% Iweld. These downslope end currents, along with the previously discussed downslope times, defined the nose of a "C"-shaped curve, outlining the region of significant softening.

Although all downslope maps showed the characteristic C-curve described above, there is evidence on some of the plots of a "double nose." This is most clearly seen on the 1.55-mm (0.061-in.) dual-phase steel (Figure 6), and the 0.094-mm (0.037-in.) martensitic steel. Similar double-nose curves were not observed on the other two downslope diagrams.

As mentioned previously, weld failure modes on peel testing were superimposed on the downslope diagrams for the purpose of correlating hardness values with failure mode. The peel test results are also presented in Tables 7-10. Failure modes in the 0.83-mm (0.031-in.) dual-phase steel were mostly full buttons, regardless of the hardness value (only a few instances of interfacial failure occurred). These interfacial failures were located in the hardest areas of the plot. Similarly, failure modes in the 0.94-mm (0.037-in.) martensitic steel were also biased toward full buttons. However, a locus of interfacial failures occurred toward long downslope times and very low-end currents. In relation to the contour plot, this locus of points was located directly under the region of significant softening.

In the thicker sections of steel, the occurrence of interfacial failures was much more frequent. The 1.55-mm (0.061-in.) dual-phase steel showed that in the harder regions of the plot, weld failure mode was fairly evenly distributed between full buttons and interfacial failures. The region of (significant softening where hardness dropped five or more Rc points due to downslope) seemed to be outlined by predominantly full-button failures.

Similar to the 1.55-mm (0.061-in.) dual-phase steel, the 1.58-mm (0.063-in.) martensitic steel also showed a fairly even occurrence of interfacial failures and full-button failures in the regions of the plot where no softening occurred due to downslope. In contrast to the 1.55-mm (0.061-in.) dual-phase steel, the area of the plot that defined the beginning of significant softening seemed to be surrounded by interfacial failures. Welds that experienced maximum softening due to downslope predominantly failed with full-button morphologies.

4.3 Metallographic Examinations

Metallographic cross sections for the four different steels, each with the three respective downslope conditions, are presented in Figures 9-20. Accompanying each micrograph are a pair of hardness profiles, one transversing the weld, and one taken in the through-thickness direction. These hardness profiles have been scaled to match the geometry of the weld as presented in the micrograph.

The cross sections and hardness traverses generally indicate five distinct microstructural regions in the weld structure. These regions include:

1. Fusion zone
2. Fully re-austenized zone
3. Partially re-austenized zone
4. Heat-affected base metal
5. Base metal.

The fusion zone, located at the center of the cross section, is the weld nugget itself. Surrounding and containing the fusion zone is the fully re-austenitized zone. This zone is light in color, and based on the hardness plots is fully martensitic. Adjacent to the fully re-austenitized zone is a band of partially re-austenitized ($a+\gamma$) material. This zone etched relatively darkly, and is identified in the hardness traverses by the steep reduction in hardness values. The heat-affected base metal is exterior to the partially re-austenitized zone, and is characterized by an apparent drop in hardness. The base metal is then exterior to the heat-affected base metal. The five zones are present in varying degrees for each steel and downslope condition.

Microstructural characteristics of the 0.83-mm (0.033-in.) dual-phase steel welds are similar regardless of the downslope condition. The five distinct microstructural zones are visually present in each of the cross section macrographs. Hardness values through the weld area in both directions suggest the re-austenitized region is fully martensitic. This region also appears to extend fully to the electrode-sheet interface(s). It also appears that the partially re-austenitized ($a+\gamma$) region increases in thickness with increasing downslope times. This increase in thickness correlates with the through-thickness hardness traverse by an apparent softening near the electrode-sheet interfaces.

Consistent with the results for the 0.83-mm (0.33-in.) dual-phase steel, the 1.55-mm (0.061-in.) dual-phase steel also shows similar microstructural characteristics for different downslope times. As with the 0.83-mm (0.033-in.) dual-phase steel, the hardness profiles suggest a fully

martensitic re-austenitized zone, surrounded by thin band of softer partially re-austenitized material (a+γ region). This region experiences an apparent increase in thickness with slower cooling rates. Unlike the thin, dual-phase steel there is a region of heat-affected base metal adjacent to the electrode-sheet interface for each downslope condition.

Like the dual-phase steels, the 0.94-mm (0.037-in.) martensitic steel has an apparent martensitic re-austenitized zone for all downslope times. This re-austenitized zone again appears to extend fully to the electrode-sheet interface(s). The partially re-austenitized (a+γ) zone also shows an apparent coarsening with increasing downslope time. This area is also identifiable in the through-thickness traverses as it corresponds to an increase in HAZ softening near the electrode-sheet interface(s) of the weld.

Microstructure of the 1.58-mm (0.062-in.) martensitic steel is again similar for the three different downslope times. As with the other steels, the re-austenitized zone appears to be fully martensitic. The partially re-austenitized zone is present in all three samples, and becomes more defined with longer downslopes. Similar to the thick, dual-phase steel, there is also the presence of a heat-affected base metal layer at the electrode-sheet interface. Softening in the heat-affected base metal appears to increase with increasing downslope times. This is apparent in the transverse hardness profiles.

4.4 Mechanical Testing

As mentioned previously, samples for mechanical evaluations were made using the short, medium, and long downslope schedules for each respective material. Weld schedules for the three downslope conditions are presented in Table 11. Five samples were made for each material, downslope condition, and type of mechanical test. These mechanical tests include lap-shear, tensile-fatigue, cross-tension, and cross-impact testing. Test coupons were prepared, and mechanical tests carried out in a similar manner to that described in Phase 1 (Appendix 1).

Peak lap-shear tensile-strength measurements are presented in Tables 12-15 and plots of the average values are presented in Figures 21-24. These results suggest that lap-shear strength increased with increasing thickness and base metal strengths; however, that the effect of the specific downslope conditions was minimal. The dual-phase steels had the largest range of strengths for the various downslope conditions. In the 0.083-mm (0.033-in.) sections, average peak strength ranged from 9.06 kN (2036 lb) with the short downslope time, to 10.15 kN (2281 lb) with the medium downslope time, to 7.87 kN (1769 lb) with the long downslope time. The average 1.55-mm (0.061-in.) dual-phase strengths were 18.42, 17.96, and 19.31 kN (4140, 4035, and 4340 lb) for the short, medium, and long downslope conditions, respectively. Values for the martensitic steel samples were much tighter in range. Average peak lap-shear strengths for the

0.94-mm (0.037-in.) samples were 10.55, 9.99, and 10.48 kN (2370, 2245, and 2355 lb) for the short, medium, and long downslope conditions. Average peak lap-shear strengths for the 1.53-mm (0.062-in.) samples were 21.98, 21.14, and 21.40 kN (4940, 4750, and 4810 lb) for the short, medium, and long downslope conditions, respectively. Failures in these tests were almost exclusively interfacial/shear types. The only exception was for the 0.83-mm (0.033-in.) dual-phase steel welded with the intermediate downslope time. In this case all failure modes were by button peel. This mode of failure also corresponded with the highest average lap-shear strengths for this material.

Tension shear fatigue life tests were carried out for each material and downslope condition. The load-life (S-N) curves were nominally run for fatigue lives of 10^3-10^7 cycles. Families of curves for the three downslope conditions were then plotted on separate plots for each material. The results are presented in tabular form in Tables 16-19 and in graphical form in Figures 25-29. The specific downslope schedule had little significant impact on fatigue life as indicated by the data. In general, the martensitic steels had a longer fatigue life for a given load.

Cross-tension data, including peak loads to failure, average strengths, and failure mode are presented in Tables 20-23. The average values for each material and downslope condition are presented graphically in Figures 29-32. The 1.55-mm (0.061-in.) dual-phase steel resulted in the highest overall strengths during cross-tension testing. The 0.83-mm (0.033-in.) dual-phase steel resulted in the lowest overall values. As a general trend, downslope appeared to have only a minimal effect on the thin-gauge steels. Average peak load to failure for the 0.83-mm (0.033-in.) dual-phase steel ranged from 3.99 kN (896 lb) for the short downslope condition to 3.19 kN (717 lb) for the long downslope condition. Strength levels for the 0.94-mm (0.037-in.) martensitic steel ranged from 4.18 kN (940 lb) with a short downslope time to 4.01 and 4.03 kN (901 and 907 lb) using medium and long downslope times, respectively.

Strength levels for the heavier-gauge steels generally showed a slight improvement when exposed to longer downslope times. As with the thin steels, the effect of downslope was more pronounced in the dual-phase steel than in the martensitic steel. Average cross-tension strength of the dual-phase steel ranged from 6.6 kN (1483 lb) using the short downslope time to 7.32 kN (1644 lb) using the long downslope time. Average strength in the martensitic steel ranged from 4.72 kN (1061 lb) using short downslope time to 5.13 and 4.94 kN (1153 and 1110 lb) using medium and long downslope times, respectively.

Both dual-phase steels and the 0.94-mm (0.037-in.) martensitic steel showed in full-button failures regardless of the downslope schedule. However, the 1.58-mm (0.062-in.) martensitic steel showed in an improvement in failure mode at longer downslope times. It was observed that with short downslope times, four out of five samples failed interfacially. However, using

medium downslope times, four out of five samples failed with a full-button morphology, where as samples exposed to a long downslope time all resulted in full-button failures.

Cross-tension impact results are shown in Tables 24-27. Absorbed energy and failure mode for each weld tested are presented in these tables. Average impact energies are presented in Figures 33-36. The results from the cross-tension impact tests showed that the 1.55-mm (0.061-in.) dual-phase samples absorbed the most energy [around 90 to 110 J (66 to 81 ft-lb)]. The other three materials resulted in cross-impact energy absorption levels around 45 to 60 J (33 to 44 ft-lb).

5.0 Discussion

5.1 Down-Selection of a Post-Weld Heating Method

In this study, three in-situ methods were initially evaluated for reducing weld metal hardness. These included downsloping, post-heating, and spike tempering. Downsloping and post-heating are essentially ways of reducing the cooling rate in the weld, promoting austenite decomposition modes which result in microstructures of reduced hardness and higher toughness (compared to the typically formed martensite). Spike tempering is an approach first identified in the Phase 1 work (Appendix 1). Spike tempering allows the weld to quench to martensite, and provides a short (1-3 cycles) current spike (typically higher than the welding current) to temper that martensite. This pulse effectively tempers the weld, again reducing material hardness and increasing toughness.

Initial surface hardness evaluations suggested all methods offered some potential. However, with respect to those methods attempting to reduce local cooling rates, downsloping appeared to give the most consistent results. It is of note that spike tempering appeared to offer the most affective softening with the shortest overall required welding cycle. However, the Phase 1 work already considered tempering approaches to reducing HTS, so it was decided here to evaluate the most promising cooling rate control method (downsloping) in greater detail.

5.2 Critical Cooling Rates for HSS Steels

Clearly, when resistance spot welding transformation-hardenable steels, local cooling rates define the local microstructure, as well as local properties. Cooling rates in resistance spot welds have been examined previously in the literature.[4-6] These works use numerical modeling to estimate cooling rates for some specific representative spot weld configurations. It is possible, however, to approximate such cooling rates in resistance spot welds using a simple one-dimensional thermal model.

For such a model, it is assumed that thermal losses to the surrounding steel are negligible, and all heat flow occurs from the steel into the contacting Cu electrodes. This assumption has been dealt with elsewhere.[4] It is also assumed that material constants do not vary with temperature. The governing equation for the temperature variations in the steel is then:

$$\frac{\partial^2 \Theta}{\partial x^2} = \frac{1}{a}\frac{\partial \Theta}{\partial t} \tag{1}$$

where $\Theta = T - T_o$, T_o is room temperature, x is the distance from the weld faying surface toward the electrode face, t is the time after termination of the weld current, and α is the thermal diffusivity of steel. This equation is solved by a separation of variables technique, where the resulting solution is the product of a sinusoidal term (accounting for positional related effects), and an exponentially decaying term (accounting for time-related effects). A reasonable assumption for the estimation of cooling rates is that temperature distribution in the steel at the instant current is terminated can roughly be described by a sinusoid, with peek amplitude at the weld faying surface, and a ¼ period equal to the sheet thickness. Using the above approximation, an expression presenting temperature as a function of position in the weld and time after termination of current can be obtained as follows:

$$\Theta = \left(\Theta_P - \Theta_E\right)\cos\left(\frac{p}{2\Delta x}x\right)e^{-\frac{ap^2}{4\Delta x^2}t} + \Theta_E \tag{2}$$

where Θ_P is the peak temperature in the spot weld, Θ_E is the temperature at the electrode-sheet interface (assumed to be constant in this part of the analysis), and Δx is the thickness of the sheet being welded.

The above expression, of course, assumes that the electrode-sheet interfaces remain at a constant temperature throughout the cooling cycle. This is clearly not the case, so to evaluate cooling rates over even moderate cooling times, an additional approximation must be made. Here, it is assumed that heat extraction through the electrode side of the electrode-sheet interface is much greater than that flowing from the steel side. Further, it is assumed that the thermal gradient in the electrode is linear, extending from Θ_E to the temperature of the cooling water (assumed to be room temperature for this analysis), over a distance of the electrode face thickness. This boundary condition can be summarized as:

$$\left.\frac{d\Theta}{dx}\right|_{x=\Delta x} = -\frac{k_E}{k_S}\frac{\Theta_E}{\Delta x_E} \tag{3}$$

where Δ_E is the thickness of the electrode face, and k_E and k_S are the thermal conductivities of the electrode material (Cu) and the steel, respectively. Combining Eqs. (2) and (3) above yields the following corrected expression for the variation in temperature in the steel spot weld:

$$\Theta = \Theta_P \frac{1+\left(\frac{2}{p}\right)\left(\frac{k_E}{k_S}\right)\left(\frac{\Delta x}{\Delta x_E}\right)\cos\left(\frac{p}{2\Delta x}x\right)}{1+\left(\frac{2}{p}\right)\left(\frac{k_E}{k_S}\right)\left(\frac{\Delta x}{\Delta x_E}\right)e^{\frac{ap^2}{4\Delta x^2}t}} \tag{4}$$

The resulting cooling plots, predicted by this equation for the two gauges of steels studied here, are presented in Figures 37 and 38. In these diagrams, the constants used in Eq. (3) are taken from standard reference documents.[7,8] Figure 37 presents the results for a nominally 0.8-mm (0.030-in.) -thick steel sheet. Peak temperature used here is 1725°C, and has been selected based on other, more detailed thermal modeling work.[4,5,9] These results show two factors of interest. First, cooling times for this gauge of steel are on the order of 10 cycles for all locations in the weld. This, again, is consistent with previous work.[4,5,9] Second, temperatures in the weld at the beginning of cooling (0 cycles cooling in Figure 37) range from near the $\gamma \rightarrow \gamma + \alpha$ phase field boundary, suggesting full austenization of the weld through thickness. The comparable plot for the nominally 1.55-mm (0.061-in.) steel is presented in Figure 38. Here, predicted cooling times are again consistent with previous modeling efforts,[4,9] on the order of 30 to 40 cycles. These, of course, are substantially longer than those for the thinner gauge steel presented in Figure 37. In addition, however, it is noted that temperatures in the extremities of the weld (approaching the electrode-sheet interfaces) are substantially cooler, reaching as low as 600°C. This, of course, is well below the A_3 temperature for the materials studied here, suggesting that the peripheral areas of the weld will not achieve even partial re-austenization and, therefore, not be subject to local martensite decomposition.

Cooling rates can be calculated by simply taking the partial derivative of Eq. (3) with respect to time. This new equation can be re-combined with Eq. (3) to yield cooling rates as a function of position in the weld, and temperature of that location. The resulting equation is:

$$\frac{\partial \Theta}{\partial t} = -\left(\frac{a p^2}{4\Delta x^2}\right)\left(\frac{\Theta}{\Theta_P}\right)\left(\Theta_P - \frac{\Theta}{1+\left(\frac{2}{p}\right)\left(\frac{k_E}{k_S}\right)\left(\frac{\Delta x}{\Delta x_E}\right)\cos\left(\frac{p}{2\Delta x}x\right)}\right) \quad (5)$$

This equation can be used to directly examine cooling rates for various locations in the weld for the critical 400 to 600°C temperature region. This is the region of austenite decomposition for these compositions of steels.[5,6] These results are plotted in Figures 39 and 40 for the 0.8- and 1.55-mm (0.030- and 0.061-in.) gauge materials, respectively. Again, these results are consistent with the limited published data presented elsewhere.[4-6,9] The results for the 0.8-mm (0.030-in.) steel show that natural cooling rates in this temperature regime range from roughly 8,000 to 14,000°C/s. In addition, cooling rates for the inner ¾ of the sheet thickness ($0 < x/\Delta x < 0.75$) are relatively constant, and fall with closer proximity to the electrode-sheet interface ($0.75 < x/\Delta x < 1$). The results for the 1.55-mm (0.061-in.) steel (Figure 40) show similar trends, though the magnitudes of the cooling rates are substantially lower. Here, cooling rates range from 2,000 to 4,000°C/s.

These "natural" cooling rates for spot welds in the gauges of steels studied can now be compared to recently developed CCT/TTT diagrams available for a wide range of very low-alloy steels.[6] These diagrams are based on both thermodynamic and kinematic calculations, and can be generated on-line at http://engm01.ms.ornl.gov. Appropriate diagrams for the dual-phase and martensitic steels examined in this study are presented in Figures 41 and 42. These diagrams suggest for the steels studied here, austenization temperatures are in the range of 930°C, with martensitic start temperatures of roughly 450 and 470°C for the dual-phase and martensitic steels, respectively. These diagrams suggest that austenite decomposition can occur, alternately, as ferrite + cementite, banite, or martensite, with progressively increasing cooling rates. Of note, are the critical cooling rates, taken from these diagrams for martensite formation. These critical cooling rates are measured as roughly 100 and 500°C/s, for the dual-phase steel and martensitic steel, respectively. Clearly, these critical cooling rates are dramatically lower than any of the predicted natural cooling rates for these spot welds, so martensitic transformation in the non-downsloped welds is inevitable.

5.3 Microstructural Observations in Downsloped Spot Welds

The first implication of the modeling results presented above is that the extent of the weld that exceeds the A_3 temperature and, thus, has the possibility to form martensite on cooling, is a strong function of the thickness of the steel itself. The model predicts that the nominally 0.8-mm (0.030-in.) steels will see electrode-sheet interfacial temperatures in the 800-900°C temperature

range, suggesting nominally through thickness martensite (or other decomposition products). This, in fact, appears to be the case. 0.8-mm (0.030-in.) welds made with short (5-cycle) downslope times on both materials showed a through-thickness martensitic structure, with the exception of possibly a band of partially austenized material directly against the electrode faces. Alternately, the models predict much lower temperatures at the electrode-sheet interfaces for the 1.55-mm (0.061-in.) steels, suggesting a significant band of retained ferrite adjacent to the electrodes. Again, this is clearly observed for both the dual-phase and martensitic grades of steels.

Degradation of the resulting austenite depends on the local cooling rate. The discussion presented above clearly shows that the natural cooling rates for spot welds studied here are on the order of 5 to 20 times the rates necessary to form martensite. Therefore, any possibility of reducing cooling rates rest solely in the details of the downsloping conditions used. Further, at the termination of the downslope current, cooling rates will default to the natural values defined by the cooling capability of the electrodes. This suggests that to accomplish softening by downsloping, conditions must be selected to intersect the nose of the CCT/TTT curves before termination of the downslope current. Examination of the CCT/TTT curves for the dual-phase steel (Figure 41) suggests that the minimum downslope time to prevent martensite formation is about 10 s. Clearly, such downslope times were not employed in this study, so avoidance of martensite formation in austenitized regions of these welds was impossible. This is reflected in both the micrographs and hardness profiles of the various dual-phase steel welds made, which in all cases show characteristic martensitic structures and hardnesses.

Examination of the CCT/TTT curves for the martensitic steel show a minimum downslope time to prevent martensite of roughly 1.5 s. In this case, downslope times were extended to roughly this time. Correspondingly, welds made in both gauges, but with less than 99 cycles of downslope, showed the characteristics of martensitic prior austenite regions. There is some indication in the hardness profiles and etching behavior of the welds made with 99 cycles of downslope, that the structure is not fully martensitic. This is consistent with the 1.5 minimum downslope time described above.

Note should be taken of the microstructures adjacent to the electrode-sheet surfaces in these welds. As mentioned above, these regions often did not achieve sufficient temperature to form austenite and, therefore, were not necessarily subject to martensite transformation on cooling. Depending on peak temperature achieved, these microstructures may be a mixture of ferrite + cemente ($T < A_1$) or ferrite + austenite ($T > A_1$). The hardness profiles suggest these regions are relatively soft (200-300 HV) and probably represent an over-aged base metal microstructure. Certainly, the hardnesses measured in these regions are consistent with the respective over-aged base metal observed in the transverse hardness profiles.

5.4 Applicability of the Derived Downslope Diagrams

It is clear from the discussion above that all the resistance spot welds examined in this study, regardless of the downsloping conditions used, have transformed to martensite. However, this is obviously not reflected in the temper diagrams, which indicate significant softening for selected downslope conditions. Further, in comparing the diagrams for the various steels, three features stand out:

(1) Peak hardnesses are about 5-10 R_C lower for the heavier-gauge steels. This is true even though the underlying weld hardnesses (for the dual-phase and martensitic steels, respectively) are identical.

(2) The kinetics of softening for all four configurations (gauges and steel types) is similar.

(3) An "upper current shelf" is apparent, above which no softening can be achieved regardless of downslope time.

To better understand these diagrams, it is first necessary to remember that the hardnesses reported are based on surface measurements. These measurements, by their nature, preferentially sample the microstructure on the free surface. As the underlying microstructures of these welds appear to be invariant (over the downslope conditions used), the measured changes must relate to the apparent un-transformed or partially transformed microstructures adjacent to the electrode-sheet interfaces. These regions are most clearly observable in the heavier-gauge steels. Such un- or partially transformed regions were also predicted from the thermal modeling results. In fact, the relative thickness of these layers is apparently the root cause of the lower measured peak hardnesses for these steel samples. The thermal modeling results also suggest such un-transformed regions on the thin-gauge steels, and these are occasionally observed in the micrographs.

Softening in these regions is believed to be largely associated with that part that is two-phase, austenite + ferrite at peak temperature. These areas are relatively easy to identify in the micrographs, as they etch relatively darkly. These regions contain grains of both ferrite and enriched austenite, which on quenching become ferrite + martensite. It is believed that the relative fraction of ferrite and austenite grains in this region can be affected by the local cooling rate, separately from how the cooling rate affects the martensite transformation. Presumably, with slower cooling, some austenite can back transform to ferrite (through growth of the stable ferrite grains) affecting the fraction of ferrite and martensite in the local structure. This, in turn, would have a direct impact on the measured surface hardness. Such back transformation is

both possible in two-phase structures, and kinetically advantageous over martensite decomposition for two reasons. First, growth of an existing ferrite grain can occur at temperatures well above the M_S temperature for these materials. Second, growth of an existing grain requires no nucleation event, the primary rate-limiting step in these reactions. The implication for these diagrams is many-faceted. For high downslope final currents, the temperature profile in the spot weld is invariant, so the fraction austenite in the two-phase region is fixed regardless of downslope time. In this case, the fraction of martensite (in the two-phase region) is fixed, so the hardness is invariant (and at a level consistent with no downslope). For extended downslope times and with reduced downslope current, back-transformation of austenite can occur, causing measurable surface softening. Where cooling rates are sufficient, however, (short downslope times, low downslope currents) back-transformation is limited, and softening does not occur. These events, in effect, define both the upper shelf of the downslope diagram, as well as the apparent C-curve profile of the diagram itself.

Again, while the diagrams do appear to reflect a change in surface hardness (at the electrode-sheet interfaces) this region is limited to a thickness of less than 200 μ, and can not be considered a measure of bulk metal, or weld, performance.

5.5 Microstructure-Mechanical Properties Relationships

As indicated above, microstructures in these welds are largely invariant over the ranges of downslope conditions studied. Not surprisingly, mechanical properties were also not noticeably affected by the various downslope conditions. Generally, mechanical properties were largely dependent on geometry. That is, in general, similar gauge materials had similar performance, regardless of strength level. The one exception was for the cross-tension results (both static and impact) for the 1.58-mm (0.063-in.) martensitic steel. This material showed both static and dynamic strengths similar to the lighter gauge steels. This is largely believed to be a constraint effect. This material combines the heaviest gauges with the highest strengths in the study. This results in the highest elastic stresses of all the configurations examined, and is more likely to promote brittle modes of failure. In fact, this was the only configuration that showed interfacial failures in the cross-tension tests.

5.6 Suitability of Downsloping for Production Spot Welding

The results above clearly show that downsloping times in the range of 0-100 cycles, is not an effective method for reducing hardness in the bulk of the weld, or for significantly modifying mechanical properties. To effectively modify the microstructures of the steels studied here, downsloping times ranging from roughly 120 cycles (martensitic steels) to over 600 cycles (dual-

phase steels) would be required. Given that these steels generally weld with roughly 10 to 20 cycles of weld time, these lengths of downslopes are considered excessive, and certainly not amenable to the high welding rates (up to 60 welds/s) used in automotive production today.

Clearly, downsloping did not provide the benefits in terms of reducing core weld metal hardness and interfacial failure as was observed for post-weld in-situ tempering in Phase 1 (Appendix 1). This is largely because the in-situ tempering was found to modify the weld microstructure, and impart a degree of improved toughness. Obviously, post-weld in-situ tempering is the preferable approach of the two methods studied.

One area only lightly addressed in these studies has been spike tempering. The results of Phase 1 suggested that given the kinetics of heating in the resistance welding machine, as well as that of the tempering response itself, that tempering could be done as a very short high-current pulse. The preliminary work described in this report suggests that tempering in the 1- to 3-cycle range can be done quite reproducibly. Based on the results of Phase 1 and Phase 2 investigations, spike tempering now appears to be the best compromise between effective improvement of resistance weld properties (for HSS) and cycle time. For example, for the 0.8-mm product, a proper weld cycle would include 10 cycles of weld time, 10-20 cycles of cool, and 2-3 cycles of temper. This suggests a total processing time of roughly 20-30 cycles, which is compatible with most production resistance welding systems. It is believed that spike tempering will also have a secondary advantage over other methods of reducing HTS. That is, heating times of such short duration tend to be adiabatic. This suggests that a much more uniform temperature distribution will be achieved on tempering, and not result in the gradations in microstructure observed with longer tempering times (Appendix 1). This should result in the most uniform distributions in microstructures in the resulting spot weld, and the most stable mechanical performance. For these reasons, it is believed that spike tempering should be the focus of any future work.

6.0 Conclusions

This report covers work conducted to investigate in-process methods of reducing HTS for resistance spot welds on a range of HSS. Specific steels examined in this study included both light- [nominally 0.8-mm (0.030-in.)] and heavy-gauge [nominally 1.55-mm (0.061-in.)] 980-MPa dual-phase and 1300-MPa martensitic grades of steels. In the final year of the program, the use of downsloping techniques has been studied. Work has included generating downsloping maps for each of the candidate steels (based on surface hardness measurements), and using these maps as a guideline for conducting both metallographic investigations and mechanical properties responses. First year work is shown in Appendix 1. Specific conclusions from the second year work are listed below:

(1) **Development of Downslope Maps:** Downslope maps based on surface hardness measurements were developed for each of the four configurations of steels studied. These maps all had a characteristic C-curve shape, with a nose of the curve occurring at roughly 40-cycles of downslope time.

(2) **Differences Between Maps for Various Gauges and Steels:** For a given gauge, base hardness (that without downslope) scaled with the strength of the base material. It was of note that non-downsloped hardnesses or the heavier-gauge steels were less than those for the thin-gauge steels.

(3) **Microstructural Observations in Downsloped Welds:** All welds were essentially martensitic, regardless of downslope condition. All heavy-section welds showed a transformation (ferrite + martensite) region adjacent to this martensitic core, with an apparently un-transformed ferrite region adjacent to the electrodes themselves. These additional microstructural zones were intermittently observed on the thin-gauge steels.

(4) **Mechanical Properties Variations for Different Downslope Conditions:** In nearly all cases, mechanical property response (tensile-shear, shear-fatigue, cross-tension, cross-tension impact) was only a function of material geometry, with no apparent influence of downslope. The thin-gauge materials essentially performed identically in all the mechanical tests. The same was generally true for the two thick-section steels. The only exception was for cross-tension testing (static and dynamic) the thick-section martensitic steel. In this case, the stiffness of the thick section and high tensile strength was thought to have an impact.

(5) **Predicted Variations in Temperature During Spot Weld Cooling:** A simple model was developed to predict cooling characteristics of spot welds as function of time and relative position in the spot weld. This model suggested that the thin-gauge steels were essentially fully austenitic (through-thickness) at peak temperature, resulting in the through-thickness martensitic microstructures observed. The thick-section steels showed surface temperatures well below the A_1 temperature, suggesting the surface layers of ferrite and ferrite + martensite transformation products observed.

(6) **Prediction Variations in Cooling Rate through the Austenite Decomposition Range:** Cooling rates for all the steels studied in the 400-600^{o}C austenite decomposition ranged from 2,000-14,000^{o}C/s without downslope.

(7) **Estimations of Critical Cooling Rates and Downslope Times Based on Available CCT/TTT Diagrams:** Available CCT/TTT diagrams show that minimum downslopes for avoiding martensite decomposition are roughly 2 and 10 s for the studied martensitic steels and dual-phase, respectively. These, of course, are longer than any of the downslope times used in this study.

(8) **Downslope Diagrams as a Measure of Surface Hardness Variations:** The presented downslope diagrams are apparently a measure of hardness variation in the ferrite and ferrite + martensite surface layers, rather than an indication of any underlying microstructure change.

(9) **Mechanism of Observed Softening in the Downslope Diagrams:** The softening observed in the downslope diagrams appears related to back-transformation of austenite to ferrite in the two-phase region of the microstructure (at or near the electrode-sheet interface) during reduced cooling associated with downsloping.

(10) **Suitability of Downsloping as a Means of Reducing HTS:** For the steels studied, downslopes ranging from a few to several seconds would be required to accomplish reductions in hardness and HTS. These times are an order of magnitude greater than that required to achieve current production rates.

(11) **Comparison of Downsloping as a Means of Reducing HTS:** Downsloping was not found to be an affective means for microstructural change. In-situ tempering was found to be effective; however, the best approach appears to be spike tempering. This approach has not been examined in detail, and should be considered in future work.

7.0 References

1. Gould, J. E., Lehman, L. R., and Holmes, S., "A Design-of-Experiments Evaluation of Factors Affecting the Resistance Spot Weldability of High-Strength Steels," *Proceedings of Sheet Metal Welding Conference VII*, AWS Detroit Section, Detroit, MI (1996).

2. Chuko, W. L. and Gould, J. E., "Development of Appropriate Resistance Spot Welding Practice for Transformation-Hardened Steels," *Proceedings of Sheet Metal Welding Conference IX,* AWS Detroit Section, Detroit, MI (Oct. 2000).

3. Ford Motor Company, "Resistance Spot Weldability Tests for High Strength Steels," *Ford Laboratory Test Methods*, BA 13-4 (1980).

4. Gould, J. E., “An Examination of Nugget Development during Spot Welding using Both Experimental and Analytical Techniques,” *Welding Journal Research Supplement*, 67(1):1s-10s (1987).

5. Li, V. M., Dong, P., and Kimchi, M., “Analysis of Microstructure Evolution and Residual Stress in Resistance Spot Welds of High Strength Steels,” *Sheet Metal Welding Conference VIII*, AWS Detroit Section, Detroit, MI (1998).

6. Babu, S. S., Reimer, B. W., Santella, M. L., and Feng, Z., “Integrated Thermal-Microstructure Model to Predict the Property Gradients in Resistance Spot Steel Welds,” *Sheet Metal Welding Conference VIII*, AWS Detroit Section, Detroit, MI (1998).

7. *Metals Handbook*, American Society for Metals, Cleveland, OH (1948).

8. *Handbook of Chemistry and Physics*, The Chemical Rubber Company, Cleveland, OH (1971).

9. Chuko, W. and Gould, J. E., “Development of Appropriate Resistance Spot Welding Practice for Transformation Hardened Steels,” *Welding Journal Research Supplement*, 81(1):1s-7s (2002).

Table 1. **Electrodes Used for Phase 2 – Downslope Processing Maps** (Electrodes were selected following the Ford Specification BA 14-04. Electrode cap cone angle = 45 degrees.)

	Sample Material							
	DF140T		DF140T		M190		M190	
	(mm)	(in.)	(mm)	(in.)	(mm)	(in.)	(mm)	(in.)
Sample thickness	0.83	0.033	1.55	0.061	0.94	0.037	1.58	0.062
Electrode material	Class II	Class II	Class II	--	Class II	--	Class II	--
Electrode type	Truncated cone	--	Truncated cone	--	Truncated cone	--	Truncated cone	--
Electrode cap diameter	16	0.63	19.05	0.75	16	0.63	19.05	0.75
Electrode cap taper	RWMA 5	--	RWMA 6	--	RWMA 5	--	RWMA 6	--
Face diameter	6.35	0.25	7.9	0.31	6.35	0.25	7.9	0.31

Table 2. **Nominal Chemistry and Selected Welding Parameters used for Post-Weld Heating Comparison Trials** (Chemistry for the steels was supplied by the steel manufacturer. Welding parameters nominally followed the Ford specification BA 13-04. Welding currents were selected based upon a 4vt minimum weld nugget size.)

	Material			
	DF140T	DF140T	M190	M190
	Dual Phase		Martensitic	
Thickness [mm (in.)]	0.83 (0.033)	1.55 (0.061)	0.94 (0.037)	1.58 (0.062)
TS [MPa (ksi)]	1000 (145)	1060 (154)	1460 (212)	1410 (205)
YS [MPa (ksi)]	680 (98.9)	720 (105)	1250 (182)	1230 (179)
Carbon	0.1452	0.1537	0.1931	0.1946
Manganese	1.41	1.41	0.46	0.47
Silicon	0.319	0.321	0.055	0.021
Electrode size - face diameter [mm (in.)]	6.4 (0.25)	7.9 (0.31)	6.4 (0.25)	7.9 (0.31)
Weld force [kN (lbf)]	3.1 (700)	5.1 (1140)	3.2 (725)	5.2 (1160)
Squeeze time (cycles)	150	150	150	150
Weld current (kA)	6.7	8.8	6.5	9.1
Weld time (cycles)	10	17	10	17
$4\sqrt{t}$ button size [mm (in.)]	3.64 (0.14)	5 (0.2)	3.88 (0.15)	5.02 (0.2)
Expulsion level (kA)	9.8	12.3	8.5	12.3
Measured average button size at weld current with zero post-heat and 5-cycles hold time [mm (in.)]	3.58 (0.141)	5.26 (0.207)	3.95 (0.156)	5.79 (0.228)
Hold time used during tempering trials (cycles)	300	300	300	300
Cooling water temperature [°C (°F)]	21 (70)	21 (70)	21 (70)	21 (70)
Cooling flow rt. top electrode/bottom electrode [l/min (gpm)]	5.68 (5.68) 1.5 (1.5)	5.68 (5.68) 1.5 (1.5)	5.68 (5.68) 1.5 (1.5)	5.68 (5.68) 1.5 (1.5)

Table 3. **Averaged Rockwell C Surface Hardness Values for 0.83-mm (0.033-in.), Dual-Phase Steel** [Cooling rate was controlled using a matrix of downslope times from 5 to 99 cycles and current from 30 to 100% of the established welding current (I% weld). Rc hardness values highlighted in blue (light) are the average of three measured samples. Rc values highlighted in red (dark) were averaged from those taken from the 0-downslope condition welds.]

Downslope Final I (kA)	% of Weld I	Downslope Time (cycles)								
		0	5	10	20	30	40	60	80	99
6.7	100	40.3	41.8	42.1	41.7	41.4	40.7	41.2	39.7	42.7
6.0	90	40.8	42.9	42.7	41.5	40.2	39.8	38.4	38.5	37.7
5.4	80	41.8	41.3	42.4	41.0	40.8	40.0	37.5	34.5	35.5
4.7	70	44.0	42.3	41.7	40.1	39.0	38.7	37.5	34.3	32.8
4.0	60	44.1	43.1	42.0	40.8	38.7	39.3	37.6	34.6	32.7
3.4	50	42.6	43.7	42.1	41.5	41.5	40.6	37.8	36.4	34.8
2.7	40	44.0	44.0	42.8	43.1	41.1	41.9	38.6	38.8	34.8
2.0	30	43.9	44.8	42.9	43.1	41.5	41.4	40.1	38.9	37.4
Blue (light) values are the average of three surface hardness measurements.										
Pink (dark) values are the average of welds made with zero downslope (42.7 Rc).										

Table 4. **Averaged Rockwell C Surface Hardness Values for 1.55-mm (0.061-in.), Dual-Phase Steel** [Cooling rate was controlled using a matrix of downslope times from 3 to 99 cycles and current from 30 to 100% of the established welding current (I% weld). Rc hardness values highlighted in blue (light) were the average of three measured samples. Rc values highlighted in red (dark) were averaged from those taken from the 0-downslope condition welds.]

Downslope Final I (kA)	% of Weld I	Downslope Time (cycles)									
		0	3	5	10	20	30	40	60	80	99
8.8	100	32.0	33.9	34.0	33.2	30.5	35.3	34.5	33.8	33.8	33.8
7.9	90	31.1	33.5	32.0	33.2	32.6	32.6	31.2	34.1	33.7	33.8
7.0	80	35.2	32.7	34.0	31.0	33.3	32.8	29.4	31.6	31.9	31.2
6.2	70	34.5	31.9	30.9	33.3	30.8	31.5	31.6	30.6	26.6	28.3
5.3	60	33.0	32.6	31.5	30.7	34.6	33.4	30.8	30.1	29.3	28.2
4.4	50	33.0	33.8	37.0	39.5	31.6	29.6	31.0	30.5	28.9	26.3
3.5	40	37.4	33.8	33.8	33.8	31.2	32.1	29.8	27.8	28.2	28.4
2.6	30	34.0	33.8	33.8	33.8	31.2	31.0	31.5	29.9	29.5	29.0
Blue (light) values are the average of three surface hardness measurements.											
Pink (dark) values are the average of welds made with zero downslope (33.8 Rc).											

Table 5. **Averaged Rockwell C Surface Hardness Values for 0.94-mm (0.037-in.), Martensitic Steel** [Cooling rate was controlled using a matrix of downslope times from 5 to 99 cycles and current from 30 to 100% of the established welding current (I% weld). Rc hardness values highlighted in blue (light) were the average of three measured samples. Rc values highlighted in red (dark) were averaged from those taken from the 0-downslope condition welds.]

Downslope Final I (kA)	% of Weld I	Downslope Time (cycles)								
		0	5	10	20	30	40	60	80	99
6.5	100	44.0	44.6	43.6	44.6	43.3	43.9	43.9	45.1	45.1
5.9	90	45.5	45.0	45.0	44.6	44.4	44.5	43.7	42.6	45.1
5.2	80	44.8	46.0	46.6	44.5	43.9	43.7	41.8	42.3	41.9
4.6	70	45.5	46.0	45.1	44.6	44.0	42.9	42.1	40.4	39.8
3.9	60	46.0	44.1	44.0	44.0	43.5	42.5	40.8	38.2	37.2
3.3	50	45.5	46.9	44.2	44.9	44.4	44.0	42.6	40.8	38.8
2.6	40	46.0	45.5	44.5	44.5	43.6	43.2	42.2	39.8	40.4
2.0	30	44.5	44.0	46.0	44.0	44.3	43.6	42.8	41.6	40.0
Blue (light) values are the average of three surface hardness measurements.										
Pink (dark) values are the average of welds made with zero downslope (45.1 Rc).										

Table 6. **Averaged Rockwell C Surface Hardness Values for 1.58-mm (0.062-in.), Martensitic Steel** [Cooling rate was controlled using a matrix of downslope times from 5 to 99 cycles and current from 30 to 100% of the established welding current (I% weld). Rc hardness values highlighted in blue (light) were the average of three measured samples. Rc values highlighted in red (dark) were averaged from those taken from the 0-downslope condition welds.]

Downslope Final I (kA)	% of Weld I	Downslope Time (cycles)								
		0	5	10	20	30	40	60	80	99
9.1	100	37.0	38.0	38.0	36.5	40.1	40.3	39.0	39.0	39.0
8.2	90	39.0	42.0	38.8	37.8	36.8	37.3	34.9	39.0	39.0
7.3	80	40.5	40.5	40.9	40.3	41.1	40.8	39.9	35.6	35.4
6.4	70	40.0	44.0	39.1	40.3	38.3	37.4	36.2	34.0	30.3
5.5	60	39.0	40.5	39.2	37.8	35.7	36.0	35.8	33.8	32.0
4.6	50	42.0	39.0	37.8	38.0	36.7	34.1	32.0	31.4	28.8
3.6	40	39.5	37.5	38.7	36.8	38.3	32.8	34.1	32.4	30.7
2.7	30	37.0	39.0	40.0	39.0	39.1	37.3	37.1	34.0	31.9
Blue (light) values are the average of three surface hardness measurements.										
Pink (dark) values are the average of welds made with zero downslope (39.3 Rc).										

Table 7. **Resulting Button Morphology From Peel Testing 0.83-mm (0.033-in.) Dual-Phase Steel (Material A)** [Peel tests resulting in full buttons are represented by the letter "B" and shaded in red (dark). Peel tests resulting in interfacial failure are represented by the letter "P" or "F" and are shaded in blue (light). No data was taken for the blank areas of the table.]

Downslope Final I (kA)	% of Weld I	Downslope Time (cycles)								
		0	5	10	20	30	40	60	80	99
6.7	100	B	B	B	B	B	B	B	N/A	N/A
6.0	90	B	B	B	B	B	B	B	B	N/A
5.4	80	B	B	B	B	B	B	B	B	B
4.7	70	B	B	F	B	B	B	B	B	B
4.0	60	B	B	B	P	B	B	B	B	B
3.4	50	B	B	B	B	B	B	B	B	B
2.7	40	B	B	N/A	N/A	B	P	B	B	B
2.0	30	B	B	N/A	N/A	B	B	B	B	B
P = partial or full interfacial failure.										
B = full button morphology.										

Table 8. **Resulting Button Morphology From Peel Testing 1.55-mm (0.061-in) Dual-Phase Steel (Material B)** [Peel tests resulting in full buttons are represented by the letter "B" and shaded in red (dark). Peel tests resulting in interfacial failure are represented by the letter "P" or "F" and are shaded in blue (light). No data was taken for the blank areas of the table.]

Downslope Final I (kA)	% of Weld I	Downslope Time (cycles)									
		0	3	5	10	20	30	40	60	80	99
8.8	100	P	P	B	B	B	B	B	N/A	N/A	N/A
7.9	90	B	P	B	B	B	B	P	P	B	N/A
7.0	80	P	F	P	B	P	P	B	B	B	B
6.2	70	F	P	P	B	P	P	P	B	P	B
5.3	60	B	P	P	P	P	B	P	B	B	B
4.4	50	B	N/A	N/A	N/A	P	F	P	B	B	P
3.5	40	B	N/A	N/A	N/A	P	P	P	P	P	B
2.6	30	P	N/A	N/A	N/A	P	P	P	P	P	F
P = partial or full interfacial failure.											
B = full button morphology.											

Table 9. **Resulting Button Morphology from Peel Testing 0.94-mm (0.037-in.) Martensitic Steel (Material C)** [Peel tests resulting in full buttons are represented by the letter "B" and shaded in red (dark). Peel tests resulting in interfacial failure are represented by the letter "P" or "F" and are shaded in blue (light). No data was taken for the blank areas of the table.]

Downslope Final I (kA)	% of Weld I	Downslope Time (cycles)								
		0	5	10	20	30	40	60	80	99
6.5	100	B	P	B	B	B	B	B	N/A	N/A
5.9	90	B	B	B	B	B	B	B	B	N/A
5.2	80	B	B	B	B	B	B	B	B	B
4.6	70	B	B	B	B	B	B	B	B	B
3.9	60	B	B	B	B	B	B	B	B	B
3.3	50	B	B	B	B	B	B	F	B	P
2.6	40	B	B	B	B	B	B	F	P	P
2.0	30	B	B	B	B	B	B	B	B	P
P = partial or full interfacial failure.										
B = full button morphology.										

Table 10. **Resulting Button Morphology From Peel Testing 1.58-mm (0.062-in.) Martensitic Steel (Material D)** [Peel tests resulting in full buttons are represented by the letter "B" and shaded in red (dark). Peel tests resulting in interfacial failure are represented by the letter "P" or "F" and are shaded in blue (light). No data was taken for the blank areas of the table.]

Downslope Final I (kA)	% of Weld I	Downslope Time (cycles)								
		0	5	10	20	30	40	60	80	99
9.1	100	P	B	B	B	B	B	N/A	N/A	N/A
8.2	90	B	P	B	B	B	B	B	N/A	N/A
7.3	80	P	B	B	B	B	B	B	F	P
6.4	70	P	B	P	P	B	P	P	P	P
5.5	60	P	P	B	B	P	B	B	P	P
4.6	50	B	B	B	B	B	P	P	B	B
3.6	40	P	P	P	P	P	B	B	P	B
2.7	30	B	P	N/A	N/A	P	B	P	B	B
P = partial or full interfacial failure.										
B = full button morphology.										

Table 11. Weld and Downslope Parameters used for the Representative Metallurgical Sections and Mechanical Test Samples (Short-, medium-, and long-downslope conditions are shown for each material examined.)

Sample ID	Squeeze Time (cycles)	Weld Force kN (lb)	Weld Time (cycles)	Weld Current (kA)	Downslope Time (cycles)	Downslope End Current (kA)	Downslope Current (%Weld I)	Hold Time (cycles)	Surface Hardness Measurement (Rockwell C)
A - DF140T 0.83-mm									
Short	150	3.1 (700)	10	6.7	5	4.3	65	300	43.5
Medium	150	3.1 (700)	10	6.7	50	4.3	65	300	40
Long	150	3.1 (700)	10	6.7	99	4.3	65	300	34
B - DF140T 1.55-mm									
Short	150	5.1 (1140)	17	8.8	5	5.7	60	300	31
Medium	150	5.1 (1140)	17	8.8	40	5.7	60	300	30
Long	150	5.1 (1140)	17	8.8	99	5.7	60	300	26
C - M190 0.94 mm									
Short	150	3.2 (725)	10	6.5	5	3.9	60	300	45
Medium	150	3.2 (725)	10	6.5	60	3.9	60	300	43.4
Long	150	3.2 (725)	10	6.5	99	3.9	60	300	40.9
D - M190 1.58 mm									
Short	150	5.2 (1160)	17	9.1	5	4.4	48	300	37
Medium	150	5.2 (1160)	17	9.1	50	4.4	48	300	30
Long	150	5.2 (1160)	17	9.1	99	4.4	48	300	30

Table 12. Lap-Shear Test Results for 0.83-mm (0.033-in.) Dual-Phase Steel (Material A) [Representative samples for each of three downslope conditions (short-, medium-, and long-downslope) were tested. Peak load at failure and mode of failure are presented. Speed = 8.5 black on dial (10 mm/min).]

Sample No.	AL65-5 (I=65%, t=5 cycles)			AL65-50 (I=65%, t=50 cycles)			AL65-99 (I=65%, t=99 cycles)		
	(kN)	(lb)	Failure Mode	(kN)	(lb)	Failure Mode	(kN)	(lb)	Failure Mode
1	9.23	2075	IF (S)	10.15	2280	B	8.99	2020	B
2	7.92	1780	IF (S)	10.28	2310	B	9.01	2025	IF (S)
3	8.52	1915	IF (S)	9.88	2220	B	6.76	1520	IF (S)
4	9.50	2135	IF (S)	9.90	2225	B	7.10	1595	IF (S)
5	10.12	2275	IF (S)	10.55	2370	B	7.50	1685	IF (S)
Average:	9.06	2036		10.15	2281		7.87	1769	
STD:	0.86	193		0.28	62		1.06	239	
IF (S) = Interfacial failure in shear mode									
B = Pulled a full button									

Table 13. Lap-Shear Test Results for 1.55-mm (0.061-in.) Dual-Phase Steel (Material B) [Representative samples for each of three downslope conditions (short-, medium-, and long-downslope) were tested. Peak load at failure and mode of failure are presented. Speed = 8.5 black on dial (10 mm/min).]

Sample No.	BL60-5 (I=60%, t=5 cycles)			BL60-40 (I=60%, t=40 cycles)			BL60-99 (I=60%, t=99 cycles)		
	(kN)	(lb)	Failure Mode	(kN)	(lb)	Failure Mode	(kN)	(lb)	Failure Mode
1	18.80	4225	IF (S)	16.24	3650	IF (S)	19.14	4300	IF (S)
2	18.80	4225	IF (S)	17.02	3825	IF (S)	18.69	4200	IF (S)
3	16.47	3700	IF (S)	18.47	4150	IF (S)	19.80	4450	IF (S)
4	18.47	4150	IF (S)	19.14	4300	IF (S)	19.36	4350	IF (S)
5	19.58	4400	IF (S)	18.91	4250	IF (S)	19.58	4400	IF (S)
Average:	18.42	4140		17.96	4035		19.31	4340	
STD:	1.17	263		1.26	284		0.43	96	
IF (S) = Interfacial failure in shear mode									
B = Pulled a full button									

Table 14. Lap-Shear Test Results for 0.94-mm (0.037-in.) Martensitic Steel (Material C) [Representative samples for each of three downslope conditions (short-, medium-, and long-downslope) were tested. Peak load at failure and mode of failure are presented. Speed = 8.5 black on dial (10 mm/min).]

Sample No.	CL60-5 (I=60%, t=5 cycles)			CL60-60 (I=60%, t=60 cycles)			CL60-99 (I=60%, t=99 cycles)		
	(kN)	(lb)	Failure Mode	(kN)	(lb)	Failure Mode	(kN)	(lb)	Failure Mode
1	11.01	2475	IF (S)	10.24	2300	IF (S)	9.79	2200	IF (S)
2	11.35	2550	IF (S)	10.46	2350	IF (S)	10.79	2425	IF (S)
3	10.46	2350	IF (S)	10.01	2250	IF (S)	10.68	2400	IF (S)
4	11.01	2475	IF (S)	9.57	2150	IF (S)	10.12	2275	IF (S)
5	8.90	2000	IF (S)	9.68	2175	IF (S)	11.01	2475	IF (S)
Average:	10.55	2370		9.99	2245		10.48	2355	
STD:	0.97	219		0.37	84		0.51	114	
IF (S) = Interfacial failure in shear mode									
B = Pulled a full button									

Table 15. Lap-Shear Test Results for 1.58-mm (0.062-in.) Martensitic Steel (Material D) [Representative samples for each of three downslope conditions (short-, medium-, and long-downslope) were tested. Peak load at failure and mode of failure are presented. Speed = 8.5 black on dial (10 mm/min).]

Sample No.	DL48-5 (I=48%, t=5 cycles)			DL48-50 (I=48%, t=50 cycles)			DL48-99 (I=48%, t=99 cycles)		
	(kN)	(lb)	Failure Mode	(kN)	(lb)	Failure Mode	(kN)	(lb)	Failure Mode
1	20.47	4600	IF (S)	21.81	4900	IF (S)	21.14	4750	IF (S)
2	20.47	4600	IF (S)	22.03	4950	IF (S)	21.36	4800	IF (S)
3	23.59	5300	IF (S)	21.58	4850	IF (S)	22.25	5000	IF (S)
4	23.59	5300	IF (S)	17.36	3900	IF (S)	20.47	4600	IF (S)
5	21.81	4900	IF (S)	22.92	5150	IF (S)	21.81	4900	IF (S)
Average:	21.98	4940		21.14	4750		21.40	4810	
STD:	1.56	351		2.17	489		0.67	152	
IF (S) = Interfacial failure in shear mode									
B = Pulled a full button									

Table 16. S-N Curve Data for Tensile Fatigue Testing of Material A, 0.83-mm (0.033-in.) Dual-Phase Steel (Loading conditions and number of cycles to failure are presented for short-, medium-, and long-downslope conditions.)

DF140T 0.83 mm - I=65% (weld I), t=5 cycles (short downslope)

Sample No.	Max Load		Static Load		Dynamic Load		Cycles to Failure[a]	Failure Mode
	KN	lb	kN	lb	KN	lb		
1	6.67	1500	3.67	825	3.00	675	855	FIF
2	4.45	1000	2.45	550	2.00	450	2,743	B
3	2.67	600	1.47	330	1.20	270	19,040	B
4	1.78	400	0.98	220	0.80	180	320,274	B (HAZ cracking)
5	1.33	300	0.73	165	0.60	135	3,233,882	B (HAZ cracking)
6	1.07	240	0.59	132	0.48	108	14,638,029	B (HAZ cracking)
(a) Terminate test after 10,000,000 cycles								
FIF - Full interfacial failure			B – Button pulled out of one or both sheets					
PIF - Partial interfacial failure			B (HAZ cracking) - Button failure with crack running through HAZ					

DF140T 0.83 mm - I=65% (Weld I), t=50 cycles (medium downslope)

Sample No.	Max Load		Static Load		Dynamic Load		Cycles to Failure[a]	Failure Mode
	KN	lb	kN	lb	kN	lb		
1	6.67	1500	3.67	825	3.00	675	846	FIF
2	4.45	1000	2.45	550	2.00	450	2,418	B
3	2.67	600	1.47	330	1.20	270	22,277	B
4	1.78	400	0.98	220	0.80	180	519,332	B (HAZ cracking)
5	1.33	300	0.73	165	0.60	135	6,357,904	B (HAZ cracking)
6	1.16	260	0.64	143	0.52	117	10,946,480	
(a) Terminate test after 10,000,000 cycles								
B - Button pulled out of one or both sheets								
B (HAZ cracking) - Button failure with crack running through HAZ								

DF140T 0.83 mm - I=65% (Weld I), t=99 cycles long downslope

Sample No.	Max Load		Static Load		Dynamic Load		Cycles to Failure[a]	Failure Mode
	KN	lb	kN	lb	kN	lb		
1	6.67	1500	3.67	825	3.00	675	185	FIF
2	4.45	1000	2.45	550	2.00	450	1,944	B
3	2.67	600	1.47	330	1.20	270	22,259	B
4	1.78	400	0.98	220	0.80	180	308,289	B (HAZ cracking)
5	1.25	280	0.68	154	0.56	126	2,220,382	B (HAZ cracking)
6	1.07	240	0.59	132	0.48	108	2,331,151	B (HAZ cracking)
7	0.98	220	0.54	121	0.44	99	5,193,332	B (HAZ cracking)
8	0.89	200	0.49	110	0.40	90	14,913,469	
(a) Terminate test after 10,000,000 cycles								
B - Button pulled out of one or both sheets								
B (HAZ cracking) - Button failure with crack running through HAZ								

Table 17. S-N Curve Data for Tensile Fatigue Testing of Material B, 1.55-mm (0.061-in.) Dual-Phase Steel (Loading conditions and number of cycles to failure are presented for short-, medium-, and long-downslope conditions.)

DF140T 1.55 mm - I=60% (weld I), t=5 cycles (short downslope)

Sample No.	Max Load		Static Load		Dynamic Load		Cycles to Failure[a]	Failure Mode
	kN	lb	kN	lb	kN	lb		
1	8.01	1800	4.40	990	3.60	810	5,942	FIF
2	6.67	1500	3.67	825	3.00	675	12,430	FIF
3	4.45	1000	2.45	550	2.00	450	98,679	B (HAZ cracking)
4	2.67	600	1.47	330	1.20	270	750,263	B (HAZ cracking)
5	2.05	460	1.13	253	0.92	207	2,343,496	F (HAZ cracking)
6	1.96	440	1.08	242	0.88	198	3,981,738	F (HAZ cracking)
7	1.78	400	0.98	220	0.80	180	18,339,418	
(a) Terminate test after 10,000,000 cycles								
FIF - Full interfacial failure				B - Button pulled out of one or both sheets				
PIF - Partial interfacial failure				B (HAZ cracking) - Button failure with crack running through HAZ				

DF140T 1.55mm - I=60% (Weld I), t=40 cycles (medium downslope)

Sample No.	Max Load		Static Load		Dynamic Load		Cycles to Failure[a]	Failure Mode
	KN	lb	kN	lb	KN	lb		
1	8.01	1800	4.40	990	3.60	810	5,700	PIF
2	6.67	1500	3.67	825	3.00	675	15,023	FIF
3	4.45	1000	2.45	550	2.00	450	97,268	B (HAZ cracking)
4	2.67	600	1.47	330	1.20	270	641,961	B (HAZ cracking)
5	2.22	500	1.22	275	1.00	225	1,548,417	B (HAZ cracking)
6	1.78	400	0.98	220	0.80	180	7,382,413	B (HAZ cracking)
(a) Terminate test after 10,000,000 cycles								
FIF - Full interfacial failure				B - Button pulled out of one or both sheets				
PIF - Partial interfacial failure				B (HAZ cracking) - Button failure with crack running through HAZ				

DF140T 1.55 mm - I=60% (Weld I), t=99 cycles (long downslope)

Sample No.	Max Load		Static Load		Dynamic Load		Cycles to Failure[a]	Failure Mode
	KN	lb	kN	lb	kN	lb		
1	8.01	1800	4.40	990	3.60	810	6,706	B
2	6.67	1500	3.67	825	3.00	675	15,367	B
3	4.45	1000	2.45	550	2.00	450	85,976	B (HAZ cracking)
4	2.67	600	1.47	330	1.20	270	549,774	F (HAZ crack)
5	2.05	460	1.13	253	0.92	207	4,312,856	B (HAZ cracking)
6	1.7792	400	0.98	220	0.80	180	8,355,638	F (HAZ crack)
(a) Terminate test after 10,000,000 cycles								
FIF - Full interfacial failure				B - Button pulled out of one or both sheets				
PIF - Partial interfacial failure				B (HAZ cracking) – Button failure with crack running through HAZ				

Table 18. S-N Curve Data for Tensile Fatigue Testing of Material C, 0.94-mm (0.037-in.) Martensitic Steel (Loading conditions and number of cycles to failure are presented for short-, medium-, and long-downslope conditions.)

M190 0.94 mm - I=60% (weld I), t=5 cycles (short downslope)

Sample No.	Max Load		Static Load		Dynamic Load		Cycles to Failure[(a)]	Failure Mode
	KN	lb	kN	lb	kN	lb		
1	6.67	1500	3.67	825	3.00	675	1,013	FIF
2	4.45	1000	2.45	550	2.00	450	5,495	B
3	2.67	600	1.47	330	1.20	270	56,885	B
4	1.78	400	0.98	220	0.80	180	404,873	F (HAZ cracking)
5	1.16	260	0.64	143	0.52	117	2,603,040	F (HAZ cracking)
6	0.89	200	0.49	110	0.40	90	16,035,825	F (HAZ cracking)

(a) Terminate test after 10,000,000 cycles

FIF - Full interfacial failure

PIF - Partial interfacial failure

B - Button pulled out of one or both sheets

B (HAZ cracking) - Button failure with crack running through HAZ

M190 0.94 mm - I=60% (Weld I), t=60 cycles (medium downslope)

Sample No.	Max Load		Static Load		Dynamic Load		Cycles to Failure[(a)]	Failure Mode
	KN	lb	kN	lb	kN	lb		
1	6.67	1500	3.67	825	3.00	675	653	FIF
2	4.45	1000	2.45	550	2.00	450	3,058	PIF
3	2.67	600	1.47	330	1.20	270	52,556	B
4	1.78	400	0.98	220	0.80	180	495,905	B (HAZ cracking)
5	1.07	240	0.59	132	0.48	108	11,841,702	F (HAZ cracking)

(a) Terminate test after 10,000,000 cycles

FIF - Full interfacial failure

PIF - Partial interfacial failure

B - Button pulled out of one or both sheets

B (HAZ cracking) - Button failure with crack running through HAZ

M190 0.94 mm - I=60% (Weld I), t=99 cycles (long downslope)

Sample No.	Max Load		Static Load		Dynamic Load		Cycles to Failure[(a)]	Failure Mode
	KN	lb	kN	lb	kN	lb		
1	6.67	1500	3.67	825	3.00	675	605	PIF
2	4.45	1000	2.45	550	2.00	450	3,885	B
3	2.67	600	1.47	330	1.20	270	56,756	B
4	1.78	400	0.98	220	0.80	180	379,893	B (HAZ cracking)
5	1.07	240	0.59	132	0.48	108	4,225,588	F(HAZ cracking)
6	0.8896	200	0.49	110	0.40	90	18,088,935	

(a) Terminate test after 10,000,000 cycles

FIF - Full interfacial failure

PIF - Partial interfacial failure

B - Button pulled out of one or both sheets

B (HAZ cracking) - Button failure with crack running through HAZ

Table 19. S-N Curve Data for Tensile Fatigue Testing of Material D, 1.58-mm (0.062-in.) Martensitic Steel (Loading conditions and number of cycles to failure are presented for short-, medium-, and long-downslope conditions.)

M190 1.58 mm - I=48% (weld I), t=5 cycles (short downslope)

Sample No.	Max Load		Static Load		Dynamic Load		Cycles to Failure[(a)]	Failure Mode
	kN	lb	kN	lb	kN	lb		
1	8.01	1800	4.40	990	3.60	810	10,821	FIF
2	6.67	1500	3.67	825	3.00	675	19,148	FIF
3	4.45	1000	2.45	550	2.00	450	115,471	B (HAZ cracking)
4	2.67	600	1.47	330	1.20	270	659,390	F (HAZ cracking
5	1.78	400	0.98	220	0.80	180	7,681,776	B (HAZ cracking)

(a) Terminate test after 10,000,000 cycles

FIF - Full interfacial failure	B - Button pulled out of one or both sheets
PIF - Partial interfacial failure	B (HAZ cracking) - Button failure with crack running through HAZ

M190 1.58 mm - I=48% (Weld I), t=50 cycles (medium downslope)

Sample No.	Max Load		Static Load		Dynamic Load		Cycles to Failure[(a)]	Failure Mode
	KN	lb	kN	lb	kN	lb		
1	6.67	1500	3.67	825	3.00	675	4,935	FIF
2	4.45	1000	2.45	550	2.00	450	104,485	B (HAZ cracking)
3	2.67	600	1.47	330	1.20	270	700,223	B (HAZ cracking)
4	1.78	400	0.98	220	0.80	180	3,007,259	F (HAZ cracking)
5	1.33	300	0.75	168	0.60	135	18,503,807	B (HAZ cracking)

(a) Terminate test after 10,000,000 cycles

FIF – Full interfacial failure	B – Button pulled out of one or both sheets
PIF - Partial interfacial failure	B (HAZ cracking) - Button failure with crack running through HAZ

M190 1.58 mm - I=48% (Weld I), t=99 cycles (long downslope)

Sample No.	Max Load		Static Load		Dynamic Load		Cycles to Failure[(a)]	Failure Mode
	KN	lb	kN	lb	kN	lb		
1	8.01	1800	4.40	990	3.60	810	8,813	B
2	6.67	1500	3.67	825	3.00	675	18,663	B
3	4.45	1000	2.45	550	2.00	450	141,773	B (HAZ cracking)
4	2.67	600	1.47	330	1.20	270	743,644	B (HAZ cracking)
5	1.78	400	0.98	220	0.80	180	4,164,898	F (HAZ cracking)
6	1.60	360	0.88	198	0.72	162	13,381,630	B (HAZ cracking)

(a) Terminate test after 10,000,000 cycles

FIF - Full interfacial failure	B - Button pulled out of one or both sheets
PIF - Partial interfacial failure	B (HAZ cracking) - Button failure with crack running through HAZ

Table 20. Cross-Tension Tensile Test Results from Material A, 0.83-mm (0.033-in.) Dual-Phase Steel [Loading conditions and number of cycles to failure are presented for short-, medium-, and long-downslope conditions. Speed = 8.5 on dial (10 mm/min).]

DF140T 0.83 mm

Sample No.	Short (l=65%, t=5 cycles)			Medium (l=65%, t=50 cycles)			Long (l=65%, t=99 cycles)		
	(kN)	(lb)	Failure Mode	(kN)	(lb)	Failure Mode	(kN)	(lb)	Failure Mode
1	4.03	905	B	3.07	690	B	3.56	800	B
2	5.01	1125	B	3.38	760	B	3.20	718	B
3	3.38	760	B	3.38	760	B	2.93	658	B
4	3.49	785	B	3.83	860	B	2.92	657	B
5	4.03	905	B	3.63	815	B	3.36	754	B
Average:	3.99	896		3.46	777		3.19	717	
STD:	0.64	144		0.29	64		0.28	62	
B = Full button mode of failure									

Table 21. Cross-Tension Tensile Test Results from Material B, 1.55-mm (0.061-in.) Dual-Phase Steel [Loading conditions and number of cycles to failure are presented for short-, medium-, and long-downslope conditions. Speed = 8.5 on dial (10 mm/min).]

DF140T 1.55 mm

Sample No.	Short (l=60%, t=5 cycles)			Medium (l=60%, t=40 cycles)			Long (l=60%, t=99 cycles)		
	(kN)	(lb)	Failure Mode	(kN)	(lb)	Failure Mode	(kN)	(lb)	Failure Mode
1	6.72	1510	B	7.39	1660	B	7.63	1715	B
2	5.63	1265	B	6.50	1460	B	7.23	1625	B
3	7.36	1655	B	6.81	1530	B	7.34	1650	B
4	6.45	1450	B	7.36	1655	B	7.52	1690	B
5	6.83	1535	B	7.23	1625	B	6.85	1540	B
Average	6.60	1483		7.06	1586		7.32	1644	
STD:	0.64	143		0.39	88		0.30	68	
B = Full button mode of failure									

Table 22. Cross-Tension Tensile Test Results from Material C, 0.94-mm (0.037-in.) Martensitic Steel (Loading conditions and number of cycles to failure are presented for short-, medium-, and long-downslope conditions.)

M190 0.94 mm

Sample No.	Short (I=60%, t=5 cycles)			Medium (I=60%, t=60 cycles)			Long (I=60%, t=99 cycles)		
	(kN)	(lb)	Failure Mode	(kN)	(lb)	Failure Mode	(kN)	(lb)	Failure Mode
1	4.01	901	B	4.37	982	B	4.24	953	B
2	4.01	902	B	4.01	900	B	4.00	898	B
3	4.34	976	B	3.20	720	B	4.28	962	B
4	4.15	932	B	4.37	983	B	4.05	911	B
5	4.40	989	B	4.09	919	B	3.60	809	B
Average:	4.18	940		4.01	901		4.03	907	
STD:	0.18	41		0.48	108		0.27	61	
B = Full button mode of failure									

Table 23. Cross-Tension Tensile Test Results from Material D, 1.58-mm (0.062-in.) Martensitic Steel (Loading conditions and number of cycles to failure are presented for short-, medium-, and long-downslope conditions.)

M190 1.58 mm

Sample No.	Short (I=48%, t=5 cycles)			Medium (I=48%, t=50 cycles)			Long (I=48%, t=99 cycles)		
	(kN)	(lb)	Failure Mode	(kN)	(lb)	Failure Mode	(kN)	(lb)	Failure Mode
1	4.14	930	IF	5.14	1155	B	4.81	1080	B
2	4.90	1100	IF	4.96	1115	B	5.15	1158	B
3	4.83	1085	IF	5.25	1180	B	5.21	1170	B
4	4.03	905	IF	5.30	1190	B	4.41	990	B
5	5.72	1285	B	5.01	1125	IF	5.12	1150	B
Average:	4.72	1061		5.13	1153		4.94	1110	
STD:	0.68	153		0.15	33		0.34	76	
B = Full button mode of failure									
IF = Interfacial failure									

Table 24. Cross-Tension Impact Results for Material A, 0.83-mm (0.033-in.) Dual-Phase Steel (Absorbed energy was measured and failure mode was recorded for samples from each downslope condition. Full-button failure is denoted by the letter “B”. Partial interfacial failure is denoted by the letters “PIF”.)

140T

	Short Downslope Time			Medium Downslope Time			Long Downslope Time		
Sample No.	AI65-5			AI65-50			AI-65-99		
	(J)	(ft-lb)	Failure Mode	(J)	(ft-lb)	Failure Mode	(J)	(ft-lb)	Failure Mode
1	66.49	49	B	51.56	38	B	58.34	43	B
2	56.99	42	B	71.91	53	B	56.99	42	B
3			N/A	58.34	43	B	55.63	41	B
4	56.99	42	B	55.63	41	B	48.85	36	B
5	61.06	45	B	54.27	40	B	50.20	37	B
Average:	60.38	44.50		58.34	43.00		54.00	39.80	
STD:	4.50	3.32		7.97	5.87		4.23	3.11	
B = Full button failure mode									

Table 25. Cross-Tension Impact Results for Material B, 1.55-mm (0.061-in.) Dual-Phase Steel (Absorbed energy was measured and failure mode was recorded for samples from each downslope condition. Full-button failure is denoted by the letter “B”. Partial interfacial failure is denoted by the letters “PIF”.)

140T

	Short Downslope Time			Medium Downslope Time			Long Downslope Time		
Sample No.	BI60-5-			BI60-50-			BI60-99-		
	(J)	(ft-lb)	Failure Mode	(J)	(ft-lb)	Failure Mode	(J)	(ft-lbs.)	Failure Mode
1	81.41	60	B	107.19	79	B	107.19	79	B
2	97.69	72	B	104.48	77	B	111.26	82	B
3	93.62	69	B	118.05	87	B	109.91	81	B
4	94.98	70	B	108.55	80	B	107.19	79	B
5	100.41	74	B	100.41	74	B	115.33	85	B
Average:	93.62	69.00		107.73	79.40		110.18	81.20	
STD:	7.31	5.39		6.55	4.83		3.38	2.49	
B = Full button failure mode									

Table 26. Cross-Tension Impact Results for Material C, 0.94-mm (0.037-in.) Martensitic Steel (Absorbed energy was measured and failure mode was recorded for samples from each downslope condition. Full-button failure is denoted by the letter "B".)

Sample No.	Short Downslope Time			Medium Downslope Time			Long Downslope Time		
	CI60-5			CI60-60			CI60-99		
	(J)	(ft-lb)	Failure Mode	(J)	(ft-lb)	Failure Mode	(J)	(ft-lb)	Failure Mode
1	59.70	44	B	62.42	46	B	69.20	51	B
2	59.70	44	B	59.70	44	B	56.99	42	B
3	67.84	50	B	54.27	40	B	63.77	47	B
4	56.99	42	B	65.13	48	B	65.13	48	B
5	62.42	46	B	59.70	44	B	59.70	44	B
Average:	61.33	45.20		60.24	44.40		62.96	46.40	
STD:	4.12	3.03		4.03	2.97		4.76	3.51	
B = Full button failure mode									

Table 27. Cross-Tension Impact Results for Material D, 1.58-mm (0.062-in.) Martensitic Steel (Absorbed energy was measured and failure mode was recorded for samples from each downslope condition. Full-button failure is denoted by the letter "B". Partial interfacial failure is denoted by the letters "PIF". Full interfacially failed welds are denoted by the letters "FIF".)

Sample No.	Short Downslope Time			Medium Downslope Time			Long Downslope Time		
	DI48-5			DI48-50			DI48-99		
	(J)	(ft-lb)	Failure Mode	(J)	(ft-lb)	Failure Mode	(J)	(ft-lb)	Failure Mode
1	59.70	44	B	65.13	48	LT	71.91	53	B
2	65.13	48	B	59.70	44	B	43.42	32	LT
3	59.70	44	B	63.77	47	B	63.77	47	IF(S)
4	63.77	47	IF(S)	62.42	46	B	55.63	41	B
5	61.06	45	IF(S)	54.27	40	B	51.56	38	B
Average:	61.87	45.60		61.06	45.00		57.26	42.20	
STD:	2.46	1.82		4.29	3.16		11.00	8.11	
B = Full button failure mode									
IF(S) = Interfacial failure (shear mode)									
LT = Lamellar tear									

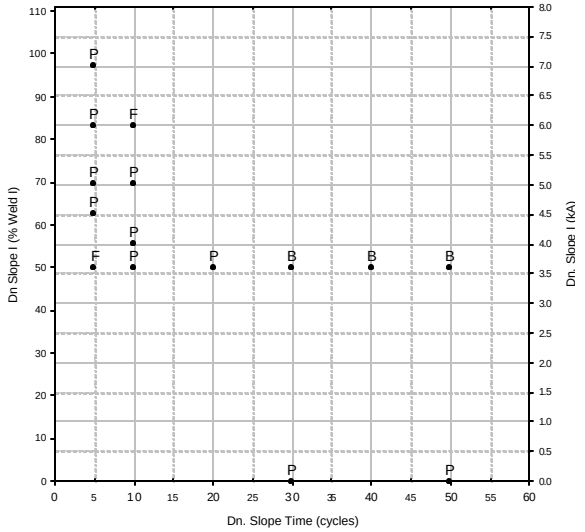

(a) Downslope evaluation results from 0.83-mm dual-phase steel

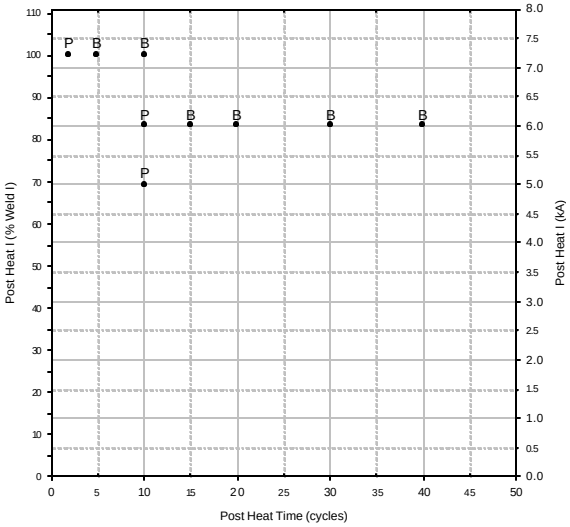

(b) Post-heat evaluation results from 0.83-mm dual-phase steel

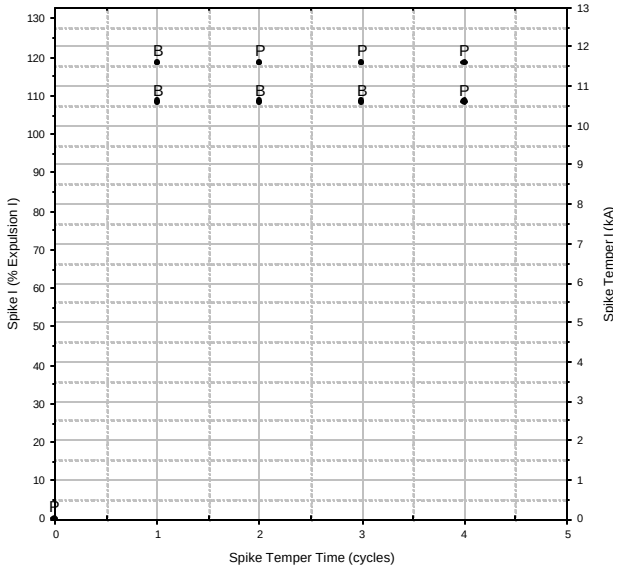

(c) Spike-temper evaluation results from 0.83-mm dual-phase steel

Figure 1. Downslope, Post-Heat, and Spike-Temper Results from Material A, 0.83-mm (0.033-in.) Dual-Phase Steel (200 cycles of hold time was used after each post-weld heating condition. Current in the downslope and post-heat plots is presented as a function of the established welding current. Current in the spike-temper plot is presented as a function of the expulsion current. "F" and "P" represent full and partial weld failure during peel testing. "B" represents full-button failure.)

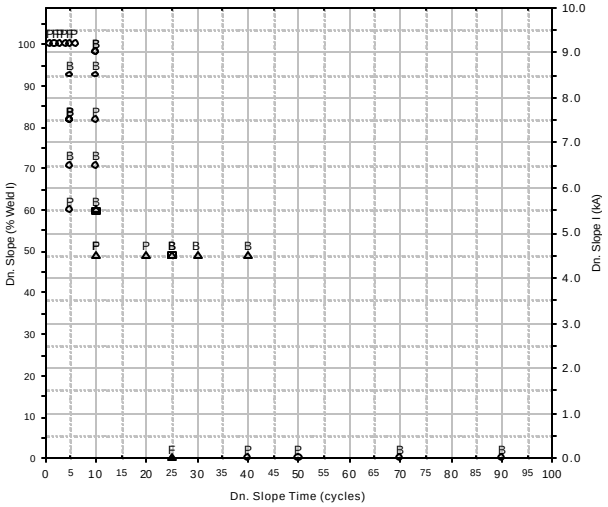

(a) Downslope evaluation results from 1.55-mm dual-phase steel – hold-time was increased from 60 to 200 cycles during evaluation.

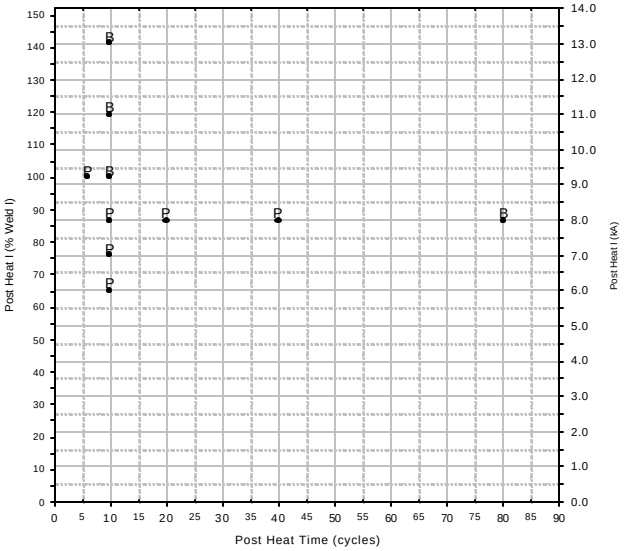

(b) Post-heat evaluation results for 1.55-mm dual-phase steel

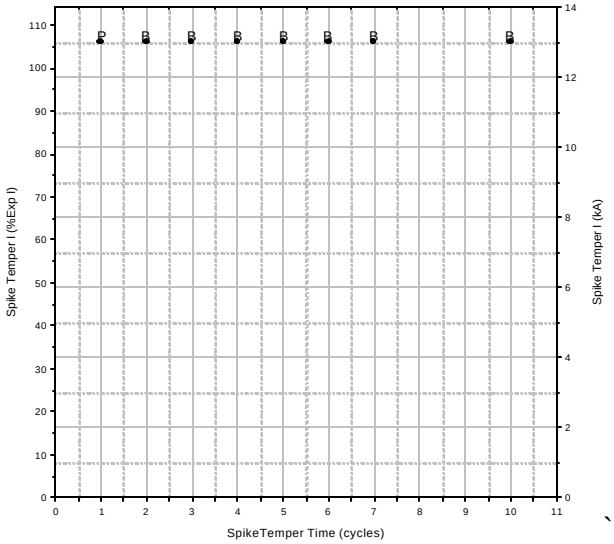

(c) Spike-temper evaluation results for 1.55-mm dual-phase steel

Figure 2. Downslope, Post-Heat, and Spike-Temper Results from Material B, 1.55-mm (0.061-in.) Dual-Phase Steel (Hold time after downsloping was increased from 60 to 200 cycles during evaluation. 200 cycles of hold time was used for all other post-weld heating evaluations. Current in the downslope and post-heat plots is presented as a function of the established welding current. Current in the spike-temper plot is presented as a function of the expulsion current. “F” and “P” represent full and partial weld failure during peel testing. “B” represents full-button failure.)

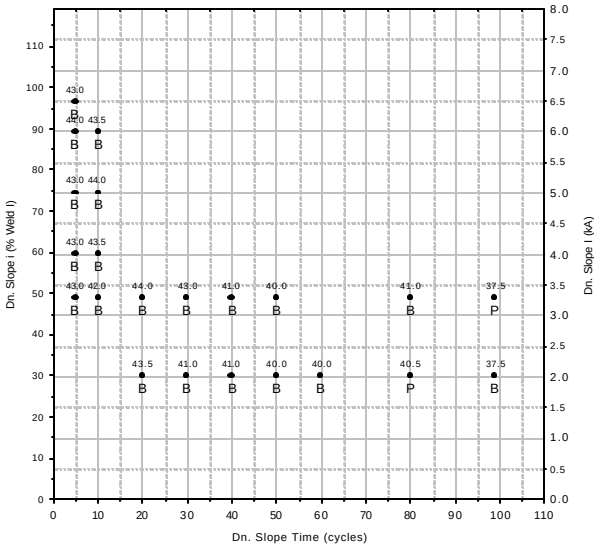

(a) Downslope evaluation results for 0.94-mm martensitic steel

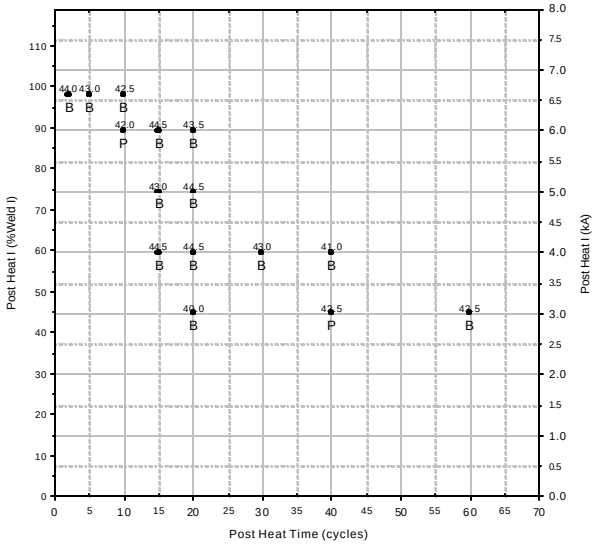

(b) Post-heat evaluation results for 0.94-mm martensitic steel

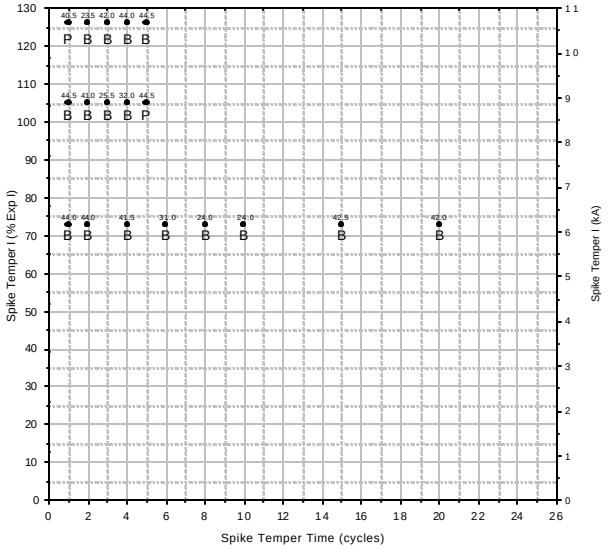

(c) Spike-temper evaluation results for 0.94-mm martensitic steels

Figure 3. Downslope, Post-Heat, and Spike-Temper Results from Material C, 0.94-mm (0.037-in.) Martensitic Steel (200 cycles of hold time was used following each post-heat heating condition. Current in the downslope and post-heat plots is presented as a function of the established welding current. Current in the spike-temper plot is presented as a function of the expulsion current. Rockwell C surface hardness measurements are presented on each plot. "F" and "P" represent full and partial weld failure during peel testing. "B" represents full-button failure.)

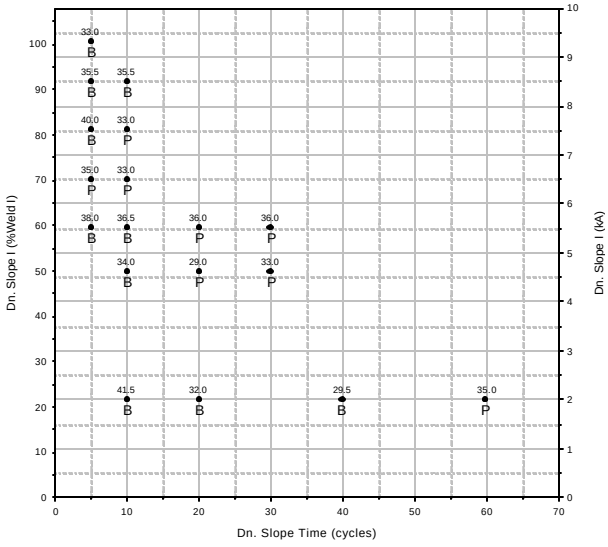

(a) Downslope evaluation results for 1.58-mm martensitic steel

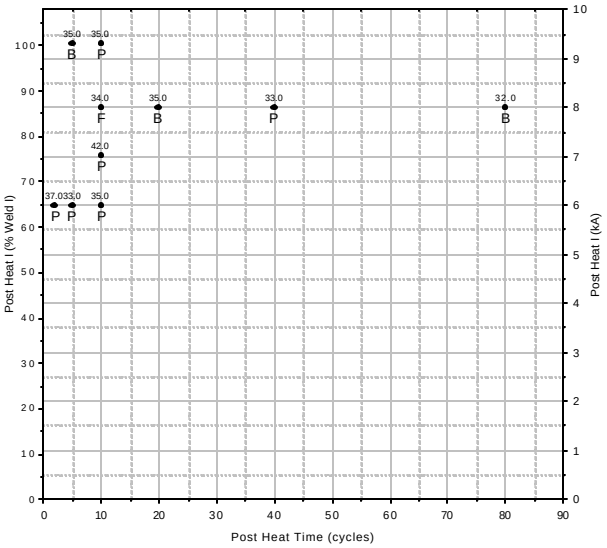

(b) Post-heat evaluation results for 1.58-mm martensitic steel

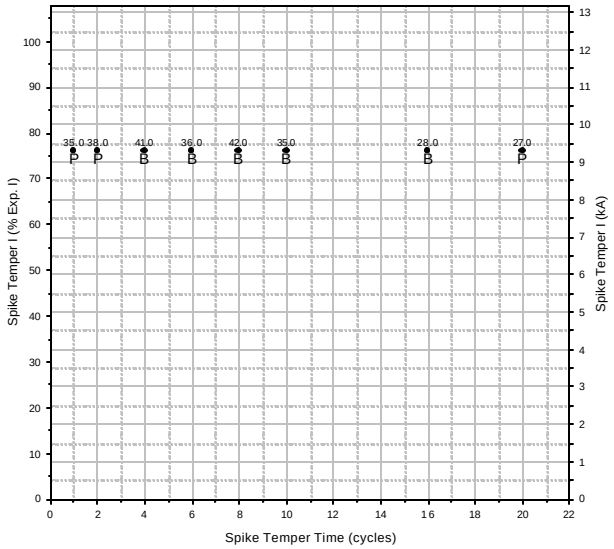

(c) Spike temper evaluation results for 1.58-mm martensitic steel

Figure 4. Downslope, Post-Heat, and Spike-Temper Results from Material D, 1.58-mm (0.062-in.) Martensitic Steel (200 cycles of hold time was used following each post-weld material condition. Current in the downslope and post-heat plots is presented as a function of the established welding current. Current in the spike-temper plot is presented as a function of the expulsion current. Rockwell C surface hardness measurements are presented on each plot. "F" and "P" represent full and partial weld failure during peel testing. "B" represents full-button failure.)

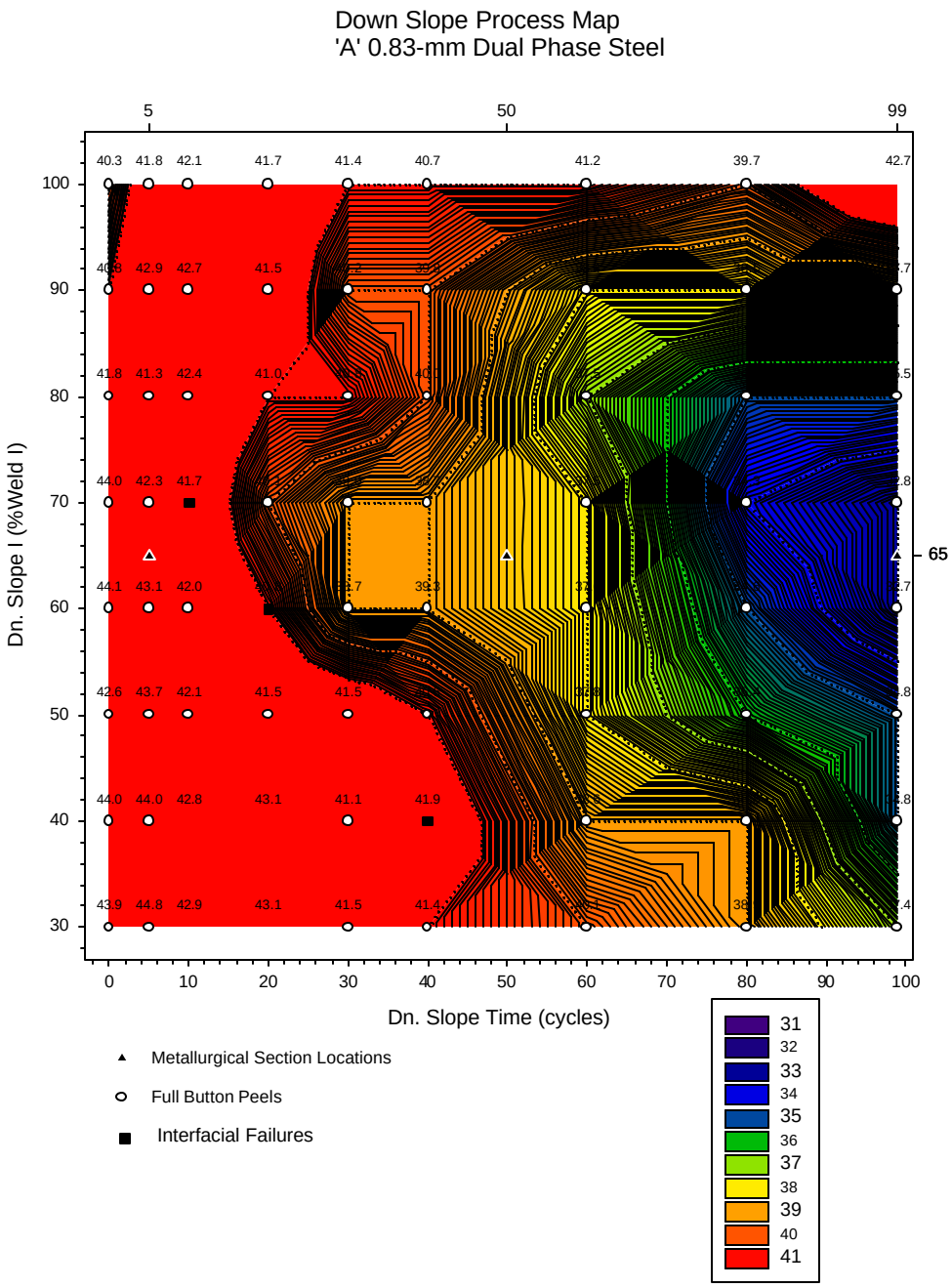

Figure 5. **Downslope Processing Map for 0.83-mm (0.033-in.) Dual-Phase Steel (Material A)** (The matrix of downslope times and downslope end currents was applied to welded samples immediately following welding. Surface measurements of hardness of the weld were performed using the Rc scale. Hardness results were then plotted as a function of downslope time and a percentage of the welding current using a contour plot. Resulting peel test results showing the button morphology were overlaid onto the contour plot. Reference points showing the downslope conditions used for the metallurgical and mechanical test samples are also shown.)

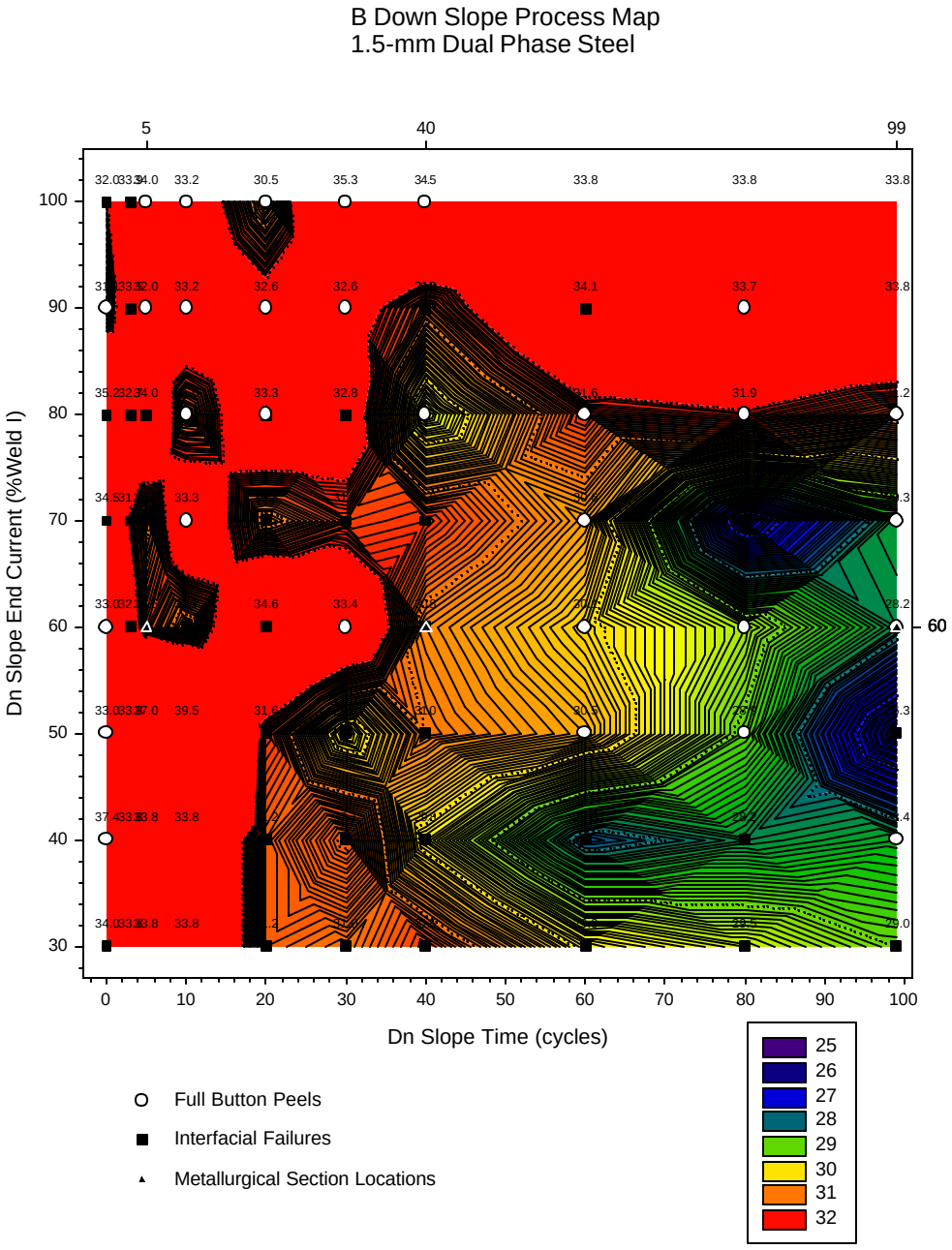

Figure 6. **Downslope Processing Map for 1.55-mm (0.061-in.) Dual-Phase Steel (Material B)** (The matrix of downslope times and downslope end currents was applied to welded samples immediately following welding. Surface measurements of hardness of the weld were performed using the Rc scale. Hardness results were then plotted as a function of downslope time and a percentage of the welding current using a contour plot. Resulting peel test results showing the button morphology were overlaid onto the contour plot. Reference points showing the downslope conditions used for the metallurgical and mechanical test samples are also shown.)

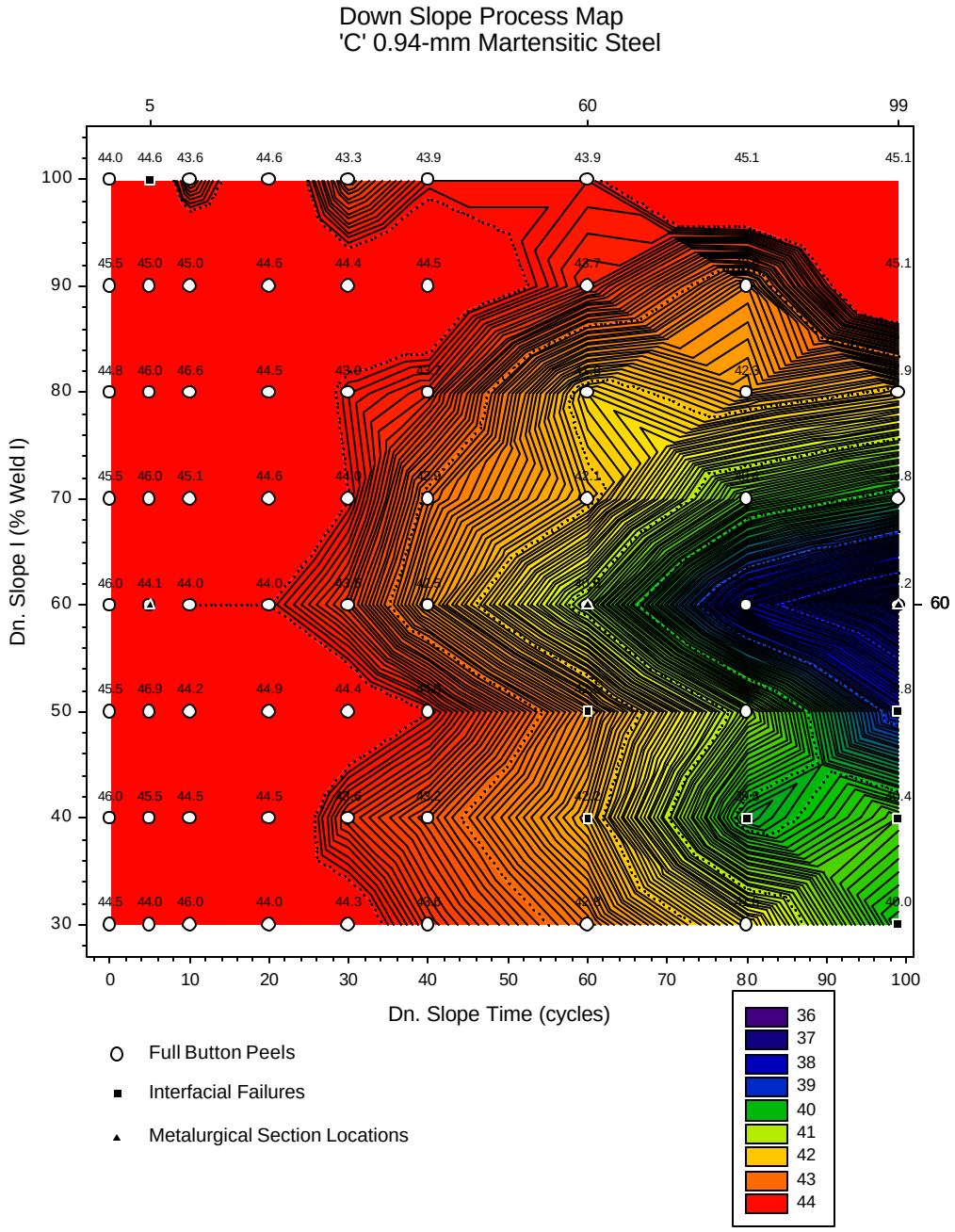

Figure 7. **Downslope Processing Map for 0.94-mm (0.037-in.) Martensitic (Material C)** (The matrix of downslope times and downslope end currents was applied to welded samples immediately following welding. Surface measurements of hardness of the weld were performed using the Rc scale. Hardness results were then plotted as a function of downslope time and a percentage of the welding current using a contour plot. Resulting peel test results showing the button morphology were overlaid onto the contour plot. Reference points showing the downslope conditions used for the metallurgical and mechanical test samples are also shown.)

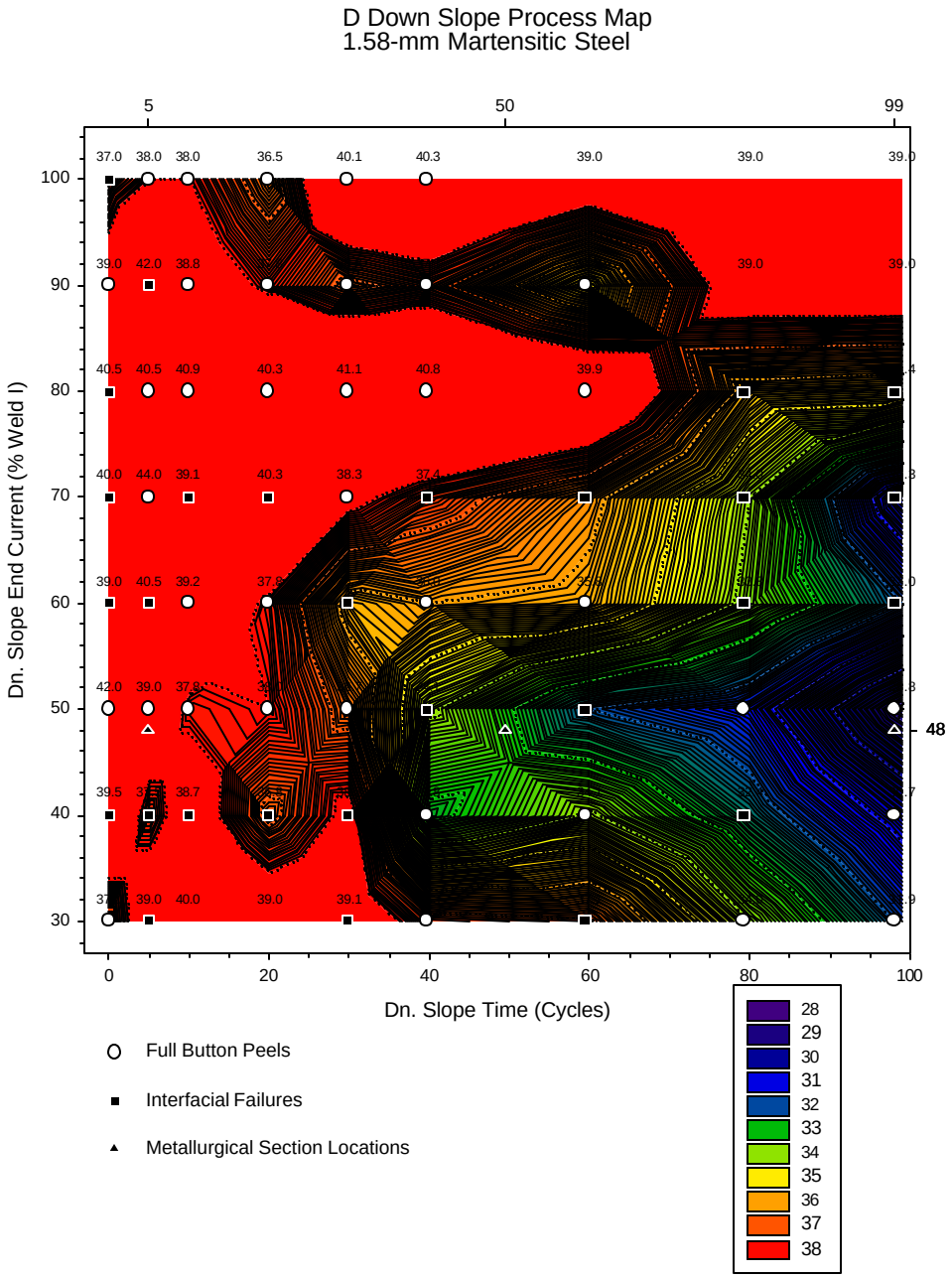

Figure 8. **Downslope Processing Map for 1.58-mm (0.062-in.) Martensitic (Material D)** (The matrix of downslope times and downslope end currents was applied to welded samples immediately following welding. Surface measurements of hardness of the weld were performed using the Rc scale. Hardness results were then plotted as a function of downslope time and a percentage of the welding current using a contour plot. Resulting peel test results showing the button morphology were overlaid onto the contour plot. Reference points showing the downslope conditions used for the metallurgical and mechanical test samples are also shown.)

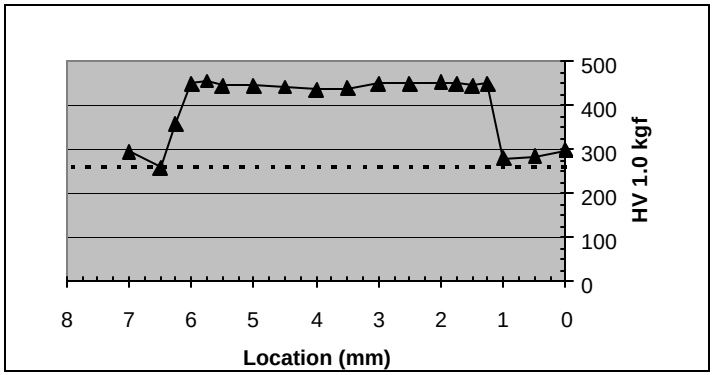

(a) Diagonal Hardness Traverse of 0.83-mm DF140T with short downslope time.

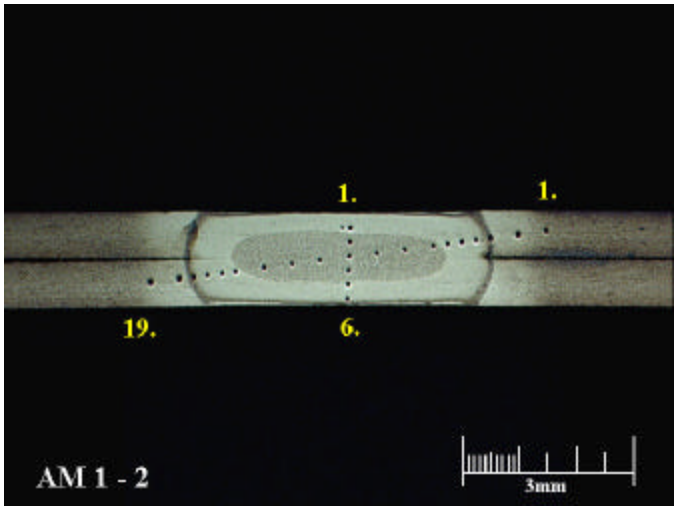

(b) Micrograph of 0.83-mm DF140T with short downslope time.

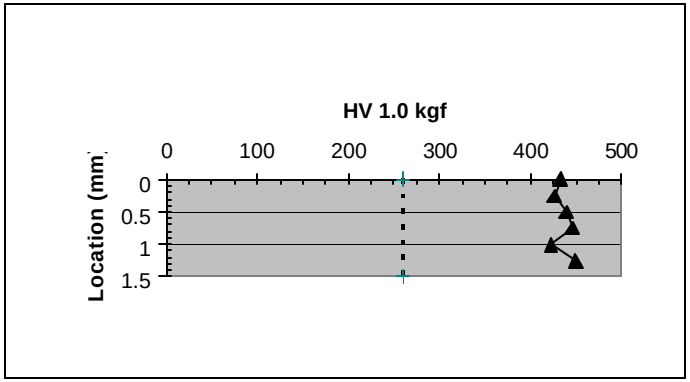

(c) Vertical hardness traverse of 0.83-mm DF140T with short downslope time.

Figure 9. Hardness Traverse Plots for Material A, 0.83-mm (0.033-in.) Dual-Phase Steel with Short Downslope Time
[The sample was welded using established parameters for Material A. This was immediately followed by a 5-cycle downslope time to a final current of 65% (4.3 kA) of the welding current and a 300-cycle hold time. Results from the diagonal and through-thickness hardness traverses are presented using the VHN scale. The dashed line represents an independent measure of base metal hardness.]

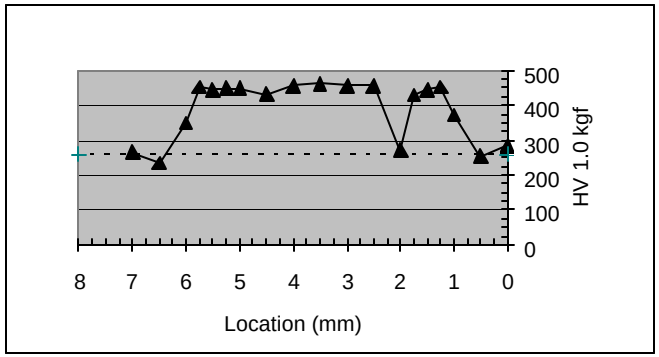

(a) Diagonal hardness traverse of 0.83-mm DF140T with medium downslope time

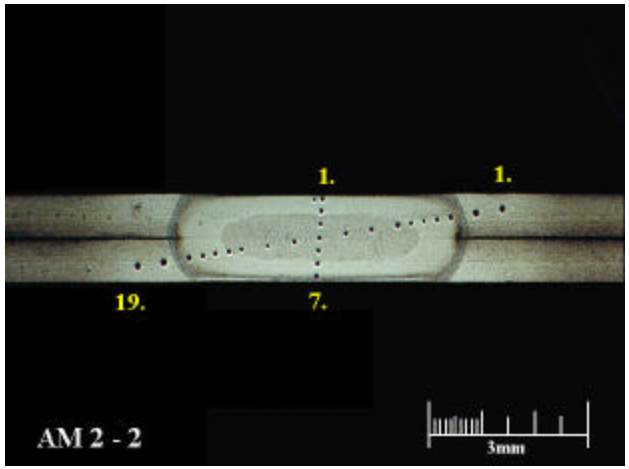

(b) Micrograph of 0.83-mm DF140T with medium downslope time.

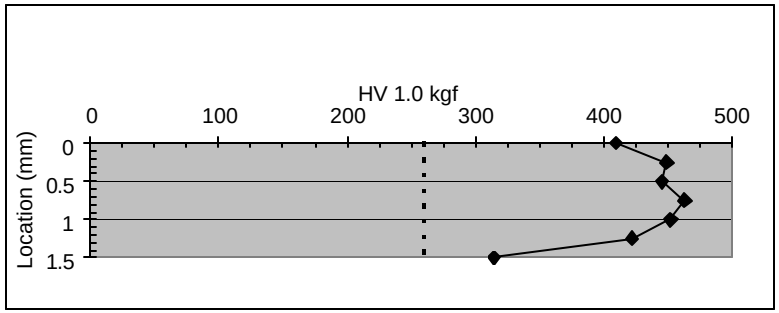

(c) Through-thickness hardness traverse of 0.83-mm DF140T with medium downslope time.

Figure 10. Hardness Traverse Plots for Material A, 0.83-mm (0.033-in.) Dual-Phase Steel with Medium Downslope Time
[The sample was welded using established parameters for Material A. This was immediately followed by a 50-cycle downslope to a final current of 65% (4.3 kA) of the welding current and a 300-cycle hold time. Results from the hardness traverse in the diagonal and through-thickness directions are presented using the VHN scale. The dashed line represents an independent measure of the base metal hardness.]

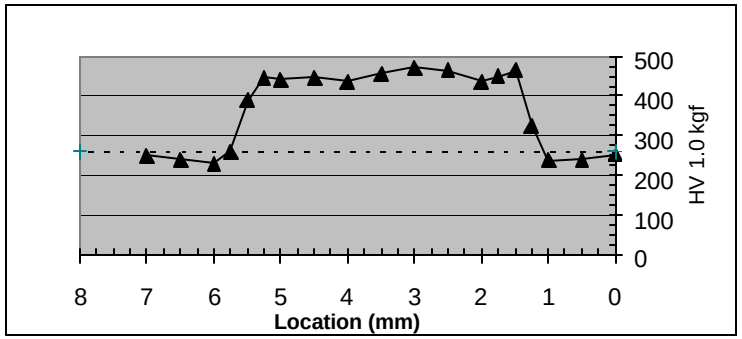

(a) Horizontal hardness traverse of 0.83-mm DF140T with long downslope time.

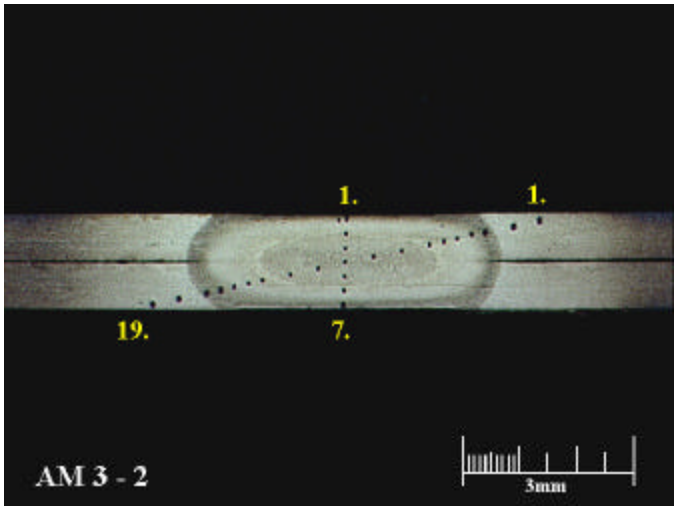

(b) Micrograph of 0.83-mm DF140T with long downslope time.

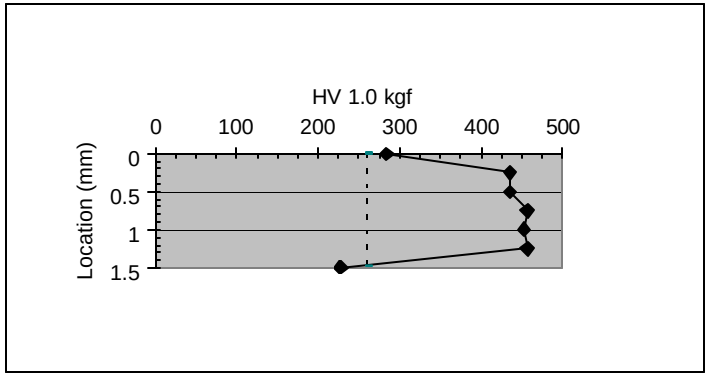

(c) Through-thickness hardness traverse of 0.83-mm DF140T with long downslope time.

Figure 11. Hardness Traverse Plots for Material A, 0.83-mm (0.033-in.) Dual-Phase Steel with Long Downslope Time
[The sample was welded using established parameters for Material A. This was immediately followed by 99-cycles of downslope to a final current of 65% (4.3 kA) of the welding current. After the downslope the sample was held under full force for an additional 300-cycles with no additional welding current. Results from the hardness traverse in the diagonal and vertical directions are presented using the VHN scale. The dashed line represents an independent hardness measurement of the base metal.]

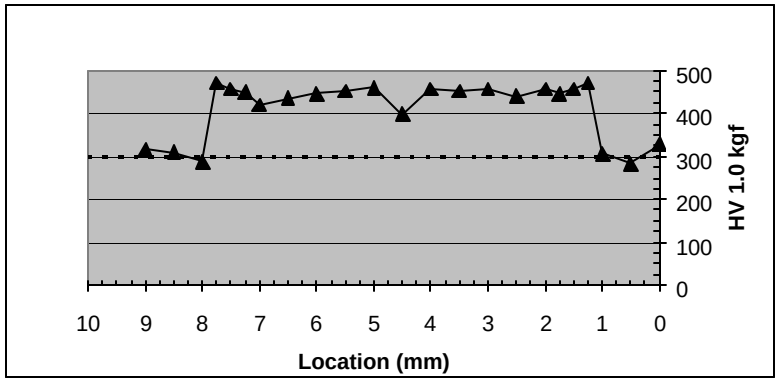

(a) Diagonal hardness traverse of 1.55-mm DF140T with short downslope time.

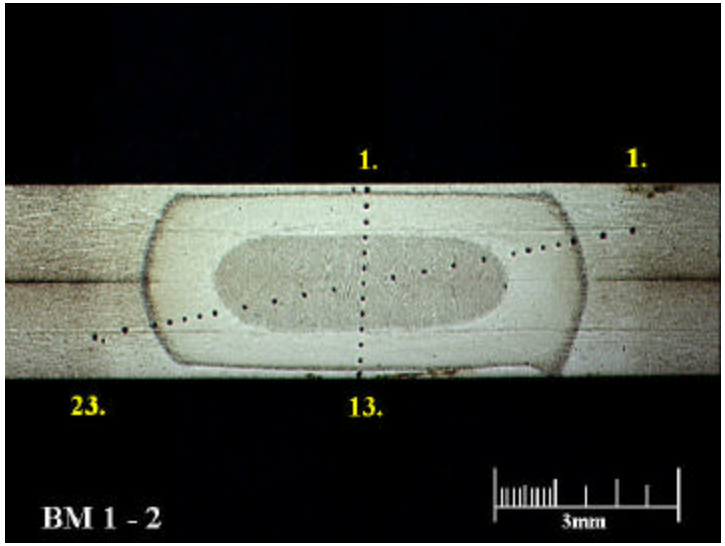

(b) Micrograph of 1.55-mm DF140T with short downslope time.

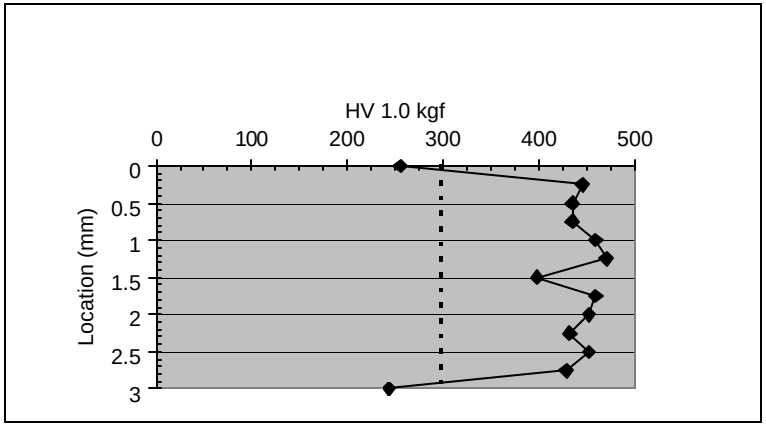

(c) Through-thickness hardness traverse of 1.55-mm DF140T with short downslope time.

Figure 12. Hardness Traverse Plots for Material B, 1.55-mm (0.061-in.) Dual-Phase Steel with Short Downslope Time
[The sample was welded using established parameters for Material B. This was immediately followed by a 5-cycle downslope time to a final current of 60% (5.3 kA) of the welding current and a 300-cycle hold time. Results from the diagonal and through-thickness hardness traverses are presented using the VHN scale. The dashed line represents an independent hardness measurement of unwelded base metal.]

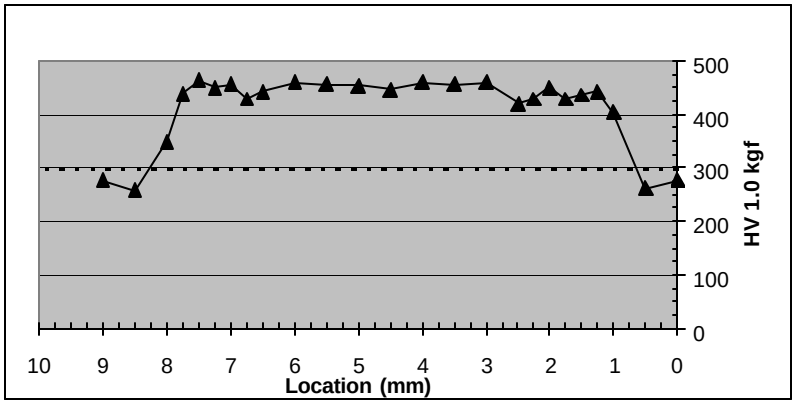

(a) Diagonal hardness traverse of 1.55-mm DF140T with medium downslope time.

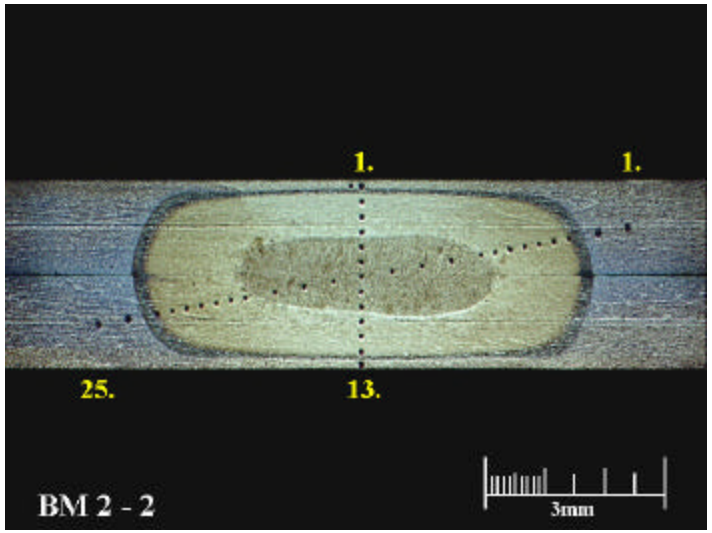

(b) Micrograph of 1.55-mm DF140T with medium downslope time.

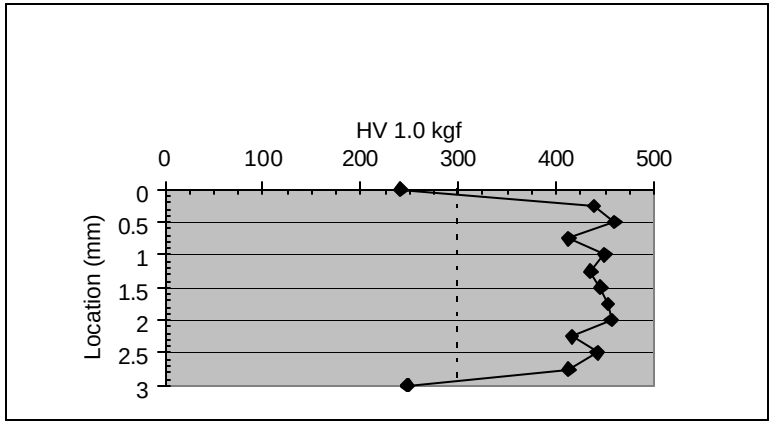

(c) Through-thickness hardness traverse of 1.55-mm DF140T with medium downslope time.

Figure 13. Hardness Traverse Plots for Material B, 1.55-mm (0.061-in.) Dual-Phase Steel with Medium Downslope Time
[The sample was welded using established parameters for Material B. This was immediately followed by a 40-cycle downslope to a final current of 60% (5.3 kA) of the welding current and a 300-cycle hold time. Results from the hardness traverse in the diagonal and through-thickness directions are presented using the VHN scale. The dashed lines represent independent hardness measurements of the unwelded base metal.]

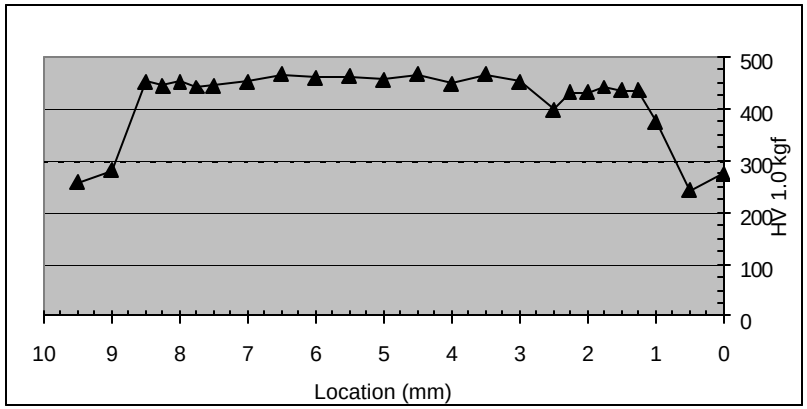

(a) Horizontal hardness traverse of 1.55-mm DF140T with long downslope time.

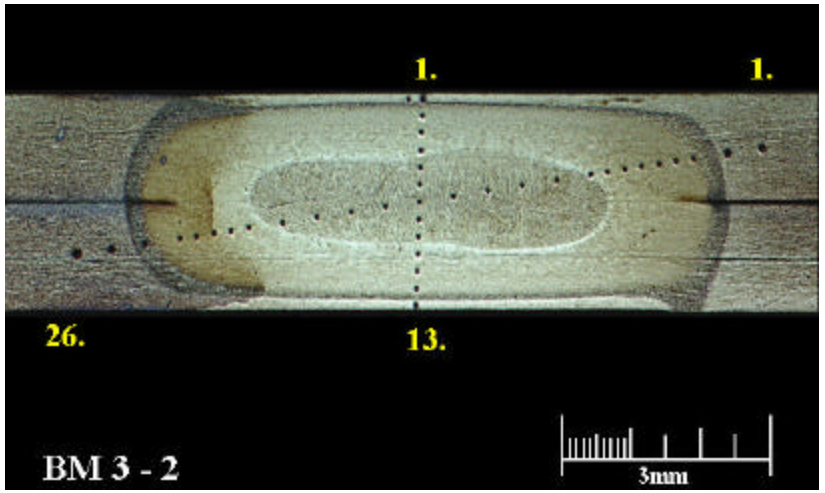

(b) Micrograph of 1.55-mm DF140T with long downslope time.

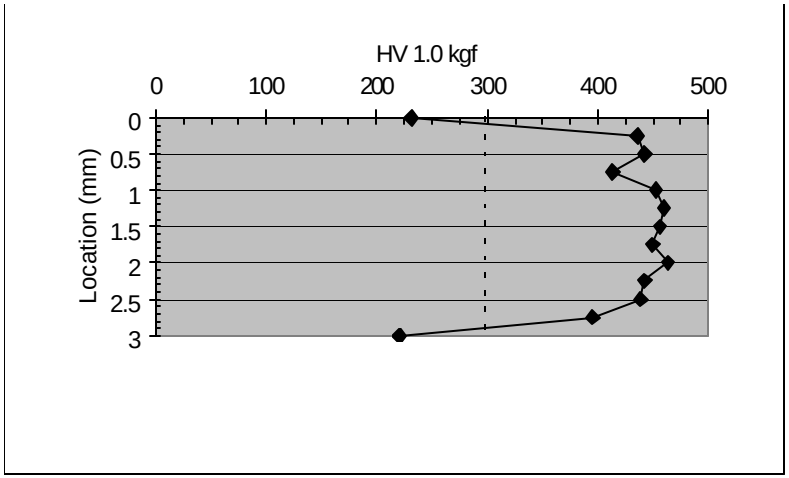

(c) Through-thickness hardness traverse of 1.55-mm DF140T with long downslope time.

Figure 14. Hardness Traverse Plots for Material B, 1.55-mm (0.061-in.) Dual-Phase Steel with Long Downslope Time
[The sample was welded using established parameters for Material B. This was immediately followed by a 99-cycle downslope time to a final current of 60% (5.3 kA) of the welding current. The sample was then held under full force for an additional 300-cycles without additional current. Results from the hardness traverse in the diagonal and through thickness directions are presented using the VHN scale. The dashed lines represent independent hardness measurements of the unwelded base metal.]

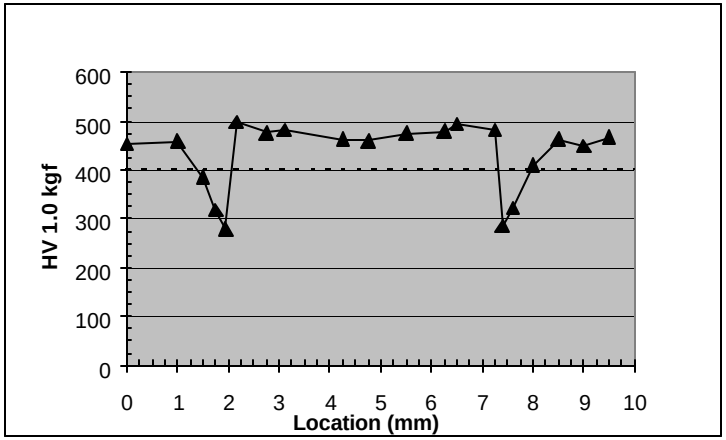

(a) Diagonal hardness traverse of 0.94-mm M190 with short downslope time.

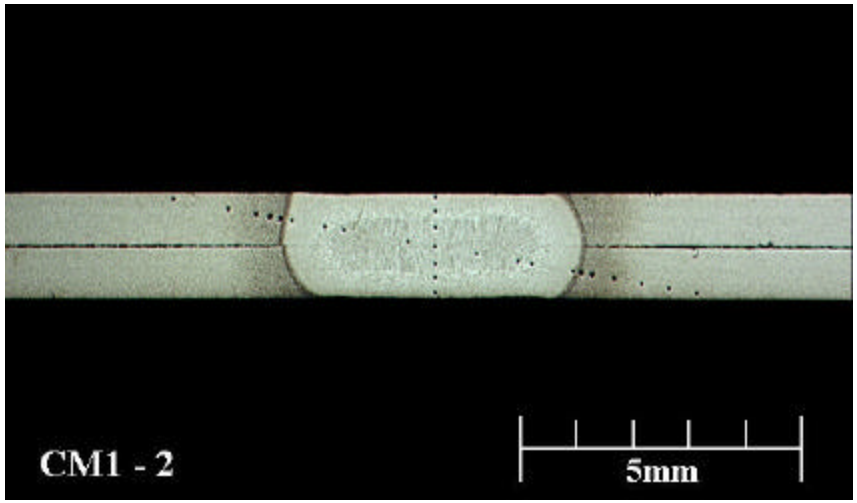

(b) Micrograph of 0.94-mm M190 with short downslope time.

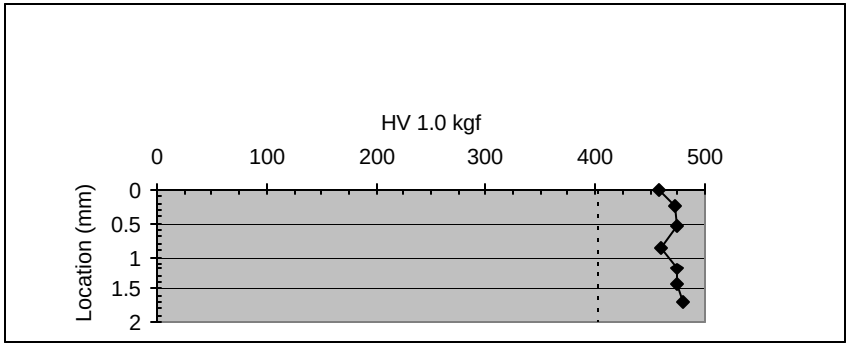

(c) Vertical hardness traverse of 0.94-mm M190 with short downslope time.

Figure 15. Hardness Traverse Plots for Material C, 0.94-mm (0.037-in.) Martensitic Steel with Short Downslope Time
[The sample was welded using established parameters for Material C. This was immediately followed by a 5-cycle downslope time to a final current of 60% (3.9 kA) of the welding current and a 300-cycle hold time. Results from the diagonal and the through-thickness hardness traverse are presented using the VHN scale. The dashed line represents an independent hardness measurement of unwelded base metal.]

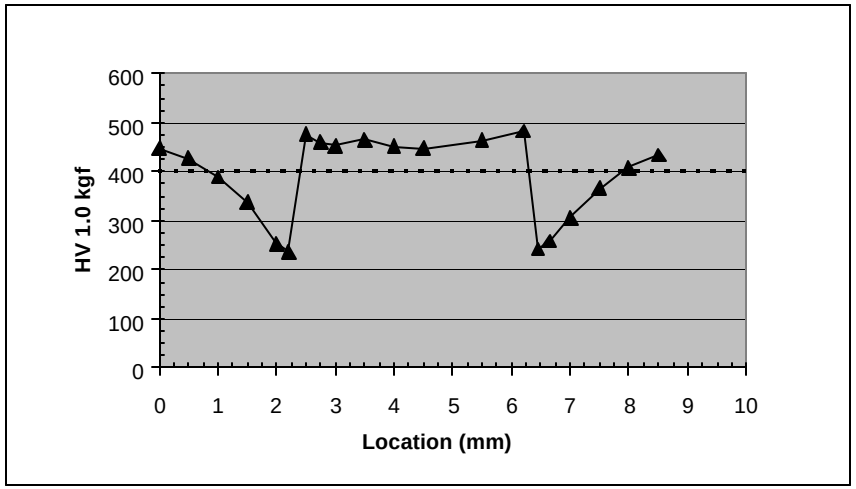

(a) Diagonal hardness traverse of 0.94-mm M190 with medium downslope time.

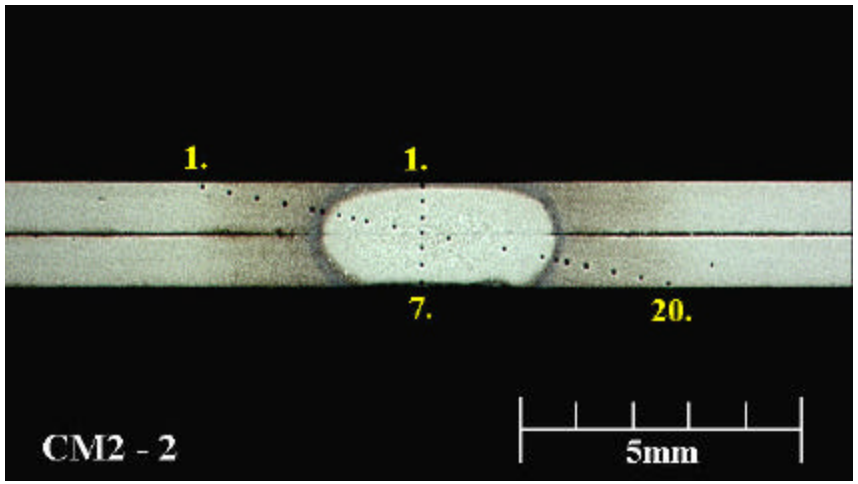

(b) Micrograph of 0.94-mm M190 with medium downslope time.

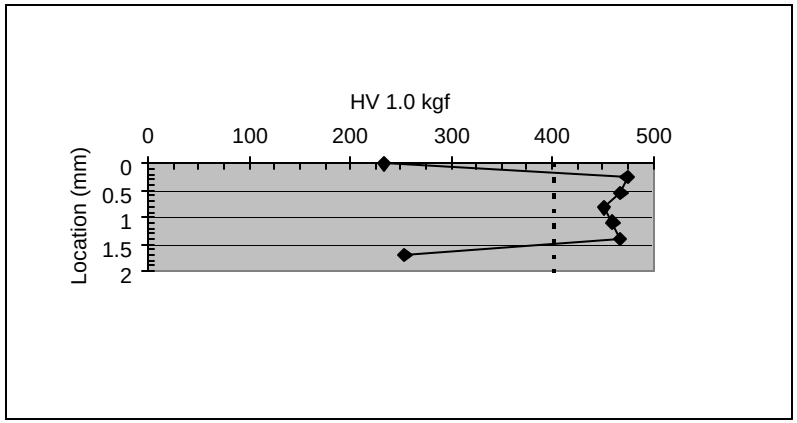

(c) Through-thickness hardness traverse of 0.94-mm M190 with medium downslope time.

Figure 16. Hardness Traverse Plots for Material C, 0.94-mm (0.037-in.) Martensitic Steel with Medium Downslope Time
[The sample was welded using established parameters for Material C. This was immediately followed by a 60-cycle downslope time to a final current of 60% (3.9 kA) of the welding current and a 300-cycle hold time. Results from the diagonal and the through-thickness hardness traverse are presented using the VHN scale. The dashed line represents an independent hardness measurement of unwelded base metal.]

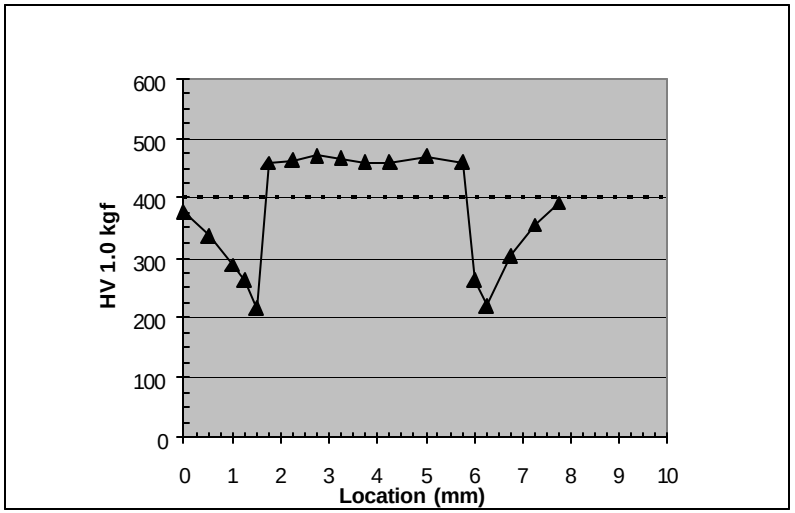

(a) Horizontal hardness traverse of 0.94-mm M190 with long downslope time.

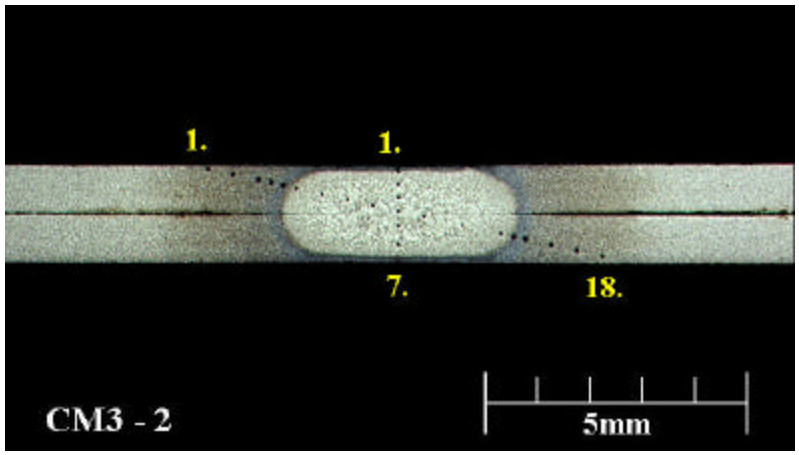

(b) Micrograph of 0.94-mm M190 with long downslope time.

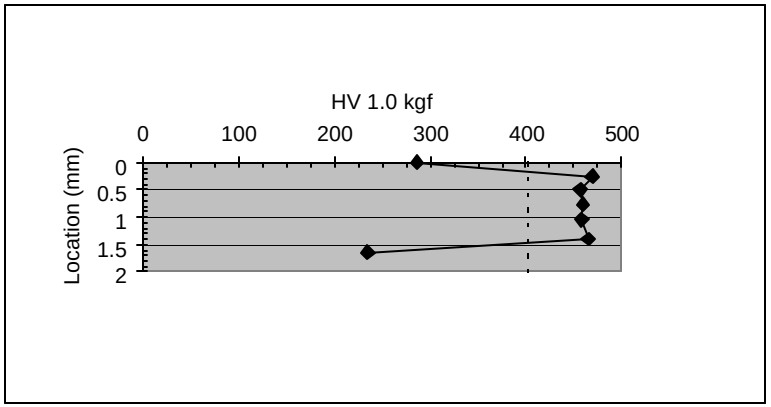

(c) Through-thickness hardness traverse of 0.94-mm M190 with long downslope time.

Figure 17. Hardness Traverse Plots for Material C, 0.94-mm (0.037-in.) Martensitic with Long Downslope Time [The sample was welded using established parameters for Material C. This was immediately followed by a 99-cycle downslope time to a final current of 60% (3.9 kA) of the welding current. After the downslope the sample was held under full force for an additional 300 cycles without additional current. Results from the hardness traverse in the vertical direction and the standard hardness traverse are presented using the VHN scale.]

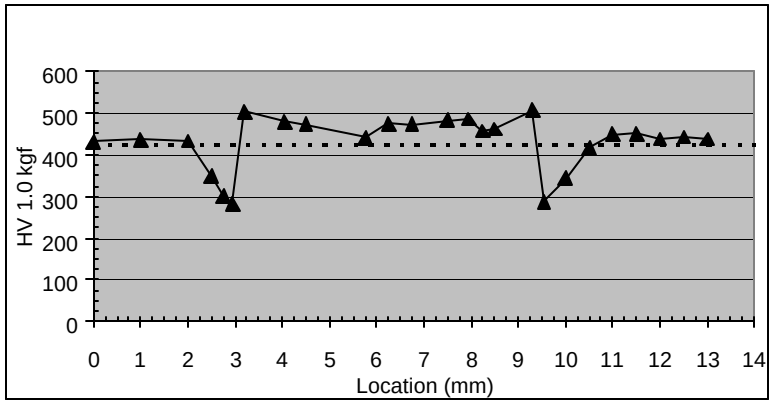

(a) Diagonal hardness traverse of 1.58-mm M190 with short downslope time.

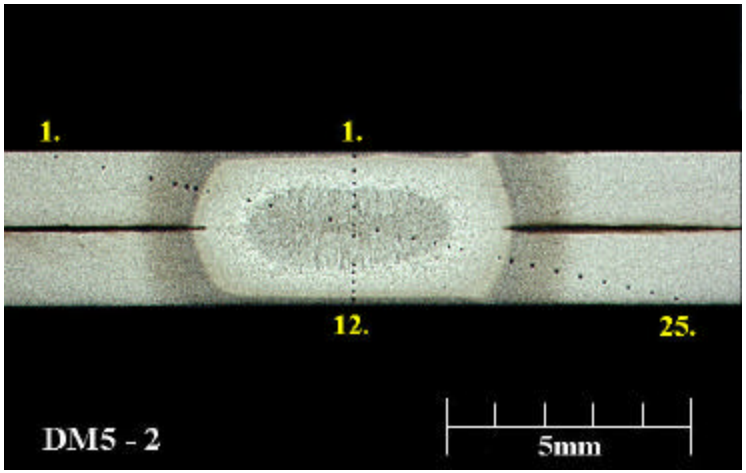

(b) Micrograph of 1.58-mm M190 with short downslope time.

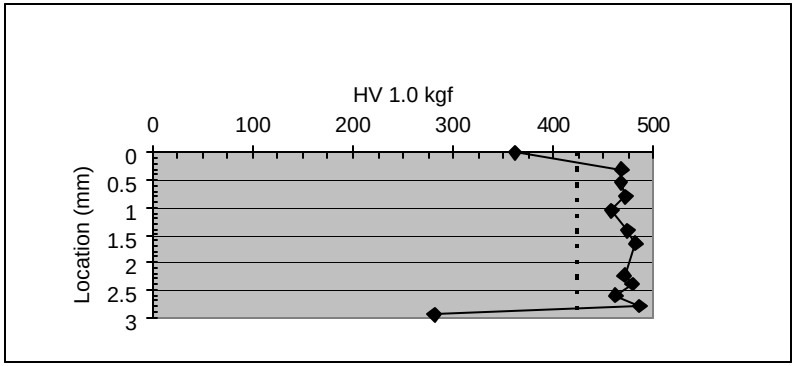

(c) Through-thickness hardness traverse of 1.58-mm M190 with short downslope time.

Figure 18. Hardness Traverse Plots for Material D, 1.58-mm (0.062-in.) Martensitic Steel with Short Downslope Time
[The sample was welded using established parameters for Material C. This was immediately followed by a 5-cycle downslope time to a final current of 48% (4.4 kA) of the welding current and a 300-cycle hold time. Results from the diagonal and through-thickness hardness traverses are presented using the VHN scale. The dashed lines represent independent measurements of unwelded base metal.]

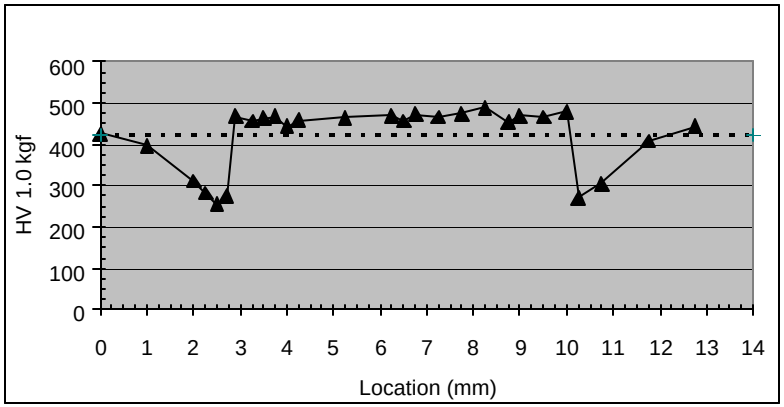

(a) Diagonal hardness traverse of 1.58-mm M190 with medium downslope time.

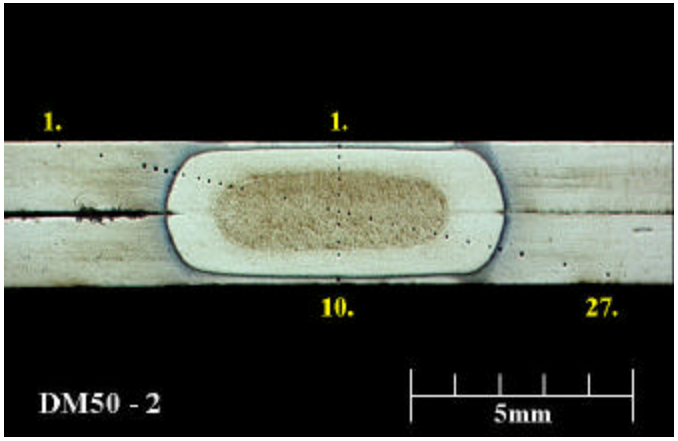

(b) Micrograph of 1.58-mm M190 with medium downslope time.

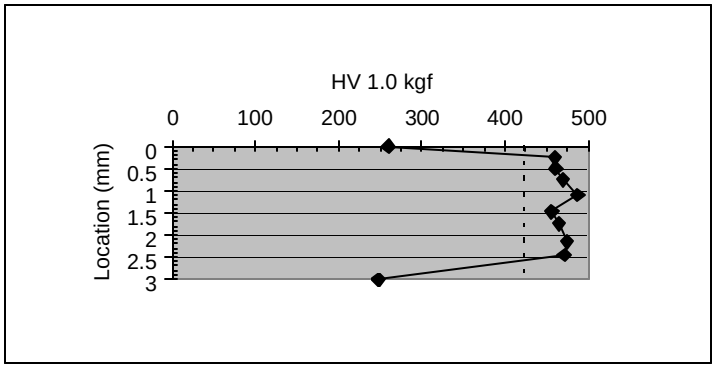

(c) Through-thickness hardness traverse of 1.58-mm M190 with medium downslope time.

Figure 19. Hardness Traverse Plots for Material D, 1.58-mm (0.062-in.) Martensitic Steel with Medium Downslope Time
[The sample was welded using established parameters for Material D. This was immediately followed by a 50-cycle downslope to a final current of 48% (4.4 kA) of the welding current and a 300-cycle hold time. Results from the hardness traverse in the diagonal and through-thickness directions are presented using the VHN scale. The dashed lines represent an independent hardness measurement of unwelded base metal.]

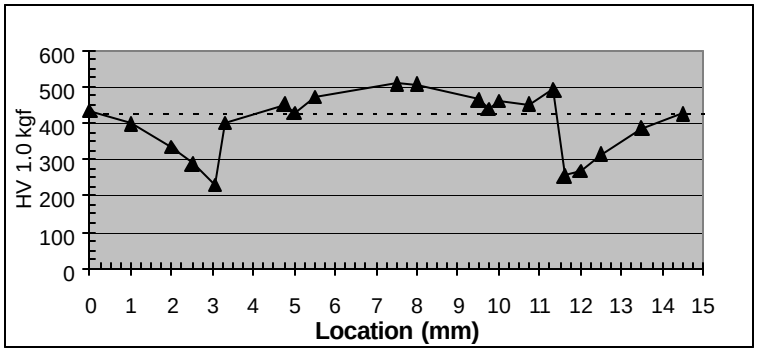

(a) Horizontal hardness traverse of 1.58-mm M190 with long downslope time.

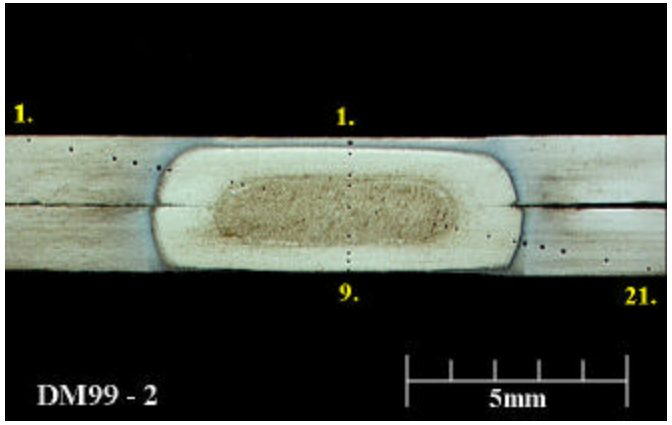

(b) Micrograph of 1.58-mm M190 with long downslope time.

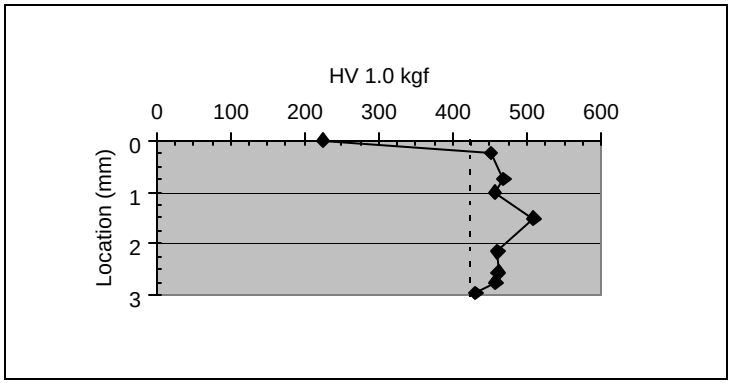

(c) Through-thickness hardness traverse of 1.58-mm M190 with long downslope time.

Figure 20. Hardness Traverse Plots for Material D, 1.58-mm (0.062-in.) Martensitic Steel with Long Downslope Time
[The sample was welded using established parameters for Material C. This was immediately followed by a 99-cycle downslope time to a final current of 48% (4.4 kA) of the welding current. The sample was then held under full force for an additional 300-cycles without additional current. Results from the hardness traverses in the through thickness and diagonal directions are presented using the VHN scale. The dashed lines represent an independent hardness measurement of unwelded base metal.]

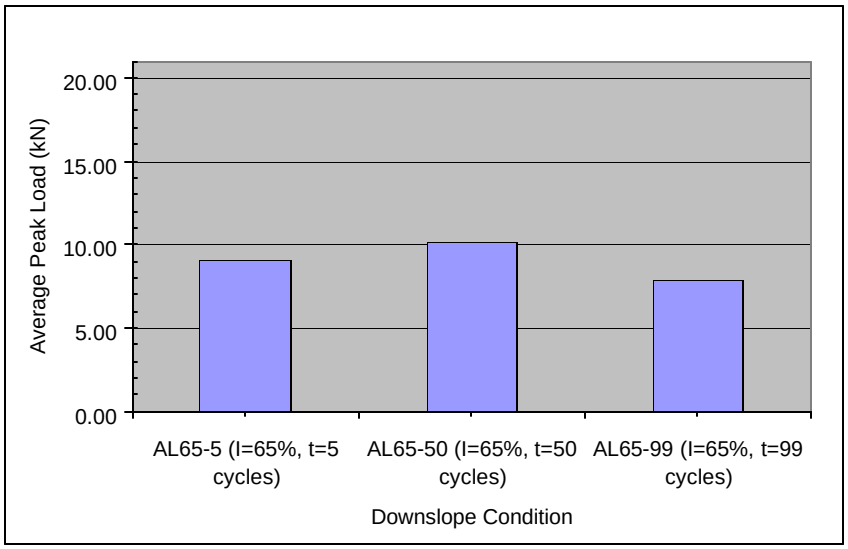

Figure 21. Lap-shear Tensile Test Results for Material A, 0.83-mm (0.033-in.) Dual-Phase Steel [All samples were welded with the established welding parameters for Material A. The cooling rate was controlled using a linear downslope from the welding current to a predefined percentage of the established welding current (65% weld current for Material A). The time used for short, medium and long downslope was 5-, 50-, and 99-cycles respectively.]

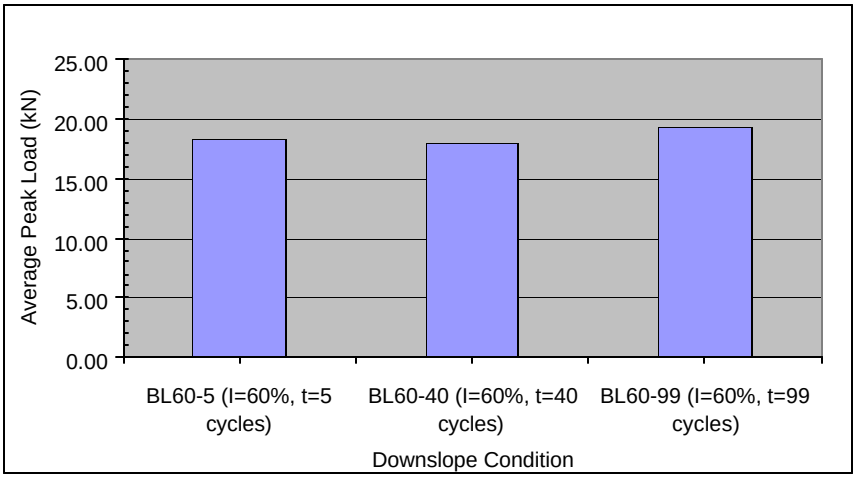

Figure 22. Lap-shear Tensile Test Results for Material B, 1.55-mm (0.061-in.) Dual-Phase Steel [All samples were welded with the established welding parameters for Material B. The cooling rate was controlled using linear downslope from the welding current to a predefined percentage of the established welding current (60% weld current for Material B). The time used for short, medium and long downslope was 5-, 40-, and 99-cycles respectively.]

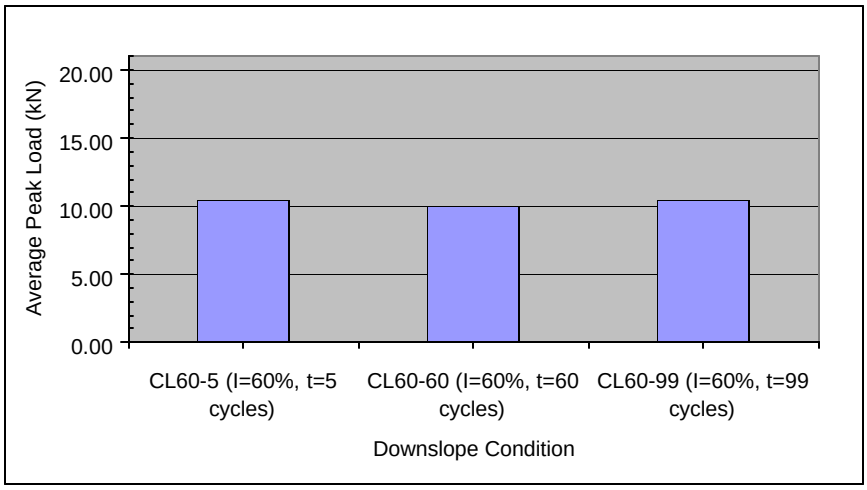

Figure 23. Lap-shear Tensile Test Results for Material C, 0.94-mm (0.037-in.) Martensitic Steel [All samples were welded with the established welding parameters for Material C. The cooling rate was controlled using linear downslope for the welding current to a predefined percentage of the established welding current (60% weld current for Material C). The time used for short, medium and long downslope was 5-, 60-, and 99-cycles respectively.]

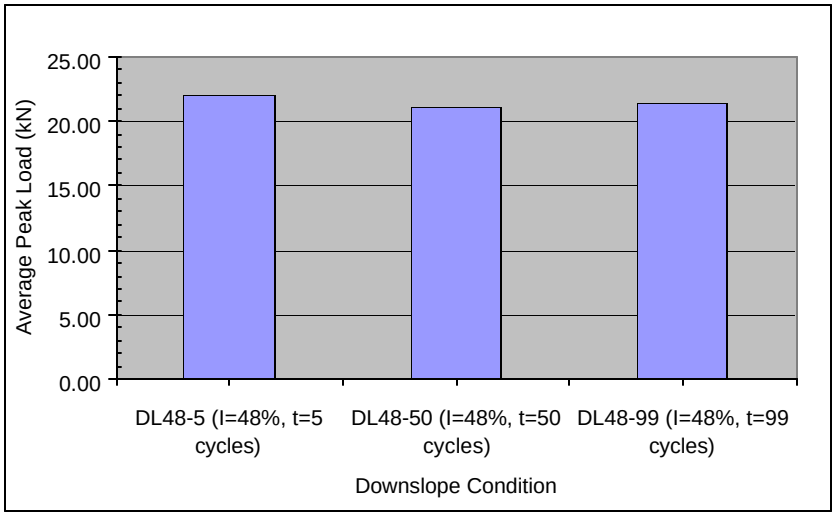

.

Figure 24. Lap-shear Tensile Test Results for Material D, 1.58-mm (0.062-in.) Martensitic Steel [All samples were welded with the established welding parameters for Material D. The cooling rate was controlled using linear downslope for the welding current to a predefined percentage of the established welding current (48% weld current for Material D). The time used for short, medium and long downslope was 5-, 50-, and 99-cycles respectively.]

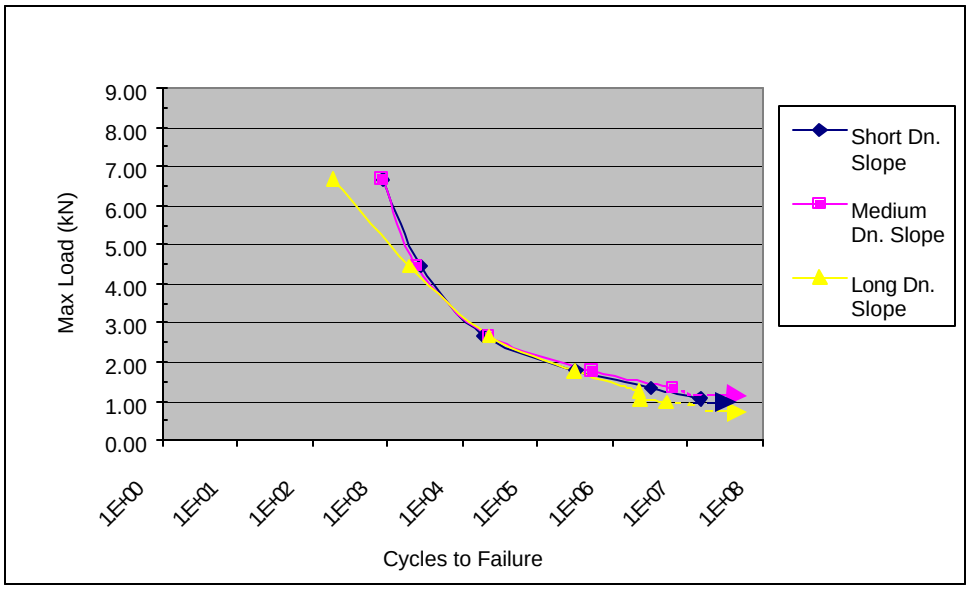

Figure 25. **S-N Curves for Material A, 0.83-mm (0.033-in.) Dual-Phase Steel** (Short-, medium-, and long-downslope conditions are plotted. Fatigue testing was halted after 10,000,000 cycles. This is represented by the dotted arrows.)

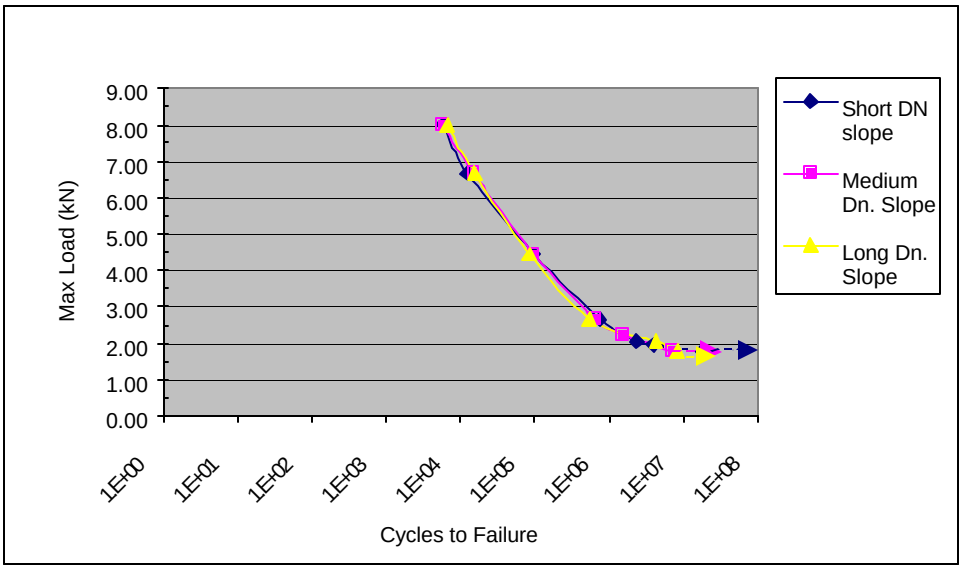

Figure 26. **S-N Curves for Material B, 1.55-mm (0.061-in.) Dual-Phase Steel** (Short-, medium-, and long-downslope conditions are plotted. Fatigue testing was halted after 10,000,000 cycles. This is represented by the dotted arrows.)

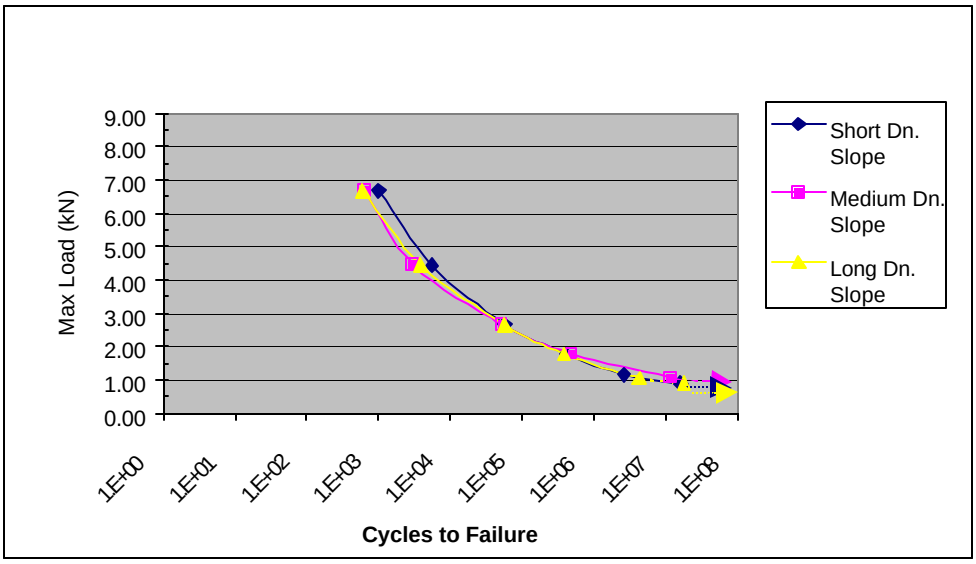

Figure 27. **S-N Curves for Material C, 0.94-mm (0.037-in.) Martensitic Steel** (Short-, medium-, and long-downslope conditions are plotted. Fatigue testing was halted after 10,000,000 cycles. This is represented by the dotted arrows.)

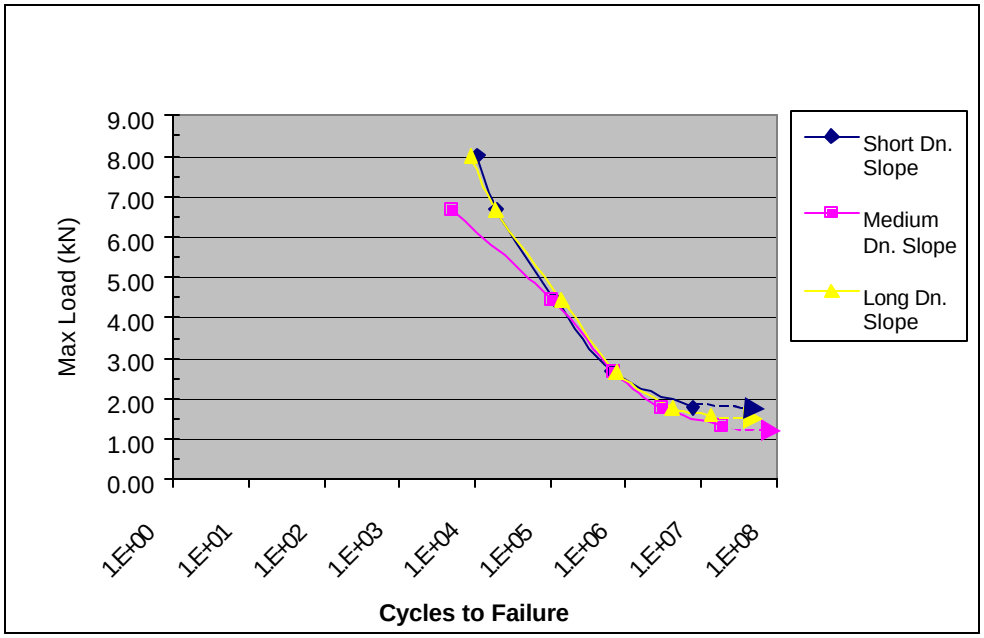

Figure 28. **S-N Curves for Material D, 1.58-mm (0.062-in.) Martensitic Steel** (Short-, medium-, and long-downslope conditions are plotted. Fatigue testing was halted after 10,000,000 cycles. This is represented by the dotted arrows.)

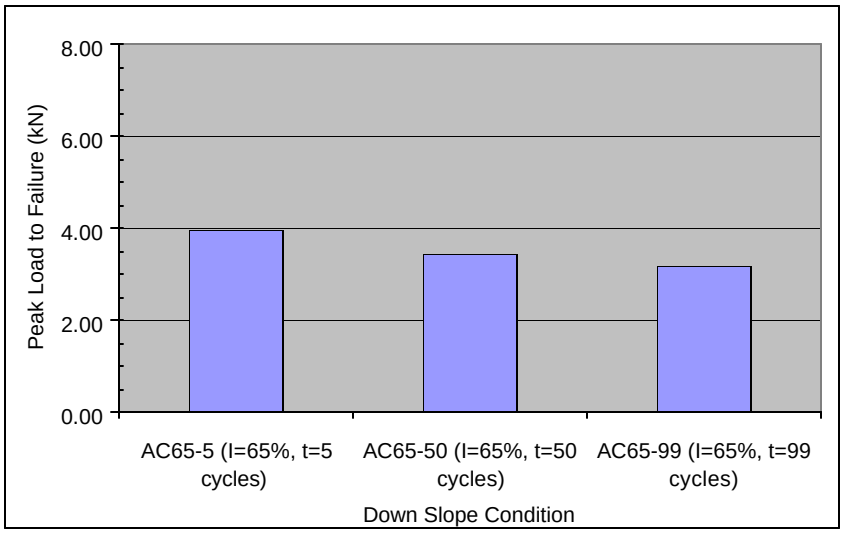

Figure 29. Cross-Tension Testing Results for Material A, 0.83-mm (0.033-in.) Dual-Phase Steel (Short-, medium-, and long-downslope conditions are plotted. "I" is the downslope end current expressed as a percentage of the established welding current. "t" is the time that downslope was applied.)

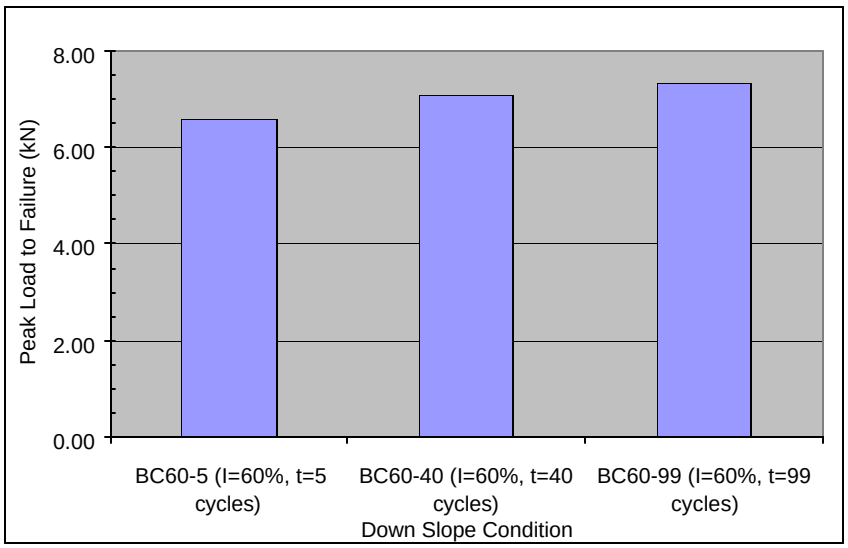

Figure 30. Cross-Tension Testing Results for Material B, 1.55-mm (0.061-in.) Dual-Phase Steel (Short-, medium-, and long-downslope conditions are plotted. "I" is the downslope end current expressed as a percentage of the established welding current. "t" is the time that downslope was applied.)

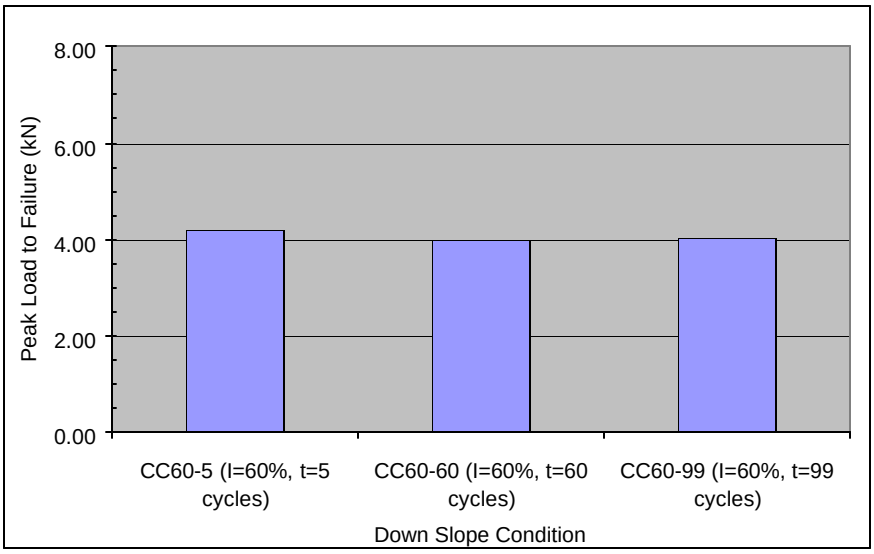

Figure 31. Cross-Tension Testing Results for Material C, 0.94-mm (0.037-in.) Martensitic Steel (Short-, medium-, and long-downslope conditions are plotted. "I" is the downslope end current expressed as a percentage of the established welding current. "t" is the time that downslope was applied.)

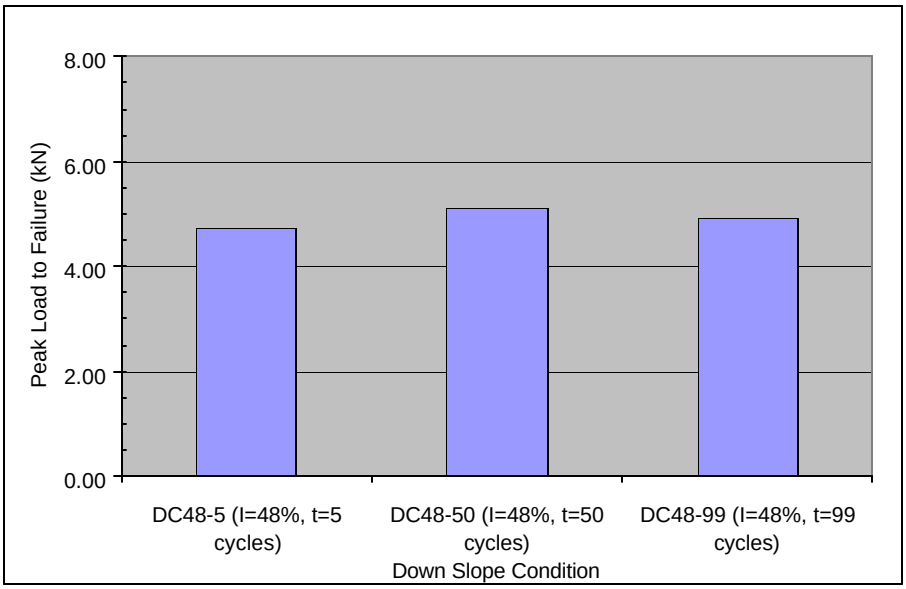

Figure 32. Cross-Tension Testing Results for Material D, 1.58-mm (0.062-in.) Martensitic Steel (Short-, medium-, and long-downslope conditions are plotted. "I" is the downslope end current expressed as a percentage of the established welding current. "t" is the time from that downslope was applied.)

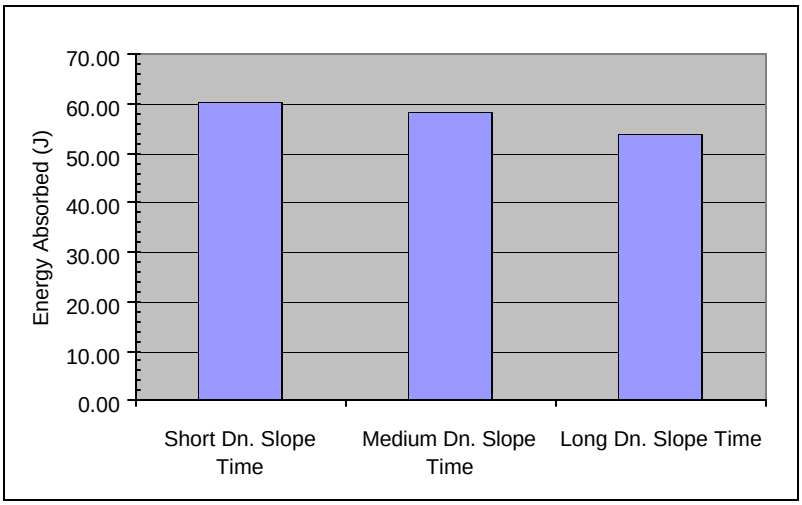

Figure 33. Cross-Tension Impact Results for Material A, 0.83-mm (0.033-in.) Dual-Phase Steel [All samples were welded with the established welding parameters for Material A. The cooling rate was controlled using a linear downslope from the welding current to a predefined percentage of the established welding current (65% weld current for Material A). The time used for short, medium and long downslope was 5-, 50-, and 99-cycles respectively.]

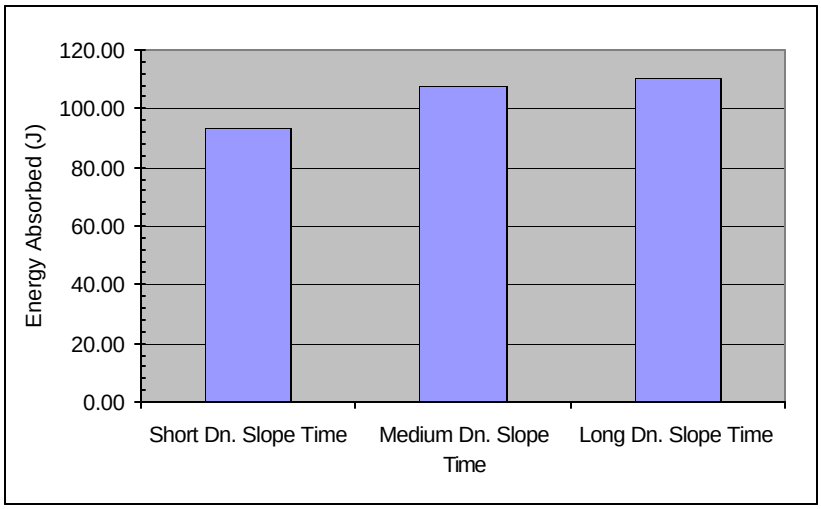

Figure 34. Cross-Tension Impact Results for Material B, 1.55-mm (0.061-in.) Dual-Phase Steel [All samples were welded with the established welding parameters for Material B. The cooling rate was controlled using linear downslope from the welding current to a predefined percentage of the established welding current (60% weld current for Material B). The time used for short, medium and long downslope was 5-, 40-, and 99-cycles respectively.]

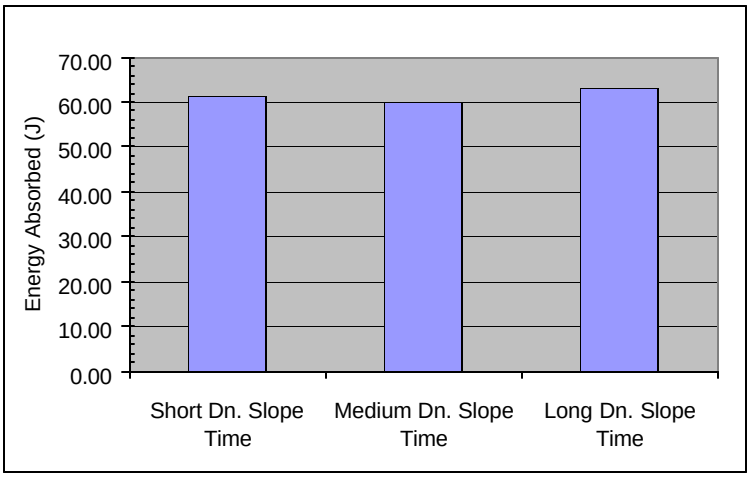

Figure 35. Cross-Tension Impact Results for Material C, 0.94-mm (0.037-in.) Martensitic Steel [All samples were welded with the established welding parameters for Material C. The cooling rate was controlled using linear downslope for the welding current to a predefined percentage of the established welding current (60% weld current for Material C). The time used for short, medium and long downslope was 5-, 60-, and 99-cycles respectively.]

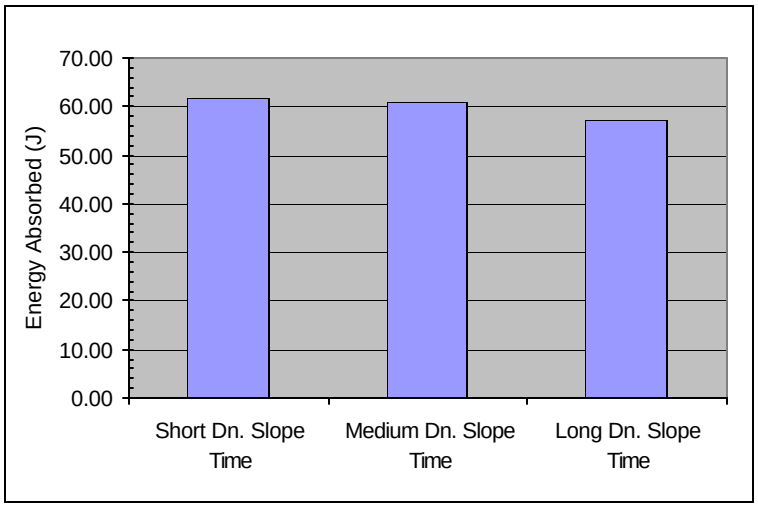

Figure 36. Cross-Tension Impact Results for Material D, 1.58-mm (0.062-in.) Martensitic Steel [All samples were welded with the established welding parameters for Material D. The cooling rate was controlled using linear downslope for the welding current to a predefined percentage of the established welding current (48% weld current for Material D). The time used for short, medium and long downslope was 5-, 50-, and 99-cycles respectively.]

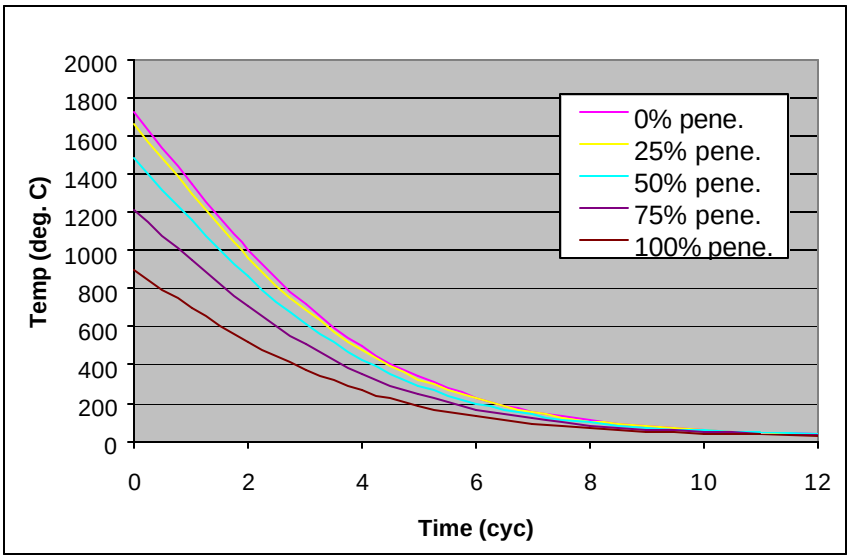

Figure 37. Predicted Cooling Profiles for a 0.8-mm (0.030-in.) -Thick Material Resistance Spot Weld [Results are presented for different levels of penetration in the workpiece, ranging from 0% (faying surface), to 100% (electrode-sheet surface).]

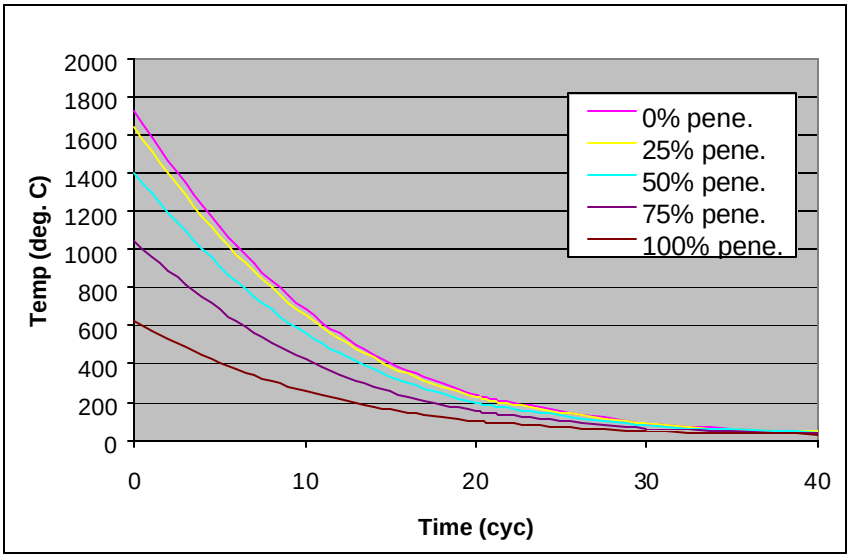

Figure 38. Predicted Cooling Profiles for a 1.55-mm (0.061-in.) -Thick Material Resistance Spot Weld [Results are presented for different levels of penetration in the workpiece, ranging from 0% (faying surface), to 100% (electrode-sheet surface).]

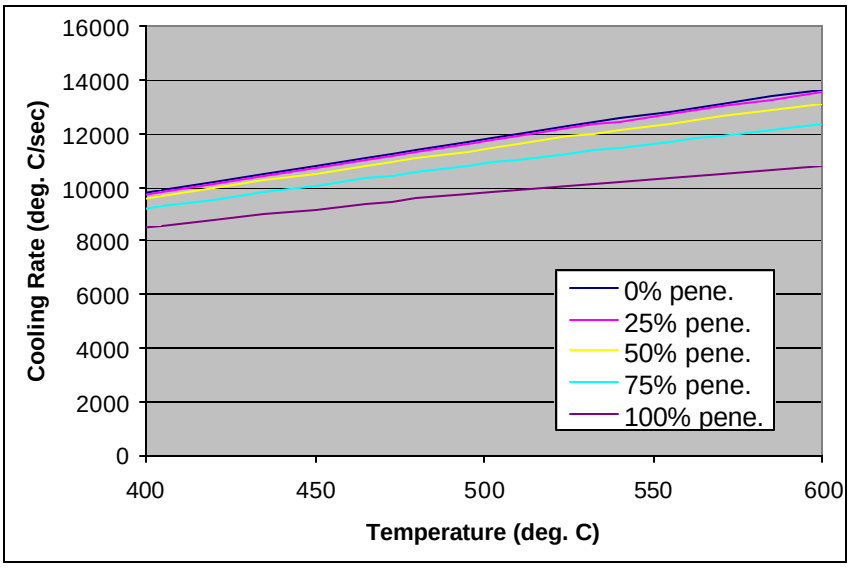

Figure 39. Predicted Cooling Rates for the Critical 400-600°C Temperature Regime on a 0.8-mm (0.030-in.) -Thick Material Resistance Spot Weld [Results are presented for different levels of penetration in the workpiece, ranging from 0% (faying surface), to 100% (electrode-sheet surface).]

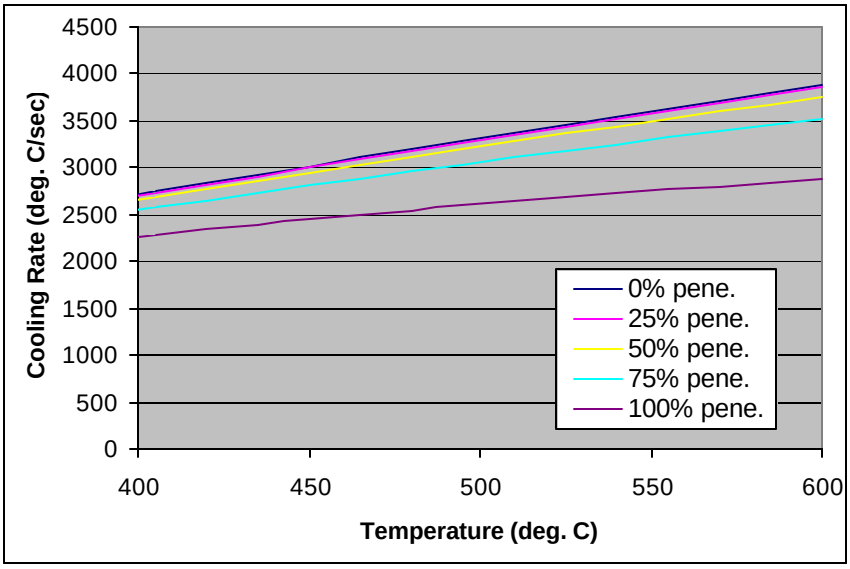

Figure 40. Predicted Cooling Rates for the Critical 400-600°C Temperature Regime on a 1.55-mm (0.061-in.) -Thick Material Resistance Spot Weld [Results are presented for different levels of penetration in the workpiece, ranging from 0% (faying surface), to 100% (electrode-sheet surface).]

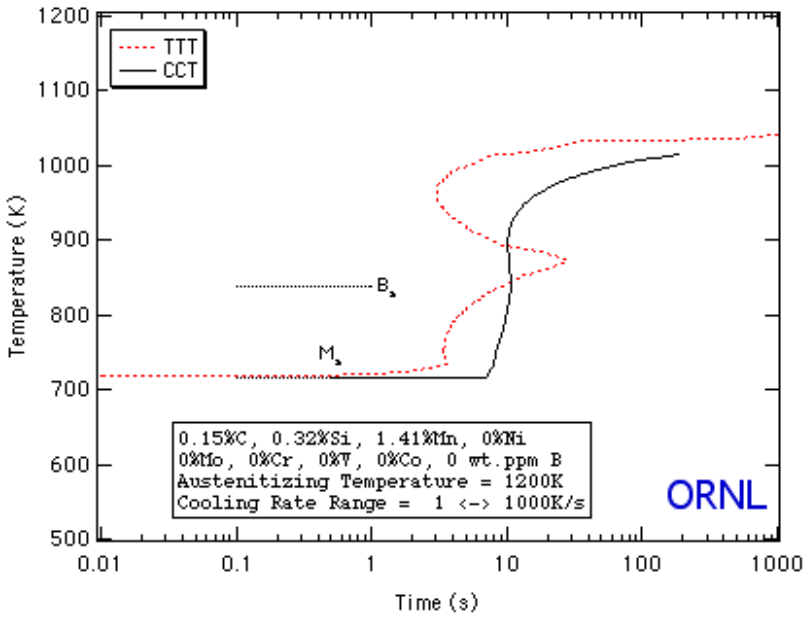

Figure 41. CCT/TTT Diagram for the Dual-Phase Steel used in this Study (Diagram was obtained using a phase-transformation model developed at Oak Ridge National Laboratory, and accessed at http://engm01.ms.ornl.gov.)

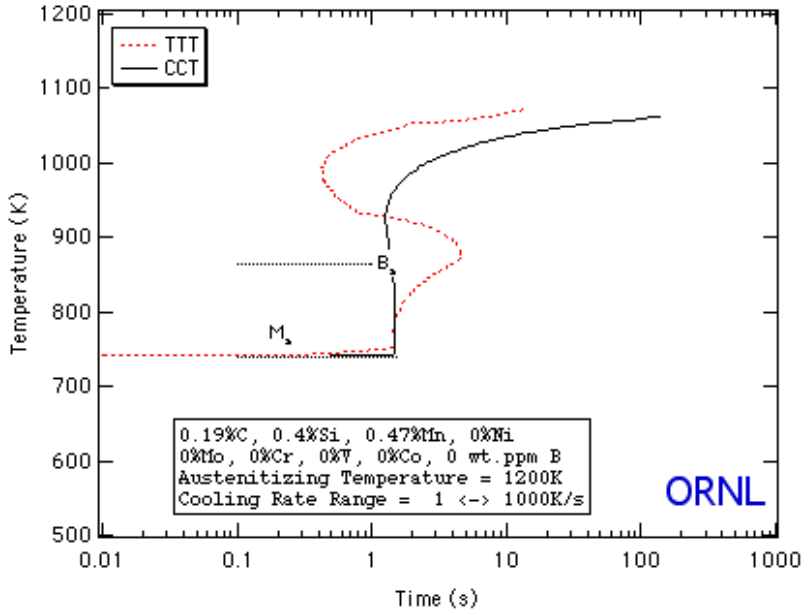

Figure 42. CCT/TTT Diagram for the Martensitic Steel used in this Study (Diagram was obtained using a phase-transformation model developed at Oak Ridge National Laboratory, and accessed at http://engm01.ms.ornl.gov.)